4. SITE 794[1]

Shipboard Scientific Party[2]

HOLE 794A

Date occupied: 26 June 1989

Date departed: 29 June 1989

Time on hole: 2 days, 12 hr, 15 min

Position: 40°11.41′N, 138°13.86′E

Bottom felt (rig floor; m; drill-pipe measurement): 2821.7

Distance between rig floor and sea level (m): 10.70

Water depth (drill-pipe measurement from sea level, m): 2811.0

Total depth (rig floor; m): 2821.70

Penetration (m): 351.3

Number of cores (including cores with no recovery): 37

Total length of cored section (m): 351.30

Total core recovered (m): 302.16

Core recovery (%): 86

Oldest sediment cored:
Depth sub-bottom (m): 351.30
Nature: clay/claystone
Earliest age:
Latest age: late Miocene?
Measured velocity (km/s):

Hard rock:
Depth sub-bottom (m):
Nature:
Measured velocity (km/s):

Basement:
Depth sub-bottom (m):
Nature:
Measured velocity (km/s):

Drill below core (m):

Comments: velocity not determinable due to equipment problem.

HOLE 794B

Date occupied: 29 June 1989

Date departed: 4 July 1989

Time on hole: 5 days, 8 hr, 15 min

Position: 40°11.40′N, 138°13.87′E

Bottom felt (rig floor; m; drill-pipe measurement): 2821.7

Distance between rig floor and sea level (m): 10.70

Water depth (drill-pipe measurement from sea level, m): 2811.0

Total depth (rig floor; m): 2821.70

Penetration (m): 249.2

Number of cores (including cores with no recovery): 27

Total length of cored section (m): 249.20

Total core recovered (m): 87.40

Core recovery (%): 35

Oldest sediment cored:
Depth sub-bottom (m): 414.50
Nature: dolomitic claystone
Earliest age:
Latest age: middle Miocene
Measured velocity (km/s): 4.5

Hard rock:
Depth sub-bottom (m):
Nature:
Measured velocity (km/s):

Basement:
Depth sub-bottom (m):
Nature:
Measured velocity (km/s):

Drill below core (m):

Comments:

HOLE 794C

Date occupied: 4 July 1989

Date departed: 11 July 1989

Time on hole: 6 days, 14 hr, 30 min

Position: 40°11.40′N, 138°13.86′E

Bottom felt (rig floor; m; drill-pipe measurement): 2820.0

Distance between rig floor and sea level (m): 10.70

Water depth (drill-pipe measurement from sea level, m): 2809.3

Total depth (rig floor; m): 2820.00

Penetration (m): 93.3

Number of cores (including cores with no recovery): 14

Total length of cored section (m): 93.90

Total core recovered (m): 33.21

Core recovery (%): 35

Oldest sediment cored:
Depth sub-bottom (m): 646.04
Nature: tuff and tuffaceous silty claystone
Earliest age: Undetermined
Latest age:
Measured velocity (km/s): 3.5

Hard rock:
Depth sub-bottom (m): 653.70
Nature: Fine- to medium-grained dolerite
Measured velocity (km/s): 4.5

Basement:
Depth sub-bottom (m):
Nature:
Measured velocity (km/s):

Drill below core (m):

Comments:

[1] Tamaki, K., Pisciotto, K., Allan, J., et al., 1990. *Proc. ODP, Init. Repts.*, 127: College Station, TX (Ocean Drilling Program).

[2] Shipboard Scientific Party is as given in the list of participants preceding the contents.

Principal results: The specific objectives at Site 794, located in the northern Yamato Basin, were: (1) to determine the nature and age of the basement; (2) to measure the direction of the present stress field; and (3) to characterize the sedimentation, subsidence, and oceanographic evolution of the area. The results at Site 794 are summarized below and in Figures 1A through 1D. The principal results are:

1. A dolerite sill complex was encountered in the deepest penetration. The age of the claystone above the uppermost sill gives a minimum age of basin initiation at this site of 14.8–16.2 Ma. The exact age and nature of basement, however, is still uncertain because: (a) the tuff and claystone beneath the 100 m-thick interval of dolerite sills could not be dated; and (b) the acoustically-opaque seismic interval, which underlies the highly reflective dolerite sill complex and which may represent true basement, was not penetrated.
2. The *in-situ* stress field determinations could not be completed because the logging and packer tools used to make the measurements could not be run past the stuck pipe in Hole 794C.
3. The lithologic and paleontologic data available indicate that this area of the northern Yamato Basin evolved in four notable stages: (a) a pre-middle Miocene stage, represented by only about 1.5 m of bioturbated, graded and slump-folded tuff and tuffaceous claystone, was probably deposited in an oxygenated basinal setting during a period of explosive volcanism. This strata was later intruded by dolerite sills. (b) a middle Miocene period characterized by bioturbated, hemipelagic calcareous claystones, gravity-flow tuffs, and minor glauconite, deposited at upper middle bathyal depths (~500 m) in suboxic marine waters on a slope or borderland ridge; followed by (c) subsidence to lower middle bathyal depths (~>1500 m) during the late Miocene and deposition of hemipelagic diatomaceous sediments with increasing amounts of volcanic ash through the early Pliocene in cool, well-oxygenated waters; and finally, (d) a late Pliocene to Holocene period in which surface water temperatures varied and the basin continued to subside to its present-day lower bathyal depth. During this stage diatomaceous sedimentation shut down, volcanic ash production and terrigenous input increased, and oscillating climate and tectonic activity conspired to produce interbedded dark and light hemipelagic sediments. Except for parts of the Quaternary, preservation of primary biogenic carbonate is poor, suggesting a consistently shallow carbonate compensation depth (CCD) (<1500 m) or corrosive bottom waters. In addition, burial diagenesis has led to wholesale dissolution of siliceous microfossils in the lower part of the Miocene-Pliocene diatomaceous interval and the formation of opal-CT and quartz.

Location and Approach

Site 794 is located in the northernmost Yamato Basin at proposed Site J1b-1 as planned. The site was confirmed by two *JOIDES Resolution* seismic lines. The first crossing was along multichannel seismic Line 108 on which the original Site J1b-1 is located. Two sonobuoys of rather old vintage were dropped along this line, but both failed only 30–45 min following deployment. After the confirmation of the site, a second crossing was made that was parallel with DELP multichannel Line E. After reconfirming the site on this crossing to avoid any local closure, the *JOIDES Resolution* continued past the site then turned and retraced the line with seismics. On the third crossing of the site, the beacon was dropped.

Lithology

The sedimentary section cored in Holes 794A and 794B consists mostly of fine-grained hemipelagic sediments of Quaternary to early middle/late early Miocene age. Tuffs and tuffaceous sediments were recovered from Hole 794C between dolerite sills. The division of units is as follows:

Unit I (0–92.3 mbsf): Quaternary-late Pliocene clay and silty clay. The upper 63.8 m consists of alternating light bioturbated zones and dark laminated zones with common thin ash layers. The lower 28.5 m is similar to the upper interval but with fewer dark zones. Diatoms increase downsection.

Unit II (92.3–293.5 mbsf): late Pliocene–late Miocene diatom ooze and clay. The upper 201.2 m consists of bioturbated ooze and clayey ooze with sparse ash layers. Diatomaceous clay comprises the lower 76.6 m. Diatoms decrease and opal-CT cement increases in this interval.

Unit III (293.6–491.7 mbsf): 8.1–~14.6 Ma late Miocene–middle Miocene clay and siliceous claystone. The upper 57.8 m is bioturbated clay and siliceous claystone with minor ash, pyrite, and micritic carbonate. The lower 140.3 m is bioturbated claystone with rare laminated intervals. Porcellanites occur at several levels and dolomitic, sideritic, siliceous cements and calcareous lenses are common.

Unit IV (491.7–520.6 mbsf): middle Miocene tuff and claystone. This unit consists of interbedded tuff, lapilli tuff, and claystone. Tuffs are variously thin- to thick-bedded, normal to inversely graded with sharp basal contacts. Some beds contain planar, convolute, and cross laminations. Others contain burrowed intervals and are massive and poorly sorted with claystone fragments. Interbedded claystones are moderately bioturbated.

Unit V (520.6–543 mbsf): middle Miocene claystone. This unit consists of interbedded claystones of variable compositions with minor interbedded tuff. From top to bottom, silty claystone, claystone, and black claystone are the dominant lithologies. Minor thin intervals and lenses of glauconitic claystone, secondary carbonate, and pyrite are also present in these moderately bioturbated claystones. Sparse, thin tuff layers display cross laminations and flame structures.

Unit VI (644.1–645.6 mbsf: middle Miocene(?) tuff and tuffaceous claystone. This unit is separated from Unit V by 100 m of dolerite. It consists of bioturbated claystone and massive to laminated, fine-grained tuff. The tuff also shows convolute laminations, small slump folds, normal size grading, and bioturbated tops.

Age and Sediment Accumulation Rate

Ages of sediments are well constrained by diatom zones in Unit I and Unit II (0–293.5 mbsf). Below this level the diatoms decrease in abundance; the coincident increase in opal-CT indicates dissolution of diatoms due to burial diagenesis. Foraminifers, nannofossils, and radiolarians occur sporadically throughout these cores. Where present, they confirm diatom dates but, because of poor preservation and/or sparse populations, they do not add accuracy or precision. In contrast, an excellent paleomagnetic reversal record is present up to almost the bottom of the Gilbert epoch (~5 Ma at 150 mbsf), giving precise time marks from the Pleistocene to Pliocene. Below Unit III (293.5 mbsf), only sparse, poorly preserved calcareous nannofossils and planktonic foraminifers provide age control. The oldest paleontologic age assigned is in the range 14.8–16.2 Ma for the claystone overlying the dolerite (530.3–543 mbsf). Using all of the age data, the sedimentation rates for three of the four depositional stages of evolution are: 36–38 m/m.y. for the middle Miocene sediments, 25–54 m/m.y. for the upper Miocene through upper Pliocene sediments, and 30–35 m/m.y. for the uppermost Pliocene-Quaternary sediments. Reliable estimates of sedimentation rates for the early middle (?) Miocene tuffs and claystones was not possible because of poor age control and the presence of intrusive dolerites. All rates are computed using present-day compacted sediment thicknesses. Uncompacted rates show the same relative variations.

Magnetics

Magnetic susceptibilities were generally very low, below 10 ($4+ \times 10^{-6}$ cgs units) except for the uppermost portion of Hole 794A, where ash layers caused susceptibilities to range between 20 and 50. The magnetic intensities of the sediments were also low (usually below 5 Ma/m). The paleomagnetic results were able to identify the chrons and subchrons for the Pleistocene and Pliocene (from the Brunhes to Gilbert chrons, in the upper 150 m of core), but results derived from all XCB and RCB cores are inconclusive.

The magnetic susceptibility of the igneous rocks from Hole 794C ranges from 1000 to 2500, increasing from top to bottom.

Geochemistry

Sediments from Holes 794A and 794B are characterized by low organic carbon contents (TOC), range (0.1%–3.0%; average (0.7%) and by increases in diagenetic silica and carbonate with depth, particularly below 300 mbsf. Diatoms (opal-A) and volcanic glass decrease markedly below this level. Biogenic carbonate is sparse through-

out much of the sediment column. Interstitial water profiles also show pronounced gradient changes below the 300-mbsf level. In particular, Ca increases and Mg, K, and Li decrease sharply, coincident with diagenesis of the sediments. Sulfate is present throughout, indicating that the entire section is within the zone of sulfate reduction. Virtually no hydrocarbon gases were detected. Methane levels from headspace analysis were only a few ppm and indistinguishable from background levels measured in the shipboard laboratory. No gas was observed in core liners, and this was confirmed by Vacutainer gas samples. No safety problems related to gas were encountered at this site.

Igneous Rocks

Dolerite of tholeiitic composition is the principal igneous rock type recovered in Holes 794B and 794C. The penetration below the first contact between the dolerite and sediments (543 mbsf) is 6 m in Hole 794B and 109.4 m in Hole 794C. A total of 34.5 m were recovered below this contact (including sedimentary Unit VI: 1.5 m thick, 644.1–645.6 mbsf). The igneous rocks are divided into six units based on chemistry and texture as shown below. The upper two units have rather high acoustic velocities (4.6–5.2 km/s) compared to the lower units (3.5–4.3 km/s). Each unit is thought to represent a separate intrusive sill. Most of the igneous rocks are highly altered and the ages are unknown.

Unit 1 (542 mbsf to 545–560 mbsf): moderately plagioclase phyric dolerite. A horizontal contact is observed at the top of this unit, with a thin zone of baked clay sediment above and a chilled margin of moderately plagioclase phyric basalt below.

Unit 2 (545–560 mbsf to 593 mbsf): moderately to highly plagioclase phyric dolerite. This unit is primarily massive and dense, with some highly fractured intervals.

Unit 3 (593 mbsf to 617–623 mbsf): aphyric dolerite. This unit is moderately vesicular, massive, and highly fractured.

Unit 4 (617–623 mbsf to 629–634 mbsf): aphyric dolerite. This unit is composed of massive, vesicular, medium to fine grained aphyric dolerite. The upper half of the unit is highly fractured, whereas the lower half has few fractures.

Unit 5 (629–634 mbsf to 644 mbsf): aphyric dolerite. This unit is highly vesicular. The lower boundary of the unit is sharply defined by a baked contact with tuffaceous sediments.

Unit 6 (646–647 mbsf): aphyric basalt. The top of this unit is defined by a chilled, intrusive margin against tuffaceous sediments.

Seismic Stratigraphy

Six distinct seismic intervals occur at the site. From top to bottom they are: (1) an upper weakly stratified interval; (2) a transparent interval containing some hummocky reflectors; (3) a middle strongly stratified interval; (4) a lower moderately well stratified interval; (5) a lowermost highly reflective interval, and (6) an unstratified, acoustically-opaque zone. Interval 1 correlates to Unit I and upper part of Unit II. Interval 2 correlates to the lower part of Unit II. Interval 3 corresponds to the upper part of Unit III; its top is coincident with the opal-A/opal-CT transition. Interval 4 corresponds to the lower part of Unit III and all of Units IV and V. Interval 5 includes igneous Units 1–6 and interbedded sedimentary Unit VI. Seismic Interval 6 corresponds to acoustic basement, which was not penetrated in Holes 794A, 794B, or 794C. All seismic interval boundaries correspond to stratal boundaries except the top of Interval 2/base of Interval 1, which is the diagenetic boundary between opal-A and opal-CT.

Heat Flow and Temperature

Successful temperature measurements were made using the Uyeda probe at 13 horizons down to 351 mbsf in Hole 794A. The measured temperature gradient is 125°C/km. The calculated heat flow value using this gradient and measured thermal conductivities is 103 mW/m^2. This value matches the average heat flow value of the Yamato Basin (97 ± 12 Mw/m^2).

Logging and Physical Properties

Three successful logging runs were completed in Hole 794B. The tool strings run were the geophysical/lithodensity, geochemistry, and the formation microscanner (combination of Sonic/Lithodensity/Temperature/DIT, Geochem, and FMS). The shallow basement penetration (5 m) did not permit logging of the basement-sediment contact. The maximum logging depth reached was 6 m above the basement (537 mbsf, basement 543 mbsf) contact. Of the data processed and examined on board, the resistivity, velocity, and bulk density profiles characterize the sedimentary section. The boundary between Units II and III at 293 mbsf is clearly shown on all three profiles by an increase in density, resistivity, and sonic velocity. This corresponds to the opal-A/opal-CT transition. Significant noise problems are evident in the sonic log from 335 to 365 mbsf, possibly indicating a complex structure of alternating high and low velocity layers. Another break occurs at about 400 mbsf, within Unit III at the opal-CT/quartz transition. Unit IV, the interval of tuff and claystone, shows up clearly between 490 and 520 mbsf as a zone of low density, velocity, and resistivity.

The physical properties correlate well with the recognized lithologic units. In the sedimentary section the most notable changes occur at the opal-A/opal-CT boundary. In the igneous units, physical properties correlate with variations in the alteration and porosity.

BACKGROUND AND OBJECTIVES

Background

Location and Bathymetry

Site 794 lies along the eastern margin of the Japan Sea, approximately 175 km from the nearest landfall at the Oga Peninsula, northern Honshu (Fig. 2). The site is situated in 2811 m of water on a gentle, north-dipping slope that comprises the northeastern margin of the Yamato Basin. This position coincides with the axial part of the Yamato Basin between the Yamato Rise and the continental slope of northern Honshu. To the immediate north lies the much larger and deeper Japan Basin, while east and west of the site are local bathymetric highs. The western high, the Meiyo-Daisan Seamount, represents the northernmost extent of the Yamato seamount chain. To the east is the northern extension of the Sado Ridge, a complex series of ridges that bound the Yamato Basin. Outboard of each high lie two north-trending deep-sea channels, the Toyama Channel to the west and the Mogami Channel to the east. Site 794 is isolated from these two channels by the highs, so it presently receives little coarse sediment.

Crustal Structure

The crustal structure of the Yamato Basin in the vicinity of Site 794 is inferred principally from seismic refraction data that was acquired south and southwest of the site (Ludwig et al., 1975; Hirata et al., in press). Figure 3 shows the projected position of Site 794 along the longitudinal refraction profile through the Yamato and Japan Basins. Using ocean crust terminology and proceeding from southwest to northeast, "Layer 3" thickens abruptly in the vicinity of DSDP Site 299 at the expense of "Layer 2," then thins toward the Japan Basin as "Layer 2" remains thin. The intersection of the profile with the Yamato Seamount chain may partially explain this abrupt transition. Alternately, the change may mark the boundary between rifted continental crust of the Yamato Basin and "oceanic" crust of the Japan Basin. Site 794 lies within or just north of this crustal transition. Thus, although we expected basic volcanic rocks, the spectrum of possible rock types comprising acoustic basement at this locality is rather broad.

Heat Flow

The measured heat-flow values in the area surrounding Site 794 lie in the range 75–116 Mw/m^2, which is quite typical for the basin areas of the Japan Sea, particularly the Yamato Basin (Yoshii and Yamano, 1983; Tamaki, 1986). Using a correlation between age and heat flow (Davis and Lister, 1977; Parsons and Sclater, 1977), a first approximation of the age of basin initia-

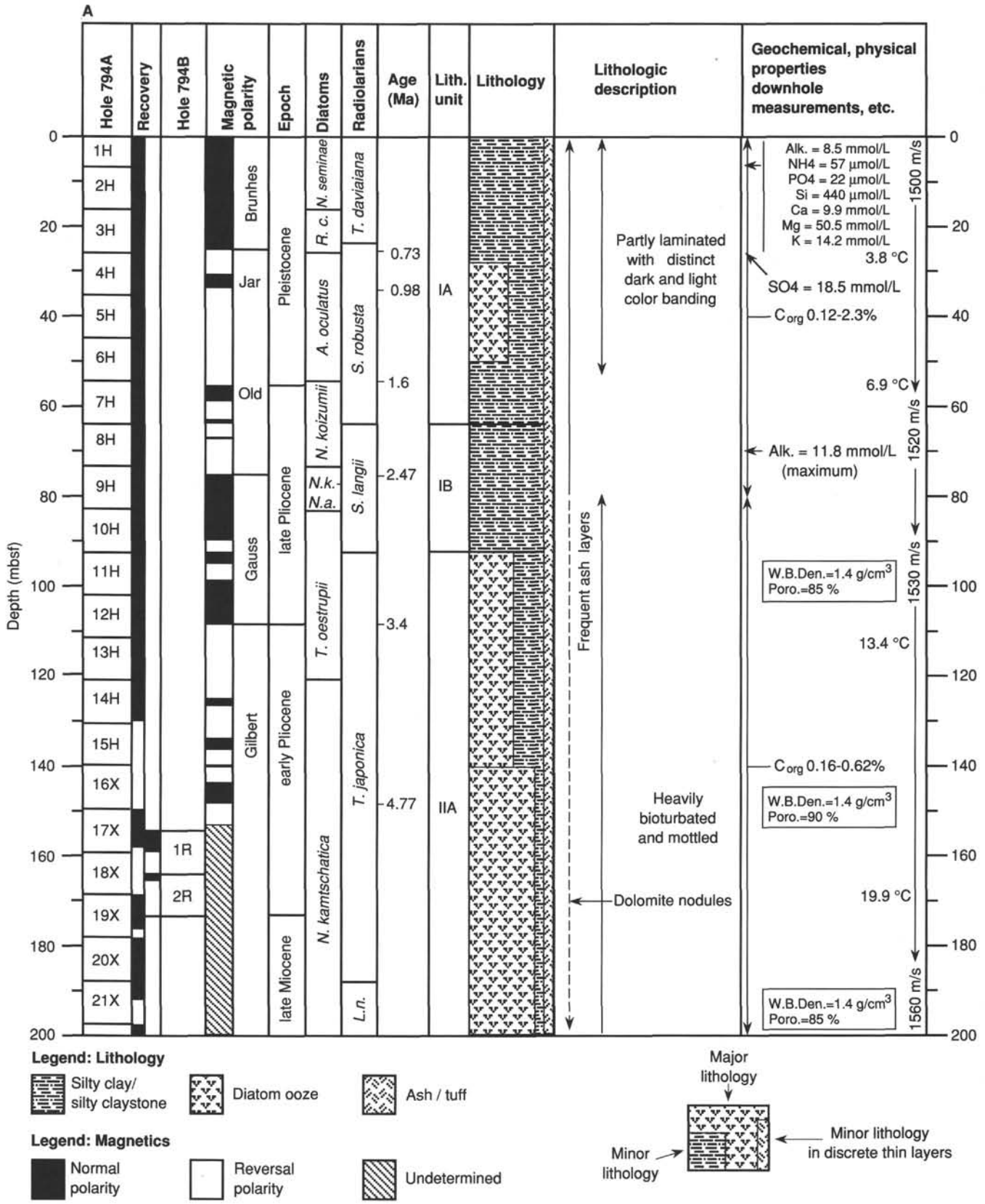

Figure 1. **A–D.** Stratigraphic summary column for Site 794.

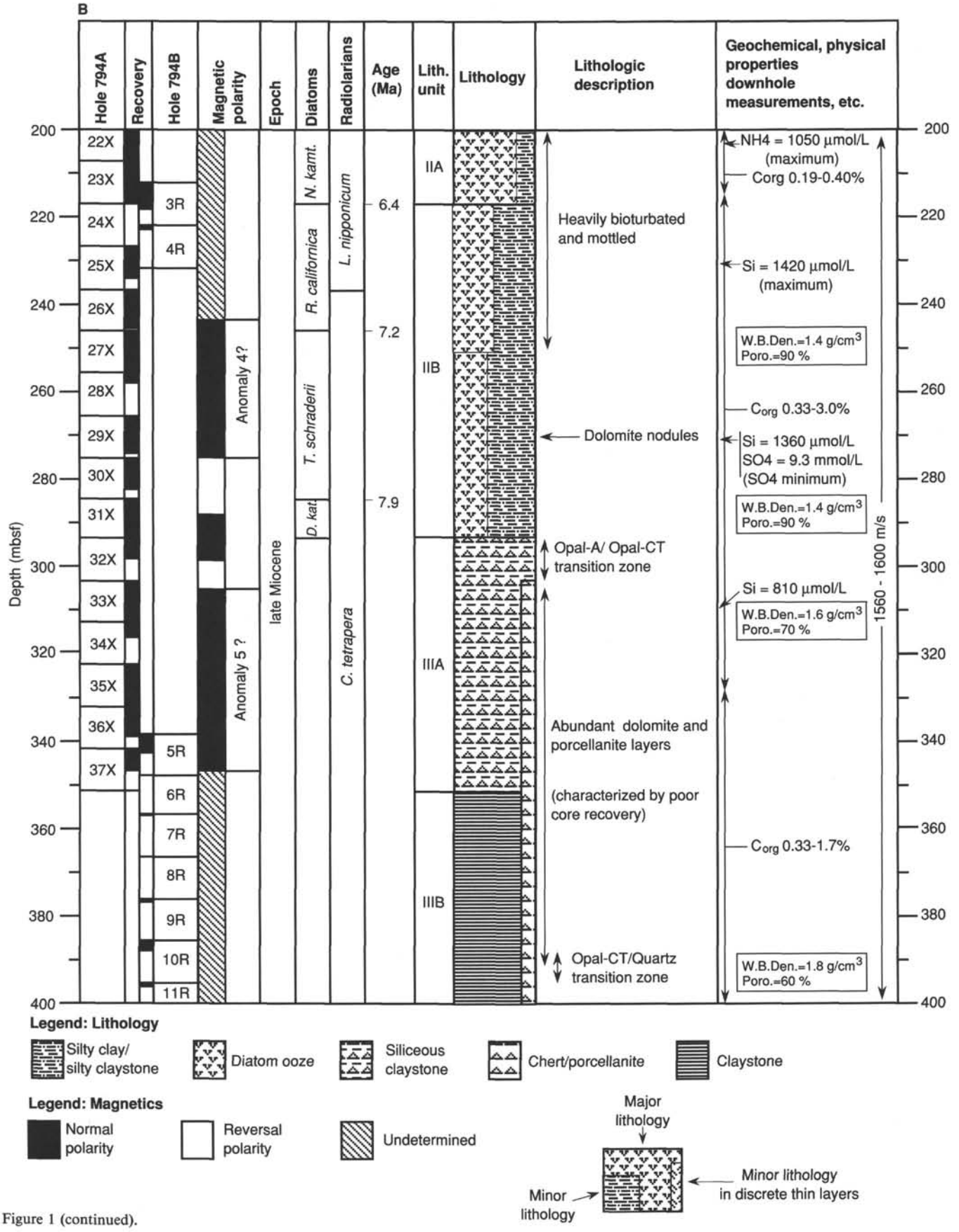

Figure 1 (continued).

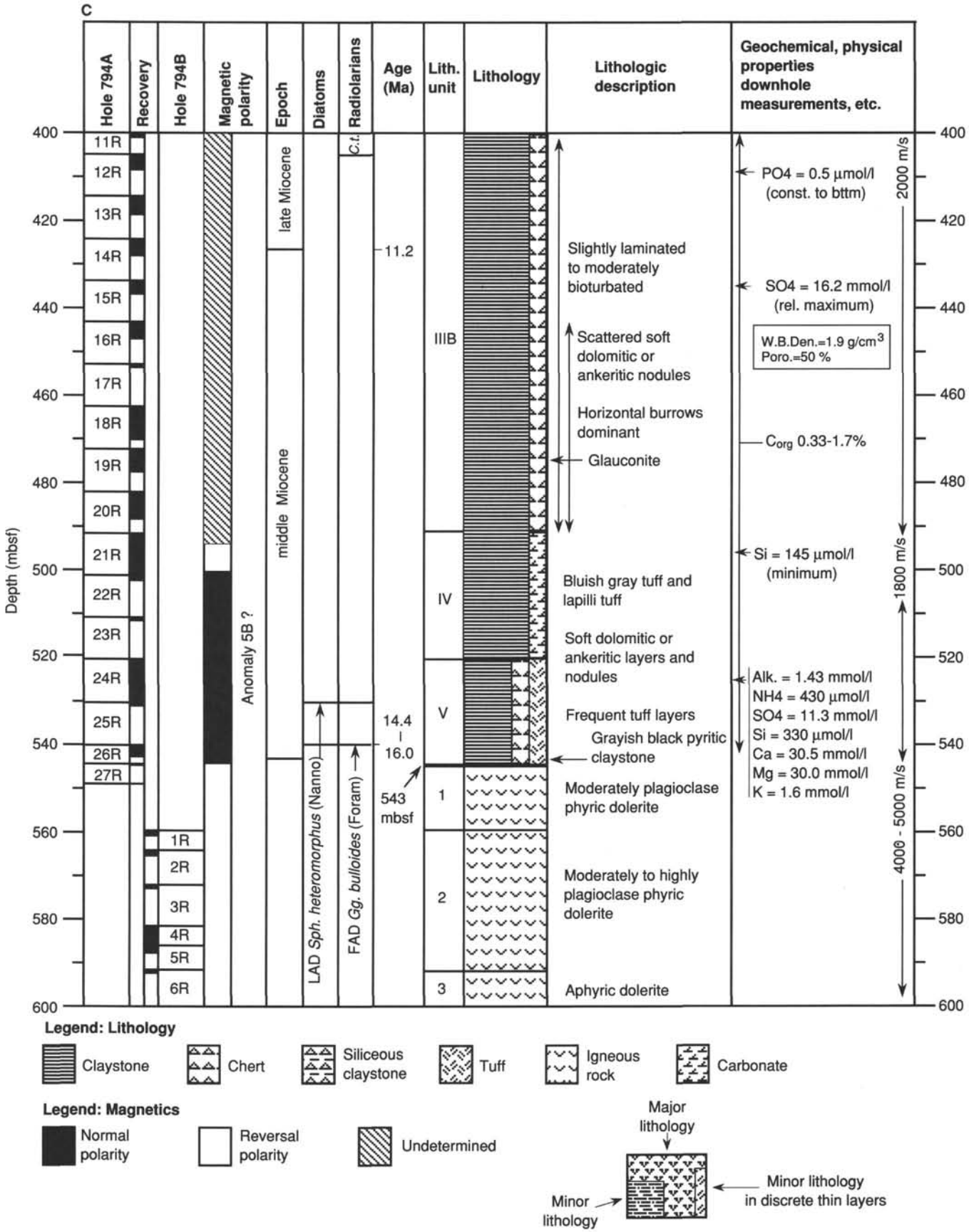

Figure 1 (continued).

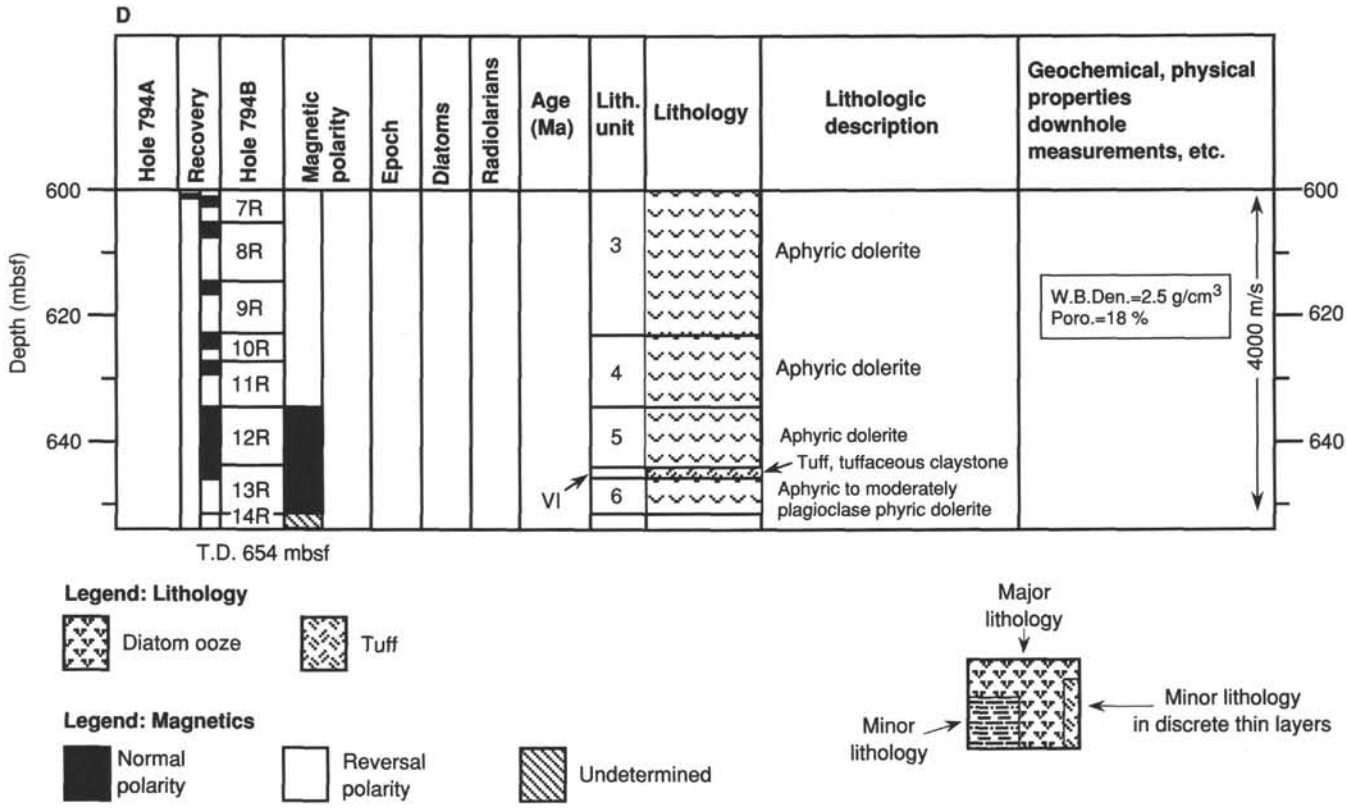

Figure 1 (continued).

tion at the Site 794 location is 23–26 Ma if the site is underlain by oceanic basement. This estimate is tentative because the correlation between age and heat flow developed for oceanic crust may not apply in this marginal sea.

Magnetics and Gravity

Magnetic anomalies with peak-to-peak amplitudes of as much as 200 nT and wavelengths of about 10 km are observed around Site 794 (Fig. 4). The pattern is highly complex and representative of much of the Yamato Basin area. The high frequency, relatively low amplitude, and relatively chaotic nature of these anomalies suggest a shallow source with pronounced lateral variability, such as volcanic terranes in a rifted continental or arc setting. In contrast, magnetic anomalies just to the north in the Japan Basin show short, disrupted linear segments similar to those found in areas of propagating spreading ridges (Hey, 1977; Tamaki et al., 1988). This change in anomaly character just north of the site location is approximately coincident with the crustal transition suggested by the refraction data.

Free-air gravity anomalies around the site range from 0 to 20 mgal and, for the most part, mirror the seafloor topography (Fig. 5). The gravity values are some 20 mgal higher than those in the deepest part of the Yamato Basin and reflect the shallower depth of basement at the site location.

Basement Rocks

Direct information on the nature and age of basement rocks in the vicinity of Site 794 comes from analyses of marine dredge samples and from extrapolations from onshore Japan. Figure 6 summarizes the distribution, age, and type of igneous rocks recovered from dredging the seamounts, bank tops, and escarpments near Site 794 as reported and compiled by Kaneoka (1986), Tamaki (1988), Kaneoka and Yuasa (1988), Ishii et al. (1988), Yamashita (1988), and Kaneoka et al. (in press). The nearest dredge samples come from the western slope of Meiyo-Daisan Seamount about 30 km west of the site. The recovered materials include lignite and siltstone of uncertain age that probably represent this sedimentary cover overlying the volcanic rocks of the seamount. Further to the southwest along the Yamato Seamount chain, the recovered dredge materials consist mostly of volcanic rocks. Eight trachyandesites and one basalt from four of these seamounts yielded ^{40}Ar-^{39}Ar ages in the range 10–16.9 Ma (Kaneoka et al., in press). These ages are slightly older than previously reported K-Ar values (Kaneoka, 1986) but are probably more reliable because the ^{40}Ar-^{39}Ar dating method is less affected by seafloor alteration. Thus, the most recent volcanic activity along this seamount chain occurred during a period that spanned the middle Miocene.

East and southeast of Site 794, the basement dredge samples are somewhat older and more variable than those from the seamount chain. Many of these dredge samples have been described in detail by Iwabuchi (1968) and Honza (1979) and have been incorporated in the seafloor outcrop map by Tamaki et al. (1981). Radiometric ages have been determined for some of these rocks. A basalt sample recovered from the steep western slope of a submarine promontory, about 75 km east of the site, yielded an ^{40}AR-^{39}Ar age of 62 Ma (Kaneoka and Yuasa, 1988). In contrast, three other igneous rock samples of variable compositions and from widely separated localities along the western shelf and slope of Honshu gave more reliable ^{40}Ar-^{39}Ar ages in the range 22.0–23.9 Ma. From northeast to southwest these are: (1) a 23.6-Ma trachyte from the slope west of the Oga Peninsula; (2) a 22.0-Ma granite from a flat bank top on the Sado Ridge north of Sado Island; and (3) a 23.9-Ma andesite from the slope north of Noto Peninsula (Kaneoka and Yuasa, 1988). Assuming that all three samples are autochthonous and that the observed min-

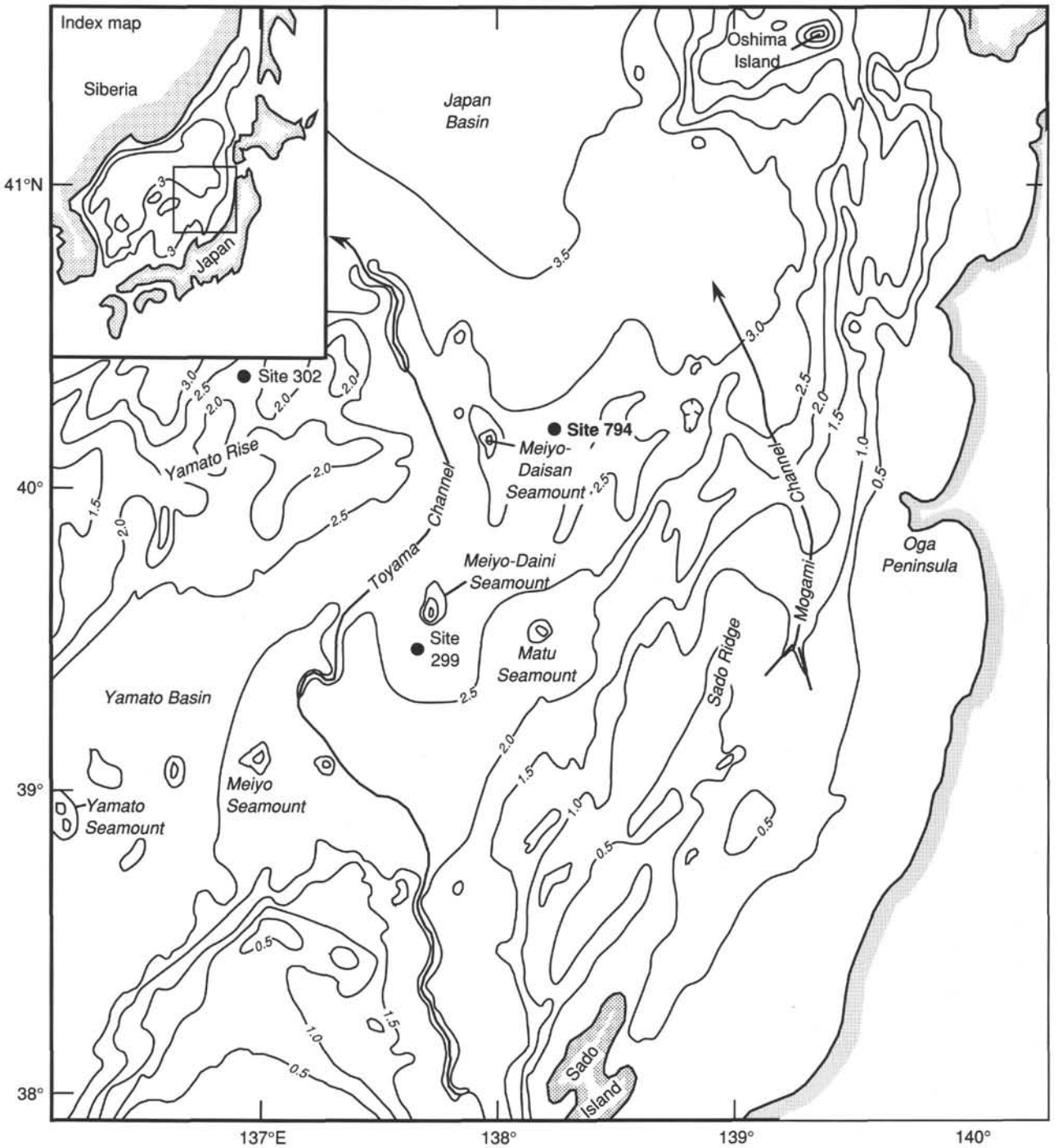

Figure 2. Location map of area surrounding Site 794 showing bathymetric features and DSDP Sites. Bathymetric contours are in kilometers.

eral alterations have not resulted in significant differential argon loss, these results describe a period of extrusive and intrusive activity along the western shelf of Honshu and eastern flank of the Yamato Basin that occurred about 22–24 Ma.

In the western Yamato Basin area, basalts and andesites have been dredged from the eastern flank of the Yamato Rise, west of the Yamato Seamount chain and 300–400 km west-southwest of Site 794. These samples provide information on the age and composition of the eastern Yamato Rise, which extends to within about 75 km of the site. Reported K-Ar dates for these rocks fall in a broad range of 20 to 76 Ma (Kaneoka, 1986). One andesite sample has been dated by the more reliable ^{40}Ar-^{39}Ar method, yielding an age of 26.3 Ma. This age is slightly older than those obtained from igneous samples recovered from the Japan shelf and eastern Yamato Basin (Kaneoka and Yuasa, 1988).

Additional volcanic rocks were recovered in a dredge from the steep western flank of Oshima Plateau about 140 km north-northeast of Site 794 (Fig. 6). These rocks are welded tuffs and have been dated at 72 Ma (K-Ar method) and 64–69 Ma (^{40}Ar-^{39}Ar method) by Kaneoka (1986) and Kaneoka et al. (in press).

In summary, a variety of igneous rocks have been recovered by dredging in the region surrounding Site 794. None of these have a distinct seismic signature that can be traced directly from the sampling locality to the site. Instead, these samples simply

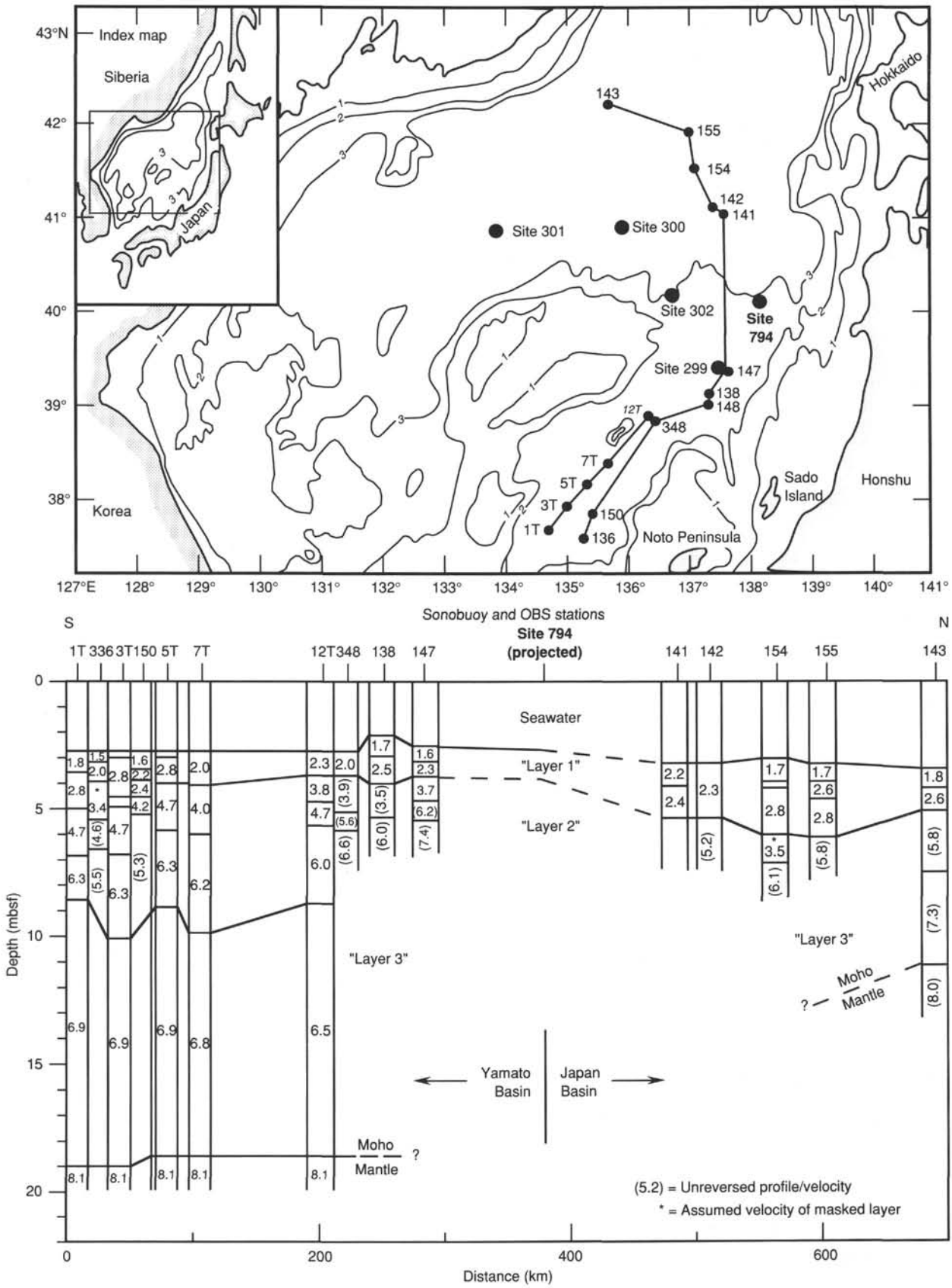

Figure 3. Location of the section and sonobuoy and OBS stations (top) and a longitudinal crustal section for Yamato and Japan Basins (bottom). OBS stations are from Hirata et al. (1987) and designated by the suffix T; all other stations are sonobuoys taken from Ludwig et al. (1975). Also shown are the earlier DSDP sites. Bathymetric contours are in kilometers. Crustal section is based on seismic refraction data.

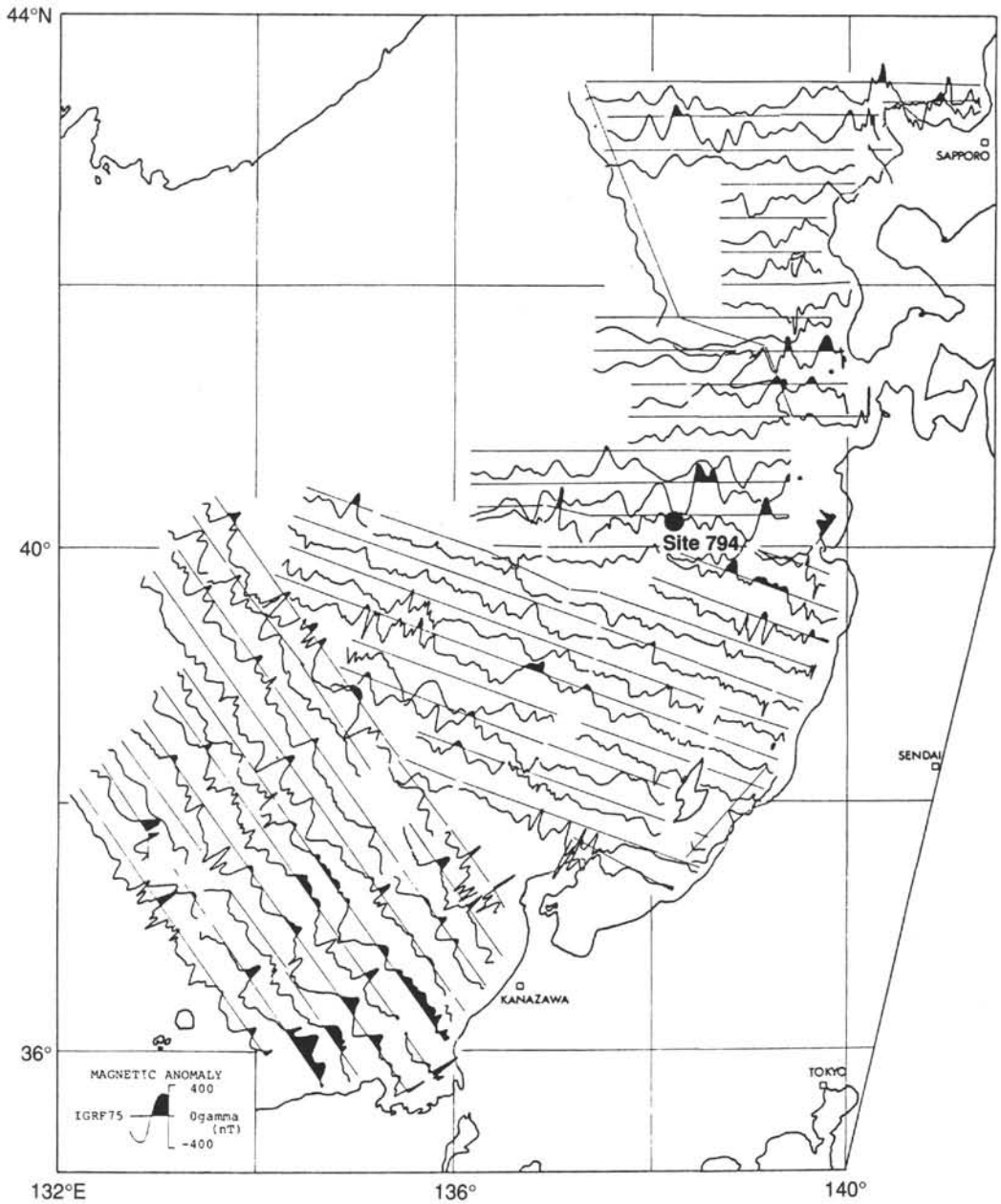

Figure 4. Magnetic anomalies along ship's tracks around Site 794. Data are from Honza (1979). Bathymetric contours are in kilometers.

provide a nonexclusive range of rock types that may constitute acoustic basement in the area. These rocks fall into three groups: (1) Upper Cretaceous–lower Paleocene (?) (62–72 Ma) welded tuffs and andesites typified by the samples from the Japan shelf east and northeast of the site; (2) lower Miocene (22–24 Ma) igneous rocks, mostly basalts and andesites, such as those from the east and west flanks of the Yamato Basin; and (3) middle Miocene (10–18 Ma) andesites and basalts similar to those of the Yamato Seamount chain. Furthermore, it is important to note that nearly all of the published descriptions of these dated samples report mineral alterations that could affect argon and potassium content and result in ages that are wrong.

Extrapolations of outcrop information from northern Honshu, southwestern Hokkaido, and the offshore islands about the nature of the acoustic basement at Site 794 are even more tentative. Besides the obvious lack of continuous seismic data, the principal obstacle to any such extrapolations is the disruption of the shelf margin along the eastern Japan Sea by faulting and folding. Nevertheless, because of the proximity of the site to the coast, the onshore data provide additional perspective.

Cenozoic volcanic rocks cover extensive areas of northern Honshu, southwestern Hokkaido, and the offshore islands (Geological Survey of Japan, 1982). These form two distinct groups distinguished by age and origin. The younger group consists principally of Quaternary andesites, rhyolites, and dacites, and represents arc volcanism related to Pacific Plate subduction. Most of these occur along the eastern flank of northern Honshu. The older group encompasses a broader age range, occurs along the western flank of northern Honshu and on the offshore islands, and is also arc related. These rocks are mostly upper Miocene to Oligocene (9–37 Ma) andesites, basalts, dacites, and rhyolites. The majority of these volcanic rocks are middle

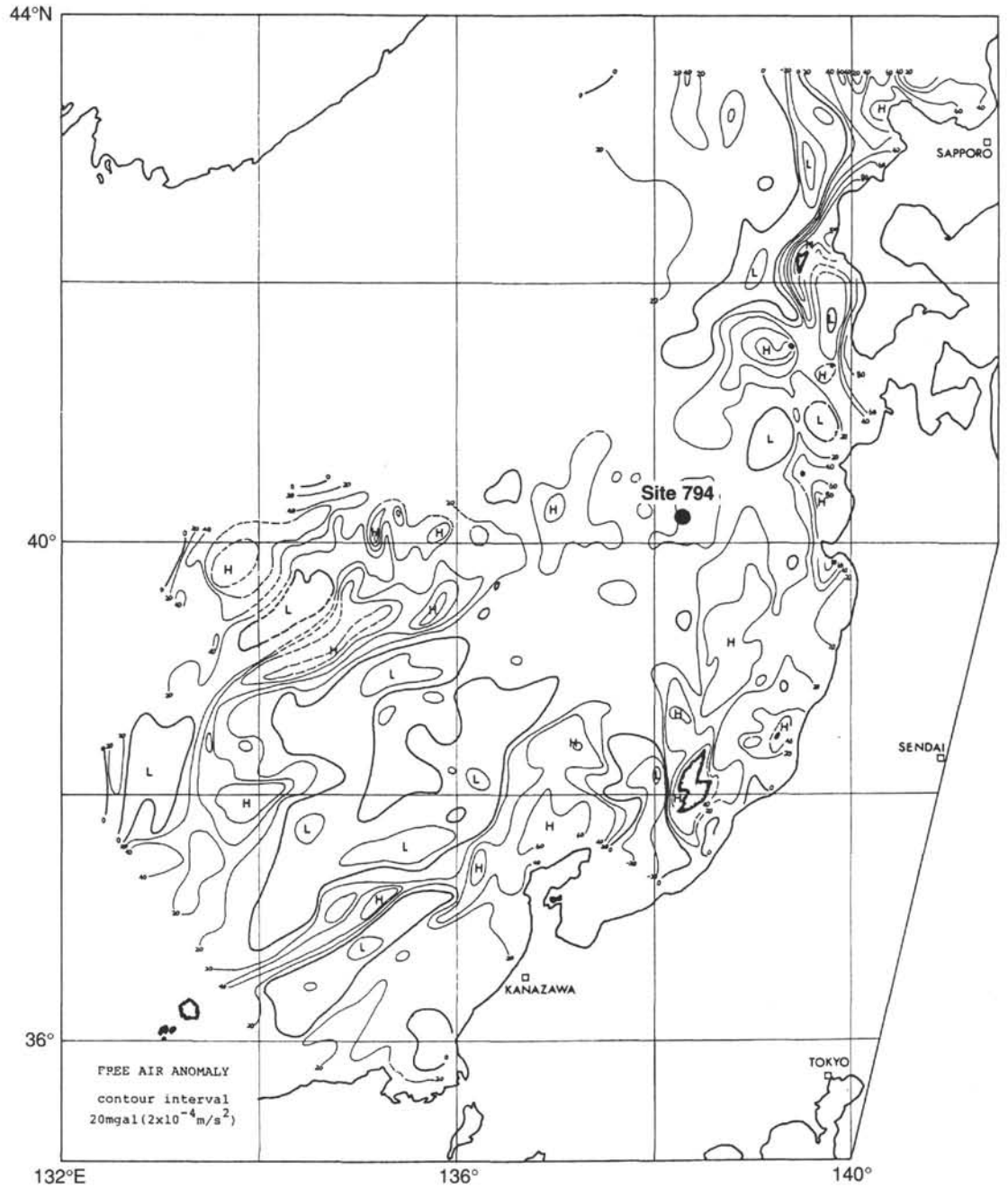

Figure 5. Free-air gravity anomaly profiles along ship's tracks around Site 794. Data are from Honza (1979).

to early Miocene in age (9–22 Ma) and includes the so-called "green tuff" unit of northern Honshu. Paleocene to Upper Cretaceous granitic rocks (55–93 Ma) also crop out in northern Honshu but are areally less extensive than the Tertiary volcanic rocks. These rocks could also comprise acoustic basement in parts of the eastern Japan Sea, but the onshore outcrop trends do not permit any clear extrapolations. Similarly, local outcrops of Mesozoic and older sedimentary and igneous rocks in northwestern Honshu may underlie parts of the eastern Japan Sea but data are too sparse to predict their consequences. In short, the onshore data document two distinct periods of volcanism in the Cenozoic: (1) an Oligocene to late Miocene period represented by extensive outcrops in northwestern Honshu and the offshore islands; and (2) a Quaternary pulse manifested by a linear belt of volcanoes.

Tectonic Setting

Site 794 lies approximately 50 km west of the most active tectonic belt in the Japan Sea (Fig. 7). This belt extends along the eastern shelf and slope of Hokkaido and northern Honshu and is characterized by a series of north-trending faults and folds, by linear ridge-basin morphology, and by shallow seismicity (Fukao and Furamoto, 1975; Tamaki et al., 1981; Seno and Eguchi, 1983; Tamaki and Honza, 1985; Tamaki, 1988). Based on single-channel and multichannel seismic data, many of the faults within this zone are thrust or reverse faults with moderate to steep, east or west dips. A number of these faults are coincident with seafloor escarpments and ridge flanks. An eastward-dipping thrust fault is situated 50 km east of Site 794 (Fig. 8). In 1983 the central Japan Sea earthquake of magnitude 7.7 oc-

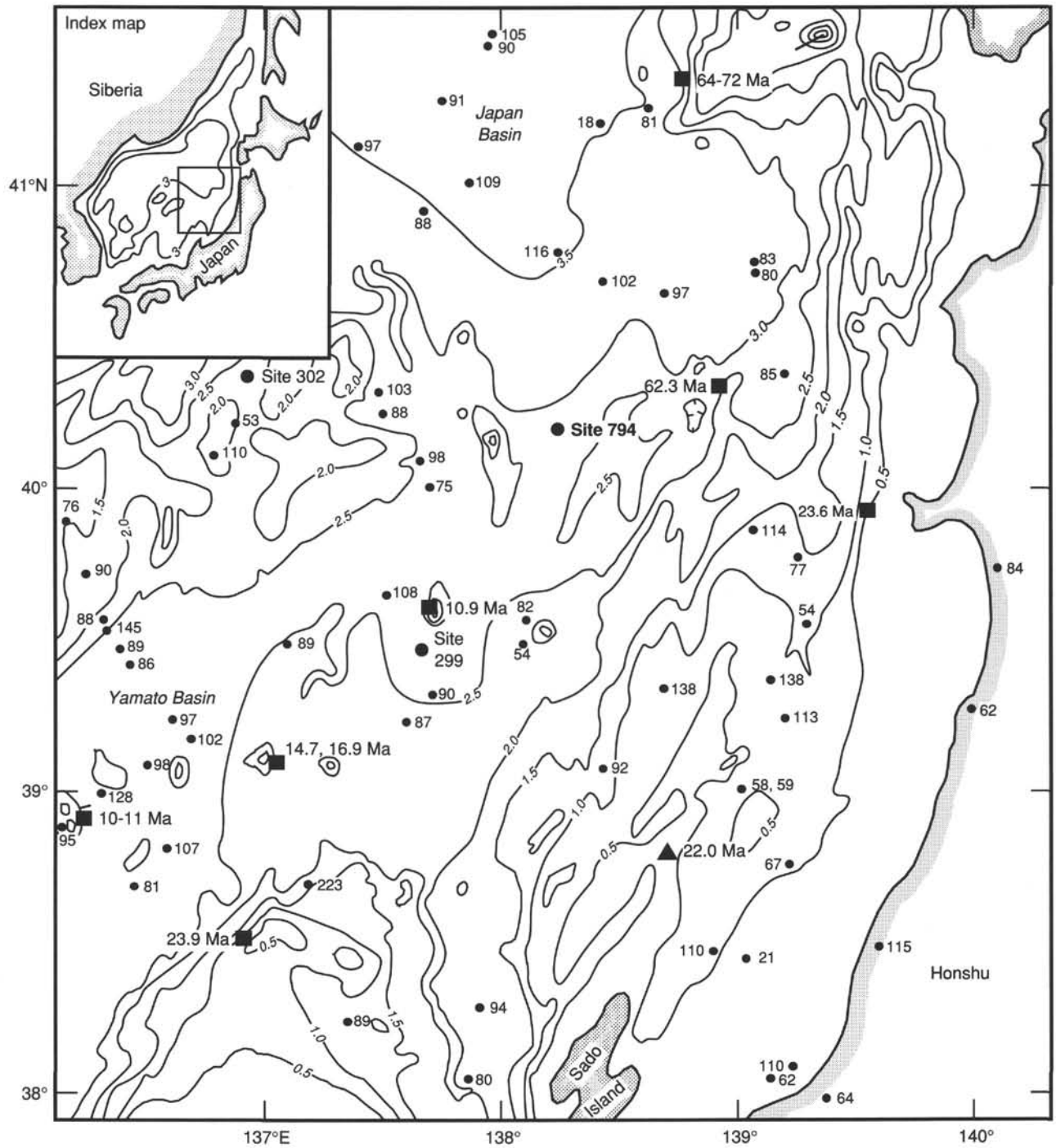

Figure 6. Location map of heat-flow values and basement dredge samples. Heat-flow values are represented by small dots; units are mW/m^2, and data are from Yoshii and Yamano (unpublished data). Basement samples are represented by solid squares (volcanic rocks) and a triangle (granite); ^{40}Ar-^{39}Ar ages are given in Ma (see text for references). Bathymetric contours are in kilometers.

curred in association with this fault (Tamaki and Honza, 1985). The epicenter was located at 40°21.4′N, 139°04.6′E and the focal depth of the earthquake was 14 km. The focal mechanism solution suggests that this earthquake was compressional with an axis of N70°W (Ishikawa, 1984). Another earthquake of magnitude 6.9 occurred in 1964 near this thrust fault. This earthquake was also compressional with an axis of N59°W (Fukao and Furumoto, 1975). The focal mechanism solutions for these earthquakes demonstrated that the failures occurred on the same east-dipping fault plane at depths of 14–19 km (Ichikawa, 1971; Ishikawa et al., 1984). Occurrence of these earthquakes indicates that the present-day compressional stress field trends east-west to northwest-southeast in this part of the Japan Sea. Associated with many of the faults in the east Japan Sea tectonic zone are complex folds involving mostly pre-Quaternary units. Fold axes are parallel or subparallel to the faults and there is no consistent pattern of vergence (Fig. 7).

Faults are also present on the eastern Yamato Rise about 75 km west of Site 794. The faults in this area are mostly steep normal faults involving acoustic basement. Based on age con-

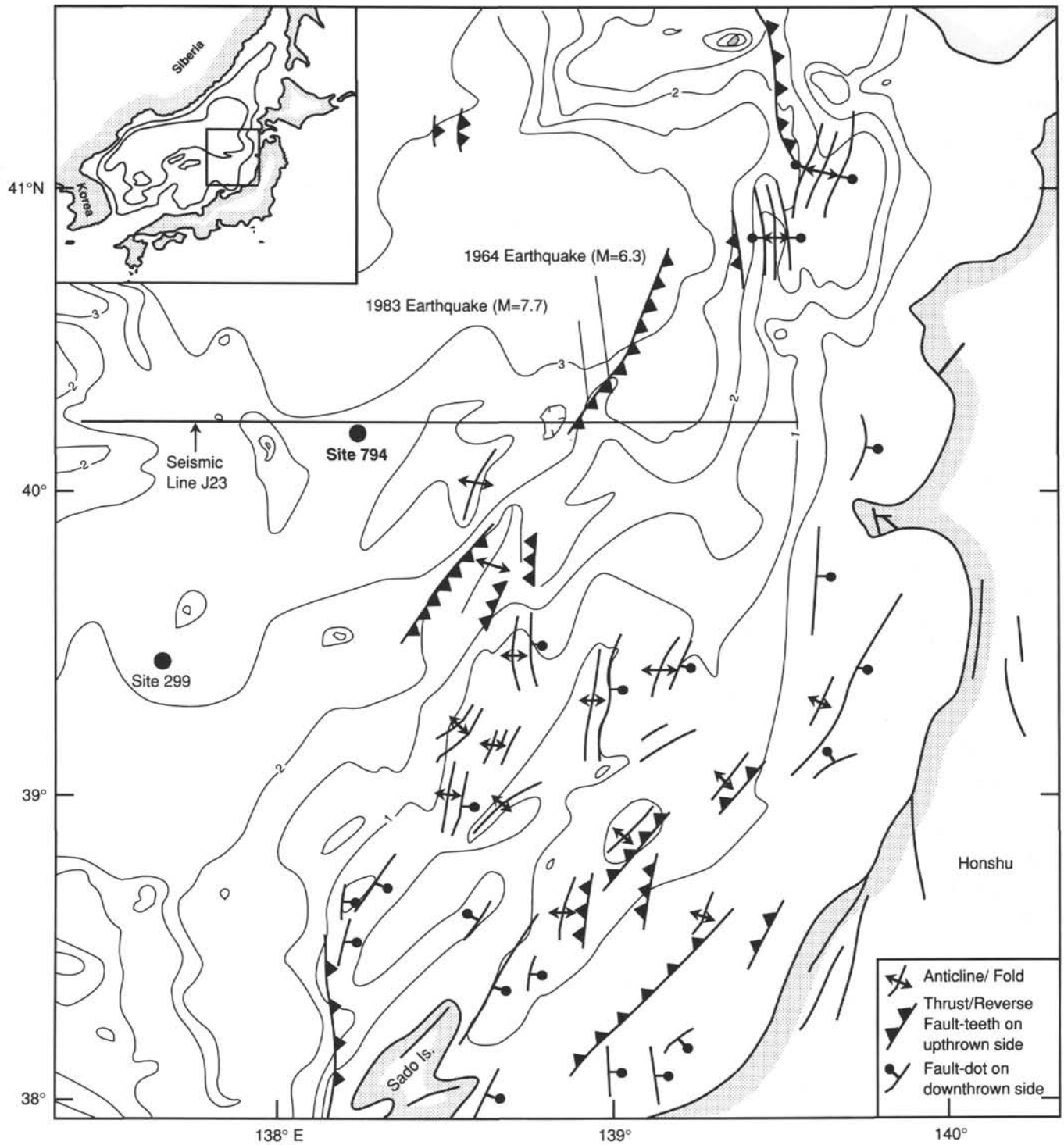

Figure 7. Map of the eastern Japan Sea tectonic zone in the vicinity of Site 794 area showing recognized faults, fold axes, and recent earthquake epicenters. The location for the seismic line shown in Figure 8 is also noted. Bathymetric contours are in kilometers.

straints provided by DSDP Site 302 (Karig, Ingle, et al., 1975; Koizumi, 1979), the principal activity on these faults occurred prior to the late Miocene during rifting of this part of the Japan Sea. No significant folding occurs in this area.

North and south of Site 794, and also in the immediate vicinity of the site, structural disruption of acoustic basement and the overlying sedimentary section is minimal. Except for minor irregularities in the basement surface, no significant faults or folds occur.

Sedimentation

The sedimentary section that overlies acoustic basement in the vicinity of Site 794 is on the order of 500–700 m thick (Fig. 8). The seismic facies present include: (1) an upper stratified interval characterized by parallel reflectors of moderate amplitude and good lateral continuity; (2) a middle transparent unit typified by low-amplitude parallel reflectors; and (3) a lower stratified unit distinguished by subparallel reflectors of moder-

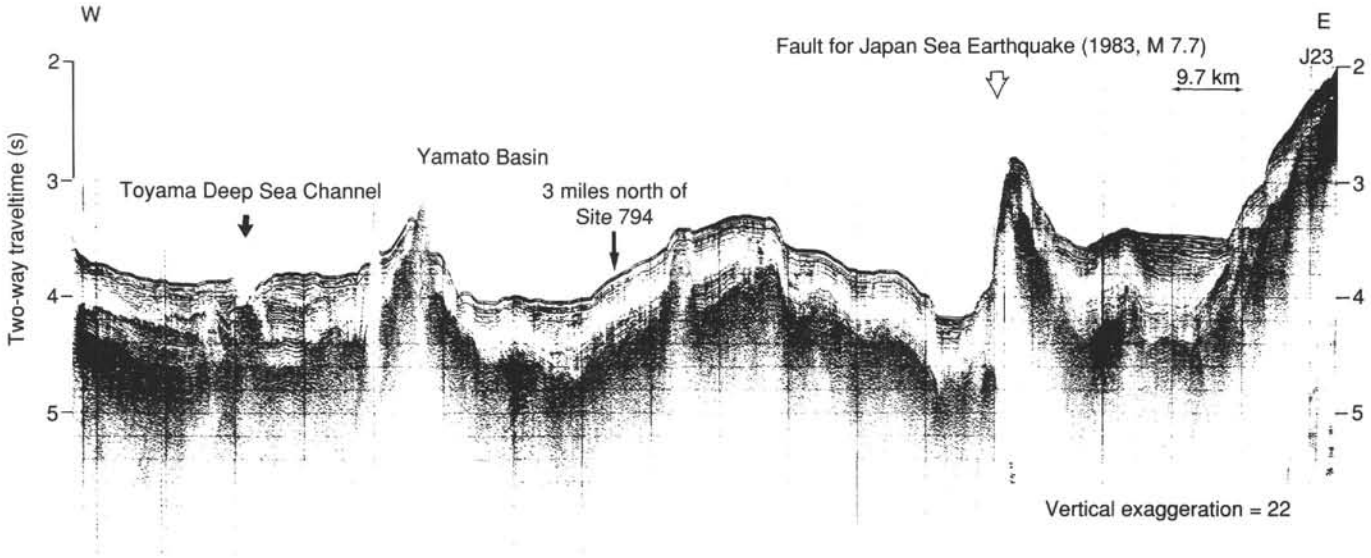

Figure 8. East-west seismic profile crossing Site 794, showing the thrust fault where the central Japan Sea earthquake (M = 7.7) occurred in 1983. See Figure 7 for line location. Data from Honza (1979).

ate amplitude and limited lateral extent (Tamaki, 1988). The sedimentary section thickens to the northwest and to the southwest, toward the Japan and Yamato Basins, respectively. Based on correlations with DSDP Sites 299, 301, and 302 (Karig, Ingle, et al., 1975), these thickness increases occur largely in the upper stratified seismic interval and correspond to greater amounts of upper Pliocene-Quaternary terrigenous sediments. In the Yamato Basin, sediments comprising the Toyama Channel and deep-sea fan system account for much of the thickening, particularly in the upper part of the section (Bouma, 1975; Tamaki et al., 1981; Boggs, 1984). In the Japan Basin, the Toyama system also contributed to the sedimentation during this period with additional input from the Mogami Channel system. Site 794 lies between these two clastic deposystems and has been effectively isolated from them since the late Pliocene by basement highs to the east and west (Fig. 2). Prior to drilling, the thickness of the upper stratified unit was estimated at 308 m.

The transparent and lower stratified seismic intervals that occur at the Site 794 location correlate with hemipelagic diatomaceous clay of early Pliocene to early late Pliocene and late Miocene ages, respectively, at DSDP Site 302 and at nearby piston core locations on the Yamato Rise (Karig, Ingle, et al., 1975; Koizumi, 1979; Tamaki, 1988). Based on pre-drilling estimates, these units retain a relatively uniform thickness of about 300 m in the vicinity of Site 794, consistent with a hemipelagic origin.

Objectives

Style and Dynamics of Back-arc Rifting

The principal drilling objective at Site 794 was to determine the nature and age of the acoustic basement at a basin location in the Japan Sea. Previously, basement samples had been recovered only from high-standing blocks and seamounts in this marginal sea. While these rocks established the existence of volcanic terranes and foundered continental blocks that underpin parts of the large highs, they shed little light on the nature of the basement or the ages of formation of the intervening basins. Only successful drilling and recovery of basement rocks and sediments immediately overlying basement from the basin areas can provide these essential data.

Site 794 is strategically located at the northeastern end of the Yamato Basin near the transition to the Japan Basin and at the axial zone of the Yamato Basin. Along with the basement results from additional sites drilled during Legs 127 and 128, these data from Site 794 would fill the key gap in the vast geological and geophysical data base for the Japan Sea. Together these data would permit assessment of the style and dynamics of rifting of the Japan Sea. The results will also address the more fundamental issue of understanding the processes and mechanisms of back-arc rifting of continental arcs as distinct from oceanic island arcs.

In-situ Stress Field

A second goal of the drilling at Site 794 was the determination and assessment of the present stress field of the eastern Japan Sea. Site 794 is situated near the zone of east-west to southeast-northwest compression that is an expression of a newly-formed plate boundary separating the Eurasian Plate and the North American Plate (Nakamura, 1983). Packer/hydrofracturing experiments in the basement rock of this site associated with borehole televiewer observations before and after the experiment were planned to determine the magnitude and direction of maximum compressional stress at this site. These data constitute indispensable information on the stress field of this developing plate boundary and make a basic contribution to the study of stress of incipient convergent plate boundaries.

Oceanographic and Sedimentation History

A further objective of the drilling at Site 794 was characterization of the history of sedimentation and water-mass fluctuations at a key position on the bathymetric sill separating the Yamato Basin from the northern Japan Basin. The site was located so as to obtain mostly hemipelagic sediments rather than terrigenous gravity flow deposits because the former are more likely to contain the diagnostic microfossil assemblages and lithofacies needed for temporal reconstructions of climate, water mass, and subsidence. Of specific interest were: (1) the history of anoxia, circulation, and sea level in relation to climate and subsidence; (2) fluctuations in the CCD; and (3) time- and temperature-controlled post-depositional processes, particularly

those involving organic matter, biogenic silica, and carbonates. The integration of these results with other regional offshore and onshore data would form the basis for an understanding of the sedimentation and oceanographic history of the Japan Sea and the western Pacific margin.

OPERATIONS

Preamble

Leg 127 of the Ocean Drilling Project began at 1600 hr local time on 23 June 1989 with the departure of the *JOIDES Resolution* (SEDCO/BP 471) from Tokyo, Japan, following a 5-day port call. After steaming southward to clear the approaches to Tokyo Wan, we headed north along the eastern coast of Honshu. Progress was slowed slightly by heavy ship traffic and by reduced visibility due to rain and fog. We reached Tsugaru Strait between Honshu and Hokkaido on 25 June, turned west into the teeth of 42-kt winds and strong opposing currents, and completed the transit to the Japan Sea late in the day. The weather improved greatly on the morning of 26 June 1989 and by 0930 hr of the same day we were in position to begin the pre-site survey.

Site Approach

Our survey plan for Site 794 was to obtain several crossings of the site along existing multichannel seismic lines to confirm the location and to avoid any local structural closures. Seismic data were to be acquired using the single-channel seismic reflection system aboard the *Resolution* and, because of the timing of our arrival, navigation was to be by Loran C. In addition, we planned to acquire magnetic data along all survey lines and to deploy a sonobuoy along the longest crossing line to obtain deeper refraction data.

We approached Site 794 from the southeast along Ocean Research Institute seismic Line 108 (Figs. 9, 10A, and 11A). Our first crossing line began 6 nmi southeast of the site and proceeded to the northwest along a bearing of 310 degrees for a distance of 12 nmi. A sonobuoy was deployed at the start of this line, but it expired after only about an hour. A second sonobuoy was dropped, but it too lasted less than an hour. After proceeding 6 nmi beyond the site, we turned the vessel to the east, increased our speed to about 7 kt, and proceeded to a position 5 nmi northeast of the site. At this point we turned to the south, returned to a slower profiling speed, and acquired a crossing line parallel to and just east of DELP Line E (Figs. 9, 10B, and 11B). After crossing the site and confirming the location and the absence of structural closure, we continued 3 nmi further to the southwest before turning to a reciprocal course on a bearing of 20°. We launched a beacon on the third pass of the site at 1515 hr on 26 June 1989, then slowed to pull in the gear and position the ship.

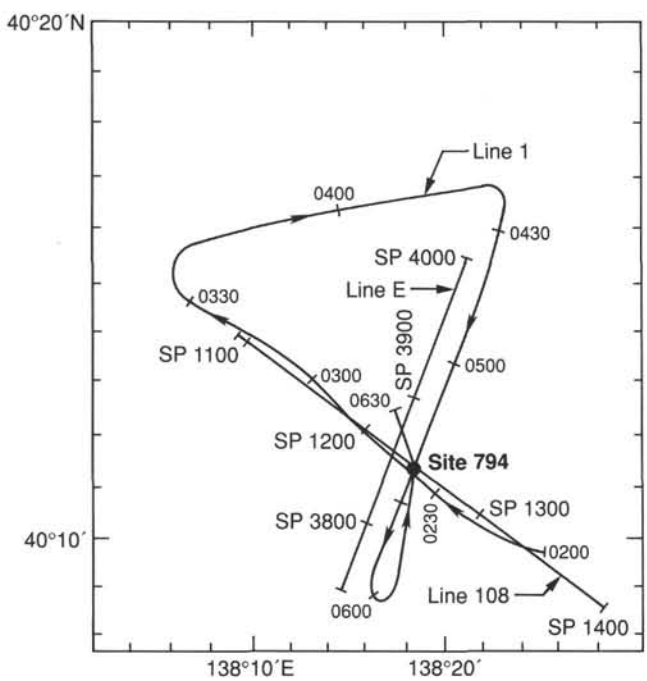

Figure 9. Chart showing the locations of the *JOIDES Resolution* approach lines and pre-existing seismic lines for Site 794.

Drilling and Logging Summary

Our plan at Site 794 was to drill three adjacent holes to achieve our scientific objectives. Hole 794A was planned as an APC/XCB hole into indurated sediments to recover a complete and relatively undisturbed sedimentary section. Hole 794B was to be an RCB hole beginning at the Hole 794A total depth and carrying 20 m into hard basement rocks. We planned to log the complete sedimentary section of this hole. Finally, Hole 794C was designed as a re-entry hole that was to be drilled and cased to basement at the total depth level achieved in Hole 794B, then drilled and cored a further 100 m into basement. We planned an extensive logging program and packer/hydrofracture experiment in the basement interval of this hole. Casing to basement would provide a stable hole for re-entry and the extended basement coring that we planned. In addition, this cased hole would be used by Leg 128 to complete a critical oblique seismic experiment and to deploy a long-term bottom-hole seismometer.

Hole 794A

Hole 794A was spudded at 0215 hr on 27 June 1989 with a mud-line core which established the seafloor depth as 2821.7 m from the driller's datum. Calm weather provided optimum coring conditions. Fifteen cores were taken using a polycrystalline diamond compact bit and the advanced piston corer (APC) to a depth of 139.8 mbsf before it became necessary to change to the extended core barrel (XCB) (Table 1). Core recovery using the APC was excellent (>100%) and drilling disturbance was minimal. All APC cores were oriented beginning with Core 127-794A-2H. The Barnes/Uyeda water sampler and temperature probe tool (WSTP) was run after every third core.

Following the APC coring, 22 XCB cores were taken between 139.8 and 351.3 mbsf (Table 1). Recovery was good but somewhat variable and many of the cores were broken and fractured by the drilling process. WSTP runs were continued to the base of the XCB coring (351.3 mbsf) at a frequency of every third core. Operations terminated in Hole 794A at 351.3 mbsf and a round trip was made to retrieve the bottom hole assembly (BHA) for rotary coring in Hole 794B.

Hole 794B

Hole 794B was spudded at 1945 hr on 29 June 1989. The bit and drill string were jetted 100 m into the sediment without rotation to determine the depth for setting the conductor casing on the re-entry cone planned for Hole 794C. Following the successful jetting test, the sediments were drilled to 154 mbsf where two RCB cores were planned to fill an interval of missed core recovery in Hole 794A. The "wash barrel" was retrieved and the first core of the two was cut. As the core barrel was being retrieved, the coring line parted at the winch drum and about 1500 m of cable, with the core barrel attached, fell back down the drill pipe. After a 5-hr delay to fish and recover the broken

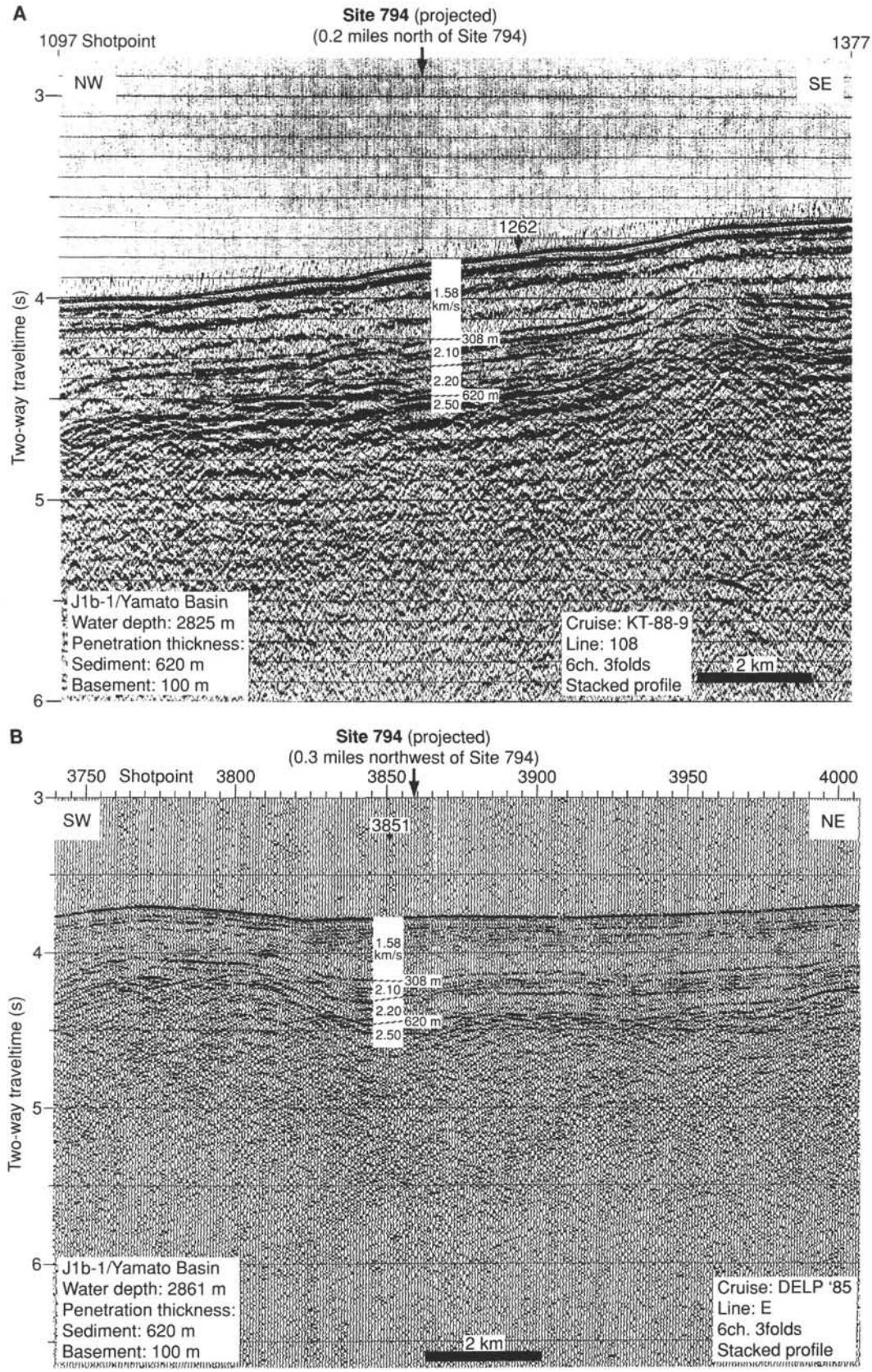

Figure 10. Pre-existing multichannel seismic lines near Site 794. Locations are given in Figure 9. **A.** Ocean Research Institute seismic line 108. **B.** DELP line E.

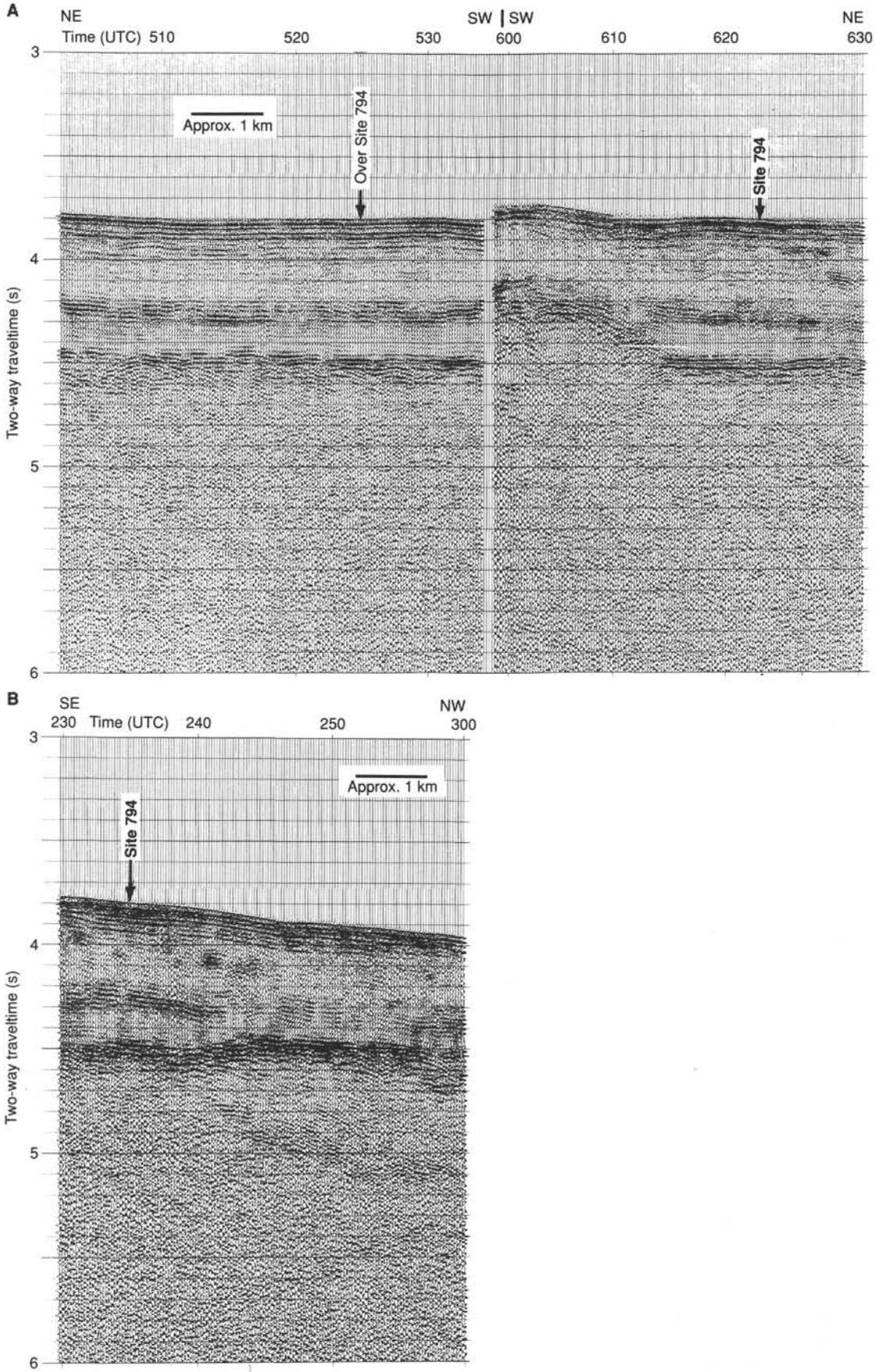

Figure 11. *JOIDES Resolution* single-channel seismic line 1 over Site 794. Location is given in Figure 9.

Table 1. Coring summary for Site 794.

Core no.	Date (June 1989)	Time (UTC)	Depth (mbsf)	Cored (m)	Recovered (m)	Recovery (%)	Age
127-794A-							
1H	26	1805	0.0–6.8	6.8	6.80	100.0	Quaternary
2H	26	1910	6.8–16.3	9.5	9.99	105.0	Quaternary
3H	26	2015	16.3–25.8	9.5	9.97	105.0	Quaternary
4H	26	2300	25.8–35.3	9.5	9.92	104.0	Quaternary
5H	26	2330	35.3–44.8	9.5	9.81	103.0	Quaternary
6H	27	0030	44.8–54.3	9.5	9.97	105.0	Quaternary
7H	27	0250	54.3–63.8	9.5	9.85	103.0	Quaternary
8H	27	0340	63.8–73.3	9.5	9.89	104.0	L. Pli.
9H	27	0430	73.3–82.8	9.5	9.97	105.0	L. Pli.
10H	27	0700	82.8–92.3	9.5	9.77	103.0	E. Pli.
11H	27	0740	92.3–101.8	9.5	9.96	105.0	E. Pli.
12H	27	0835	101.8–111.3	9.5	9.83	103.0	E. Pli.
13H	27	1110	111.3–120.8	9.5	9.94	104.0	E. Pli.
14H	27	1155	120.8–130.3	9.5	9.76	103.0	L. Mio.
15H	27	1315	130.3–139.8	9.5	9.92	104.0	L. Mio.
16X	27	1545	139.8–149.5	9.7	9.41	97.0	L. Mio.
17X	27	1645	149.5–159.2	9.7	9.69	99.9	L. Mio.
18X	27	1745	159.2–168.5	9.3	0.00	0.0	L. Mio.
19X	27	1945	168.5–178.2	9.7	7.66	78.9	L. Mio.
20X	27	2030	178.2–187.9	9.7	9.76	100.0	L. Mio.
21X	27	2115	187.9–197.5	9.6	7.05	73.4	L. Mio.
22X	28	0000	197.5–207.2	9.7	9.54	98.3	L. Mio.
23X	28	0155	207.2–216.9	9.7	9.70	100.0	L. Mio.
24X	28	0235	216.9–226.5	9.6	0.02	0.2	L. Mio.
25X	28	0320	226.5–236.2	9.7	7.55	77.8	L. Mio.
26X	28	0525	236.2–246.0	9.8	9.00	91.8	L. Mio.
27X	28	0615	246.0–255.7	9.7	9.63	99.3	L. Mio.
28X	28	0720	255.7–265.4	9.7	2.57	26.5	L. Mio.
29X	28	0915	265.4–275.1	9.7	8.81	90.8	L. Mio.
30X	28	1015	275.1–284.6	9.5	7.28	76.6	L. Mio.
31X	28	1115	284.6–293.5	8.9	9.34	105.0	L. Mio.
32X	28	1345	293.5–303.3	9.8	5.01	51.1	Unknown
33X	28	1445	303.3–312.6	9.3	9.73	104.0	Unknown
34X	28	1545	312.6–322.2	9.6	3.31	34.5	Unknown
35X	28	1645	322.2–331.9	9.7	9.71	100.0	Unknown
36X	28	1845	331.9–341.6	9.7	6.93	71.4	Unknown
37X	28	1945	341.6–351.3	9.7	5.11	52.7	Unknown
Coring totals				351.3	302.16	86.0	
127-794B-							
1R	29	1945	154.4–164.0	9.6	4.73	49.3	L. Mio.
2R	29	2030	164.0–173.5	9.5	1.51	15.9	L. Mio.
3R	29	2350	212.2–221.9	9.7	6.27	64.6	L. Mio.
4R	30	0035	221.9–231.6	9.7	1.13	11.6	L. Mio.
5R	30	0440	338.3–347.8	9.5	4.31	45.3	Unknown
6R	30	0530	347.8–356.6	8.8	0.14	1.6	Unknown
7R	30	0640	356.6–366.3	9.7	0.49	5.1	L. Mio.
8R	30	0800	366.3–376.0	9.7	0.05	0.5	L. Mio.
9R	30	0930	376.0–385.6	9.6	0.94	9.8	L. Mio.
10R	30	1100	385.6–395.2	9.6	2.43	25.3	Unknown
11R	30	1230	395.2–404.9	9.7	0.90	9.3	Unknown
12R	30	1400	404.9–414.5	9.6	3.44	35.8	Unknown
13R	30	1530	414.5–424.2	9.7	4.18	43.1	Unknown
14R	30	1700	424.2–433.8	9.6	3.88	40.4	
15R	30	1830	433.8–443.2	9.4	3.08	32.7	
16R	30	2000	443.2–452.9	9.7	3.98	41.0	
17R	30	2110	452.9–462.6	9.7	0.79	8.1	
18R	30	2230	462.6–472.3	9.7	7.66	78.9	
	(July 1989)						
19R	01	0000	472.3–482.0	9.7	5.30	54.6	
20R	01	0110	482.0–491.7	9.7	6.38	65.8	
21R	01	0220	491.7–501.2	9.5	9.79	103.0	
22R	01	0325	501.2–510.9	9.7	1.24	12.8	
23R	01	0445	510.9–520.6	9.7	0.87	9.0	
24R	01	0600	520.6–530.3	9.7	9.84	101.0	
25R	01	0720	530.3–540.0	9.7	0.82	8.5	
26R	01	0930	540.0–544.3	4.3	2.79	64.9	
27R	01	1600	544.3–549.0	4.7	0.46	9.8	
Coring totals				249.2	87.40	35.1	

Table 1 (continued).

Core no.	Date (June 1989)	Time (UTC)	Depth (mbsf)	Cored (m)	Recovered (m)	Recovery (%)	Age
127-794C-							
1R	07	2115	559.8–564.0	4.2	1.25	29.7	
2R	08	0045	564.0–572.0	8.0	1.28	16.0	
3R	08	0355	572.0–581.5	9.5	0.97	10.2	
4R	08	0620	581.5–586.0	4.5	4.89	108.0	
5R	08	0950	586.0–591.7	5.7	1.85	32.4	
6R	08	1330	591.7–600.9	9.2	0.82	8.9	
7R	08	1900	600.9–605.1	4.2	1.87	44.5	
8R	09	0140	605.1–614.6	9.5	2.40	25.2	
9R	09	0710	614.6–622.8	8.2	2.05	25.0	
10R	09	1215	622.8–627.3	4.5	2.54	56.4	
11R	09	1700	627.3–634.3	7.0	2.06	29.4	
12R	09	2330	634.3–643.7	9.4	8.89	94.6	
13R	10	0440	643.7–651.7	8.0	2.34	29.2	
14R	10	0700	651.7–653.7	2.0	0.00	0.0	
Coring totals				93.9	33.21	35.4	

coring line, spot-coring and drilling continued to a depth of 338.3 mbsf.

Hole 794B was continuously cored using the RCB from 338.3 to 549.0 mbsf. Twenty-five cores were taken over this interval and recovery varied from 0.5–105% (Table 1). Recovery was poor in the brittle siliceous claystones between about 340 and 370 mbsf and below 544 mbsf in the hard, fractured dolerites at the base of the hole. Drilling rates of these rocks were also slow. In comparison, recovery of the intervening claystones and tuffs was fair to good and the drilling much faster.

We planned to core about 20 m of the hard dolerite before abandoning Hole 794B, but elected to terminate the drilling at 549 mbsf after drilling only 6 m because of the slow penetration rates and jamming of the bit. A wiper trip was made to 55 mbsf and the hole was found to be in good condition. With the bit back at total depth, we flushed the hole with high viscosity mud, then released the bit. The hole was then filled with KCl-inhibited drilling mud and the drill string was raised to a depth of 101 mbsf to facilitate logging operations.

Three logging runs were made in Hole 794B. The first run was made with the so-called "quad combo," a string of logging tools that includes sonic, density, conductivity, and neutron-porosity devices, along with gamma ray, caliper, and temperature instruments. The first attempt with these logs was aborted after running into the hole because the sonic tool began drawing too much current during calibrations at the seafloor. The second attempt was successful, although there was some difficulty in getting the long tool string through the BHA. The hole was found to be unobstructed to 8 m above the total drilled depth. The second logging run with the geochemical combination tool went smoothly. The final logging run with the formation microscanner also went smoothly after a short 1.25-hr delay due to a minor cable head problem. We pulled out of Hole 794B at 2030 hr on 3 July, following the successful logging operations, and began preparations to deploy the re-entry cone for Hole 794C.

Hole 794C

The re-entry cone and 16-in. casing for Hole 794C were launched at 1545 hr on 4 July 1989. A commandable beacon was attached to the cone, which we would deactivate upon leaving the site, thus saving it for Leg 128 operations. Unfortunately, this beacon failed on the trip in. The casing and cone were jetted into the sediments to a depth of 2898.5 m below the driller's datum before the running tool prematurely unlatched. After a short delay to reconnect the tool, further jetting was attempted but no additional progress was made. This left the mud-skirt on the re-entry cone at a depth of 2808.5 m below the driller's datum. We thought that the seafloor was either 13 m higher than at Hole 794B or that the sediment had reconstituted and stiffened around the casing during the tool unlatching, thus preventing further penetration. At this point the tool was deliberately unlatched and a 14¾ in. hole was drilled to 3349.6 m below the driller's datum. Hard drilling was encountered at 3333 m below the driller's datum, suggesting that the top of the dolerite was 31 m higher at this hole than at Hole 794B. We flushed the hole several times with mud and recovered the drill string to run in and set 11¾ in. casing. At this point, the original Benthos beacon began to fade and a backup Datasonics UAB-354A S/N 516 beacon was launched.

With the 11¾-in. casing made up, the drill string, casing, and camera were lowered to the seafloor to check the depth uncertainty before re-entering the hole. The seafloor depth was found to be 2820 m below the driller's datum or only about 1.5 m higher than at Hole 794B. It was later discovered from a pipe tally that one full stand of pipe (30 m) had not been counted during the trip in to set the 16-in. casing and re-entry cone. As a result, we drilled about 10 m further into the dolerite than at Hole 794B and missed recovering that interval in cores. In addition, the mud-skirt at the base of the re-entry cone stood about 10 m above the seafloor and the casing was set about 25 m above the top of the dolerite rather than 10 m or so into it as planned. Fortunately, the calipers for successive logs in Hole 794B showed only two intervals of potentially troublesome swelling clay at 355–357 mbsf and 506–509 mbsf; both of these were behind casing at Hole 794C.

Fourteen RCB cores were taken in Hole 794C from 559.8–653.7 mbsf. Recovery averaged 36% but varied considerably (Table 1). A number of times, the core barrel became jammed during coring, and we elected to pull the cores before advancing the full 9.5 m to improve recovery. Drilling rates in the dolerites between 559.8 and 631 mbsf were generally slow, about 1.5–2.5 m/hr. A drilling break occurred at 631 mbsf (Core 127-794C-11R), and drilling rates increased to 6 m/hr for the next 3 m. The core barrel was pulled to avoid losing this softer material but the bit jammed and only hard dolerite was recovered. The pump rate was set at 60 spm for the next core on the prospect that interbedded soft material was present. The drilling rate settled in again at about 1.5–2.5 m/hr, and Core 127-794C-12R was pulled after 8.9 m with 95% recovery of hard dolerite. We continued coring hard material in Core 127-794C-13R and in-

creased the pump pressure from 60 spm to 100 spm. About 15 min after changing the pump pressure, the circulation pressure jumped from 1300 to 4000 psi, indicating an obstruction to fluid flow. We immediately pulled the core barrel and recovered 2.34 m of interbedded dolerite, tuff, tuffaceous sandstone, and claystone, and minor basalt. With the core barrel removed, the circulation pressure remained high even though all other parameters (e.g., torque and drag) were normal. The core barrel was pumped down and with Core 127-794C-14R we attempted to determine the presence or absence of an obstruction within the pipe. When the barrel returned empty, we concluded that the inner core barrel had become unlatched during the cutting of Core 127-794C-13R, permitting core material to fill the float valve cavity and force the flapper valve shut. This predicament made further coring untenable and successful deplugging unlikely. We could only pull the drill string and clear the bit.

As we began pulling out, the pipe stuck with the bit only about 15 m above the base of the hole (638.7 mbsf). This level lies 4–5 m below the base of the fast-drilling interval in the dolerites (631–634 mbsf). The pipe's inability to circulate effectively suggested that the sticking of the pipe was caused by cuttings constricting the annulus. We continued to work the pipe for the next 6.5 hr, dropping a core breaker and pumping a mud pill but without success. Finally we were able to back off and retrieve the drill string, leaving the BHA (about 175 m) stuck in the hole with the top of the pipe at about 3275 m below the driller's datum.

At this point our strategy was to abandon Hole 794C and move north to our second site. This decision provided the greatest flexibility to return to Site 794 to attempt a fishing job or, if unsuccessful, to drill a fourth hole with a re-entry cone but no 11¾ in. casing. We departed Site 794 at 1100 hr on 11 July 1989.

LITHOSTRATIGRAPHY

Lithologic Units

The stratigraphic section at Site 794 consists of 544 m of interbedded clay, silty clay, and diatomaceous clay and ooze, with lesser amounts of volcanic ash, tuff, and calcareous, siliceous, and glauconitic clay and claystone. The age of the sediment ranges from Holocene to middle Miocene, and basal sediments rest on plagioclase phyric dolerite. An additional 1.5 m section of tuff and tuffaceous, silty claystone occurs between dolerite and basalt layers at 644 mbsf. We use the purely objective criteria of mineralogy, grain size, microfossil abundance, and bedding characteristics to divide the stratigraphic section into five major lithologic units (Fig. 12). Units I, II, and III are each further divided into two subunits. Generalized composition of the major lithologic units, determined by smear-slide analysis, is shown in Figure 13.

Unit I (0–92.3 mbsf)

Interval 127-794A-1H through 127-794A-10H.

Unit I is 92.3 m thick and consists dominantly of clay and silty clay with a significant admixture of vitric ash. It is divided into two subunits on the basis of variations in bedding characteristics, sedimentary structures, and color. Subunit IA is characterized by dark-colored, well-laminated and bedded clay and silty clay that alternate with light-colored, poorly laminated clay; sediments in Unit IB are light colored, intensely bioturbated, and contain few dark-colored layers with laminations.

Subunit IA (0–63.8 mbsf)

Subunit IA, Cores 127-794A-1H through 127-794-7H, is 63.8 m thick and is composed mainly of light olive gray to greenish gray clay and silty ashy clay. Diatoms occur in some dark-colored layers in the middle part of the section. These sediments are characteristically poorly bedded, with few laminae or distinct layers other than thin (1–5 cm) interbedded ash layers and a few laminated diatom-bearing layers. Vitric ash is disseminated throughout the unit and occurs also as numerous thin (0.5–15 cm), discrete layers. Ash beds thicker than a few centimeters typically display normal size grading with bioturbation at the top. The glassy component of these fine ashes is well preserved bubble-wall shards and pumice. Trace amounts of hornblende and feldspar are also present.

The upper 55 m of Subunit IA is characterized by zones of distinct, planar lamination and bedding; the scale of bedding ranges from thick laminae to thin beds (Fig. 14). Well-laminated units are noticeably darker in color than the intervening nonlaminated intervals. The darker color is caused by the presence of organic matter, fine disseminated pyrite, or both. Organic carbon analyses of some diatom-bearing dark layers show that the organic carbon content ranges from about 1.0 to 3.0 wt%, whereas that of the lighter colored units is generally less than about 0.5 wt%. Boundaries of laminated units are commonly sharp; however, some boundaries are blurred or gradational, probably as a result of bioturbation. Commonly, these thicker, nonlaminated, lighter colored units are slightly to highly bioturbated.

Subunit IB (63.8–92.3 mbsf)

Subunit IB, Cores 127-794A-8H through 127-794A-10H, consists of 28.5 m of clay and silty clay that is similar to Subunit IA, except that it contains very few well-laminated, dark-colored zones. The sediments are mostly light olive gray to dark greenish gray clay, silty clay, claystone, and silty claystone that contain few or no laminations. Some sediments of this facies display indistinct, wispy laminations; most appear either homogeneous or mottled. Mottles and other biogenic traces suggest that the sediments of this facies are slightly to highly bioturbated. Layering, defined largely by color changes, ranges from a few centimeters to a few meters thick. The silt fraction of the sediments may include quartz, ash, and minor amounts of siliceous microfossils. Some units contain diagenetic dolomite or ankerite.

Unit II (92.3–293.5 mbsf)

Interval 127-794A-11H through 127-794A-15H; 127-794A-16X through 127-794-31X.

Unit II is 201.2 m thick and is dominantly diatom ooze and clay. It is divided into two subunits on the basis of relative abundance of clay and diatoms. Subunit IIA is composed mainly of diatom ooze; Subunit IIB is diatom clay.

Subunit IIA (92.3–216.9 mbsf)

Subunit IIA, Cores 127-794A-11H through 127-794A-15H; 127-794A-16X through 127-794A-23X; composed of 124.6 m of greenish gray diatom ooze and clayey diatom ooze. Diatoms are abundant throughout the section. Vitric ash and minor pyrite are sparsely disseminated throughout the ooze. Ash also occurs as distinct thin beds 1–5 cm thick. Laminae in these layers are generally indistinct and wispy. Bioturbation ranges from moderate to intense, and many units display distinctive mottling (Fig. 15). The nonbiogenic silt fraction of Facies 3 sediment may include volcanic ash and quartz, and some units contain diagenetic dolomite or ankerite.

Subunit IIB (216.9–293.5 mbsf)

Subunit IIB, Cores 127-794A-24X through 127-794A-31X, consists of 76.6 m of largely diatomaceous clay. It is similar in

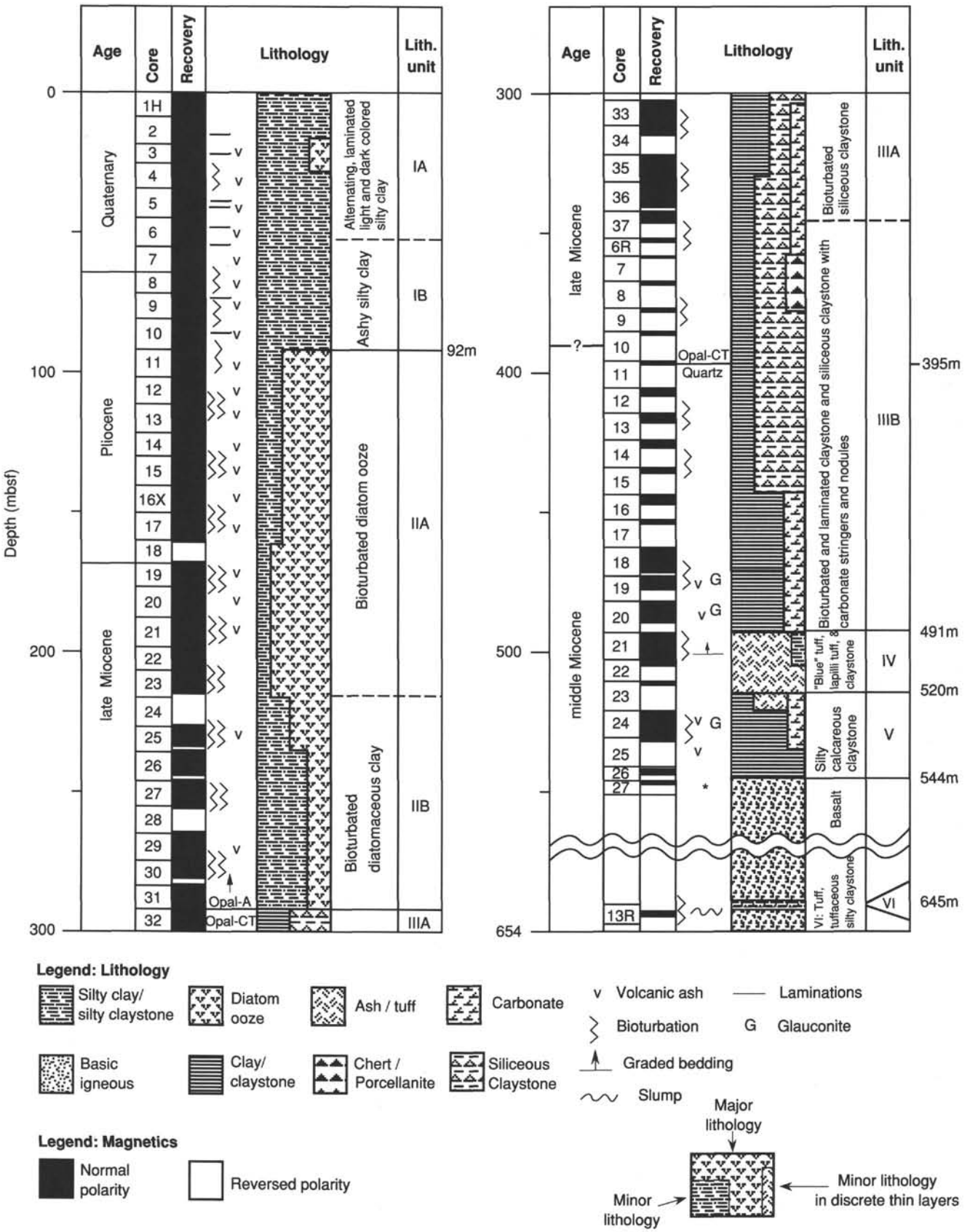

Figure 12. Lithostratigraphic column, Site 794.

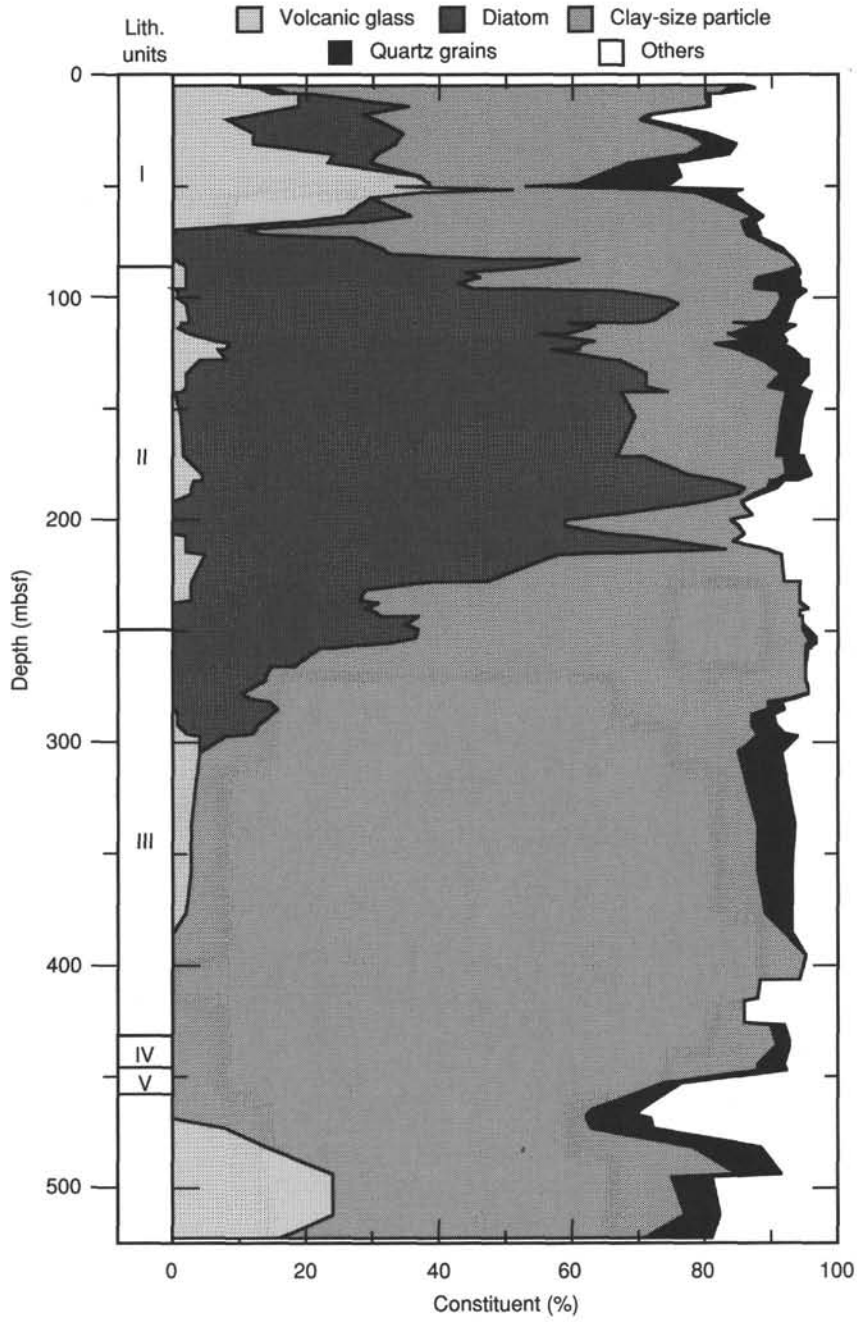

Figure 13. Generalized particle composition of Site 794 sediments, interpreted from smear-slide examination of selected samples.

lithology to Subunit IIA; however, diatoms are less abundant. Diatom abundance decreases downward and diatoms disappear at the base of this section. X-ray data indicate that opal-CT first appears near the base of this unit, replacing opal-A.

Unit III (293.5–491.7 mbsf)

Interval 127-794A-32X through 127-794A-37X; 127-794B-5R through 127-794B-20R.

Unit III is 198.2 m thick and is composed mostly of clay or claystone; diatoms are absent, and silica in the unit consists mainly of opal-CT. It is divided into two subunits on the basis of diagenetic constituents. Subunit IIIA contains few visible diagenetic minerals. Subunit IIIB contains moderate amounts of dolomite, ankerite, and silica in the form of cements and lenses.

Subunit IIIA (293.5–351.3 mbsf)

Subunit IIIA, Cores 127-794A-32X through 127-794A-37X, is 57.8 m thick and is composed mainly of olive gray to gray green clay and siliceous claystone with few to no laminations. Sapropel-bearing clay occurs in some parts of the section. Dolomitic layers, pyrite, and ash are present. The clay and claystone are highly bioturbated and mottled in lighter-colored layers from a few centimeters to a few meters thick. Darker colored layers are slightly to moderately bioturbated. Many of the burrows are horizontal with little vertical relief. The dominant silica phase in this unit is opal-CT (Fig. 16).

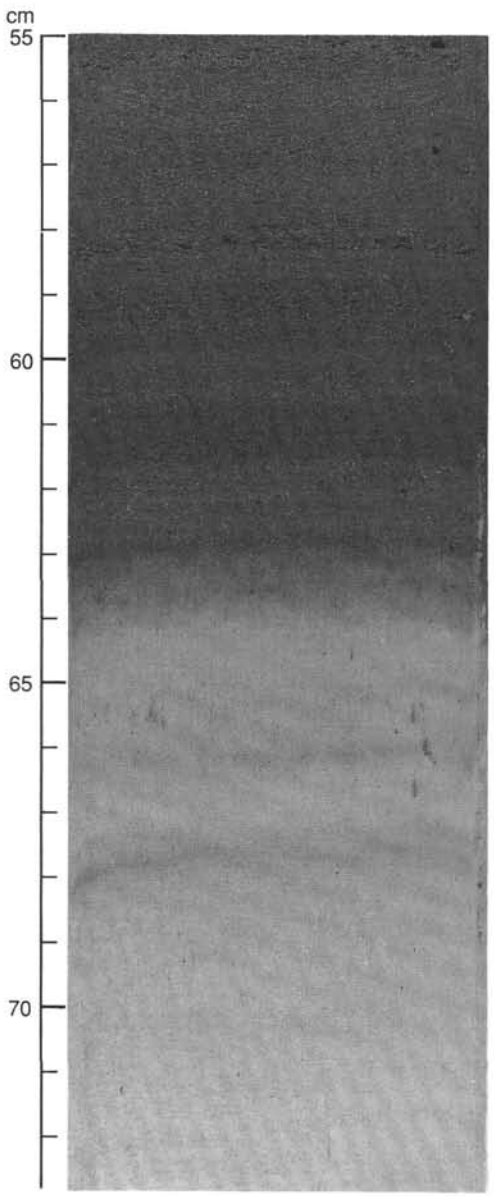

Figure 14. Core photograph of well-laminated, dark-colored clay in gradational contact with underlying poorly laminated-to-homogeneous light-colored clay (Section 127-794A-3H-2, 55–73 cm).

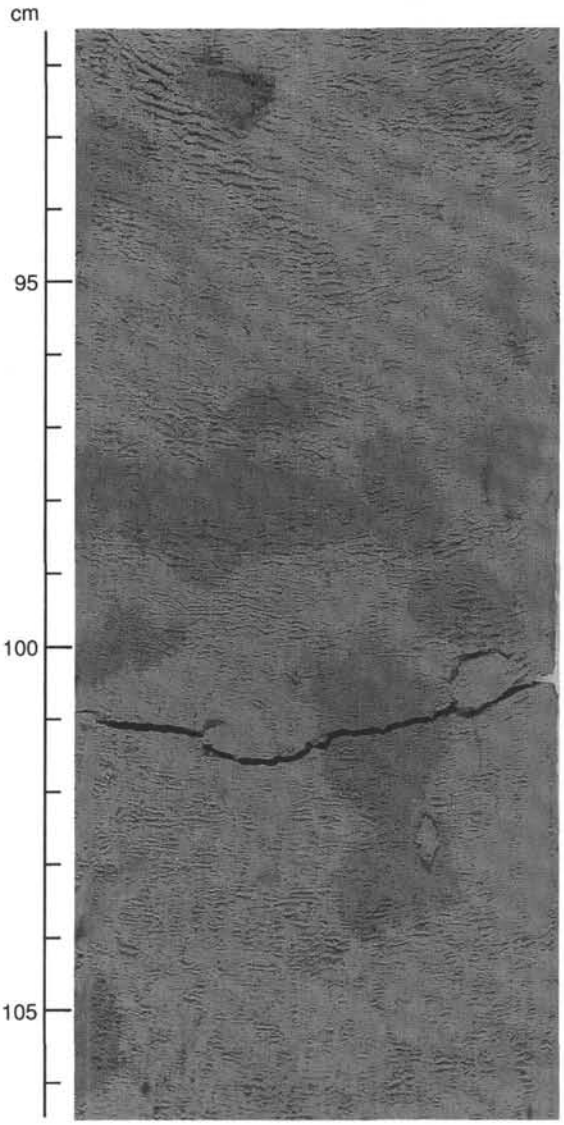

Figure 15. Core photograph of mottled, highly bioturbated, dark-colored diatomaceous ooze (Section 127-794A-11X-3, 91–107 cm).

Subunit IIIB (347.8–491.7 mbsf)

Subunit IIIB, Cores 127-794B-6R through 127-794B-20R consists of 143.9 m of olive to gray green, highly bioturbated claystone similar in appearance to Subunit IIIA, with the exception of rare, faint laminations, especially toward the base of the unit. The subunit differs from Subunit IIIA mainly by the increased abundance of dolomite, ankerite, and silica cements, stringers, and lenses in some parts of the section. The silica phase is opal-CT in the top part of Unit IIIB, but this phase is replaced by quartz at about 395 mbsf (Fig. 16). The unit also contains glauconitic clay at about 475 mbsf and some thin-bedded (1–4 cm) altered tuff.

Unit IV (491.7–520.6 mbsf)

Interval 127-794B-21R through 127-794B-23R.

Unit IV consists of 28.9 m of blue gray to grayish green or dark gray tuff, lapilli tuff (Facies 7), and claystone. Tuff beds range in thickness from a few centimeters to 385 cm. Many of the beds display sharp basal contacts and inverse-to-normal size grading, normal grading, or both. Some tuff beds contain a distinctive sequence of sedimentary structures that grades upward from planar lamination to cross-lamination, and convolute lamination (Fig. 17). The upper part of most tuff beds is bioturbated and gradational to overlying silty claystones. The basal portion of some thick lapilli tuffs is massive and poorly sorted, and contains claystone rip-up clasts and pumice fragments. Tuff and lapilli tuff are composed of slightly vesicular vitric and euhedral crystal fragments. Much of the vitric material is replaced by mixed-layer clay minerals, tentatively identified as chlorite-smectite; however, preservation of shard morphology is commonly good. The tuff occurs interbedded with bioturbated claystone.

Unit V (520.6–544.3 mbsf)

Interval 127-794B-24R through 127-794B-26R.

Unit V is made up of 23.7 m of olive gray, grayish black, and dark yellow brown claystone, silty claystone, and calcareous claystone, with minor glauconitic claystone and altered vitric tuff.

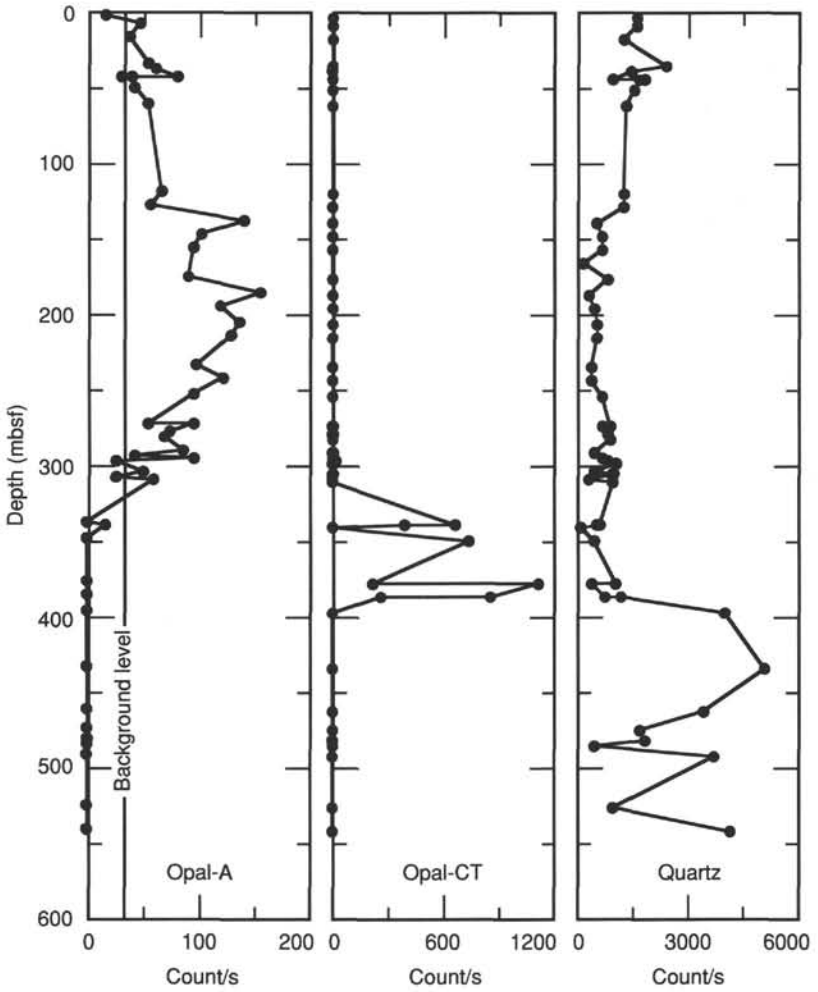

Figure 16. Relative abundance of opal-A, opal-CT, and quartz in sediments at Site 794, determined by XRD analyses.

The unit contains significant diagenetic dolomite and ankerite. Dolomite and ankerite are concentrated in isolated micro nodules, irregular stringers and lenses, and along distinct, thin (< 1.0 mm) laminae. Most of the claystone is moderately bioturbated throughout, although some sections contain faint, deformed laminae. Some tuffs are characterized by cross-lamination and flame structures. Organic matter appears to be moderately abundant, and fine pyrite is disseminated through much of the claystone.

Unit VI (644.1–645.6 mbsf)

Interval 127-794C-13R.

Unit VI consists of 0.86 m of bluish gray to greenish gray, fine-grained tuff, overlain by 0.69 m of dark gray, tuffaceous, silty claystone. The tuff is composed dominantly of bubble-wall glass shards, which are highly altered but retain primary textures. Other constituents include a significant admixture of volcanic lithic fragments and minor quartz, plagioclase, and biotite. Bedding in the tuff ranges from massive to laminated, with normal size grading. These and other structures suggest (see below) deposition from "cold" sediment gravity flows. Small slump folds and convolute laminations indicate minor syndepositional soft-sediment deformation. Bioturbation is confined to the tops of the tuff beds. The claystone is highly bioturbated and well indurated; the top 10 cm are altered and hardened by heat.

Unit VI occurs between two moderately thick units of dolerite and basalt (see description of igneous rocks), which appear to be sills. Thin-section analysis of bubble-wall shards in the tuffs show preferred orientation and plastic deformation of many of the shards (Fig. 18). These textures suggest collapse and moderate compaction of the shards at elevated temperature. Increased temperature likely resulted from intrusion of the tuff and claystone by magma prior to significant lithification; post-depositional reheating by the magmas during intrusion was sufficient to induce incipient plastic deformation of the glass shards.

Clay Mineralogy

X-ray diffraction analyses of whole-rock samples show that clay minerals in Site 794 samples include kaolinite and illite, which are probably detrital, as well as some smectite, chlorite, and mixed-layer clays. The mixed-layer clays may include illite/smectite and chlorite/smectite; however, positive identification of these clays could not be made from bulk sample analyses. Available data are insufficient to define a definite clay-mineral diagenetic sequence as a function of burial depth and temperature.

Sediment Grain Size

Grain-size analyses were carried out on selected samples from Cores 127-794A-IH through 127-794A-25X (0–235 mbsf). Sediment from greater depths is too well lithified to permit disaggre-

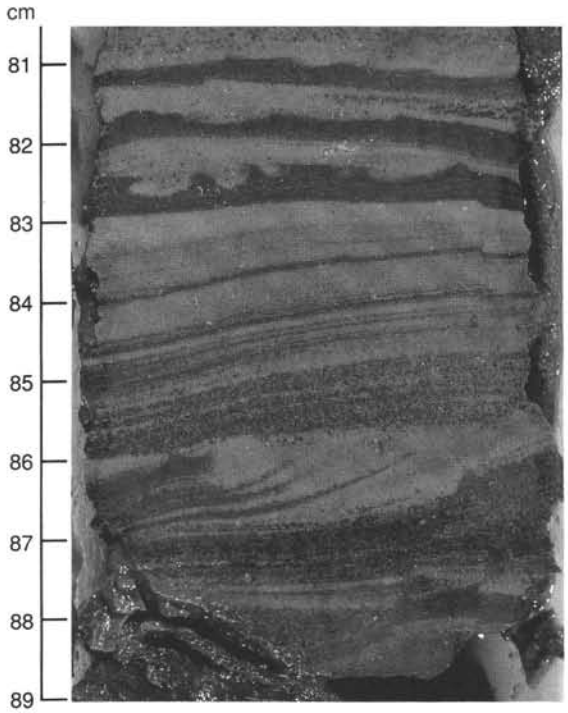

Figure 17. Core photograph. Sequence of sedimentary structures in a thick tuff bed, grading upward from basal parallel lamination through cross-lamination to parallel and convolute lamination with flame structures (Section 127-794B-24R-3, 80–89 cm).

gation. Disaggregated samples were analyzed using the shipboard Lab-Tec 100 particle-size analyzer, calibrated by the use of natural-sediment standards. Data from the analyzer were output as histograms and cumulative frequency curves. Mean grain size of each sample was calculated from these curves.

Results of 46 grain-size analyses are presented in Figure 19. This figure shows that the mean grain size of sediment in Units I and II (late Miocene-Quaternary) ranges from about 5.5–18 μm (clay-silt). The overall mean size falls mainly within the very fine to fine silt range. The predominance of mean sizes in the silt range results from the presence of diatoms and admixed fine ash, which causes the grain size to be biased toward silt. Smear-slide analysis commonly shows the presence of abundant clay-size material, indicating that the nonbiogenic fraction of the sediment is dominantly clay.

Although not analyzed with the Lab-Tec analyzer, the sediments below Core 127-794A-25X appear from smear-slide examination to be generally similar in grain size to the sediments analyzed. A notable exception is the grain size of tuffs in Unit IV (middle Miocene). These tuffs range in grain size from <2 mm to >1 cm (ash and lapilli).

Frequency of Ash-Layer Occurrence

The frequency with which discrete layers of ash (identified by crystal and shard morphology) occur in sediments at Site 794 provides a record through time of explosive volcanic activity in the region surrounding the Japan Sea. A plot of the number of ash layers per core vs. core depth is shown in Figure 20. All discrete ash layers identified in the cores, regardless of thickness, are used in this plot. Figure 20 shows a maximum in ash-layer frequency in Quaternary and Pliocene sediments, a minimum in upper Miocene and uppermost middle Miocene sediments, and another maximum in upper middle Miocene sediments. Four distinct peaks in ash-layer frequency occur in the Pliocene-Quaternary section. These peaks suggest periodic episodes of intense explosive volcanic activity in the Japan Sea region during Pliocene-Pleistocene time; however, these peaks must be correlated with data from other cores recovered in the Japan Sea to confirm this interpretation.

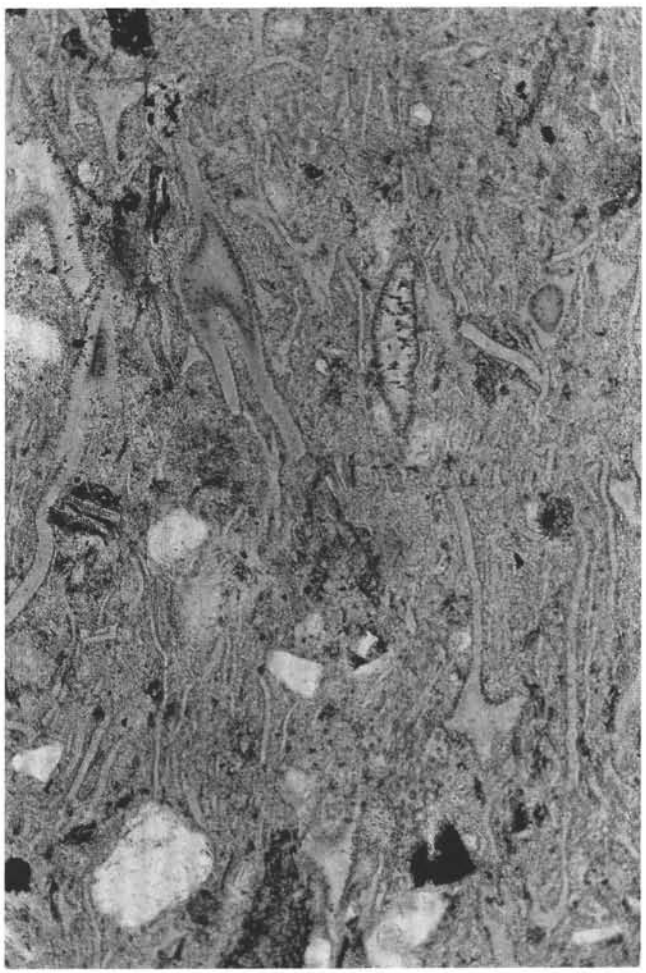

Figure 18. Photomicrograph of aligned and incipiently welded glass shards (now altered to clay + zeolite) from Sample 127-794C-13R-2, 52–54 cm.

The high ash-layer frequency recorded in middle Miocene sediments is based on the presence of thick tuff beds in Cores 127-794B-24R and -25R. This maximum may not have the same significance with respect to intensity of volcanism as that of the thin ash beds in the upper part of the section. Nevertheless, the tuffs record a period of active explosive volcanism during this part of the middle Miocene. They appear to have originated by submarine volcanism, with subsequent redeposition by sediment gravity flows.

The apparent minimum in ash-layer frequency in upper middle Miocene and upper Miocene sediments suggests low frequency of explosive volcanism in the Japan Sea region during this time. These data must be used with caution, however, owing to poor core recovery, although low-ash layer frequency and poor core recovery are not strongly correlated. Also, bioturbation may have obscured the record of ash layers by destroying some ash layers initially present. It seems unlikely, however, that bioturbation obliterated all evidence of thicker ash beds. Therefore, the observed minimum in ash-layer frequency in these sediments is probably real. Also, a minimum in ash-layer frequency in upper middle Miocene and upper Miocene sediments along the Japan Trench transect drilled during Leg 57 of the Deep-Sea

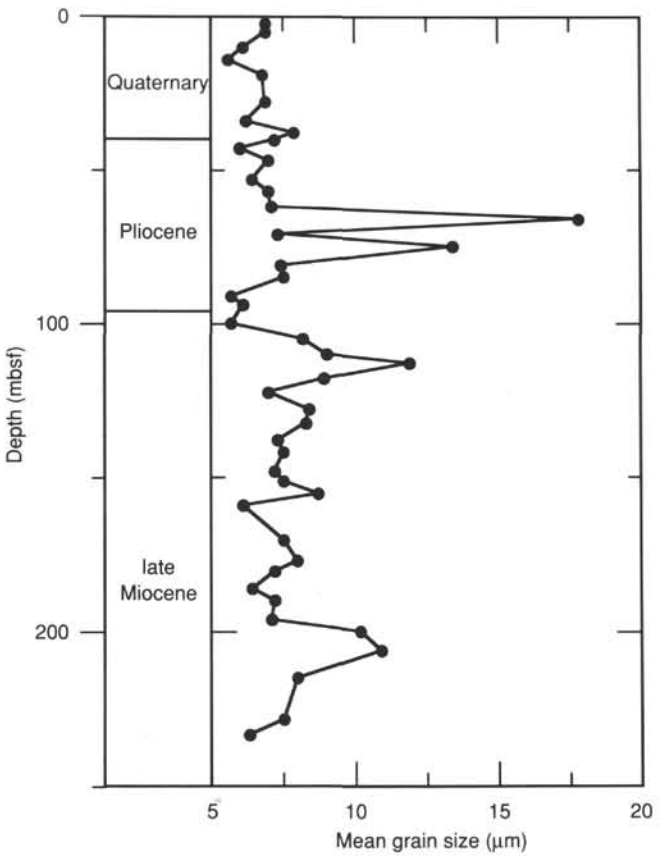

Figure 19. Mean grain size of Quaternary to upper Miocene sediment at Site 794.

Drilling Project is reported by Cadet and Fujioka (1980). This minimum suggests a low level of explosive volcanic activity in the Japan Sea region during late middle Miocene and middle Miocene time.

Depositional History

Sediments at Site 794 range in age from Quaternary to middle Miocene, and consist predominantly of clay and silty clay, with a significant fraction of diatoms in late Miocene and early Pliocene age units. Sedimentary structures include well-developed lamination and thin bedding in dark-colored units, whereas light-colored units are commonly bioturbated and mottled. Thin (0.5–15 cm), discrete ash layers and fine disseminated ash occur throughout much of the stratigraphic section. Coarse-grained turbidites appear to be absent at Site 794, with the possible exception of some middle Miocene tuff units. Uncorrected sedimentation rates calculated by shipboard paleontologists show that sedimentation rates for the entire section are low; however, the sedimentation rate was apparently somewhat higher during late Miocene time (45 m/m.y.) compared to that during other periods (30 m/m.y.).

On the basis of clay and diatom abundance and paucity of sands and turbidites, we suggest that the sediments at Site 794 were deposited in a basin or slope site that was shielded from influx of coarse, terrigenous sediments. The depositional site may have been separated from land by a submarine ridge system that created a barrier to coarse sediment transport by sediment gravity flows or bottom currents. Benthic foraminifer occurrence suggests that water depth in the basin was generally "off-shelf" bathyal; that is, deeper than 200 m. Few data are available to constrain the maximum depth; however, the presence of glauconite in middle Miocene sediments suggests that water depth at that time probably did not exceed about 1500 m and could have been much shallower. Water depths may have increased somewhat following middle Miocene time.

The generally high levels of bioturbation that characterize most of the sediment section suggest that bottom waters were oxygenated during much of middle Miocene to Holocene time. Recurring, well-laminated, organic-rich layers indicate, however, that episodic reduction of oxygen levels must have occurred, especially during the Quaternary and possibly part of middle Miocene time. At least three possible interactive mechanisms may have been responsible for producing variations in oxygen levels. First, the onset of reduced oxygen levels may have been triggered by physiographic changes that affected bottom-water conditions. These changes could have been produced by climate-driven fluctuations in sea level; alternatively, tectonic movements may have affected sill depths and water circulation patterns, resulting in restricted circulation and reduced bottom-water oxygen levels. Second, increased organic productivity in the photic zone, related to cycles of enhanced nutrient availability, could have induced anoxia at the sediment/water interface owing to depletion of oxygen by oxidation of some of the organic matter. Finally, episodic ash falls from subaerial or submarine eruptions may have blanketed the seafloor with ash, temporarily lowering oxygen levels within the sediment. Available evidence confirms that some of the dark-colored layers are indeed ash rich.

BIOSTRATIGRAPHY

Introduction

Microfossils occur with variable abundance and states of preservation throughout Holes 794A and 794B. In general, calcium carbonate microfossils are most abundant and best preserved in the Pleistocene sequence of clay and silty clay from Samples 127-794A-1H, CC, to 127-794A-6H, CC. In contrast, siliceous microfossils are most abundant and best preserved in lower Pleistocene and upper Pliocene clay and silty clay and lower Pliocene and upper Miocene diatomaceous ooze and clay from Samples 127-794A-7H, CC, to 127-794A-30, CC. Microfossils are rare to absent beneath the opal-A/opal-CT boundary, which occurs in Cores 127-794A-31X and 127-794B-6R.

The diatom zonation (Fig. 21, Table 2) best divides the sequences at Hole 794A. Diatom datum levels are generally consistent with magnetostratigraphic boundaries at the site and with datum levels of the North Pacific Ocean (Koizumi and Tanimura, 1985). Placement of the Pliocene/Miocene boundary based on diatom biostratigraphy, however, differs from placement of the boundary based on magnetostratigraphy. The discrepancy is most likely due to diachroneity of first and last appearances of diatoms in the Japan Sea compared to the North Pacific Ocean at this time (Koizumi and Tanimura, 1985). Marginal seas frequently differ environmentally and depositionally from open oceans, so species can be excluded from or persist longer in isolated seas than in open oceans. Diachronous first and last appearances are frequent among radiolarians in the Japan Sea.

Zonation of the six basal cores of Holes 794A and 794B below Core 127-794B-5R is problematic due to diagenetic destruction of microfossils. Sporadic occurrences of radiolarians, calcareous nannofossils, and planktonic foraminifers are consistent with late Miocene and middle Miocene ages, as indicated on Figure 22. Extrapolation (Fig. 30) from a calcareous nannofossil and a planktonic foraminifer apparent LAD and FAD in Samples 127-794B-24R, CC, and 127-794B-25R, CC, suggests that the age of the claystone overlying the basal sill in Core 127-794B-26R is 14.8 to 16.2 Ma (Fig. 22).

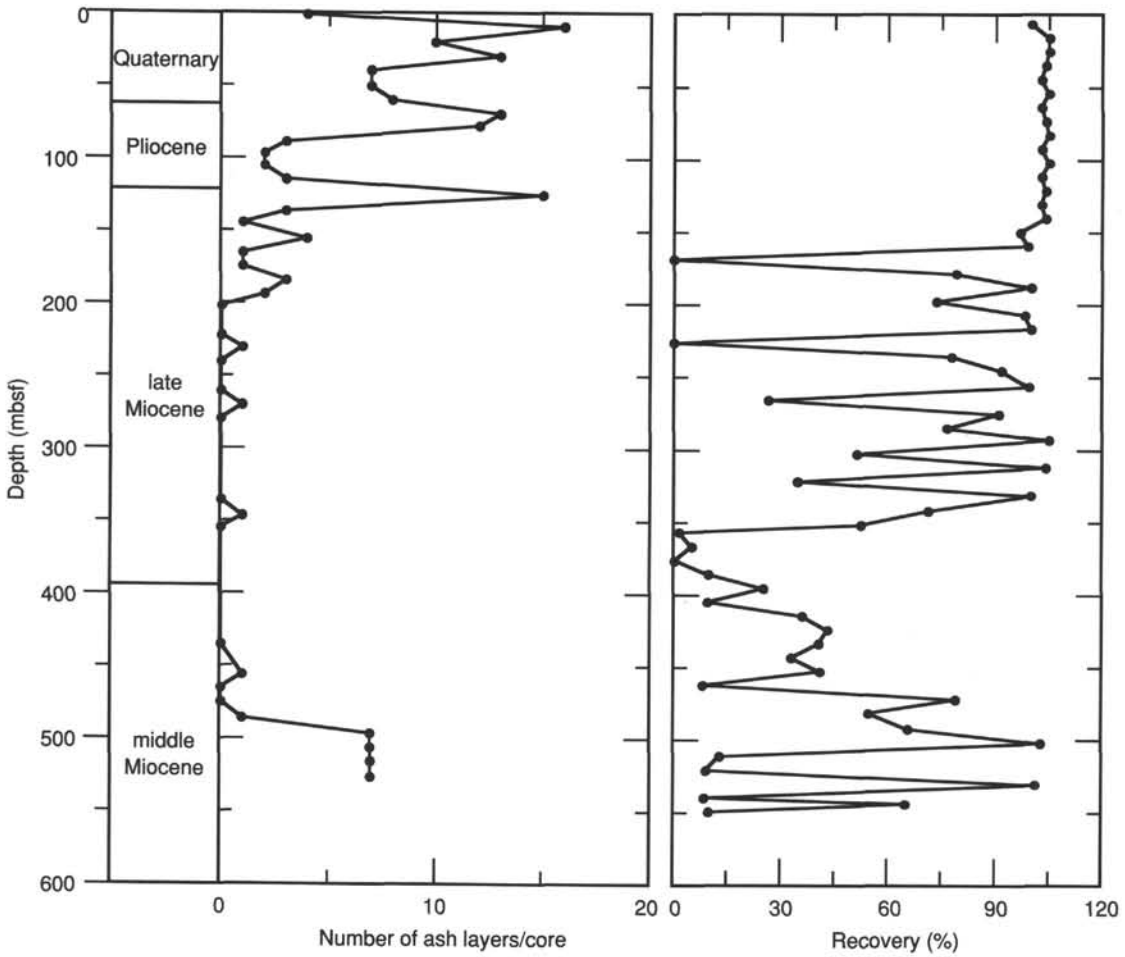

Figure 20. Frequency of occurrence of ash layers per core at Site 794 (left), with a comparison plot of core recovery vs. depth (right).

Diatoms

Samples 127-794A-1H, CC, through 127-794A-8H, CC, consist of clay and silty clay and yielded diatoms with variable abundance and preservation. Samples 127-794A-1H, CC, and 127-794A-3H-3, 98–99 cm, are assigned to the following Pleistocene diatom zones: the *Neodenticula laseminae* Zone, based on the presence of *N. seminae* and the absence of *Rhizosolenia curvirostris*; and the *Rhizosolenia curvirostris* Zone, based on the presence of *R. curvirostris* (Fig. 21). Samples 127-794A-7H, CC, and 127-794A-8H, CC, both have common *Neodenticula koizumii* and belong to the upper Pliocene *Neodenticula koizumii* Zone. The Pleistocene/Pliocene boundary lies between the *Actinocyclus oculatus* Zone and the *Neodenticula koizumii* Zone, and though the *Actinocyclus oculatus* Zone was not identified in Hole 794A, the Pleistocene/Pliocene boundary is placed in Core 127-794A-7H at the top of the *Neodenticula koizumii* Zone (Fig. 21).

Samples 127-794A-9H, CC, through 127-794A-30X, CC, are mostly diatomaceous clays and oozes with abundant to common diatoms that show good to moderate preservation. Sample 127-794A-9H, CC, has both *N. koizumii* and *N. kamtschatica* and belongs to the upper Pliocene *Neodenticula koizumii–Neodenticula kamtschatica* Zone. The lower Pliocene *Thalassiosira oestrupii* Zone occurs in Samples 127-794A-10H, CC, through 127-794A-13H, CC, based on the occurrences of *N. kamtschatica*, *Thalassiosira zabelinae*, and *T. oestrupii*. The uppermost Miocene *Neodenticula kamtschatica* Zone occurs in Samples 127-794A-14H, CC, through 127-794A-23X, CC, and Samples 127-794B-1R, CC, through 127-794B-3R, CC, based on the occurrence of *N. kamtschatica* (Figs. 21 and 22). The Pliocene/Miocene boundary (5.3 Ma) in the northwest Pacific region occurs in the uppermost part of the *Neodenticula kamtschatica* Zone, near the boundary with the *Thalassiosira oestrupii* Zone (Koizumi, 1985). At Site 794, the boundary is placed in Core 127-794A-14H (Fig. 21). At present, the position of the Pliocene/Miocene boundary at Site 794 differs from that suggested by magnetostratigraphy, which places it in Core 127-794A-17X.

The upper Miocene *Rouxia californica* Zone occurs in Samples 127-794A-24X, CC, through 127-794A-26X, CC, and Sample 127-794B-4R, CC (Figs. 21 and 22), as suggested by the presence of *R. californica* and the absence of *N. kamtschatica*. The *Thalassionema schraderi* Zone occurs in the intervals from Samples 127-794A-27X, CC, through 127-794A-30X, CC. The absence of *T. schraderi* and the presence of *D. katayamae* in Sample 127-794A-31X, CC, suggest it is part of the *Denticulopsis katayamae* Zone.

A few reworked Miocene diatoms, such as *Neodenticula kamtschatica*, *Denticulopsis katayamae*, and *Denticulopsis dimorpha*, are present in Sample 127-794A-1H, CC. Sample 127-794A-8H, CC, is characterized by common occurrences of marine tychopelagic and benthic diatoms such as *Cocconeis* spp., *Diploneis* spp., and *Paralia sulcata*.

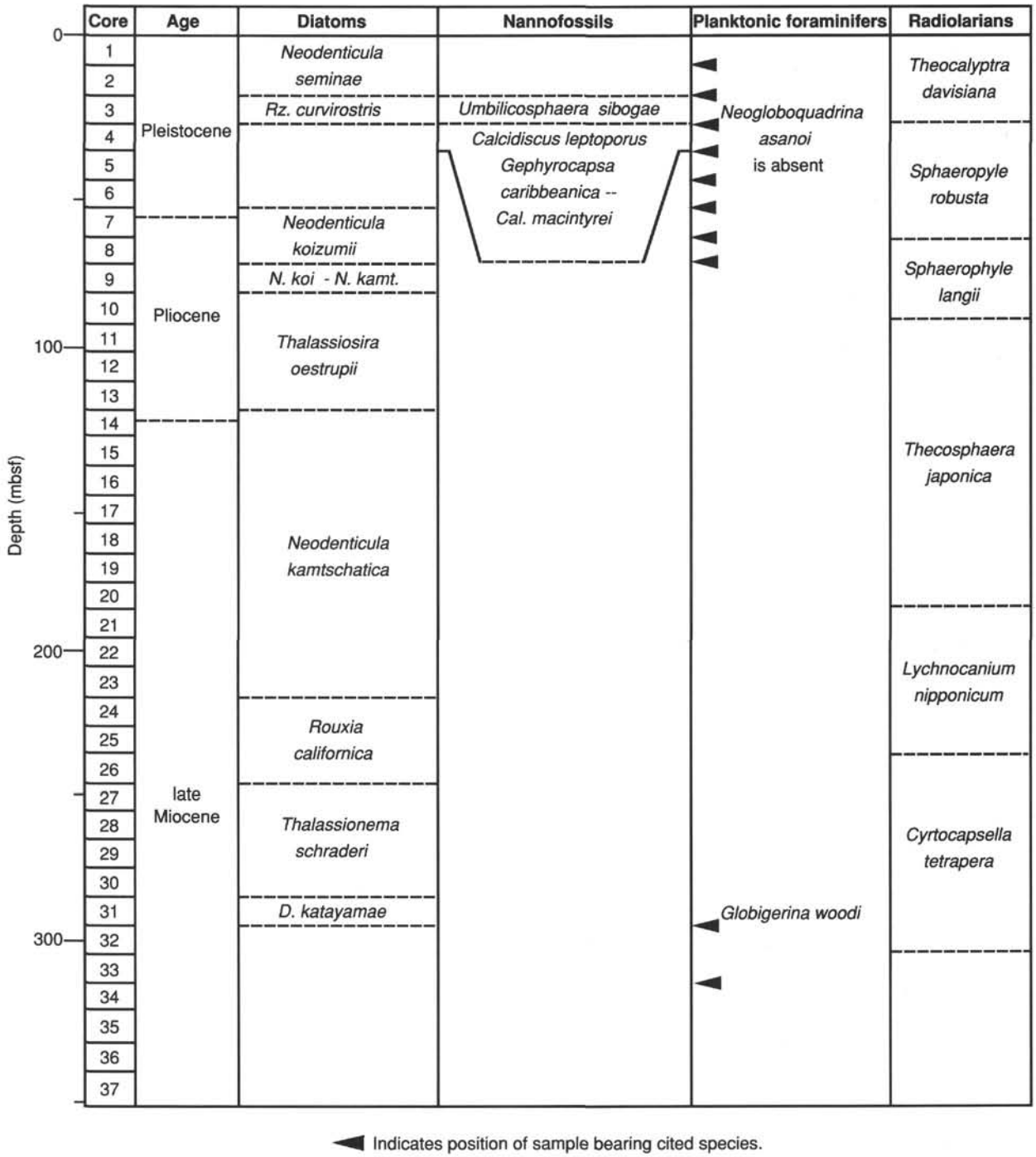

Figure 21. Planktonic microfossil zones in Hole 794A.

Calcareous Nannofossils

Most of the studied samples are barren of calcareous nannofossils. Wherever present, the assemblages are low in diversity in contrast to open-ocean nannofossil assemblages at latitudes similar to Site 794. Of 37 cores recovered from Hole 794A, only two, Cores 127-794A-3H and 127-794A-4H, yielded recognizable nannofossils of early Pleistocene age. The assemblage consists of only a few species, which are moderately preserved with relative abundances varying from rare to common. Due to the absence of nannofossils in most of the cores, age assignment of the entire sedimentary sequence was not possible. Core 127-794A-3H is assigned to the *Umbilicosphaera sibogae* Zone based on the presence of *Gephyrocapsa oceanica*, and *Gephyrocapsa caribbeanica* with the rare occurrence of *Pseudoemiliania lacunosa*. *Coccolithus pelagicus* is common in this zone. Core 127-794A-4H is assigned to the undifferentiated *Calcidiscus leptoporus* Zone and *Gephyrocapsa caribbeanica–Calcidiscus macintyrei* Zone. The LAD of *Calcidiscus macintyrei*, which marks the boundary between these two zones, was not recognizable. The assemblage consists of rare amounts of *G. caribbeanica*, *C. pelagicus*, and common, small *Reticulofenestra* sp.

Table 2. Abundance and preservation of microfossils in Hole 794A.

Core	Diatoms		Nannofossils		Planktonic foraminifers		Radiolarians		Benthic foraminifers	
	Abundance	Preservation	Abundance	Preservation	Abundance	Preservation	Abundance	Preservation	Abundance	Preservation
1H, CC	Common	Moderate	Barren		Few	Poor	Few	Good	Barren	
2H, CC	Rare	Poor	Barren		Rare	Poor	Rare	Moderate	Barren	
3H, CC	Rare	Poor	Abundant	Moderate	Abundant	Moderate	Rare	Moderate	Few	Poor
4H, CC	Barren		Barren		Few	Moderate	Abundant	Good	Few	Moderate
5H, CC	Barren		Barren		Common	Poor	Rare	Moderate	Few	Moderate
6H, CC	Barren		Barren		Rare	Poor	Barren		Barren	
7H, CC	Rare	Moderate	Barren		Rare	Poor	Common	Good	Barren	
8H, CC	Abundant	Good	Barren		Rare	Poor	Abundant	Good	Few	Moderate
9H, CC	Abundant	Good	Barren		Barren		Abundant	Good	Barren	
10H, CC	Abundant	Good	Barren		Barren		Abundant	Moderate	Rare	Moderate
11H, CC	Abundant	Good	Barren		Barren		Abundant	Moderate	Barren	
12H, CC	Abundant	Good	Barren		Barren		Few	Moderate	Few	Poor
13H, CC	Common	Moderate	Barren		Barren		Common	Good	Rare	Poor
14H, CC	Common	Moderate	Barren		Barren		Common	Good	Rare	Poor
15H, CC	Abundant	Good	Barren		Barren		Abundant	Good	Rare	Poor
16X, CC	Common	Good	Barren		Barren		Abundant	Moderate	Rare	Poor
17X, CC	Abundant	Good	Barren		Barren		Common	Moderate	Rare	Poor
18X, CC	Abundant	Good	Barren		Barren		Few	Moderate	Rare	Poor
19X, CC	Common	Moderate	Barren		Barren		Common	Moderate	Barren	
20X, CC	Common	Good	Barren		Barren		Few	Moderate	Rare	Poor
21X, CC	Common	Moderate	Barren		Barren		Common	Moderate	Rare	
22X, CC	Common	Moderate	Barren		Barren		Common	Moderate	Rare	
23X, CC	Abundant	Good	Barren		Barren		Common	Moderate	Rare	
24X, CC	Abundant	Moderate	Barren		Barren		Few	Moderate	Rare	
25X, CC	Abundant	Good	Barren		Barren		Common	Moderate	Rare	
26X, CC	Abundant	Moderate	Barren		Barren		Few	Moderate	Rare	
27X, CC	Abundant	Moderate	Barren		Barren		Few	Moderate	Rare	
28X, CC	Abundant	Moderate	Barren		Barren		Few	Moderate	Barren	
29X, CC	Common	Moderate	Barren		Barren		Few	Moderate	Barren	
30X, CC	Common	Moderate	Barren		Barren		Few	Moderate	Few	Poor
31X, CC	Few	Poor	Barren		Rare	Poor	Rare	Moderate	Few	Moderate
32X, CC	Barren		Barren		Barren		Rare	Poor		
33X, CC	Barren		Barren		Rare	Poor	Barren			
34X, CC	Barren		Barren		Barren		Barren			
35X, CC	Barren		Barren		Barren		Rare	Poor		
36X, CC	Barren		Barren		Barren		Barren			
37X, CC	Barren		Barren		Barren		Barren			

Nannofossils are more diverse at Hole 794B than at Hole 794A, and they occur sporadically throughout the sedimentary sequence. Their relative abundance varies from rare to few, and the state of preservation varies from good to poor. Most of the marker species, upon which the early Pliocene and Miocene nannofossil zones are based, are absent in this hole. The sporadic occurrence of nannofossils of relatively poor preservation precludes detailed zonal assignments.

Cores 127-794B-1R to 127-794B-10R range between late Miocene and early Pliocene in age based on nannofossils. The assemblage in this interval is characterized by *Reticulofenestra pseudoumbilica*, *Sphenolithus abies*, *Sphenolithus neoabies*, *Discoaster brouweri*, *Coccolithus pelagicus*, *Dictycoccites productus*, *Calcidiscus macintyrei* and small *Reticulofenestra* sp. All species except *R. pseudoumbilica* are few to rare in abundance. In the lower part of this sedimentary interval there are rare, reworked nannofossils of middle Miocene and Eocene age. In Sample 127-794B-10R-1, 70–71 cm, the presence of the delicate species, *Pontosphaera multipora* and *Pontosphaera japonica*, indicates good preservation. Within this sample, *Discoaster brouweri* is the only discoaster and occurs rarely. This suggests that the absence of most of the biostratigraphically useful nannofossil taxa at the present site in part is due to unfavorable paleoecological conditions (e.g., surface water temperature, salinity) as well as to dissolution.

Rare occurrence of *Discoaster hamatus* in Sample 127-794B-12R-1, 86–87 cm, tentatively marks the base of the late Miocene. The rest of the sedimentary section is assigned to a middle Miocene age based on the absence of *Sphenolithus abies*, *Sphenolithus neoabies*, and *Reticulofenestra pseudoumbilica*, and the presence of *Sphenolithus heteromorphus*, *Sphenolithus moriformis*, *Discoaster deflandre*, and *Discoaster adamanteous*. None of the species of the latter group, however, is common. The LAD of *S. heteromorphus* occurs in Sample 127-794B-24R, CC. Poorly preserved, rare specimens of *S. heteromorphus* are found down to Sample 127-794B-25R-1, 17–18 cm, below which samples are barren of nannofossils. The age of the first occurrence of *S. heteromorphus*, 17.1 Ma (Berggren et al., 1985a), provides a maximum age for the deepest nannofossil-bearing sample.

Foraminifers

The occurrence of foraminifers in Holes 794A and 794B corresponds closely to the nature of the host sediment. In general, planktonic foraminifers are common to abundant in the massive and mottled silty and ashy clay found in the upper 57 m of Hole 794A. In contrast, planktonic tests are absent to rare in the laminated clay and silty clay (Lithologic Unit IA) found in this interval of Hole 794A. Planktonic foraminifers are rare in the clay and silty clay between 57 and 90 m (Lithologic Unit IB) in Hole 794A and few to absent from the phosphate-bearing claystone (Lithologic Unit V) found below 507 m in Hole 794B. Planktonic tests are absent from intervals of diatomaceous ooze and diatomaceous clay (Lithologic Unit II) and intervals containing opal-CT or microcrystalline quartz (Lithologic Unit III). Planktonic tests are absent from the volcanic tuff (Lithofacies IV) found in Hole 794B near 500 m. In contrast, benthic foraminifers occur sporadically throughout all lithofacies except the volcanic tuff (Lithologic Unit IV). The tests are rare in number in all but two samples from the phosphate-bearing clay at the base

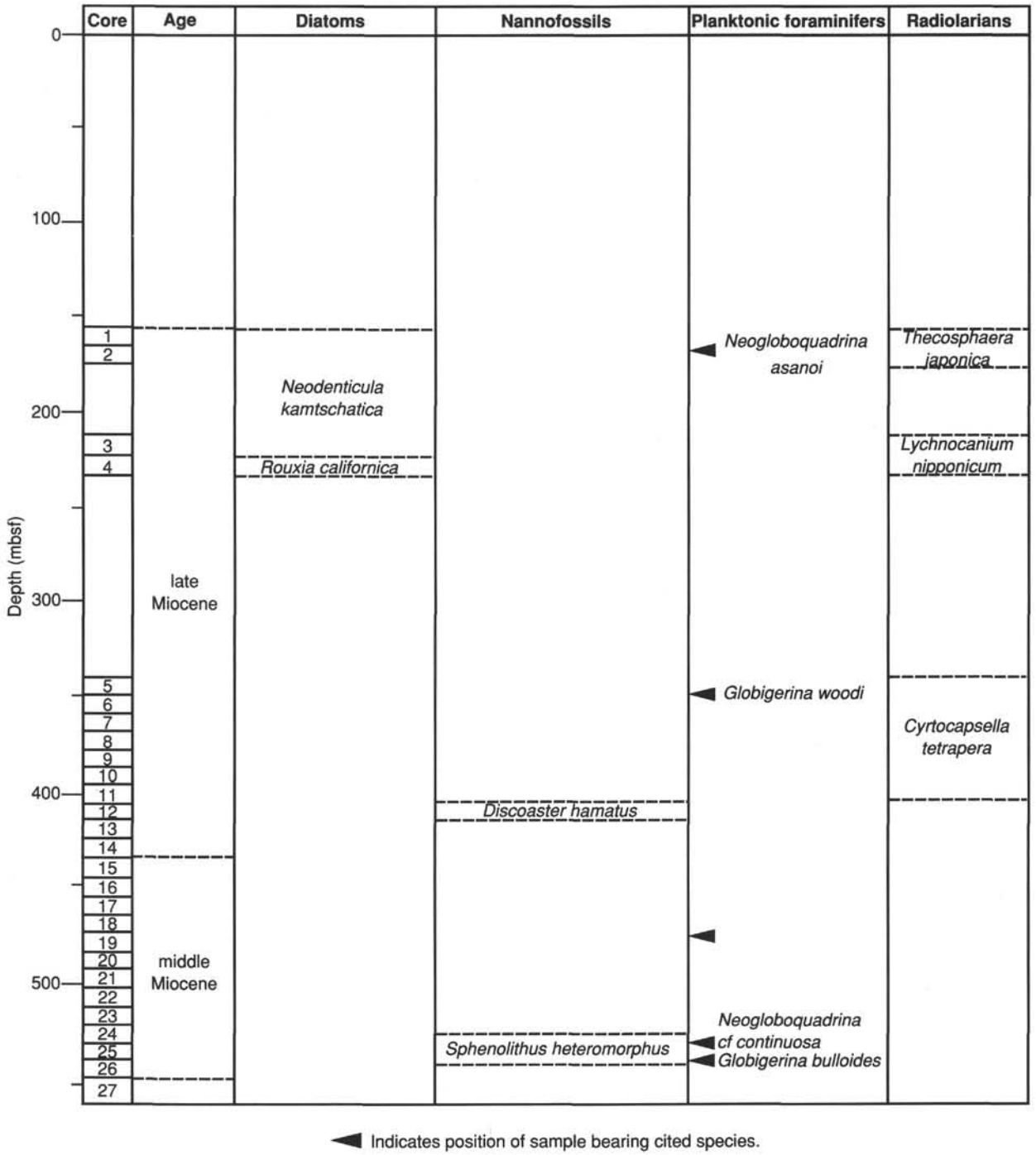

Figure 22. Planktonic microfossil zones in Hole 794B.

of Hole 794B where they are common. In general, benthonic foraminifers are absent from the most indurated intervals.

Planktonic foraminifers were recovered from 12 of 39 samples in Hole 794A and are confined to an interval from Samples 127-794A-1H, CC, to 127-794A-8H, CC, and to Samples 127-794A-31X, CC, and 127-794A-33X, CC. Tests are rare in all samples except Samples 127-794A-3H, CC, 127-794A-3H-2, 94–99 cm, and 127-794A-4H-5, 90–95 cm, in which planktonic foraminifer tests are the most abundant constituent of the sand-size fraction. Tests of robust structure, like those of *Neogloboquadrina pachyderma*, are preserved in moderate condition, but delicate species typical of subarctic assemblages, like *Globigerinita uvula*, are absent.

The species from the upper eight cores of Hole 794A are typical of a Quaternary subarctic assemblage and include *Globigerina bulloides*, *Globigerina clarkei*, *Globigerinita glutinata*, *Globigerina quinqueloba*, rare *Neogloboquadrina dutertrei*, and abundant *Neogloboquadrina pachyderma* in both its sinistral and dextral coiling forms. Sample 127-794A-3H-2, 94–99 cm, contains a cool, subarctic assemblage dominated by sinistral *N. pachyderma*, whereas Samples 127-794A-3H, CC, and 127-794A-4H-5, 90–95 cm, contain a warmer subarctic assemblage with

both dextral and sinistral *N. pachyderma*. Five specimens of the late Oligocene to late Pliocene species, *Globigerina woodi*, were picked from Sample 127-794A-31X, CC, and one specimen of the middle Miocene to Holocene species, *Globigerina bulloides*, was found in Sample 127-794A-33X, CC.

Benthic foraminifers occur in more samples than do planktonic foraminifers in Hole 794A; 28 of 39 samples bear benthonic species, whereas 10 of 37 bear planktonic foraminifers. Samples 127-794A-1H, CC, to 127-794A-10H, CC, contain *Globocassidulina*, *Miliammina*, lagenids, nodosarids, and miliolids. The assemblage has both bathyal and shelfal taxa and is consistent with the occurrence of abundant sand-size mineral grains, which may have been transported by turbidity currents from shelf and upper bathyal environments. Samples 127-794A-12H, CC, to 127-794A-27X, CC, are dominated by textularids, mostly *Martinottiella*, with rare rotalids like *Melonis*, *Globobulimina*, and *Gyroidina*, which are species typical of lower middle bathyal environments. Samples 127-794A-30X, CC to 127-794A-33X, CC contain a more diverse assemblage of rotalids, including *Globocassidulina*, lagenids, *Fontbotia wuellerstorfi*, *Pullenia*, and other rotalids, with a textularid assemblage similar to that in overlying samples. The higher diversity of rotalids is likely due to better preservation of calcite than in overlying samples.

Planktonic foraminifers were recovered in 5 of 26 core-catcher samples in Hole 794B. Tests are rare in Sample 127-794B-5R, CC, and 127-794B-18R, CC, and common in Samples 127-794B-1R, CC, 127-794B-24R, CC, and 127-794B-25R, CC. Some specimens in Sample 127-794B-24R, CC, are flattened by a post-depositional process.

The species from the upper section of Hole 794B are typical of high-latitude Pliocene assemblages. Sample 127-794B-1R, CC, bears abundant specimens of *Neogloboquadrina asanoi*, common specimens of sinistral, encrusted *Neogloboquadrina pachyderma*, rare specimens of dextral *Neogloboquadrina pachyderma*, few tests of *Globigerina bulloides*, and rare tests of *Globigerina quinqueloba*. Sample 127-794B-5R, CC, bears five specimens of *Globigerina woodi*, and Sample 127-794B-18R, CC, contains two poorly preserved specimens of *Globigerina*. Sample 127-794B-24R, CC, contains an abundant assemblage of foraminifers, including common *Globigerina woodi*, common *Globigerinella obesa*, rare *Globigerinoides quadrilobatus*, few *Globoquadrina venezuelana*, and common *Neogloboquadrina* cf. *continuosa*, an assemblage consistent with an age of middle or late Miocene. Sample 127-794B-25R, CC, contains one *Globigerina bulloides*, three *Globigerina woodi*, four *Neogloboquadrina* cf. *continuosa*, and three poorly preserved specimens of *Globigerina*.

Benthic foraminifers occur in more samples than do planktonic foraminifers at Hole 794B; 9 of 26 samples contain benthonic foraminifers, whereas 5 of 26 samples contain planktonic foraminifers. Bathyal genera and species occur in all samples. Lower middle bathyal rotalids and textularids, including *Fontbotia wuellerstorfi* and *Martinottiella* spp., co-occur and are rare in Samples 127-794B-1R, CC, to 127-794B-5R, CC. The interval from 127-794B-6R, CC, to 127-794B-23R, CC, is barren except for Samples 127-794B-13R, CC, and 127-794-18R, CC, which contain textularids, lagenids, rotalids, and miliolids, all of which occur rarely. Abundant benthonic foraminifers occur in Samples 127-794B-24R, CC, to 127-794-26R, 75–77 cm. The assemblage is dominated by *Cyclammina*, with common *Nonionella* and *Spirosigmoilinella*, several of which are characteristic of upper middle bathyal, stagnant conditions (Matoba, 1984).

Radiolarians

Site 794 yielded a relatively continuous and well-preserved record of radiolarian biostratigraphy spanning late Miocene through Pleistocene time. Diagnostic indicators of North Pacific and tropical Pacific zonations were almost entirely lacking throughout all cores of Site 794. Zonal boundaries based on the radiolarian first and last appearance datum (FAD and LAD) events were selected according to the outline found in the explanatory notes chapter and are indicated on the Site 794 barrel sheets and in Figures 21 and 22.

Radiolarians of Pleistocene age recovered from silty clays in Hole 794A (Cores 127-794A-1H through 127-794A-5H) are, in general, rare to few and moderately preserved. Sample 127-794A-4H, CC, however, yielded abundant and well-preserved tests. The diversity of the radiolarian assemblage in this sample is high, at least four times greater than in the younger samples examined. Sample 127-794A-6H, CC, is completely barren of radiolarians. The assemblage composition of the Pleistocene sediments changes dramatically between core-catcher samples. This probably resulted from (1) unique oceanographic conditions in the Japan Sea during the Pleistocene, resulting from Northern Hemisphere glaciations and/or fluctuations in sill depths, and (2) dissolution of radiolarian tests.

When present in the Pleistocene sediments of Hole 794A, North Pacific and tropical Pacific stratigraphic indicators did not usually display their expected ranges according to ages based on diatom and magnetic reversal stratigraphy. The LAD of *Stylatractus universus* (0.41 ± 0.005, Hays and Shackleton, 1976) for instance, could not be located because this species occurs only sporadically in deeper samples from Site 794 holes. *Druppatractus acquilonius* displayed a continuous range and was moderately abundant. Its last appearance event however, documented to post-date the LAD of *Stylatractus universus* (Hays, 1970), occurred closer to 1 Ma according to diatom and paleomagnetic ages (between samples 127-794A-7H, CC, and 127-794A-8H, CC). Species diagnostic of Quaternary zones (see Reynolds, 1980), such as *Botryostrobus aquilonaris*, *Eucyrtidium matuyamai*, *Eucyrtidium calvertense*, and *Lamprocyrtis nigriniae*, were completely missing from Site 794 sediments. The FAD of *Lychnocanium* sp. cf. *L. grande* occurred between 127-794A-1H, CC, and 127-794A-2H, CC. This event may be an important datum level in Japan Sea sediments because the species from this genus (*Lychnocanium* sp. cf. *L. grande* and *Lychnocanium nipponicum*) present in sediments from Site 794 appear to be well adapted to the environments of this marginal sea. They are relatively abundant, well preserved, show consistent ranges, and have FAD and LAD events that occur synchronously across the Pacific. Other events that are found in the Pleistocene sediments of Hole 794A are the LAD of *Clathrocyclas cabrilloensis* (between 127-794A-2H, CC, and 127-794A-3H, CC) and the LAD of *Sphaeropyle robusta* (between 127-794A-2H, CC and 127-794A-3H, CC).

Pliocene radiolarians from Hole 794A diatomaceous silty clays and clayey diatom oozes are more abundant and better preserved than Pleistocene radiolarians from Hole 794A. Species diversity is higher and the assemblages are less variable than Pleistocene assemblages. In general the assemblages reflect cold waters with dominant species being *Theocalyptra davisiana* and an unidentified species from the genus *Plectacantha*. Important radiolarian datum levels found in the Pliocene include the LAD of *Lipmanella* sp. aff. *Theocyrtis redondoensis* (between 127-794A-7H, CC, and 127-794A-8H, CC), the FAD of *Theocalyptra davisiana* (between 127-794A-8H, CC, and 127-794A-9H, CC), the LAD of *Thecosphaera japonica*, (between 127-794A-8H, CC, and 127-794A-9H, CC), and the FAD of *Sphaeropyle langii* (between 127-794A-10H, CC, and 127-794A-11H, CC). Datum levels of lesser stratigraphic importance appear diachronous with the same datum levels in other areas of the ocean and include the LAD of *Stylacontarium* sp. cf. *S. acquilonarium* (between 127-794A-10H, CC, and 127-794A-11H, CC), the LAD of *Botryostrobus bramlettei* (between 127-794A-10H, CC, and

127-794A-11H, CC), and the LAD of *Stichocorys peregrina* (between 127-794A-12H, CC, and 127-794A-13H, CC). The reliability of the LAD of *Botryostrobus bramlettei* is suspect because specimens were found in only three samples (127-794A-11H, CC, 127-794A-18X, CC, and 127-794B-1R, CC). If this is the true last occurrence, the fact that it occurs approximately 1 m.y. later than previously reported (Johnson and Nigrini, 1985) may indicate that this species took its last refuge before extinction in the Japan Sea.

The Miocene of Site 794 is represented below Core 14H in Hole 794A, and in all cores in Hole 794B. In general, radiolarians are few to common and preservation is moderate. Four core-catcher samples from the lower portions of Hole 794A and 11 of 27 core-catcher samples from Hole 794B were barren of radiolarians (Tables 2 and 3). These barren samples correspond to sediments that have undergone the transition from opal-A to opal-CT. Miocene radiolarian assemblages from Site 794 have a moderate species diversity that does not change significantly in species composition between core-catcher samples. This possibly reflects a stable late Miocene climate in the Japan Sea, an inference that must be confirmed by performing quantitative counts.

Datum levels that occurred in the Miocene of Site 794 are the FAD of *Lipmanella* sp. aff. *Theocyrtis redondoensis* (between 127-794A-16X, CC, and 127-794A-17X, CC), the LAD of *Theocyrtis redondoensis* (between 127-794A-18X, CC and 127-794A-19X, CC), the LAD *Sethocyrtis japonica* (between 127-794A-19X, CC, and 127-794A-20X, CC), the FAD of *Thecosphaera japonica* (between 127-794A-20X, CC, and 127-794A-21X, CC), the LAD of *Lychnocanium nipponicum* (between 127-794A-20X, CC, and 127-794A-21X, CC), the LAD of *Stichocorys delmontensis* (between 127-794A-21X, CC, and 127-794A-22X, CC), the LAD of *Tholospyris anthopora* (between 127-794A-25X, CC, and 127-794A-26X, CC), the LAD of *Tholospyris mammillaris* (between 127-794A-26X, CC, and 127-794A-27X, CC), the LAD of *Stichocoryswolfii* (between 127-794A-27X, CC, and 127-794A-28X, CC), and the LAD of *Lithatractus tochigiensis* (between 127-794A-27X, CC, and 127-794A-28X, CC). The LAD of *Cyrtocapsella tetrapera* was found in Hole 794B (between 127-794B-4R, CC and 127-794B-5R, CC). According to ages determined by diatom stratigraphy, the LAD of *Stichocorys wolfii* occurred approximately 1 m.y. later in the Japan Sea than in the Pacific. This may reflect the fact that at this site, datum levels were selected by strict morphological criteria instead of evolutionary halfway points. Because species from the genus *Stichocorys* were relatively rare at this site, an evolutionary criterion for picking these datum levels was not practical. The phyletic transition of *Stichocorys delmontensis* from *Stichocorys wolfii* is probably reflected in their overlapping ranges between samples 127-794A-28X, CC, and 127-794A-30X, CC, while no overlapping range is observed between *Stichocorys peregrina* and *Stichocorys delmontensis*. It appears that the oceanographic realm of the Japan Sea was not suitable for *Stichocorys peregrina* because it became extinct approximately 1 m.y. earlier in the Japan Sea than in the Pacific Ocean.

Paleoenvironment

Middle Miocene surface waters were cool in the northern Yamato Basin, based on assemblages of planktonic foraminifers and calcareous nannofossils at Site 794. The floor of the basin had subsided to upper middle bathyal depths (about 500 m) by this time, and deep waters were low in dissolved oxygen based on benthonic foraminifer assemblages.

Late Miocene surface waters at Site 794 were cool based on the dominance of high-latitude diatoms over other microfossil groups, and supported by the cool-water aspect of planktonic foraminifers and calcareous nannofossils where they occur. The cool surface waters appear relatively stable over time because radiolarian assemblages show no major changes in species composition. The dominance of siliceous microfossils over carbonate microfossils indicates either high productivity due to persistent upwelling or enhanced preservation of silica beneath silica-rich bottom waters. Siliceous oozes were deposited in the Japan Sea from 8 to 4 Ma as in other marginal basins of the North Pacific Ocean, such as the Bering Sea, Okhotsk Sea, Gulf of California, and northern Japan, in which the diatomaceous nature of

Table 3. Abundance and preservation of microfossils in Hole 794B.

	Diatoms		Nannofossils		Planktonic foraminifers		Radiolarians		Benthic foraminifers	
Core	Abundance	Preservation	Abundance	Preservation	Abundance	Preservation	Abundance	Preservation	Abundance	Preservation
1R, CC	Abundant	Good	Few	Poor	Few	Moderate	Abundant	Good	Barren	
2R, CC	Abundant	Good	Barren		Barren		Common	Good	Few	Poor
3R, CC	Abundant	Good	Barren		Barren		Common	Moderate	Barren	
4R, CC	Abundant	Good	Barren		Barren		Few	Moderate	Rare	Good
5R, CC	Barren		Barren		Rare	Poor	Rare	Poor	Few	Poor
6R, CC	Rare	Poor	Barren		Barren		Rare	Poor	Barren	
7R, CC	Rare	Poor	Few	Moderate	Barren		Rare	Poor	Barren	
8R, CC	Barren		Common	Poor	Barren		Barren		Barren	
9R, CC	Rare	Poor	Few	Moderate	Barren		Rare	Poor	Barren	
10R, CC	Barren		Barren		Barren		Rare	Poor	Barren	
11R, CC	Barren		Barren		Barren		Barren		Barren	
12R, CC	Barren		Barren		Barren		Barren		Barren	
13R, CC	Barren		Rare	Poor	Barren		Rare	Moderate	Few	Poor
14R, CC	Barren		Barren		Barren		Barren		Rare	Poor
15R, CC	Barren		Barren		Barren		Barren		Barren	
16R, CC	Barren		Barren		Barren		Barren		Barren	
17R, CC	Barren		Barren		Barren		Barren		Barren	
18R, CC	Barren		Barren		Rare	Poor	Barren		Few	Poor
19R, CC	Barren		Barren		Barren		Barren		Barren	
20R, CC	Barren		Barren		Barren		Barren		Barren	
21R, CC	Barren		Barren				Barren			
22R, CC	Barren		Barren				Barren			
23R, CC	Barren		Barren		Barren		Barren		Barren	
24R, CC	Barren		Rare	Poor	Few	Moderate	Rare	Poor	Few	Poor
25R, CC	Barren		Barren		Few	Poor	Barren		Few	Poor
26R, CC	Barren		Barren		Barren		Barren			
27R, CC	Barren		Barren		Barren		Barren			

the sediment is attributed to high rates of persistent upwelling. The basin floor had subsided to lower middle bathyal depths (about 1,500–2,000 m) by the late Miocene, and deep waters were better oxygenated than middle Miocene deep waters based on assemblages of benthonic foraminifers. Absence or poor preservation of calcite fossils suggests that the basin floor lay beneath or near the CCD. Microfossil assemblages suggest that environmental conditions of the early Pliocene were similar to those of the late Miocene.

Late Pliocene and Pleistocene surface waters fluctuated between subarctic and arctic conditions based on assemblages of planktonic foraminifers. Large changes in water mass character are further suggested by the great variability of radiolarian assemblage composition among core-catcher samples. The CCD migrated repeatedly across the site at approximately 2,800 m water depth based on the alternation of carbonate-rich with carbonate-barren intervals. Either low productivity or high dissolution rates caused by low-silica, young bottom waters is suggested by poor preservation of opal microfossils. The sporadic occurrence of sublittoral benthonic foraminifers mixed with those of bathyal depth, reworked Miocene diatoms, and neritic and benthic diatoms, indicates enhanced downslope transport at times during the Pleistocene.

PALEOMAGNETISM

Introduction

Paleomagnetic measurements on the recovered cores from Holes 794A, 794B, and 794C at Site 794 were made to establish the polarity of the rocks and to correlate them with the Geomagnetic Reference Time Scale (GRTS). For this purpose, we use the magnetostratigraphic scale as proposed by Berggren et al. (1985a, b).

The natural remanent magnetization (NRM) of the whole archive half of the cores were measured at 10-cm intervals using the 2G-Enterprises cryogenic magnetometer. Alternating fields (AF) of 10 and 15 mT were generally chosen for the magnetic cleaning of the rock. In a few cases, a lower peak field strength of 5 or 7 mT was used if the magnetic coercivity of the rock was not strong enough to permit using a higher demagnetizing field.

To check the reliability of the results from the archive halves, several discrete samples from the working halves were measured with the Molspin magnetometer and stepwise demagnetized until the magnetization of the rock was completely destroyed or became unstable.

The intensity of the sediments ranges between 0.1 and 100 mA/m, but is generally low. Only in the uppermost part, where the volcanic ashes are well represented, does the intensity of magnetization consistently exceed 5 mA/m. The generally weak magnetization of the sedimentary cores gave problems demagnetizing discrete samples, especially in the middle to lower part of Hole 794A where the results look inconclusive. However, stepwise demagnetization of the samples with a stronger intensity of magnetization confirmed that an AF cleaning with 15 mT was satisfactory to remove secondary components (e.g., Fig. 23A and B).

APC cores from Cores 127-794A-4H through 127-794A-15H were oriented using the multishot orientation tool. Sometimes the oriented cores provided inconsistent results, as has been previously reported from prior ODP legs. The nonoriented cores 127-794A-1H and -2H (Fig. 24A) show a clustering of their declination measurements toward north. This observation has been also noted in previous legs, and at present is unexplained. The measurements after these do not follow this trend.

Results and Magnetostratigraphy

Hole 794A

The magnetostratigraphic record of the sediments recovered in Hole 794A is of high quality over the interval 0–150 mbsf (from the top of the section to Core 127-794A-17H). This covers almost the entire interval cored using the APC. The depth plot of paleomagnetic direction of polarity after cleaning is shown in Figure 24A–24D. Figure 25 shows a correlation with the GRTS.

Nearly all chrons and subchrons existing in the GRTS have been identified for the Pleistocene and the Pliocene, from the Brunhes chron to the Gilbert chron. Their occurrence is reported in Table 4. The shortest subchrons, such as the two Reunion subchrons and the Sidufjall subchron within the Matuyama chron and the Gilbert chron, respectively, cannot be unequivocally identified in the plot of Figure 24, but the data suggest that they are present. Some boundaries between normal and reversed polarity, such as the Matuyama-Gauss or the Gauss-Gilbert chrons (Fig. 26) are sharp and can be identified within a very restricted interval of about 20 cm. On the contrary, the Brunhes-Matuyama boundary is very ambiguous and shows multiple reversals. A similar behavior of the magnetic field during the Brunhes-Matuyama transition has been found by Okada and Niitsuma (1989) in rapidly deposited sediments on the Boso Peninsula, Japan. The Cochiti subchron was completely obscured by an overprint of reverse polarity in the NRM and was clear only after cleaning at 15 mT.

The quality of the paleomagnetic measurements decreases sharply when considering the XCB drill cores (Fig. 24). Many XCB cores have been disturbed by the drilling, so that the results are often not consistent within sections of the same core. Moreover, the nature of the sediment (bioturbated diatomaceous ooze) is not very suitable for paleomagnetic study. The low intensity of the remanence in these samples (generally below 1 mA/m in NRM) did not permit the study of discrete samples. Thus, the results from the entire lower part of the hole (from Core 127-794A-17X through Core 127-794A-37X; 150–351.3 mbsf) cannot be considered conclusive.

Nevertheless, by looking at the trend of the magnetization during the cleaning, we are able to give prominence to some intervals that seem to show the same polarity. A tentative correlation of the results with the GRTS is constrained by paleontology and is shown in Figure 27. On this basis, the normal/reverse polarity pattern observed in the Cores 127-794B-3R, -4R, and 127-794A-25X could coincide with the normal/reverse polarity interval occurring before Anomaly 4. The latter could be confined between Core 127-794A-26X and the top of Core 127-794A-30X. A normal interval starting with Section 3 of Core 127-794A-31X can be correlated with the beginning of Anomaly 4A. This coincides with the first appearance of *D. Katayamae* (*D. Katayamae* Zone, 7.9–14.4 m.y.) in this core (see "Biostratigraphy" section, this chapter). If any remagnetization occurred, the long normal interval from the Section 127-794A-33X-3 through the bottom of the hole (Core 127-794A-37X) could represent part of Anomaly 5.

Hole 794B

The magnetostratigraphy of Hole 794B is difficult to construct because of the poor recovery (35.1%) and drilling disturbance of the cores. The first 13 cores (Cores 127-794B-5R through 127-794B-20R were predominantly magnetized in a normal sense. However, we suspect that some remagnetization occurred in the rock due to the effect of drilling. Core catcher samples from Cores 127-794B-18R and -19R appear to be less disturbed and indicate a reversed polarity.

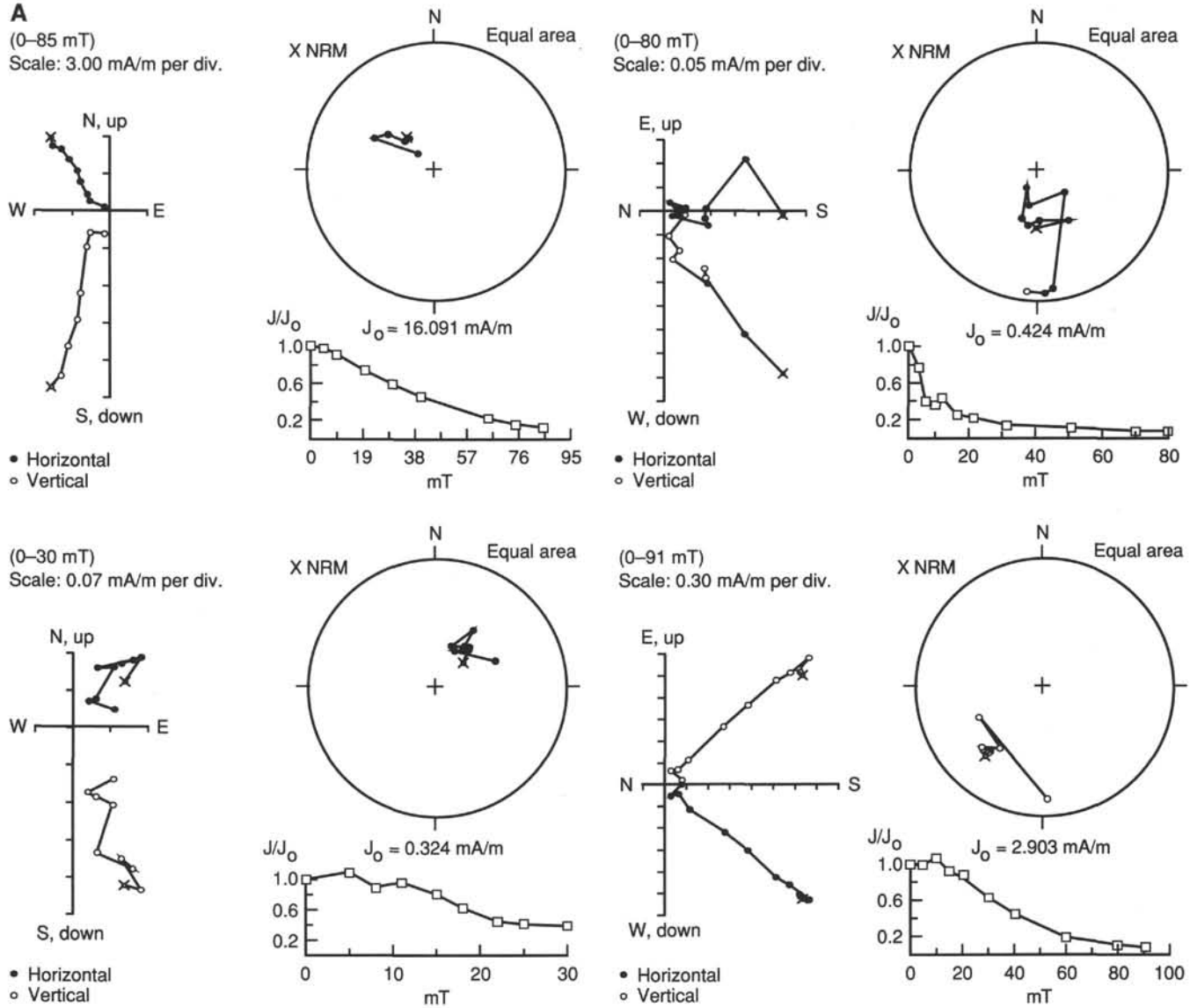

Figure 23. Zijderveld, equal-area, and intensity decay plots as a function of AF demagnetization. **A.** Two samples from Hole 794A and two samples from Hole 794B. **B.** Four samples from Hole 794C.

The first major reversed polarity zone occurs in the Sections 2, 3, and 4 of Core 127-794B-21R, while the last two sections of the same core mark a return to normal polarity. Unambiguous normal polarity continues in Cores 127-794B-22R through 127-794B-25R.

Negative inclinations, also confirmed by demagnetization of a discrete sample (Fig. 23), characterize the black mudstone recovered in Core 127-794B-26R at the bottom of this hole. According to the fossils recovered in this core, it is possible that this last reversed interval represents the reversed polarity existing between Anomalies 5B and 5C in the magnetostratigraphic scale.

Hole 794C

The igneous rocks recovered from Hole 794C were measured and demagnetized at 0, 5, 10, and 15 mT in the cryogenic magnetometer. In addition, eight discrete samples were AF-demagnetized (up to 90 mT) in 10–13 steps and measured with the Molspin magnetometer. Initial remanent intensities of the samples range from 200 to about 2000 mA/m. The Median Destructive Field (MDF) of the samples was very low, generally between 5 and 8 mT.

Two components of magnetization were obtained by demagnetizing the rocks from the first six cores. The primary component, with reversed polarity, was completely obscured by an overprint probably imparted by the present field. This overprint was successfully removed by AF demagnetization with peak-field between 10 and 15 mT. The lower part of the Core 127-794C-3R showed normal polarity (Fig. 23; Sample 127-794C-3R, 123 cm), and its meaning is not well understood (misorientation during collection?).

From Core 127-794C-7R through Core 127-794C-11R, the magnetization generally yielded only the primary direction of reversed polarity. Cores 127-794C-12R and -13R had a stable magnetization vector of normal polarity with a consistent value of inclination of about 60°. If the paleontological age of the overlying sediments is similar to the age of these rocks, then the reversed polarity of the first 11 cores is still representative of the reversed interval between Anomalies 5B and 5C, while the Cores

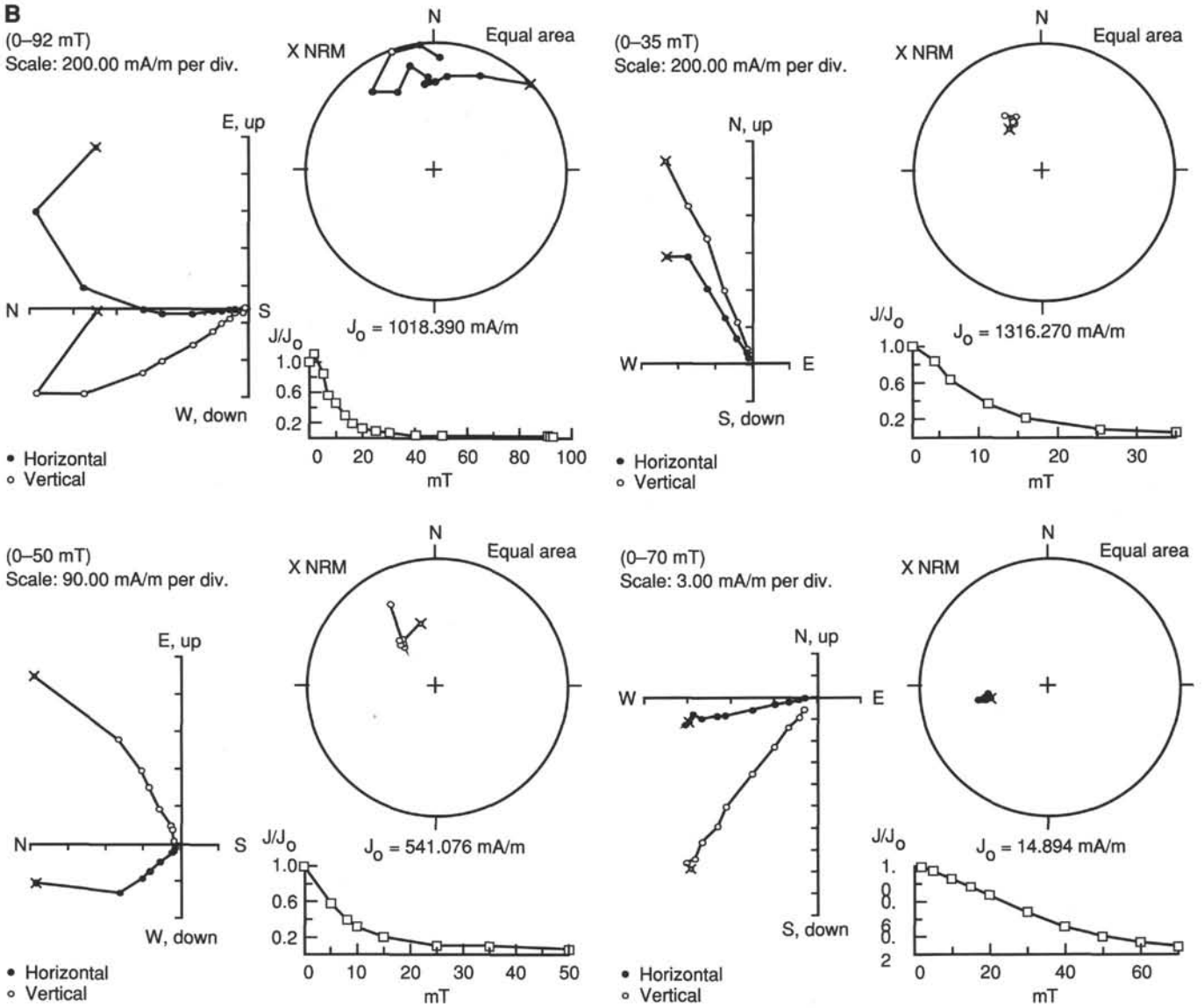

Figure 23 (continued).

127-794C-12R and -13R at the bottom of the hole can be ascribed to Anomaly 6.

Magnetic Susceptibility

Whole-core magnetic susceptibilities from Holes 794A and 794C were measured with the multisensor track. Except for the uppermost part of Hole 794A, where susceptibility ranges between 20 and 50 ($4\pi \times 10^{-6}$ SI units), values are generally below 10 and in many cases below 5 (Fig. 28). The highest values of the susceptibility near the top of the hole can be correlated with the presence of ash layers in this unit.

A significant decrease in the magnetic susceptibility occurs at about 130 mbsf in Hole 794A and may account for the worsening of the paleomagnetic data that begins at approximately the same level. This decrease could be related to an increase in the biogenic sediment component, especially because susceptibility increases again at about 300 mbsf when the biogenic sedimentary component (diatoms) disappears.

The magnetic susceptibility of the igneous rocks recovered in Hole 794C ranges from 1000 to 2500 ($4\pi \times 10^{-6}$ SI units), with a trend decreasing from top to bottom (Fig. 29).

SEDIMENT ACCUMULATION RATES

Estimates of sedimentation rates for Site 794 are based on paleomagnetic reversal stratigraphy and biostratigraphic datum levels recognized at this site. The data points include the depths and the ages of seven magnetostratigraphic boundaries, three diatom datum levels, one calcareous nannofossil datum level, and one planktonic foraminifer datum level, as shown in Table 5. A sedimentation rate for each interval was calculated from the age vs. depth relationship (Table 2 and Fig. 30). In addition, a sediment accumulation rate (g/cm^2/k.y.) was calculated from the dry-bulk density of the sediments averaged over various intervals (Table 2). The accumulation rates agree well with the sedimentation rates, but differences between the two values increase with depth. The differences are likely due to both greater compaction with depth and a lack of data levels with depth. As a result, these rates are averaged over larger intervals, leading to greater uncertainties in both types of estimates.

Sedimentation rates at Site 794 range from 29 to 54 m/m.y., with an average of 37 m/m.y. The lowest rates are in the lower Pliocene sequence, whereas the highest rates are in the upper

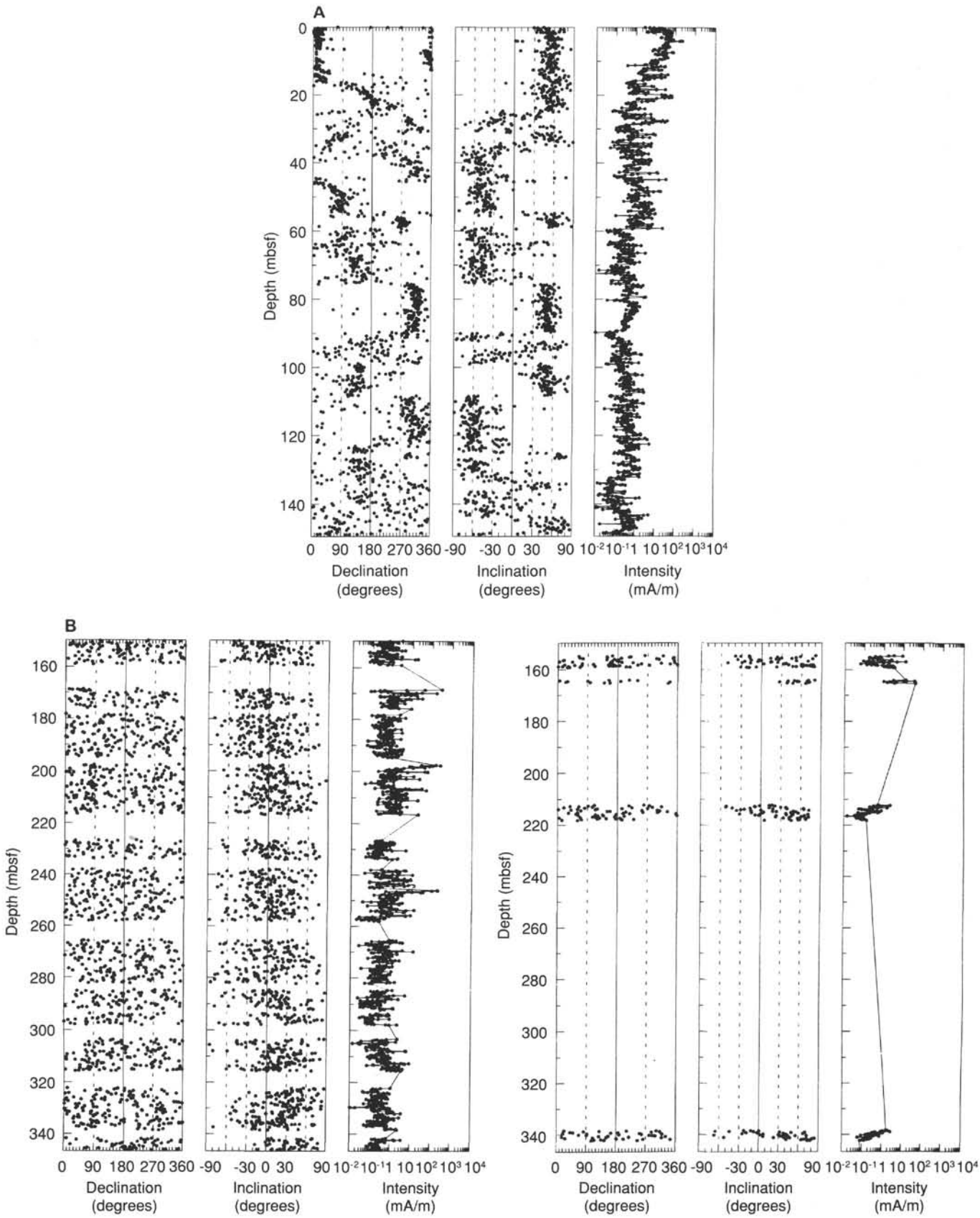

Figure 24. Paleomagnetic results vs. depth. **A.** Cores 127-794A-1H through -16X. **B.** Cores 127-794A-17X through -5R. **C.** Cores 127-794B-5R through -27R. **D.** Cores 127-794C-1R through -13R.

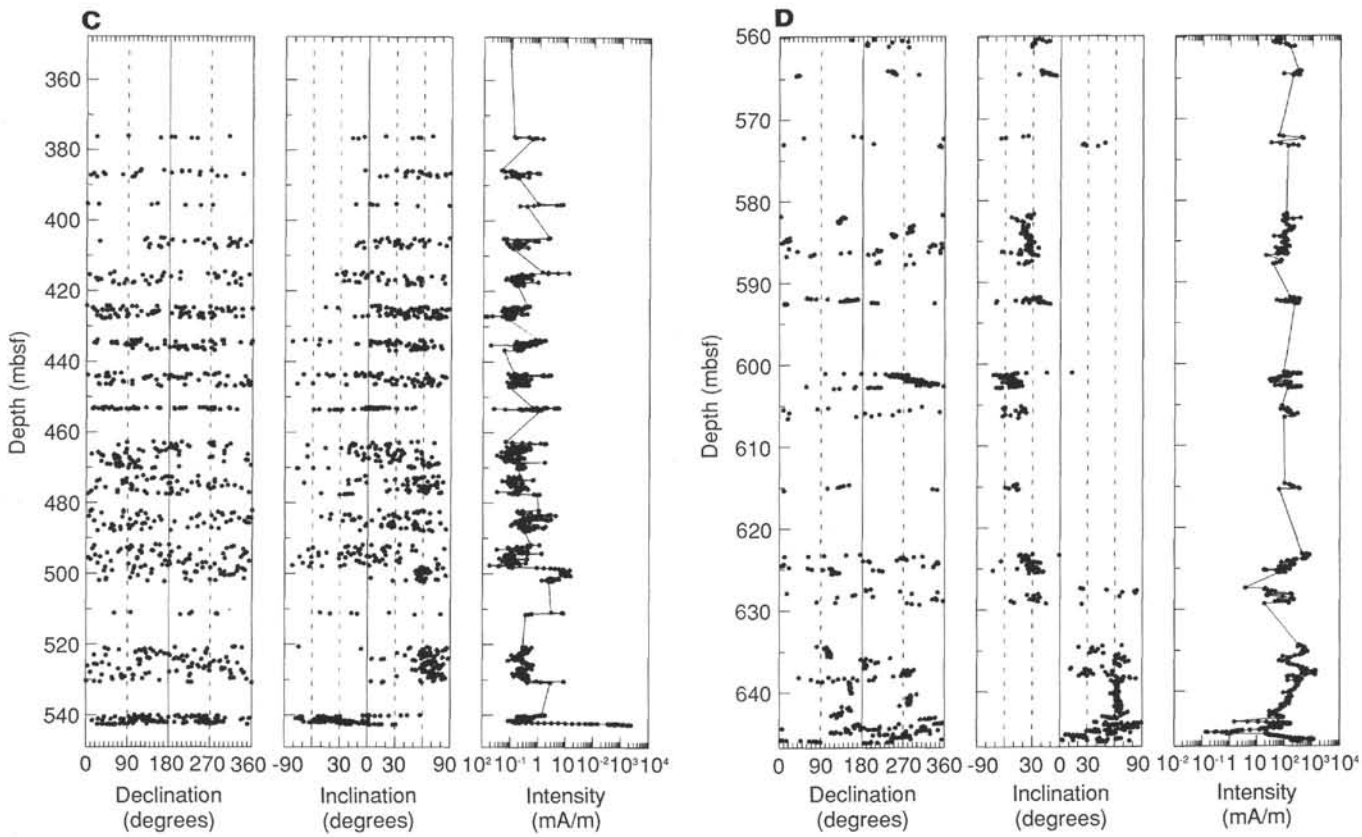

Figure 24 (continued).

Miocene section, above the opal-A/opal-CT boundary. The sedimentation rate curve below the opal-A/opal-CT boundary is not as detailed as the upper part, because of a lack of microfossil datum planes and of a detailed paleomagnetic record. The sedimentation rate estimates for the clay, claystone, and tuff of the middle Miocene are 36 m/m.y. (based on nannofossils) and 38 m/m.y. (based on foraminifers) (Fig. 30). For the diatomaceous ooze and clay of the late Miocene and early Pliocene, the sedimentation rate is estimated to be about 37 m/m.y. Clay, silty clay, and vitric ash accumulated with an average rate of 31 m/m.y. during the late Pliocene and Quaternary.

A minimum age of basement at 14.8 Ma is estimated by extrapolation from the LAD of *D. katayamae* through the LAD of *S. heteromorphus*, and a maximum age of basement at 16.2 Ma is estimated by extrapolation from the LAD of *D. katayamae* through the apparent FAD of *G. bulloides*.

INORGANIC GEOCHEMISTRY

Introduction

The shipboard inorganic geochemistry program for Site 794 focused exclusively on interstitial water analysis. Operational testing of a newly developed plastic-lined squeezer (Brumsack et al., unpubl. data), used in conjunction with the standard stainless-steel ODP squeezer (Manheim and Sayles, 1974), resulted in the acquisition of 40 pore-water samples from 23 cores.

The Barnes *in-situ* water sampler (BW) was run on three occasions, but the data are not discussed here in detail due to significant contamination of the sampled water by drill water. Assuming that the *in-situ* water samples are mixtures of pore water and seawater, a correction can be applied using the concentrations determined by squeezing the nearby interstitial waters. Whereas BW samples from Cores 127-794A-10H and -13H are contaminated by more than 50% with drill water (based on corrections performed using alkalinity, sulfate, calcium, and magnesium), the sample from Core 127-794A-16X is only diluted approximately 25% with drill water.

Data from the ODP squeezer and the Barnes sampler are presented in Table 6. The following discussion focuses on major ion concentrations in interstitial waters from Holes 794A and 794B, from which a nearly continuous section was cored from the sediment/water interface to 524 mbsf.

pH, Salinity, Sodium, and Chlorine

pH

The concentrations of several of the primary chemical indicators of interstitial water, including pH, salinity, Na, and Cl, are relatively constant down the sedimentary section sampled at Site 794. Values of pH show only a minor decrease in the upper 100 m of section and then return to slightly more alkaline conditions below 100 mbsf (Fig. 31). Waters obtained from the stainless-steel and plastic-lined squeezers yielded different pH values over essentially the same depth interval, with samples from the plastic-lined squeezer being more alkaline. This discrepancy may be due to the different water handling procedures after squeezing (see "Explanatory Notes" chapter, this volume), perhaps resulting in CO_2 loss (Gieskes and Peretsman, 1986) from the open vials used in collecting the plastic-lined squeezer samples. This variance in pH is the only example in which the compositions of major ions in the two sample sets differ significantly.

Salinity, Sodium, Chlorine

The salinity profile shows a slight decrease from the surface toward the deepest sample at 524 mbsf (Fig. 31). Sodium and chlorine amounts are virtually constant with depth, indicating no significant freshwater or brine input (Fig. 31).

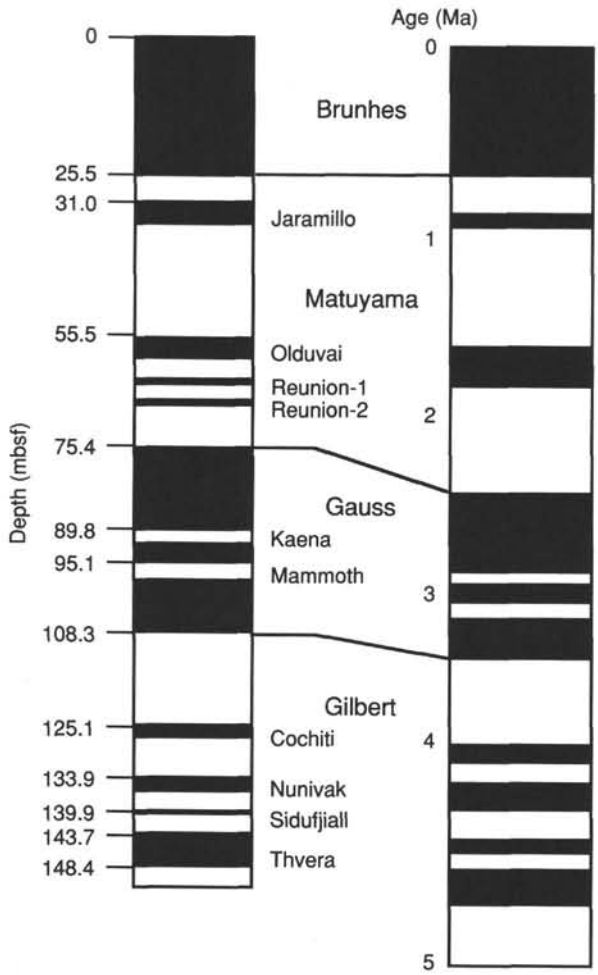

Figure 25. Correlation between the magnetostratigraphy of Hole 794A (left) for the interval 0–150 mbsf, with the magnetostratigraphic time scale (right) from Berggren et al. (1985a, b).

Table 4. Chrons and subchrons occurrence in Hole 794A (depth 0–150 mbsf).

Absolute age	Chron	Subchron	Anomaly	Depth (mbsf)
0–0.73	Brunhes		1	0–25.5
0.91–0.98		Jaramillo		31–34
1.66–1.88	Matuyama	Olduvai	2	55.5–58.8
		Reunion-1		63.1–63.8
		Reunion-2		66.9–67.2
2.47				75.4
			2A	
2.92–2.99		Kaena		89.9–92.4
	Gauss		2A	
3.08–3.18		Mammoth		95.1–98.8
			2A	
3.40				108.3
3.88–3.97		Cochiti	3	125.1–126.7
4.10–4.24	Gilbert	Nunivak	3	133.9–136.2
4.40–4.47		Sidufjall	3	139.9–140.3
4.57–4.77		Thvera	3	143.7–148.4
5.35				

Sulfate, Alkalinity, Ammonia, Phosphate

The sediments from Site 794 are characterized by a highly variable organic carbon content (see "Organic Geochemistry" section, this chapter), which exerts a fundamental control on the interstitial water composition. Sulfate, alkalinity, ammonia, and phosphate are all constituents whose behavior is influenced strongly by the bacterial degradation of organic matter in the sediment column. We discuss the downhole variability of these related constituents below.

Sulfate and Alkalinity

The sulfate content of the pore waters at Site 794 steadily decreases from an initial seawater value of 28 mM to minimum values near 10 mM at about 300 mbsf, followed by an increase to approximately 17 mM at 420 mbsf. Below this depth, sulfate decreases to 11 mM in the lowermost sediment at 524 mbsf (Fig. 31).

This sulfate profile is governed by several factors, the most important of which are the abundance (and/or availability) of organic matter and the comparably low sedimentation rate (see "Sediment Accumulation Rates" section, this chapter). The sulfate minimum also coincides with the major lithological break in the sediment column between Unit II and Unit III, the opal-A to opal-CT boundary. Sulfate reduction is more effective in the diatomaceous sediments of Unit II than in the underlying strata of Unit III, perhaps due to a reduction in porosity and/or permeability in the opal-CT dominated sediments or a change in organic matter content. In any case, sulfate reduction processes have not completely depleted sulfate in the pore waters throughout the entire sediment column, unlike near-shore settings with higher organic carbon contents and higher bulk accumulation rates such as the Gulf of California (Gieskes et al., 1982) or the Peruvian margin (Suess, von Huene, et al., 1988). The presence of undepleted sulfate in the interstitial waters is consistent with the low methane level throughout Site 794 (see "Organic Geochemistry" section, this chapter), as sulfate reduction precedes methane formation during diagenesis of organic matter. Furthermore, hydrogen sulfide, resulting from bacterial sulfate reduction, was not detected during core handling or interstitial water sampling.

The alkalinity maximum at 51 mbsf (Fig. 31) represents the modern interval of the most intense sulfate reduction. The almost linear decrease in alkalinity down core is related to the precipitation of dolomite/ankerite (see "Lithostratigraphy" section, this chapter). At approximately 500 mbsf, alkalinity values comparable to seawater are attained.

Ammonia

The ammonia concentration consistently increases to the lithologic change from the opal-A-bearing diatomaceous sediments of Unit II to the opal-CT-bearing sediments of Unit III at 290 mbsf (Fig. 31). Below this interval, ammonia values steadily decrease, perhaps reflecting incorporation into clay mineral interlayers (Wlotzka, 1972).

Phosphate

In contrast to sulfate, alkalinity, and ammonia, phosphate exhibits a pronounced maximum of 56 μmol/L at 11 mbsf and subsequently decreases steadily down hole (Fig. 31). This trend indicates rather strong first-order removal, most likely into finely disseminated sedimentary phosphatic phases. Rather low phosphate values are attained between 400 and 450 mbsf.

Silica, Lithium, Potassium, and Rubidium, Magnesium, Calcium, and Strontium

Silica

The distribution of silica in sedimentary pore waters is governed primarily by the presence of opaline silica and to a minor degree by the volcanic glass content. At Site 794 silica increases to a maximum value of approximately 1400 μmol/L at 290 mbsf, coincident with the opal-A/opal-CT transition (Fig. 32).

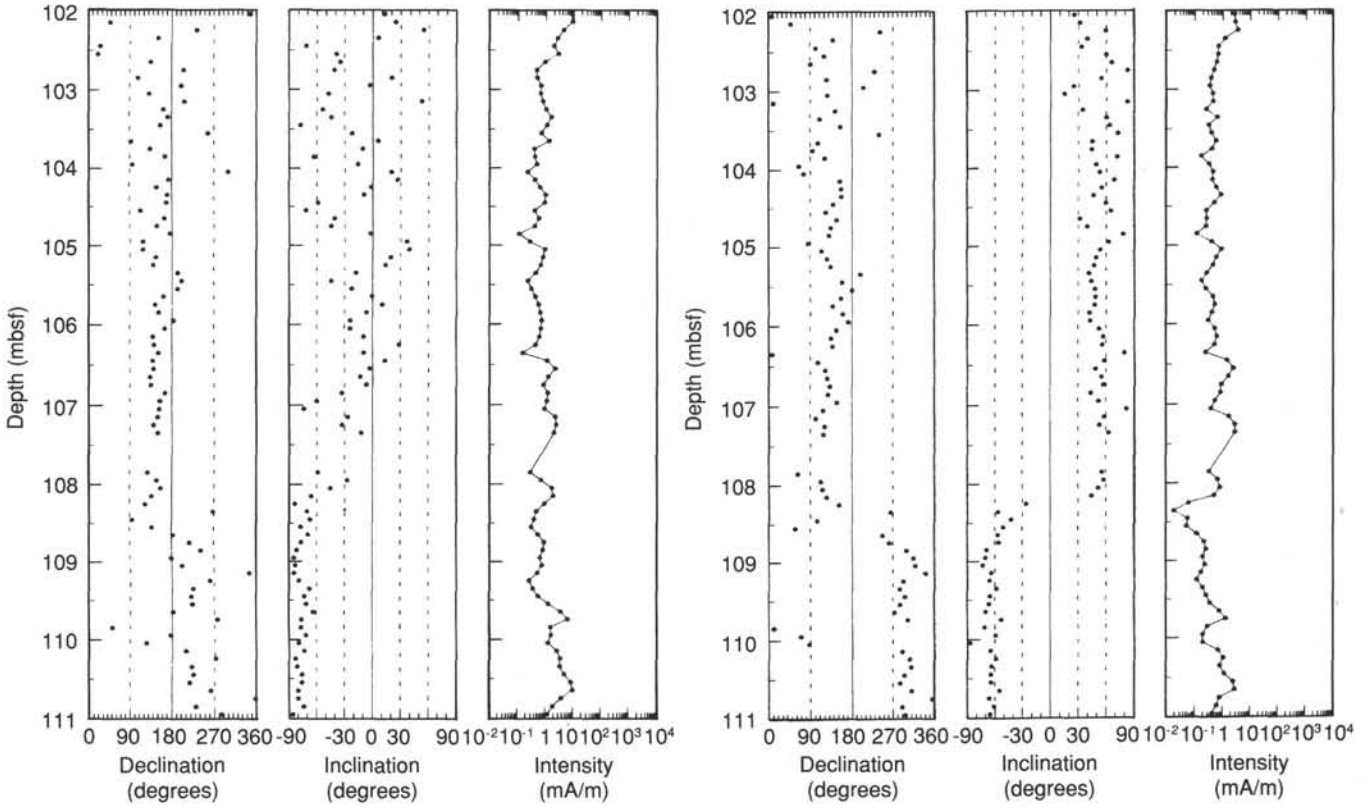

Figure 26. Paleomagnetic results vs. depth for Core 127-794A-12H, which include the Gauss-Gilbert polarity transition before (left) and after (right) cleaning.

This depth marks the position of the silicification front below which the greatest silica removal from the pore waters occurs. Dissolved silica values decrease dramatically below this interval and reach minimum values at 500 mbsf, within the quartz occurrence zone. The slight silica increase in the lowermost sample is due to dissolution of the volcanic ash and tuff of sedimentary Unit V.

Lithium

The lithium concentration profile is similar to that for silica (Fig. 32). Lithium concentrations increase from initial seawater values of approximately 25 μmol/L near the seafloor to maximum levels of nearly 90 μmol/L in Unit III at approximately 300 mbsf. Below this level, lithium values sharply decrease to a concentration of 32 μmol/L at approximately 400 mbsf, and then increase again from 430 mbsf to 524 mbsf.

Opal-A is the most likely sedimentary carrier phase for lithium at Site 794, a relationship that has been noted elsewhere (e.g., Gieskes, 1981). The dissolution of the opal-A phase, in this case diatoms, releases lithium into the interstitial water. Below the opal-A/opal-CT transition zone, lithium is removed from the interstitial waters, perhaps by incorporation into clay minerals (Steiness et al., 1972), or the replacement of Mg^{++} and Fe^{++} in some newly formed mineral phases.

Potassium and Rubidium

Potassium and rubidium both exhibit strikingly similar concentration profiles (Fig. 32), demonstrating their close chemical relationship (Heier and Billings, 1970). The observed surface maxima of both elements above their average seawater concentration may be caused by exchange with ammonia in the uppermost clay-rich units (e.g., Gieskes, 1981). The maxima probably do not represent a thermal artifact of squeezing, as such an effect would tend to decrease rather than increase the concentration. Below their surface values, both the potassium and rubidium profiles decrease consistently to Unit IIIA. The nearly linear K-gradient over this interval is −3 mM per 100 m, a slightly larger value than the average K-gradient of −2 mM per 100 m in oceanic sediments (Gieskes, 1981). This rather steep decrease in K and Rb indicates large-scale removal during interaction with phases undergoing alteration in the upper 300 m of the sediment. Alteration of the frequent ash layers of the uppermost 200 m accounts for most of the potassium and rubidium loss in pore waters. The slight decrease in the lowermost samples (460 mbsf to 524 mbsf) may reflect further removal of potassium into the tuff layers in Unit V, and/or into the sills penetrated below Unit V.

Magnesium, Calcium, and Strontium

The Mg and Ca concentrations in interstitial waters from Site 794 exhibit opposite trends (Fig. 32), as has been observed at many DSDP/ODP sites. Concentration gradients of both elements steepen sharply at 290 mbsf (e.g., Ca gradient = 2.5 mM per 100 m in the upper 300 m of Site 794 vs. 6 mM per 100 m below 300 mbsf).

These changes in interstitial water composition may be due to several different processes, such as (1) alteration reactions involving volcanic matter in the sediments or basaltic material of Layer II, and (2) dolomite/ankerite formation. Other potential factors include sepiolite formation and possible physical effects, such as a change in porosity and permeability caused by other mineralogical transformations, namely, opal-CT formation.

The change in relative concentration between calcium and magnesium (Fig. 33) is not wholly linearly correlated in a 1:1 ratio throughout the entire sediment column. This implies nonconservative behavior of these elements, especially in the upper

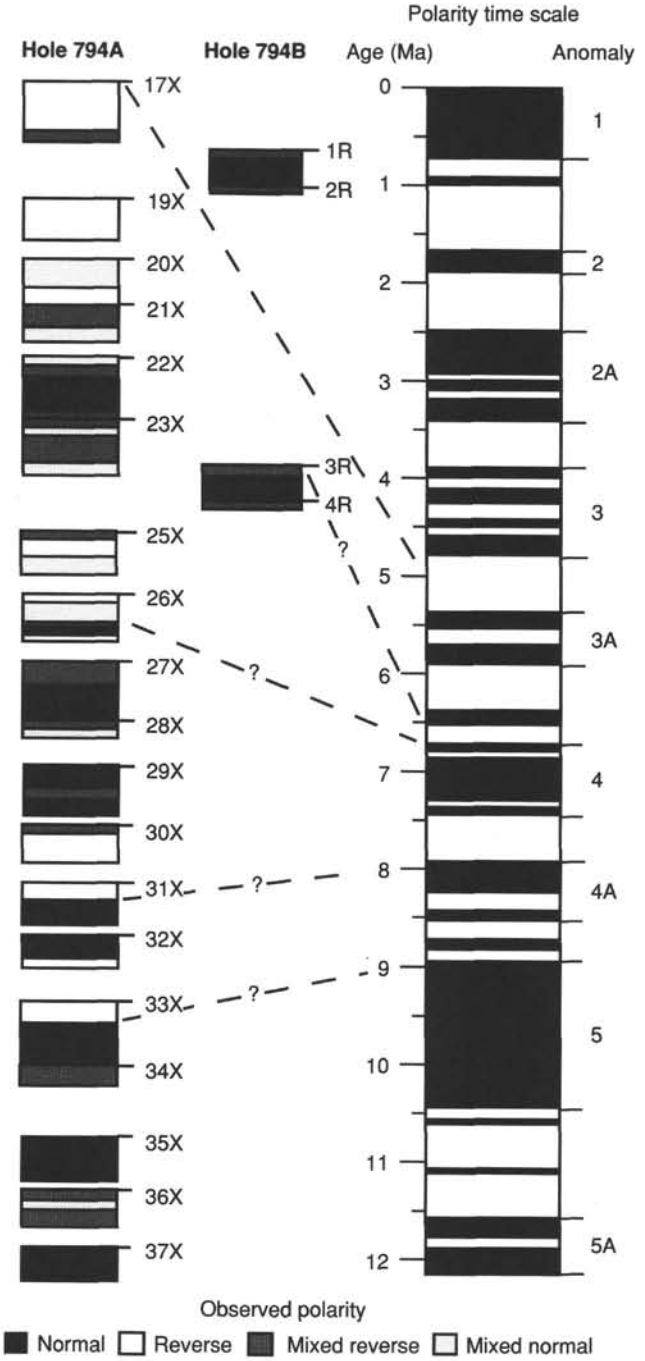

Figure 27. Tentative correlation of paleomagnetic results for Hole 794A (interval 150–338 mbsf; Cores 127-794A-17X through -37X) and Hole 794B (intervals 127-794B-1R through -4R) with the magnetostratigraphic time scale from Berggren et al. (1985a, b). The intervals with an unclear magnetization have been divided into mixed normal and reversed magnetization according to the predominance of the observed polarity.

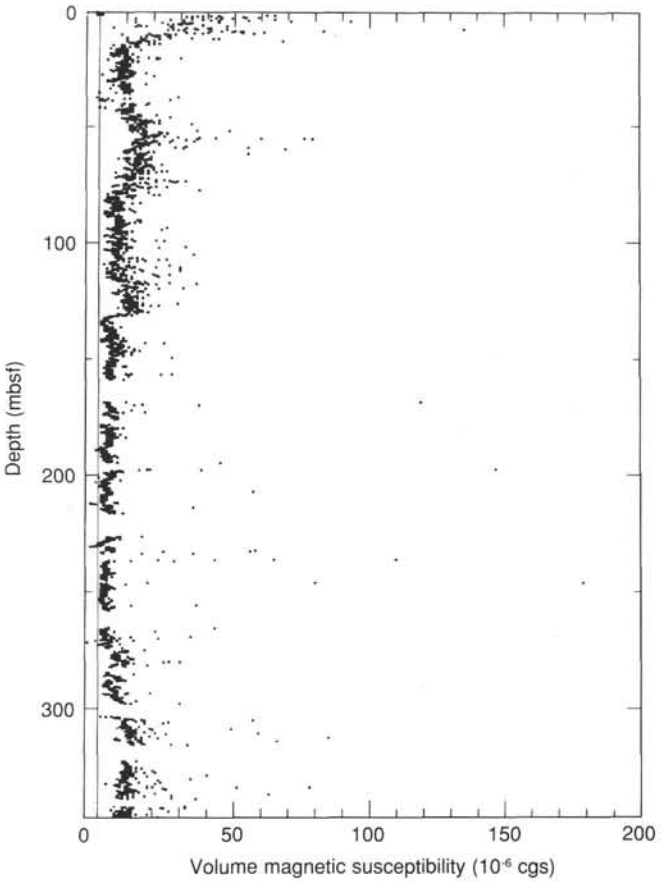

Figure 28. Downhole plot of susceptibility for Hole 794A.

sections of the sediment column. In these upper sediments (Units I and II), the calcium vs. magnesium plot exhibits a deviation from the predicted (−) 1:1 ratio of conservative behavior, indicating removal of both calcium and magnesium from the interstitial waters. In addition to removal during diagenetic carbonate formation in this high alkalinity environment, magnesium is removed by alteration of volcanic ash layers, as evidenced by the initial strong magnesium depletion with little or no calcium loss (Fig. 33). Note that these deviations from the predicted (−) 1:1 ratio are very slight and only occur in the uppermost portions of the sediment column. Deeper in the sediment column, the Ca/Mg exchange approaches a 1:1 ratio, typical for profiles influenced by basement alteration processes (McDuff and Gieskes, 1976), even though magnesium values of zero are not attained at the base of Hole 794B.

Overall, silicate alteration reactions seem to dominate at this site because, in contrast to sites where pore-water chemistry is controlled by dolomite formation (Baker and Burns, 1985), calcium increases downcore to more than three times seawater values. This large calcium increase, together with the slight degree of relative calcium and magnesium removal discussed above, implies that dolomite/ankerite formation is only a subordinate control of the chemical composition of the interstitial waters.

The strontium profile (Fig. 32) closely mimics the calcium trends, consistent with the similar geochemical behavior of the two elements. Like calcium, increasing strontium in interstitial waters may originate either from the recrystallization of biogenic carbonate (the associated strontium concentration decrease in the recrystallizing carbonate may be more than one order of magnitude) or the alteration of volcanic ash or rocks of Layer II. Because the overall carbonate content is rather poor, the alteration of Layer II rocks seems to be the most likely explanation.

Summary

The two primary controlling influences on the interstitial water chemistry at Site 794 are the biological input (organic matter

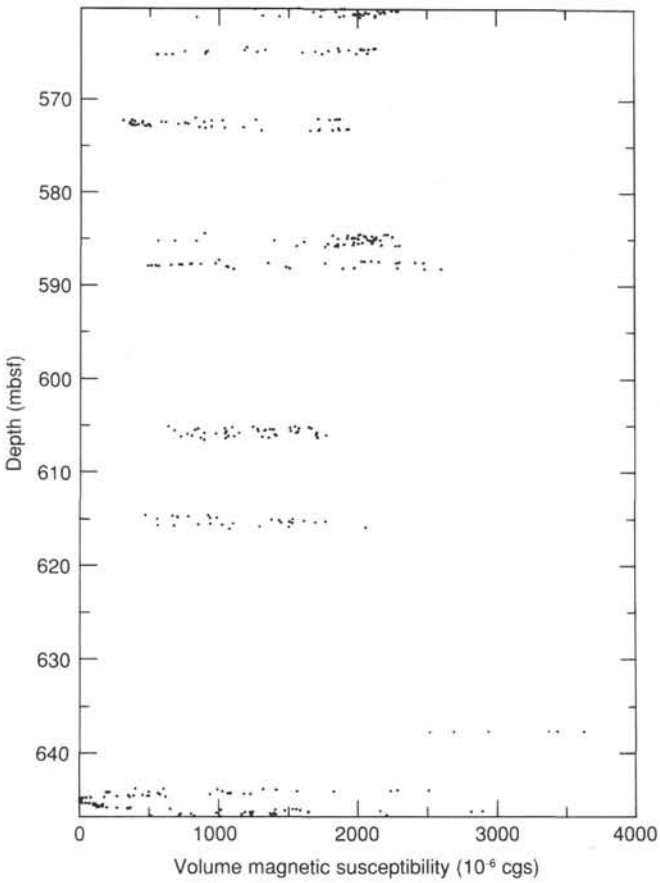

Figure 29. Downhole plot of susceptibility for Hole 794C.

introduces C, N, P, Si, and sulfate reduction) from the productive waters of the Neogene Japan Sea and the silicate alteration reactions occurring in the sedimentary column and at the basement.

The low organic carbon content and the low sedimentation rate limit the extent of pore-water sulfate depletion, which in turn influences the alkalinity of the pore water, itself a controlling parameter of carbonate formation. Although dolomite/ankerite are found in the upper sediments, the calcium, magnesium, and strontium profiles are dominated by silicate alteration reactions occurring both within the upper sedimentary column and at the basement.

The biogenic silica transformation from opal-A to opal-CT, delineated by the current silicification front at 290 mbsf, overprints most of the other chemical profiles of the sediment column. The concentration of lithium in interstitial waters, for example, clearly is controlled by the diagenesis of biogenic silica. Ammonia also exhibits a maximum at the opal-A/opal-CT transition. Physical changes attendant to the opal-A/CT and opal-CT/quartz transitions, such as porosity reduction and grain-size growth, further regulate diffusion and other chemical transport processes. This high-input of biogenic silica and the low organic carbon content combine to demonstrate the extent of early and late diagenetic processes presently active at Site 794.

The interstitial water data we present here correlate well with the organic, sedimentologic, and physical variations at Site 794. Furthermore, the consistent trends constructed from the composite data sets from the plastic-lined and stainless-steel squeezers demonstrates the success of the new plastic-lined assembly.

ORGANIC GEOCHEMISTRY

The shipboard organic geochemical analyses of sediment samples from Holes 794A and 794B included inorganic carbon; total carbon, nitrogen, and sulfur; Rock-Eval; and volatile hydrocarbon analyses. The procedures used for these determinations

Table 5. Magnetostratigraphic and biostratigraphic datum levels used to determine sedimentation rates for Site 794. The depths of zonal boundaries and datums in core-catcher samples are taken from the top or bottom of the cored interval rather than from the base of the recovered sediment.

Datum	Age (Ma)	Depth (mbsf)	Sedimentation rate m/m.y.	Sedimentation rate cm/k.y.	Mean dry-bulk density (g/cm^3)	Accumulation rate ($g/cm^2 \cdot$ k.y.)
Seafloor	0	0				
			35	3.5	0.92	3.22
1. Brunhes/Matuyama	0.73	25.5				
			33	3.3	1.00	3.30
2. Bottom of Jaramillo	0.98	34.0				
			30	3.0	1.02	3.06
3. Top of Olduvai	1.66	55.5				
			25	2.5	1.02	2.56
4. Matuyama/Gauss	2.47	75.4				
			33	3.3	0.89	2.94
5. Bottom of Kaena	2.99	92.4				
			39	3.9	0.87	3.38
6. Gauss/Gilbert	3.40	108.3				
			29	2.9	0.89	2.59
7. Bottom of Thvera	4.77	148.4				
			42	4.2	0.83	3.47
8. Base of *Ne. kamtschatica* Zone	6.40	216.9				
			49	4.9	0.80	3.93
9. Top of *Tn. schraderi* Zone	7.20	255.7				
			54	5.4	0.80	4.34
10. LAD of *D. katayamae*	7.90	293.5				
			36	3.6	1.24	4.48
11. LAD of *Sph. heteromorphus*	14.40	530.5				
			38	3.8	1.35	5.13
12. FAD of *Gg. bulloides*	16.00	540.0				

LAD = last appearance datum
FAD = first appearance datum

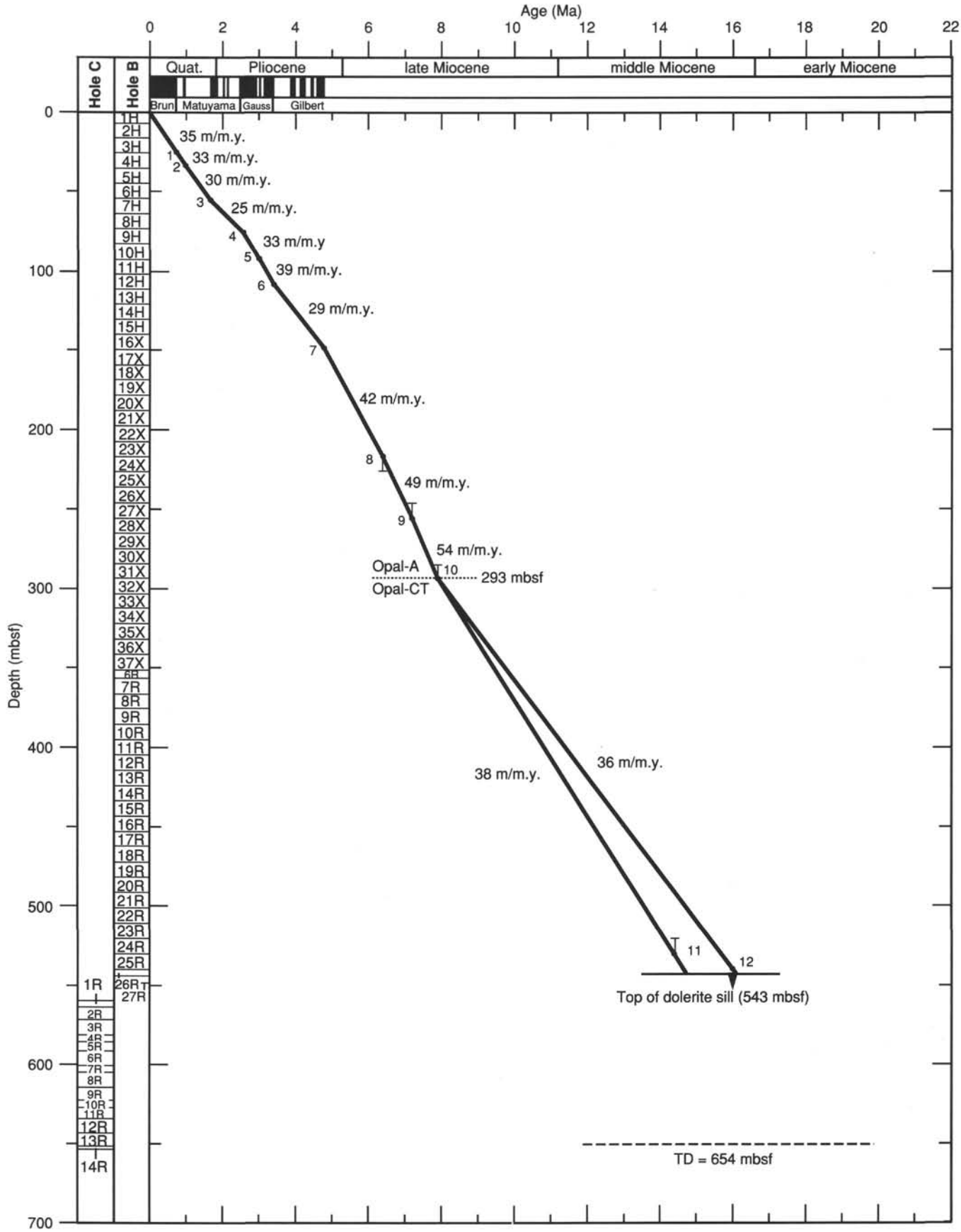

Figure 30. Age vs. depth relationship at Site 794. The error bars indicate uncertainties in the age and the precise depth of the datum levels.

Table 6. Interstitial water geochemistry data, Site 794.

Core, section, interval (cm)	Depth (mbsf)	Vol. (cm^3)	pH	Alk. (mM)	Sal. (g/kg)	Mg (mM)	Ca (mM)	Cl (mM)	SO_4 (mM)	PO_4 (μM)	NO_3 (μM)	NH_4 (μM)	SiO_2 (μM)	Mg/Ca
127-794A-														
1H-3, 140–145	4.40	5	7.72	8.450		50.50	9.90			22.0		57	440	5.10
1H-3, 145–150	4.45	1			35.0									
2H-3, 145–150	11.25	25								56.0			660	
3H-5, 140–145	23.70	5											770	
3H-5, 145–150	23.75	45	7.46	10.070	34.0	47.58	9.74	524.62	18.4	49.0		510	716	4.89
4H-4, 145–150	31.75	5								52.0			710	
5H-4, 145–150	41.25	5	7.51	9.800	34.0					41.0			800	
6H-4, 140–145	50.70	60	7.51	12.040	34.0	46.05	10.20	532.48	17.3	13.0		800	661	4.52
6H-4, 145–150	50.75	5											700	
7H-4, 145–150	60.25	5	7.73	11.704						19.0			780	
8H-4, 145–150	69.75	5	7.67	11.826						15.0			930	
9H-4, 140–145	79.20	63	7.36	11.593	34.0	44.97	10.67	532.48	16.4	10.0		860	1213	4.21
9H-4, 145–150	79.25	5											990	
10H-1, 0–10	82.80	21	7.95	5.084	35.0	50.00	10.55	547.00	20.9					4.74
10H-4, 145–150	88.75	5	7.67						14.0	11.0			1040	
12H-4, 140–145	107.70	55	7.22	11.190		44.76	11.06	512.83	14.7	10.0		930	1092	4.05
12H-4, 145–150	107.75	5											970	
13H-1, 0–10	111.30	55	7.70	5.932		49.84	10.74	547.00	20.9					4.64
15H-4, 140–145	136.20	43	7.30	10.477	33.8	43.46	11.47	530.51	13.9	6.0		970	1168	3.79
15H-4, 145–150	136.25	5											1070	
16X-1, 0–10	139.80	21	7.37	8.910	34.5	46.26	11.34	547.00	18.0					4.08
19X-4, 140–145	174.40	33	7.43	8.690	33.8	43.68	11.83	535.42	15.0	3.0		980	1168	3.69
19X-4, 145–150	174.45	5											1330	
22X-4, 140–145	203.40	33	7.34	9.320	33.0	42.17	12.29	536.41	10.8	3.0		1050	1270	3.43
22X-4, 145–150	203.45	5											1380	
25X-4, 140–145	232.40	43	7.40	8.311	33.8	41.80	12.60	531.49	10.2	2.5		990	1440	3.32
25X-4, 145–150	232.45	5											1330	
29X-4, 140–145	271.30	16	7.42	6.743	32.5	41.91	13.23	539.35	9.3	1.8		1000	1383	3.17
29X-4, 145–150	271.35	5											1360	
33X-2, 140–145	306.20	5											750	
33X-2, 145–150	306.25	18	7.61	7.772	33.0	42.33	14.29	533.46	13.3	1.0		780	816	2.96
36X-4, 140–145	337.80	13	7.58	5.843	32.5	42.47	15.81	519.71	13.7	0.7		700	764	2.69
36X-4, 145–150	337.85	5											650	
127-794B-														
12R-1, 145–150	406.35	5												
12R-2, 145–150	407.85	8	7.43	2.790		37.43	21.24	538.22	13.6	0.5		630	372	1.76
15R-1, 145–150	435.25	2			32.5	37.18	20.93	533.28	16.2	0.5		550		1.78
15R-1, 145–150	435.25	5											330	
18R-4, 145–150	468.55	13	7.61	2.363	32.5	34.76	24.58	538.22	15.2	0.4			257	1.41
21R-3, 145–150	496.15	11	7.41	1.415	32.3	30.33	28.16	537.23	11.5	0.4		620	166	1.08
24R-2, 140–145	523.50	17	7.45	1.434	32.3	30.00	30.48	527.34	11.3	0.5		430	344	0.98

Note: samples with reported data were analyzed for trace elements.

are outlined in the "Explanatory Notes" chapter (this volume), while background and detailed descriptions are given in Emeis and Kvenvolden (1986).

Carbon, Nitrogen, and Sulfur

The concentrations of inorganic, total, and organic carbon in the sediments recovered from Site 794 are presented in Table 7. The percentage of calcium carbonate ($\%CaCO_3$) was calculated from the inorganic carbon concentrations by assuming that all carbonate is in the form of calcite. Nitrogen concentrations above analytical detection are also included in Table 7 for all samples analyzed for total carbon. Few total sulfur values are reported due to inconsistent quantitation for most of the samples.

Most of the samples contain less than 1.0% calcium carbonate, although the total range is 0%–74%. The low carbonate concentrations and the poor preservation of biogenic carbonate detritus (see "Biostratigraphy" section, this chapter) suggest that sediment deposition occurred mostly below the carbonate-compensation depth (CCD). The concentration of organic carbon ($\%C_{org}$) in the whole sediments ranges from 0.02% to 4.3%, with most sediments containing less than 1.0% on a dry weight basis. The total nitrogen contents range from 0% to 0.29% of the whole sediments on the same basis. The ratio of organic carbon to total nitrogen (C/N) ranges from 0.60 to 39, with most of the sediments exhibiting values between 5.0 and 15.

The $\%CaCO_3$, $\%C_{org}$, and C/N ratio values are plotted against the sub-bottom depth in Figure 34. In the top 350 m of sediment at Site 794, carbonates are primarily at trace levels but with some notable exceptions. These high point concentrations of CaCO3 (34% and 74%) at 232–233 mbsf correspond to dolomite nodules. Additional but sporadic occurrences of high carbonate content (5%–22%) over narrow intervals in the top 350 m of section also may be authigenic in nature, although increased preservation of biogenic carbonate must also be considered. Below 350 mbsf, more frequent occurrences of carbonate suggest that conditions favoring dolomitization and/or biogenic carbonate preservation may have been more prevalent.

The downhole distribution of organic carbon in the sediments at Site 794 is characterized by predominantly low values of less than 1.0% C_{org} with occasional increases to 4.3%. In the Quaternary sediments, high C_{org} concentrations occasionally coincide with local carbonate maxima. At 4.8, 28.3, 34.2, and 41.5 mbsf, C_{org} concentrations of 3.6%, 2.3%, 4.3%, and 2.5% correspond with $CaCO_3$ concentrations of 22%, 14%, 15%, and 8.4%, respectively. Biogenic carbonate detritus is apparent in these intervals. Throughout the rest of the sedimentary column, there is no apparent relationship between carbonate and

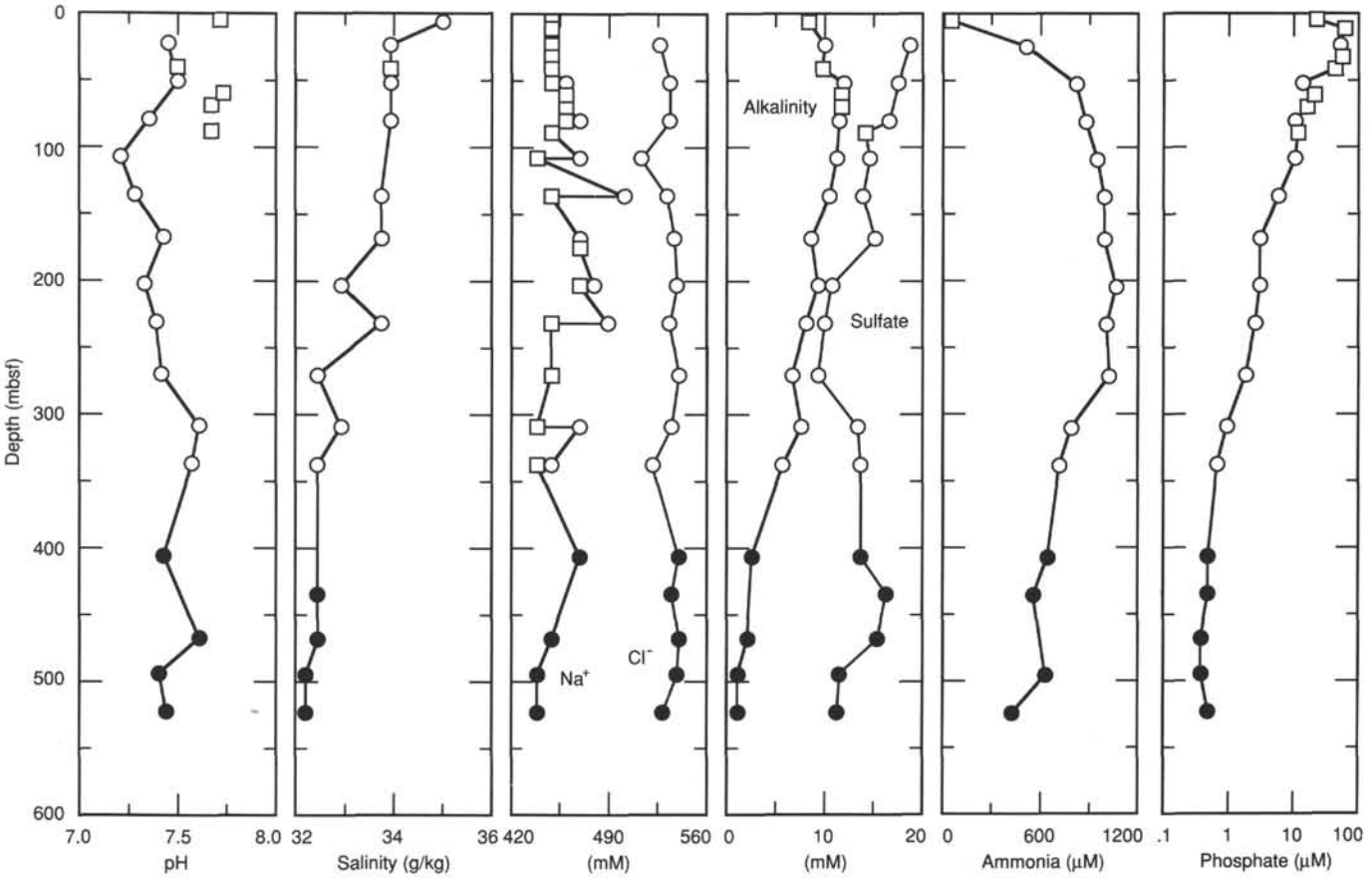

Figure 31. Depth profiles of pH, salinity, sodium, chloride, alkalinity, sulfate, ammonia, and phosphate. Open symbols: data in Hole 794A; solid symbols: data in Hole 794B. Circles: ODP squeezer; squares: Brumsack squeezer.

organic carbon content. The top 64 m of Hole 794A are characterized by an abundance of both laminated and massive intervals containing ashes, clays, silty clays, and diatoms (see "Lithostratigraphy" section, this chapter), resulting in the high variability in organic carbon. Between approximately 80 and 200 mbsf, the organic carbon averages less than 0.50%. The diatomaceous and clayey diatomaceous oozes of this unit are extensively bioturbated (see "Lithostratigraphy" section, this chapter). The lower organic content of this interval reflects the higher degree of oxidation inherent in such bioturbated sediments. Relatively high organic carbon values (1.6%–3.0%) are observed between 230 and 330 mbsf.

The C/N ratio at Site 794 remains relatively constant downhole with values usually between 5 and 10 in the upper 200 m (Fig. 34). A minor increase is observed at about 40 mbsf, and the largest value (39) is attained at 485 mbsf. An apparent slight increase in C/N values with depth is consistent with the pattern usually observed for diagenesis of organic matter. Because the nitrogen component includes both organic and inorganic nitrogen, the changes in the C/N ratio may also reflect ammonia gradients in both the pore waters or clay minerals. The general downhole constancy of the C/N ratio suggests that the primary control at this site may be either source-related (organic matter type) and/or dependent on pre-depositional processes such as oxidation at or above the sediment/water interface.

Rock-Eval Analysis

Selected samples from Site 794 were analyzed for total organic carbon (TOC), source character, and thermal maturity and hydrocarbon potential using the Rock-Eval instrument. The resulting values are presented in Table 8.

In general, the accuracy of Rock-Eval data is highly dependent on the operating conditions of the instrument and on the character of the sediments analyzed (Peters, 1986). The measurement of the parameter S_3 was particularly inconsistent during this site investigation, with the problems probably more often caused by instrument failure than by O_2 and CO_2 adsorbed to the sediments. Although interpretations based solely on the absolute value of this index are unwarranted, general trends in organic matter composition can be inferred. The composition of the sediments at this site may have contributed to some inaccuracy in the other parameters. Mineral matrix adsorption of the pyrolysates can modify both the source parameters and maturity indices of Rock-Eval analysis (Espitalié et al., 1980; Katz, 1983; Peters, 1986).

Because clay is a highly variable but significant component of the sediments at Site 794 (see "Lithostratigraphy" section, this chapter), such matrix effects, combined with overall low organic carbon concentrations, have probably affected the data by underestimating the S_2 values. Pyrograms were obtained only for the sediments above 100 mbsf and were often characterized by multiple and/or broad S_2 peaks. Such patterns suggest multiple sources and affect the reliability of the T_{max} measurements, which are based on the pyrolysis temperature at which S_2 is maximum. The interpretations that follow are therefore preliminary, and further analysis of the kerogen isolates are needed to clarify the sources of organic matter to this region of the Japan Sea.

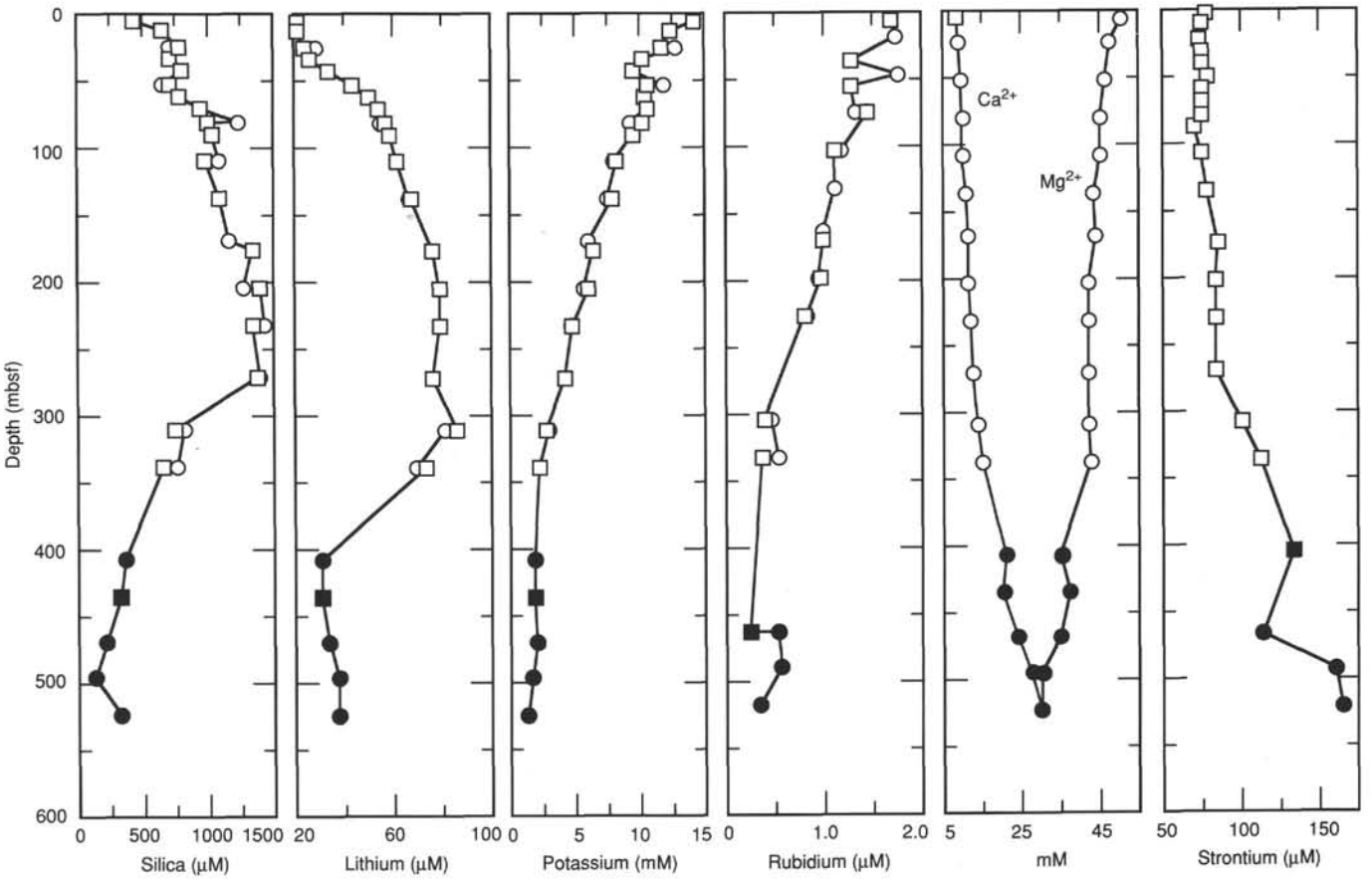

Figure 32. Depth profiles of silica, lithium, potassium, rubidium, calcium, magnesium, and strontium. Note opal-A to opal-CT transition at 290 mbsf. Open symbols: data in Hole 794A; solid symbols: data in Hole 794B. Circles: ODP squeezer; squares: Brumsack squeezer.

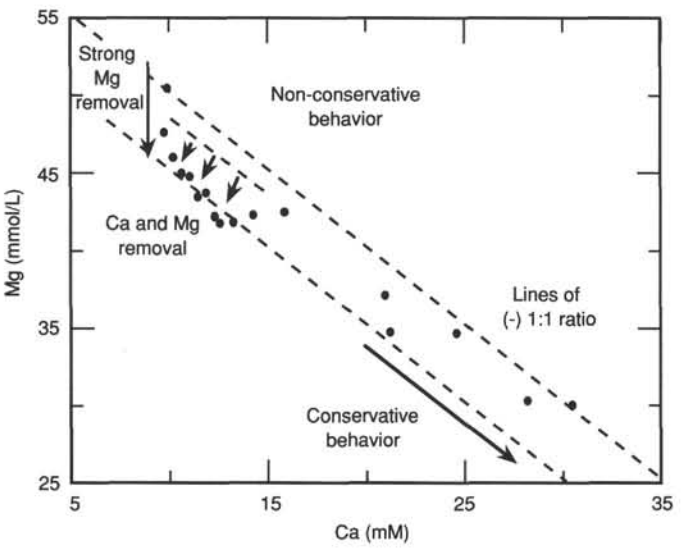

Figure 33. Calcium vs. magnesium, Holes 794A and 794B. Points trend from shallow to deep in the sediment column from the upper left to the lower right in the figure. See text for discussion of magnesium and calcium removal processes.

Total Organic Carbon

The sediment concentrations of TOC determined by Rock-Eval range from 0.02% to 2.73%. These values are comparable to the $\%C_{org}$ values determined by difference (cf. Tables 7 and 8). Most of the TOC concentrations are within 15% of the $\%C_{org}$ values. Although the TOC values occasionally differ from the $\%C_{org}$ by more than 30% of the latter values, the general downhole trends are consistent. When the organic carbon content of the sediments are fairly low, the TOC values often underestimate the percentages of organic carbon present. As the Rock-Eval TOC determinations are conducted by pyrolysis at only 600°C, the underestimations may be due to incomplete combustion as can occur with very mature samples (Emeis and Kvenvolden, 1986; Peters, 1986). This inference is supported by the high T_{max} (see following discussion) values in Table 8.

Source Character

The S_2 and S_3 values represent the amount of hydrocarbons and carbon dioxide, respectively, that can be released from the kerogen (i.e., insoluble organic matter) during pyrolysis or thermal maturation of whole sediments. When normalized to the amount of organic carbon in the sediments, the new parameters of hydrogen index (HI) and oxygen index (OI) provide an estimate of the organic type (Espitalié et al. 1977). For the sediments at Site 794, these indexes were determined using the TOC values from the Rock-Eval analysis.

The hydrogen and oxygen indexes approximate the H/C and O/C ratios of the kerogen. A Van Krevelen-type plot of the HI

Table 7. Concentrations of inorganic and organic carbon and total nitrogen and sulfur at Site 794.

Core, section, interval (cm)	Depth (mbsf)	Total carbon (%)	Inorganic carbon (%)	Organic carbon (%)	$CaCO_3$ (%)	Nitrogen (%)	Sulfur (%)	Org. C/N	Org. C/S
127-794A-									
1H-2, 27–30	1.77	0.51	0.48	0.03	4.0	0.05	0.12	0.60	0.25
1H-2, 30–31	1.80	0.54	0.34	0.20	2.8	0.05	0.14	4.00	1.40
1H-2, 100–102	2.50	0.37	0.13	0.24	1.1	0.04	0.13	6.00	1.80
1H-3, 145–150	4.45	0.91	0.06	0.85	0.5	0.11		7.70	
1H-4, 0–5	4.50	1.12	0.07	1.05	0.6	0.12		8.75	
1H-4, 31–37	4.81	6.24	2.69	3.55	22.4	0.29	3.83	12.20	0.93
1H-4, 37–43	4.87	2.21	1.05	1.16	8.7	0.13		8.92	
1H-4, 100–102	5.50	0.53	0.02	0.51	0.2	0.07	0.06	7.30	8.50
1H-5, 17–20	6.17	0.24	0.22	0.02	1.8	0.04		0.50	
1H-5, 21–22	6.21	0.75	0.24	0.51	2.0	0.07		7.30	
1H-5, 22–24	6.22	0.95	0.59	0.36	4.9	0.07		5.10	
2H-3, 100–102	10.80	0.42	0.01	0.41	0.1	0.07		5.80	
2H-4, 0–5	11.30	1.01	0.17	0.84	1.4	0.08	0.69	10.00	1.20
2H-5, 100–102	13.80	0.64	0.15	0.49	1.2	0.06	0.02	8.10	24.00
3H-2, 100–101	18.80	0.93	0.63	0.30	5.2	0.05	0.07	6.00	4.30
3H-3, 27–33	19.57	0.22	0.02	0.20	0.2	0.02		10.00	
3H-3, 80–86	20.10	1.32	0.13	1.19	1.1	0.08		14.90	
3H-5, 99–101	23.29	0.22	0.03	0.19	0.2	0.04	0.90	4.70	0.21
3H-6, 0–5	23.80	0.18	0.06	0.12	0.5	0.04	3.05	3.00	0.04
4H-2, 100–101	28.30	3.95	1.67	2.28	13.9	0.15	2.16	15.20	1.05
4H-5, 0–5	31.80	1.72	0.31	1.41	2.6	0.13	2.30	10.80	0.61
4H-5, 100–101	32.80		0.18		1.5				
4H-6, 87–90	34.17	6.06	1.74	4.32	14.5	0.28		15.40	
4H-6, 90–93	34.20	1.28	0.86	0.42	7.2	0.03		14.00	
5H-2, 100–101	37.80	0.63	0.06	0.57	0.5	0.04		14.00	
5H-3, 76–86	39.02	1.18	0.26	0.92	2.2	0.07		13.00	
5H-5, 0–5	41.30	1.42	0.01	1.41	0.1	0.07	4.72	20.10	0.30
5H-5, 16–22	41.46	3.46	1.01	2.45	8.4	0.17		14.40	
5H-5, 100–101	42.30		0.04		0.3				
6H-2, 100–101	47.30	0.27	0.07	0.20	0.6	0.04		5.00	
6H-4, 140–150	50.70	0.28	0.16	0.12	1.3	0.00			
6H-5, 0–5	50.80	0.25	0.01	0.24	0.1	0.06	0.07	4.00	3.40
6H-5, 100–101	51.80	1.44	0.12	1.32	1.0	0.11		12.00	
7H-1, 108–108	55.38	0.19	0.02	0.17	0.2	0.06	4.65	2.80	0.04
7H-1, 109–123	55.39	0.27	0.03	0.24	0.2	0.05		4.80	
7H-2, 100–102	56.80	0.34	0.07	0.27	0.6	0.06	0.07	4.50	3.80
7H-4, 143–145	60.23	0.26	0.04	0.22	0.3	0.05	0.35	4.40	0.63
7H-5, 100–102	61.30		0.01		0.1				
8H-2, 100–101	66.30	0.57	0.04	0.52	0.3	0.06	0.16	8.60	3.20
8H-5, 0–3	69.80	0.48	0.07	0.41	0.6	0.06		6.80	
8H-5, 100–101	70.80	0.89	0.06	0.83	0.5	0.09		9.20	
8H-6, 72–75	72.02	1.04	0.07	0.97	0.6	0.05		19.00	
8H-6, 75–78	72.05	1.98	0.01	1.97	0.1	0.09		21.90	
8H-6, 78–80	72.08		0.11		0.9				
8H-6, 81–82	72.11		0.37		3.1				
8H-6, 83–83	72.13		0.19		1.6				
8H-6, 83–86	72.13		0.12		1.0				
9H-2, 101–102	75.81	0.09	0.01	0.08	0.1	0.02	0.33	4.00	0.24
9H-4, 140–145	79.20	0.71	0.02	0.69	0.2	0.09		7.60	
9H-5, 0–3	79.30	0.53	0.03	0.50	0.2	0.06	0.81	8.30	0.62
9H-5, 101–102	80.31		0.02		0.2				
10H-2, 100–102	85.30	0.44	0.05	0.39	0.4	0.05		7.80	
10H-5, 0–3	88.80	0.64	0.31	0.33	2.6	0.06	0.26	5.50	1.20
10H-5, 100–102	89.80	0.42	0.03	0.39	0.2	0.06		6.50	
11H-2, 100–102	94.80	0.34	0.03	0.31	0.2	0.05		6.20	
11H-4, 0–3	96.80	0.31	0.02	0.29	0.2	0.04	0.09	7.20	3.20
11H-5, 100–102	99.30	0.50	0.03	0.47	0.2	0.07		6.70	
11H-6, 0–3	99.80	0.65	0.03	0.62	0.2	0.07		8.80	
12H-2, 100–102	104.30	0.37	0.02	0.35	0.2	0.07		5.00	
12H-4, 140–145	107.70	0.47	0.02	0.45	0.2	0.08		5.60	
12H-5, 0–2	107.80	0.37	0.04	0.33	0.3	0.05	0.87	6.60	0.38
12H-5, 100–102	108.80		0.02		0.2				
13H-2, 101–103	113.81		0.07		0.6				
13H-5, 0–3	117.30	0.48	0.02	0.46	0.2	0.08	0.43	5.70	1.00
13H-5, 99–101	118.29		0.03		0.2				
14H-2, 101–102	123.31		0.02		0.2				
14H-3, 70–76	124.50	0.55	0.02	0.53	0.2	0.08		6.60	
14H-5, 0–3	126.80	0.40	0.05	0.35	0.4	0.04	0.97	8.70	0.36
14H-5, 101–102	127.81		0.01		0.1				
15H-2, 100–101	132.80		0.02		0.2				
15H-5, 0–3	136.30	0.29	0.01	0.28	0.1	0.04	0.38	7.00	0.73
15H-5, 100–101	137.30		0.01		0.1				
16X-2, 100–101	142.30		2.01		16.7				
16X-5, 0–5	145.80	0.18	0.02	0.16	0.2	0.03	0.36	5.30	0.44
16X-5, 100–101	146.80		0.02		0.2				

Table 7 (continued).

Core, section, interval (cm)	Depth (mbsf)	Total carbon (%)	Inorganic carbon (%)	Organic carbon (%)	$CaCO_3$ (%)	Nitrogen (%)	Sulfur (%)	Org. C/N	Org. C/S
127-794A- (Cont.)									
17X-2, 100–101	152.00		0.01		0.1				
17X-5, 0–5	155.50	0.77	0.32	0.45	2.7	0.07	0.53	6.40	0.85
17X-5, 100–101	156.50		0.26		2.2				
17X-6, 102–116	158.02		0.04		0.3				
19X-2, 100–101	171.00		0.22		1.8				
19X-5, 0–5	174.50	0.25	0.01	0.24	0.1	0.05	0.98	4.80	0.24
19X-5, 100–101	175.50		0.02		0.2				
20X-2, 100–101	180.70		0.02		0.2				
20X-5, 0–5	184.20	0.31	0.01	0.30	0.1	0.04	0.63	7.50	0.47
20X-5, 100–101	185.20		0.02		0.2				
21X-2, 110–112	190.50		0.04		0.3				
21X-4, 0–5	192.40	0.39	0.03	0.36	0.2	0.07		5.10	
21X-5, 80–82	194.70		0.03		0.2				
22X-2, 110–112	200.10		0.01		0.1				
22X-4, 140–145	203.40	0.43	0.05	0.38	0.4	0.06		6.30	
22X-5, 0–5	203.50	0.42	0.02	0.40	0.2	0.10		4.00	
22X-5, 110–112	204.60		0.02		0.2				
23X-2, 100–102	209.70		0.03		0.2				
23X-5, 0–5	213.20	0.20	0.01	0.19	0.1	0.09		2.10	
23X-5, 100–102	214.20		0.02		0.2				
127-794B-									
3R-2, 102–110	214.72	0.34	0.01	0.33	0.1	0.06		5.50	
3R-4, 0–3	216.70	0.59	0.01	0.58	0.1	0.08		7.20	
3R-4, 102–110	217.72	0.71	0.02	0.69	0.2	0.11		6.30	
4R-1, 101–102	222.91	0.91	0.03	0.88	0.2	0.09		9.80	
127-794A-									
25X-2, 100–102	229.00		0.01		0.1				
25X-4, 145–150	232.45	1.02	0.14	0.88	1.2	0.07		12.00	
25X-5, 0–3	232.50		4.12		34.3	0.09			
25X-5, 34–36	232.84		8.83		73.6				
25X-5, 100–102	233.50		0.08		0.7				
26X-2, 100–102	238.70	0.55	0.03	0.52	0.2	0.06		8.60	
26X-5, 0–3	242.20		0.01		0.1				
26X-5, 100–102	243.20		0.02		0.2				
27X-2, 100–102	248.50		0.02		0.2				
27X-5, 100–102	253.00	1.61	0.03	1.58	0.2	0.15		10.50	
28X-2, 0–3	257.20	0.61	0.06	0.55	0.5	0.08		6.90	
28X-2, 84–87	258.04	0.73	0.03	0.70	0.2	0.08		8.70	
29X-1, 80–82	266.20		0.12		1.0				
29X-3, 0–3	268.40	0.97	0.06	0.91	0.5	0.10		9.10	
29X-5, 0–3	271.40	2.42	0.10	2.32	0.8	0.19		12.20	
29X-5, 80–82	272.20		0.07		0.6				
30X-2, 100–102	277.60		0.02		0.2				
30X-4, 0–3	279.60	1.23	0.25	0.98	2.1	0.10	9.80		
30X-4, 100–102	280.60		0.02		0.2				
31X-2, 100–102	287.10		0.03		0.2				
31X-4, 0–3	289.10	1.15	0.12	1.03	1.0	0.10		10.30	
31X-4, 100–102	290.10		0.06		0.5				
31X-6, 82–88	292.92	0.67	0.04	0.63	0.3	0.07		9.00	
31X-6, 114–120	293.24	3.09	0.11	2.98	0.9	0.23		12.90	
32X-2, 100–102	296.00		0.07		0.6				
32X-3, 127–128	297.77		0.07		0.6				
33X-2, 100–101	305.80		0.14		1.2				
33X-5, 0–3	309.30	0.47	0.08	0.39	0.7	0.07		5.60	
33X-5, 100–101	310.30	0.49	0.16	0.33	1.3	0.06		5.50	
34X-2, 0–5	314.10	0.81	0.11	0.70	0.9	0.09		7.80	
34X-2, 105–107	315.15		0.12		1.0				
35X-2, 100–101	324.70	2.49	0.13	2.36	1.1	0.18		13.10	
35X-5, 0–5	328.20	2.84	0.05	2.79	0.4	0.22		12.70	
35X-5, 100–101	329.20	3.02	2.25	0.77	18.7	0.09		8.50	
36X-2, 99–100	334.39		0.56		4.7				
36X-4, 0–5	336.40	0.60	0.03	0.57	0.2	0.07		8.10	
36X-4, 99–100	337.39		1.03		8.6				
36X-4, 140–145	337.80	0.47	0.04	0.43	0.3	0.05		8.60	
127-794B-									
5R-2, 100–101	340.80	0.45	0.05	0.40	0.4	0.06		6.60	
5R-3, 0–3	341.30	0.72	0.06	0.66	0.5	0.07		9.40	

Table 7 (continued).

Core, section, interval (cm)	Depth (mbsf)	Total carbon (%)	Inorganic carbon (%)	Organic carbon (%)	$CaCO_3$ (%)	Nitrogen (%)	Sulfur (%)	Org. C/N	Org. C/S
127-794A-									
37X-2, 100–101	344.10	0.53	0.02	0.51	0.2	0.05		10.00	
37X-3, 0–5	344.60	0.90	0.09	0.81	0.7	0.09		9.00	
127-794B-									
9R-1, 57–58	376.57		0.08		0.7				
10R-1, 119–121	386.79		0.45		3.7				
10R-2, 0–3	387.10	0.76	0.12	0.64	1.0	0.08		8.00	
11R-1, 59–60	395.79		0.01		0.1				
12R-1, 109–111	405.99		0.36		3.0				
12R-2, 145–150	407.85	0.71	0.01	0.70	0.1	0.06		11.00	
12R-3, 0–3	407.90	0.78	0.01	0.77	0.1	0.06		13.00	
13R-1, 118–120	415.68		0.29		2.4				
14R-2, 0–5	425.70	0.84	0.51	0.33	4.2	0.06		5.50	
15R-1, 65–67	434.45		0.01		0.1				
15R-1, 145–150	435.25		0.01		0.1				
15R-2, 0–5	435.30	1.17	0.09	1.08	0.7	0.08		13.50	
16R-1, 64–66	443.84		0.27		2.2				
18R-1, 41–49	463.01	1.20	0.02	1.18	0.2	0.08		14.70	
18R-1, 71–73	463.31		0.03		0.2				
18R-4, 145–150	468.55	1.29	0.02	1.27	0.2	0.08	15.90		
18R-5, 0–3	468.60		0.02		0.2				
19R-2, 0–3	473.80	1.54	0.42	1.12	3.5	0.08		14.00	
19R-2, 95–97	474.75		0.01		0.1				
20R-1, 44–46	482.44		0.03		0.2				
20R-3, 0–3	485.00	0.80	0.01	0.79	0.1	0.02		39.00	
21R-1, 18–27	491.88		2.59		21.6				
21R-1, 23–26	493.43		0.03		0.2				
21R-2, 101–103	494.21		0.03		0.2				
21R-4, 0–3	496.20		0.02		0.2				
21R-5, 107–108	498.77		0.02		0.2				
22R-1, 0–3	501.20		0.03		0.2				
22R-1, 52–53	501.72		0.03		0.2				
23R-1, 0–3	510.90		0.04		0.3				
24R-1, 95–96	521.55		0.01		0.1				
24R-2, 140–145	523.50	2.99	1.32	1.67	11.0	0.09		18.50	
24R-3, 70–72	524.30	0.84	0.16	0.68	1.3	0.05		13.00	
24R-4, 138–140	526.48	2.47	0.87	1.60	7.2	0.00			
24R-6, 0–3	528.10		0.03		0.2				
25R-1, 14–15	530.44		1.14		9.5				
26R-1, 0–1	540.00		0.07		0.6				
26R-1, 58–60	540.58		0.02		0.2				
26R-2, 32–37	541.82	0.52	0.00	0.52	0.0	0.00			
26R-2, 91–93	542.41		2.32		19.3				

and OI values for sediments at Site 794 is presented in Figure 35. Based on the sample distributions in this plot, the organic contents of these sediments are primarily mixtures of Type II and Type III organic matter, with the latter type of terrestrial origin usually dominant. The few samples that plot within the range of immature Type I and Type II organic matter suggest occasional episodes of increased marine/algal productivity or preservation.

Some samples exhibit OI values above 300 and are not included in this plot. The high values of OI may reflect the analytical problems with S_3 previously discussed. In combination with relatively low TOC concentrations, errors in the oxygen index are possible. In general, the oxygen indexes above 150 suggest substantial inputs of highly oxidized and reworked/recycled organic matter to the sediments of the area. Contributions of marine organic matter, though, are also suggested by the high hydrogen indexes.

The type of organic matter in sediments can also be assessed by the ratio S_2/S_3. The values in the range 0.0–2.5 normally designate terrestrial organic matter, while values above 2.5 reflect significant marine/algal inputs (Emeis and Kvenvolden, 1986). This ratio is also plotted vs. sub-bottom depth in Figure 36. The top 100 m of the sediments are characterized by rapid fluctuations between the highest (7–10) and the lowest (0–2) values of S_2/S_3, indicating rapid transitions between marine- and terrestrially-sourced organic matter, respectively. Many of the pyrograms of the sediments above 400 mbsf contain multiple S_2 peaks that confirm the presence of multiple kerogen types in the sediments. A significant increase in the ratio below 400 mbsf suggests increased input or preservation of algal organic matter.

Thermal Maturity

The T_{max} values for the sediments from Site 794 range from 302° to 600°C. Values above 500°C are usually associated with highly recycled and oxidized organic matter, although adsorption of the pyrolysate onto clay-dominated sediments can also significantly increase the values (Peters, 1986). The T_{max} values tend to support the previous interpretation of sources that indicate a steady background influx of highly recycled and oxidized detritus into the sediments of the Japan Sea at Site 794. The high T_{max} values are most often associated with a second and later-eluting S_2 peak corroborating the previous suggestion of a significant influx of recycled and refractory organic matter. A downcore comparison of T_{max} values with the S_2/S_3 ratios in Figure 36 corroborates the interpretation that recycled and/or

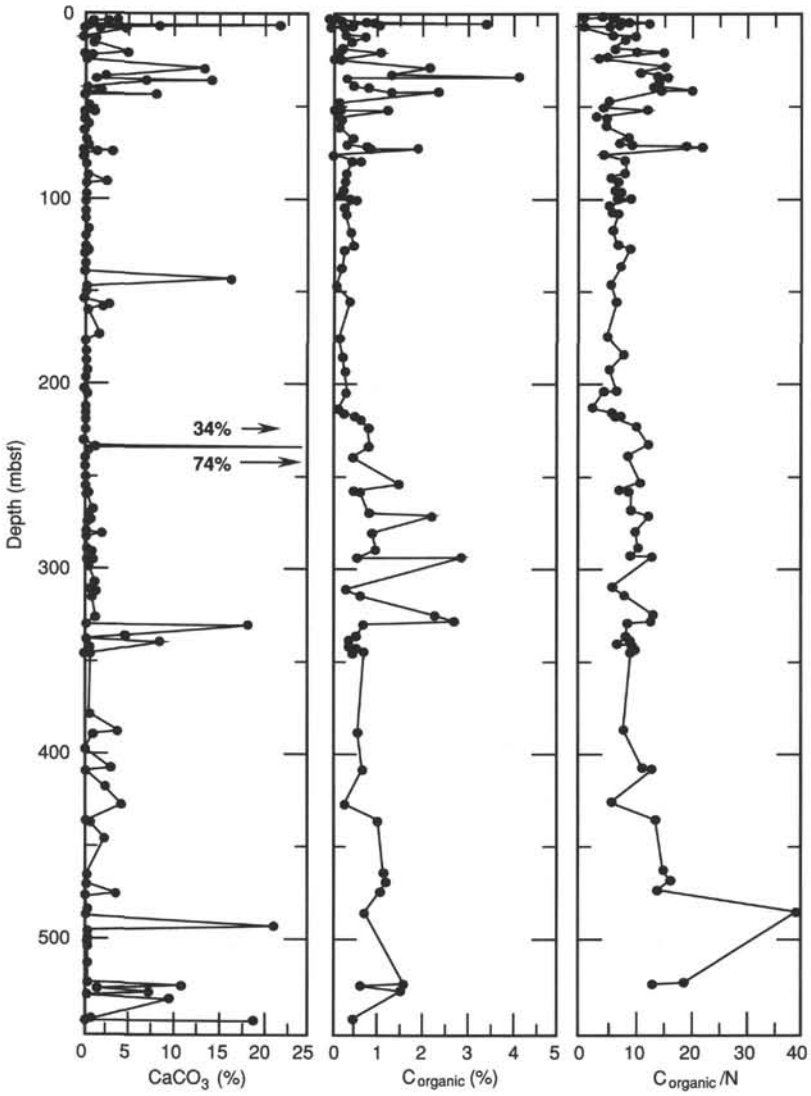

Figure 34. Downhole distributions of calcium carbonate and organic carbon concentrations as percentages of whole-dry sediments, and the ratio of organic carbon to total nitrogen in sediments at Site 794.

terrestrial organic matter is a significant component of the sediments. The rapid fluctuations in the S_2/S_3 ratio above 100 mbsf are mirrored in the T_{max} values. The apparent increase in algal input below approximately 300 mbsf corresponds quite well with an overall decrease in T_{max} to values between 400° and 430°C, temperatures which are typical of thermally immature organic matter.

Volatile Hydrocarbons

As part of the shipboard safety and pollution monitoring program, the hydrocarbon gases were continuously measured in the sediments at Site 794 using the headspace technique. Very low levels of volatile hydrocarbons, predominantly methane, were detected. The results are presented in Table 9. Methane concentrations in the headspace volumes range between 2 and 9 ppm. Compared with a laboratory background level of 2 ppm, the sedimentary concentrations are minor. Traces of ethane and ethylene were occasionally detected; the source of the latter is unknown. The low overall content of methane in the sediments suggests that either the biogenic methane usually produced during microbial metabolism of organic matter migrated out of the sedimentary column or that the conditions were not present to sustain methanogenesis. Methanogens tend to flourish only after sulfate contents have been diminished because they are unable to compete with the sulfate-reducers (Oremland and Taylor, 1978). In the sediments of Site 794, the sulfate levels were never completely depleted (see "Inorganic Geochemistry" section, this chapter), and the subsequent stage of methanogenesis was never attained. The originally deposited organic matter may have been too low in metabolizable components to sustain sulfate-reduction. On the other hand, high sulfate levels in the pore waters may have allowed sulfate reduction to completely oxidize the organic matter before sulfate depletion and subsequent methanogenesis. These two possible controls are difficult to distinguish and are not mutually exclusive. Because most of the organic matter preserved in the sediments of this site appears to be recycled (refractory) and/or deposited under oxygenated conditions, low proportions of readily metabolized organic carbon may have been the dominant control effecting the absence of methanogenesis.

Table 8. Results of Rock-Eval analysis for Site 794.

Core, section, interval (cm)	Depth (mbsf)	S_1 (10^{-3} g/g)	S_2 (10^{-3} g/g)	S_3 (10^{-3} g/g)	TOC (%)	PC	HI	OI	T_{max} (deg. C)	PI	S_2/S_3
127-794A-											
1H-3, 145–150	4.45	0.29	2.56	1.47	0.62	0.23	412	237	589	0.10	1.74
1H-4, 0–5	4.50	0.47	2.72	1.55	0.58	0.26	468	267	588	0.15	1.75
1H-4, 100–102	5.50	0.33	2.55	1.26	0.40	0.24	637	315	556	0.11	2.02
2H-3, 100–102	10.80	0.19	3.53	0.40	0.37	0.31	954	108	481	0.05	8.82
2H-4, 0–5	11.30	0.24	2.19	1.08	0.82	0.20	267	131	592	0.10	2.02
3H-2, 100–101	18.80	0.13	1.32	3.57	0.18	0.12	733	1983	584	0.09	0.36
3H-5, 82–85	23.12	0.08	3.30	0.44	0.56	0.28	589	78	568	0.02	7.50
3H-5, 145–150	23.75	0.12	1.04	0.97	0.47	0.09	221	206	423	0.10	1.07
3H-6, 0–5	23.80	0.14	1.25	0.81	0.20	0.11	625	405	576	0.10	1.54
3H-7, 29–33	25.59	1.97	7.86	7.57	3.89	0.81	202	194	402	0.20	1.03
3H-CC, 10–14	26.08	0.16	2.55	0.71	0.31	0.22	822	229	572	0.06	3.59
4H-1, 85–88	26.65	0.77	4.70	6.00	2.79	0.45	168	215	419	0.14	0.78
4H-2, 100–101	28.30	0.65	4.25	5.20	1.70	0.40	250	305	415	0.13	0.81
4H-CC, 11–18	35.59	0.10	3.05	1.45	0.43	0.26	709	337	586	0.03	2.10
5H-5, 0–5	41.30	0.26	7.13	0.75	1.54	0.61	462	48	426	0.04	9.50
6H-5, 0–5	50.80	0.02	3.59	0.45	0.40	0.30	897	113	489	0.01	7.98
7H-2, 100–102	56.80	0.05	2.66	0.84	0.34	0.22	782	247	526	0.02	3.16
8H-2, 100–102	66.30	0.13	3.41	0.85	0.67	0.29	508	126	528	0.04	4.01
9H-4, 140–145	79.20	0.06	1.33	0.54	0.58	0.11	229	93	445	0.04	2.46
11H-6, 0–5	99.80	0.08	1.49	0.78	0.54	0.13	275	144	598	0.05	1.91
12H-4, 140–145	107.70	0.03	0.35	0.85	0.32	0.03	109	265	408	0.08	0.41
12H-5, 0–2	107.80	0.29	1.71	1.00	0.34	0.16	502	294	593	0.14	1.71
15H-5, 0–3	136.30	0.04	1.10	0.64	0.25	0.09	440	256	580	0.04	1.71
16X-5, 0–5	145.80	0.07	1.28	0.71	0.23	0.11	556	308	566	0.05	1.80
17X-5, 0–5	155.50	0.05	0.56	3.95	0.35	0.05	160	1128	566	0.08	0.14
19X-5, 0–5	174.50	0.03	1.11	0.64	0.23	0.09	482	278	585	0.03	1.73
20X-5, 0–5	184.20	0.14	1.12	0.77	0.24	0.10	466	320	593	0.11	1.45
21X-4, 0–5	192.40	0.26	1.62	0.89	0.27	0.15	600	329	592	0.14	1.82
23X-5, 0–5	213.20	0.07	0.87	0.23	0.17	0.07	511	135	595	0.07	3.78
127-794B-											
3R-4, 0–3	216.70	0.24	1.08	0.40	0.50	0.11	216	80	540	0.18	2.70
127-794A-											
28X-2, 0–3	257.20	0.23	1.09	0.68	0.35	0.11	311	194	596	0.17	1.60
28X-2, 84–87	258.04	0.29	1.79	0.70	0.67	0.17	267	104	539	0.14	2.55
29X-3, 0–3	268.40	0.17	1.89	1.05	0.76	0.17	248	138	600	0.08	1.80
31X-4, 0–3	289.10	0.17	1.60	1.92	0.94	0.14	170	204	544	0.10	0.83
31X-6, 114–120	293.24	0.54	6.73	2.56	2.91	0.60	231	87	421	0.07	2.62
32X-2, 100–102	296.00	0.19	1.56	1.30	1.06	0.14	147	122	399	0.11	1.20
33X-5, 0–3	309.30	0.00	0.42	1.15	0.30	0.03	140	383	543	0.00	0.36
34X-2, 0–5	314.10	0.02	0.66	1.60	0.66	0.05	100	242	420	0.03	0.41
35X-2, 100–101	324.70	0.25	4.69	2.50	2.32	0.41	202	107	425	0.05	1.87
35X-5, 0–5	328.20	0.14	5.70	1.54	2.73	0.48	208	56	425	0.02	3.70
36X-4, 0–5	336.40	0.00	0.71	0.59	0.51	0.05	139	115	500	0.00	1.20
37X-3, 0–5	344.60	0.01	0.83	1.13	0.63	0.07	131	179	422	0.01	0.73
127-794B-											
10R-2, 0–3	387.10	0.01	0.70	0.81	0.56	0.05	125	144	409	0.01	0.86
12R-3, 0–3	407.90	0.02	1.38	0.19	0.68	0.11	202	27	409	0.01	7.26
15R-1, 145–150	435.25	0.04	1.42	0.19	0.80	0.12	177	23	411	0.03	7.47
18R-1, 41–49	463.01	0.15	1.53	0.29	1.03	0.14	148	28	411	0.09	5.27
19R-2, 0–3	473.80	0.02	1.90	1.12	1.00	0.16	190	112	421	0.01	1.69
20R-3, 0–3	485.00	0.00	0.30	2.36	0.23	0.02	130	1026	584	0.00	0.12
23R-1, 0–3	510.90	0.00	0.28	0.11	0.02	0.02	1400	550	469	0.00	2.54
24R-1, 95–96	521.55	0.00	0.05	0.02	0.20	0.00	25	10	430	0.00	2.50
24R-3, 70–72	524.30	0.00	0.62	0.93	0.67	0.05	92	138	418	0.00	0.66
24R-4, 138–140	526.48	0.03	2.51	2.17	1.50	0.21	167	144	423	0.01	1.15
25R-1, 14–15	530.44	0.04	2.09	3.44	1.58	0.17	132	217	420	0.02	0.60
26R-2, 32–37	541.82	0.01	0.00	0.10	0.48	0.00	0	20	302	0.00	0.00

Abbreviations: S_1 (mg HC/g rock) = volatile hydrocarbons; S_2 (mg HC/g rock) = kerogen-derived hydrocarbons; S_3 (mg CO_2/g rock) = organic CO_2 from kerogen; TOC = % total organic carbon; PC = principal component; HI (100 S_2/C_{org}) = Hydrogen Index; OI (100 S_3/C_{org}) = Oxygen Index; T_{max} = temperature (°C) of maximum hydrocarbon generation from kerogen; PI = productivity index ($S_1 + S_2$).

BASEMENT ROCKS

Introduction

A total of 32 m of igneous basement rock was recovered from Holes 794B and 794C, representing a core recovery of 33%. Identification of the stratigraphic extent of individual units was made on the basis of diagnostic mineralogy, texture, and compositional data. The definition of unit boundaries in Hole 794C was augmented by the wet-bulk density, thermal conductivity, acoustic velocity, and porosity rock measurements as discussed in the "Physical Properties" section (this chapter). Determination of the basement lithology for Site 794 was com-

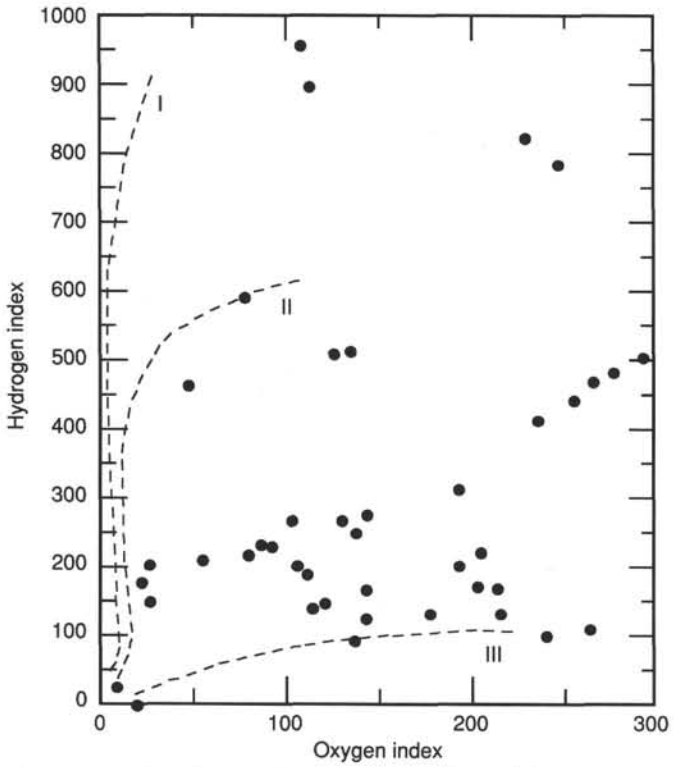

Figure 35. Van Krevelen-type diagram of the hydrogen index vs. oxygen index of sediments from Site 794.

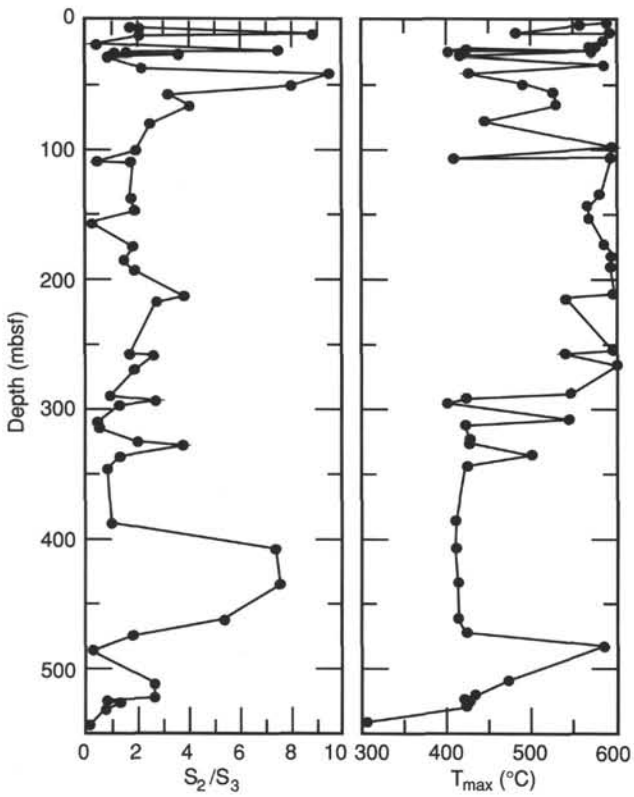

Figure 36. Downhole distributions of Rock-Eval indexes of source type S_2/S_3, and thermal maturity, T_{max}, in sediments at Site 794.

Table 9. Hydrocarbon gas data for Site 794.

Core, section, interval (cm)	Depth (mbsf)	C_1 (ppm)	C_2 (ppm)	C_3 (ppm)	C_1/C_2
127-794A-					
1H-4, 0–5	4.50	3			
2H-4, 0–5	11.30	5			
3H-6, 0–5	23.80	6			
4H-5, 0–5	31.80	6			
5H-5, 0–5	41.30	8			
6H-5, 0–5	50.80	7			
7H-4, 143–145	60.23	6			
8H-5, 0–3	69.80	4			
9H-5, 0–3	79.30	5			
10H-5, 0–3	88.80	5			
11H-4, 0–3	96.80	3			
12H-5, 0–3	107.80	3			
13H-5, 0–3	117.30	3	1	3.00	
14H-5, 0–3	126.80	3			
15H-5, 0–3	136.30	3			
16X-5, 0–5	145.80	2			
17X-5, 0–5	155.50	2			
19X-5, 0–5	174.50	2			
20X-5, 0–5	184.20	2			
21X-4, 0–5	192.40	3			
22X-5, 0–0	203.50	3			
23X-5, 0–0	213.20	4			
3R-4, 0–5	216.70	2			
3R-4, 0–3	216.70	2			
25X-5, 0–3	232.50	4			
26X-5, 0–3	242.20	3			
28X-2, 0–3	257.20	3			
28X-2, 84–87	258.04	4			
29X-3, 0–3	268.40	4			
31X-4, 0–3	289.10	6			
32X-2, 0–3	295.00	4			
33X-5, 0–3	309.30	3			
34X-2, 0–5	314.10	3			
35X-5, 0–5	328.20	4			
36X-4, 0–5	336.40	3			
127-794B-					
5R-3, 0–3	341.30	3			
127-794A-					
37X-3, 0–5	344.60	5			
127-794B-					
10R-2, 0–3	387.10	6			
12R-3, 0–3	407.90	5			
14R-3, 0–3	427.20	9	1		9.00
15R-2, 0–5	435.30	6	1		6.00
18R-5, 0–3	468.60	6			
19R-2, 0–3	473.80	6			
20R-3, 0–3	485.00	5			
21R-4, 0–3	496.20	7			
22R-1, 0–3	501.20	5			
23R-1, 0–3	510.90	7			
24R-6, 0–3	528.10	5			
26R-1, 0–1	540.00	3			

C_1 = methane, C_2 = ethane, C_3 = propane

plicated by gaps in core recovery and by the highly altered nature of the rocks. We identified six dolerite and basalt units and interpreted them to represent sills intruded into soft sediments.

Lithology

Figure 37 shows a compilation of the basement lithologic units for Holes 794B and 794C. Uncertain and approximate unit boundaries are shown by dashed lines. The following is a summary description of the six igneous lithological units. Visual core descriptions and petrographic descriptions are given in Section 3, near the back of the book.

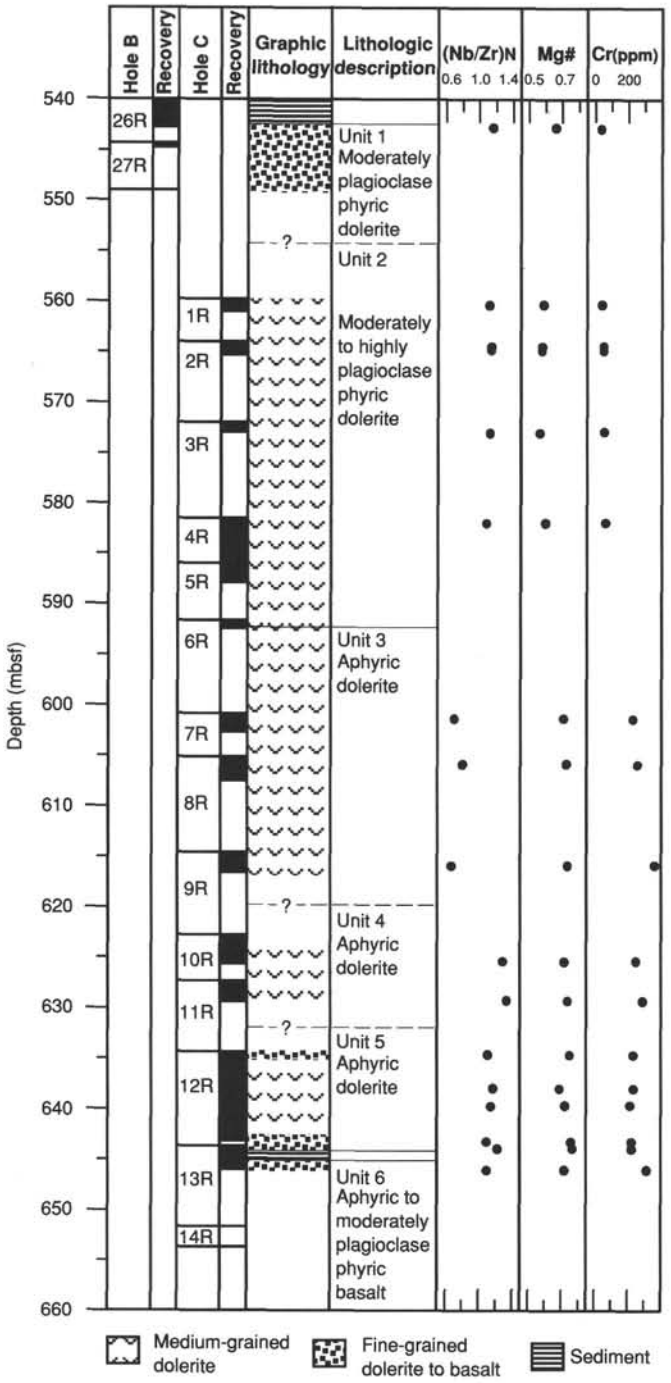

Figure 37. Unit boundaries, geochemical variation, and basement core recovery of igneous rocks at Site 794.

Unit 1: Moderately Plagioclase Phyric Dolerite

This unit is defined from Section 127-794B-26R-2, 97 cm, to Section 127-794B-27R-1, Piece 11B (542.4–544.8 mbsf, or 2.4 m). A horizontal contact occurs at the top of the unit, with a thin (10-cm thick) segment of bleached, baked clay sediment above and a chilled marginal facies of moderately plagioclase phyric basalt immediately below. The bottom of the unit was not observed. The bulk of the unit is massive and dense, although a near-vertical, thin, clay (chlorite?) filled fracture occurs in Section 127-794B-26R-CC. The unit interior is composed of fine-grained, moderately phyric dolerite with no identifiable phenocryst phases other than euhedral to subhedral plagioclase. The groundmass is dominated by laths of plagioclase, and a few percent of subhedral to skeletal magnetite (to 0.5 mm) also occurs. The groundmass of the upper chilled margin is totally replaced by clays, but replacement textures suggest that it may have originally been glassy to spherulitic. The coarser interior is also highly altered, with all of the mesostasis and mafic silicate minerals replaced by chlorite and brown clays. The sparse vesicles are filled with clays, and most of the plagioclase phenocrysts are very highly altered to clay. High whole-rock K_2O contents (Table 10) and X-ray diffraction data indicate that the brown clays include kaolinite and saponitic mixed clays. The coarser portion of the unit contains occasional secondary biotite, intimately intergrown with chlorite in the groundmass and as a replacement of plagioclase phenocrysts. Occasional irregular grains of sulfide (pyrite?) are up to 1 mm in size.

Unit 2: Moderately to Highly Plagioclase Phyric Dolerite

This unit is defined from Section 127-794C-1R-1, Piece 1 to Section 127-794-6R-1, Piece 10 (560.0–592.6 mbsf, or 32.6 m). No upper or lower contacts were observed. The lower limit of the unit is defined by a change from doleritic texture to a highly phyric basalt with a microlitic groundmass. Above this, the unit is much coarser, consisting of coarsely porphyritic dolerite (Fig. 38) with a seriate texture and an intersertal to intergranular groundmass. The dominant phenocryst phase is zoned, euhedral to subhedral plagioclase, up to 5 mm in size and frequently glomeroporphyritic. The groundmass is dominated by laths of plagioclase with subordinate and anhedral clinopyroxene, and small amounts of euhedral to subhedral magnetite (to 0.5 mm) also occur. The unit is massive and dense, and is highly fractured in Sections 127-794C-4R-1 to 127-794C-6R-1. A vertical fracture in Section 127-794C-2R, Pieces 9A–9C, shows vertical slickensides developed in soft, green clay (chlorite?). Other subhorizontal fractures are filled by veins of soft, green clays that are up to 2 cm thick (Fig. 39). The sparse vesicles are also filled with clays.

Unit 2 is highly altered, with most of the mafic silicate crystals totally replaced by greenish-brown clays. Plagioclase is slightly to highly altered to brown clays, the interiors of phenocrysts typically being the most thoroughly altered. Trace amounts of irregular sulfide (pyrite?, to 1 mm) are also found.

Unit 3: Aphyric Dolerite

This unit is defined from Section 127-794C-6R-1, Piece 11, to Section 127-794C-9R-2, Piece 8 (592.6–617.0 mbsf, or 24.4 m). No upper or lower contacts were observed. The top of the unit is defined by a reduction in grain size and by an abrupt change in lithology from porphyritic (Unit 2) to aphyric dolerite (Unit 3). The base of the unit is poorly located between Sections 127-794C-9R-2 and 127-794C-10R-1, and is defined by a slight reduction in grain size and by a change in the $(Nb/Zr)_N$ of the rock.

The bulk of Unit 3 is fine- to medium-grained dolerite, dominated by plagioclase, with rare, relict subophitic clinopyroxene, and small amounts of euhedral to skeletal magnetite (to 0.5 mm in size). The unit is moderately vesicular, massive, and highly fractured, with either network or random fracture orientation (Fig. 40). Some fractures are filled with veins up to 1 cm thick of unidentified clay minerals, and the vesicles are filled with clays as well. The unit as a whole is highly altered, with virtually all of the mafic silicate phases (clinopyroxene and olivine) and all of the mesostasis replaced by greenish-brown clays. Plagioclase is partially replaced by brown clays.

Table 10. Chemical analyses of basement rocks from Holes 794B and 794C. Mg# refers to $Mg/(Mg + Fe^{2+})$, where $Fe^{2+} = Fe^{total} \cdot 0.9$. $(Nb/Zr)_N$ represents the chondrite-normalized ratio of these elements (Sun et al., 1979).

Hole	794B	794C	794C	794C	794C	794C	794C	794C	794C	794C	794C	794C	794C	794C	794C	794C	794C
Section	26R-2	1R-1	2R-1	2R-1	3R-1	4R-1	7R-1	8R-1	9R-1	10R-2	11R-2	12R-1	12R-3	12R-4	12R-7	13R-1	13R-2
Interval (cm)	101–103	48–50	34–36	77–79	122–124	42–44	46–48	65–67	130–132	102–104	57–59	25–27	71–73	85–86	17–19	21–23	93–95
Unit	1	2	2	2	2	2	3	3	3	4	4	5	5	5	5	5	6
SiO_2	51.67	50.82	50.71	50.49	50.57	51.21	51.53	51.65	51.46	50.10	51.08	51.35	50.06	50.96	50.47	50.69	48.78
TiO_2	1.49	1.37	1.37	1.24	1.14	1.09	1.26	1.13	1.18	1.25	1.16	1.26	1.19	1.32	1.16	1.14	1.21
Al_2O_3	18.23	18.45	18.77	19.28	21.18	20.23	17.80	17.70	17.86	16.58	16.94	17.08	17.69	16.97	16.39	16.32	16.86
FeO	8.66	9.21	8.10	8.14	8.02	7.81	7.83	7.38	8.08	8.73	8.64	8.18	8.56	7.36	8.85	8.80	10.21
MnO	0.09	0.17	0.13	0.12	0.12	0.13	0.15	0.14	0.16	0.12	0.14	0.10	0.13	0.16	0.12	0.09	0.15
MgO	8.48	7.02	5.68	5.69	5.45	5.98	9.81	9.81	11.46	11.32	12.26	12.00	10.19	9.42	14.00	14.69	13.25
CaO	3.47	6.83	9.33	8.92	10.75	10.60	6.21	7.18	5.80	6.87	7.02	5.28	9.06	9.09	4.52	2.54	3.40
Na_2O	4.05	3.44	3.78	3.71	3.33	3.39	3.89	3.35	3.48	3.15	2.84	3.27	2.67	2.84	2.85	2.53	2.65
K_2O	2.68	1.50	0.68	0.68	0.55	0.60	0.82	0.73	0.67	0.75	0.68	1.40	0.28	0.71	1.52	3.30	1.72
P_2O_5	0.30	0.26	0.30	0.25	0.20	0.22	0.20	0.20	0.19	0.22	0.20	0.23	0.21	0.23	0.19	0.19	0.20
Total	99.12	99.07	98.85	98.52	101.31	101.26	99.50	99.27	100.34	99.09	100.96	100.15	100.04	99.06	100.07	100.29	98.43
LOI	4.22	2.23	1.72	1.93	1.95	1.86	2.52	3.17	3.68	3.37	3.74	3.53	2.52	2.05	4.09	5.45	5.56
Nb	8.4	7.6	8.3	7.9	6.2	6.7	4.5	5.0	3.9	8.6	8.3	7.9	7.6	8.6	6.5	7.1	3.2
Zr	103	97	103	98	77	88	92	90	83	95	89	101	92	108	84	83	41
Y	18.6	20.4	21.2	20.7	15.2	17.6	17.9	17.5	17.0	18.1	17.6	21.7	19.8	23.0	16.8	13.8	12.2
Sr	257	349	387	411	424	405	273	260	255	248	243	238	278	275	204	139	190
Rb	11.3	21.2	7.1	6.9	5.6	6.7	10.3	10.9	7.3	7.8	8.4	8.8	1.2	6.0	9.9	17.6	9.0
Zn	45	286	75	71	60	66	69	67	71	72	60	52	59	67	74	72	68
Cu	22	77	44	42	43	40	62	53	56	52	54	95	51	60	31	58	60
Ni	15	11	15	15	16	17	100	132	165	133	53	69	91	80	81	97	132
Cr	33	40	51	48	55	63	229	259	364	254	291	236	235	214	223	224	316
V	270	263	245	254	236	212	309	259	297	253	256	262	245	294	252	233	271
Ce	23	21	27	23	19	28	28	26	16	21	20	21	18	23	23	17	8
Ba	166	274	162	175	129	135	166	160	154	129	120	142	98	160	115	152	89
Mg#	0.660	0.602	0.581	0.581	0.574	0.603	0.713	0.725	0.734	0.720	0.738	0.744	0.702	0.717	0.758	0.768	0.720
$(Nb/Zr)_N$	1.16	1.12	1.15	1.15	1.15	1.09	0.70	0.80	0.67	1.29	1.33	1.11	1.18	1.14	1.10	1.23	1.10

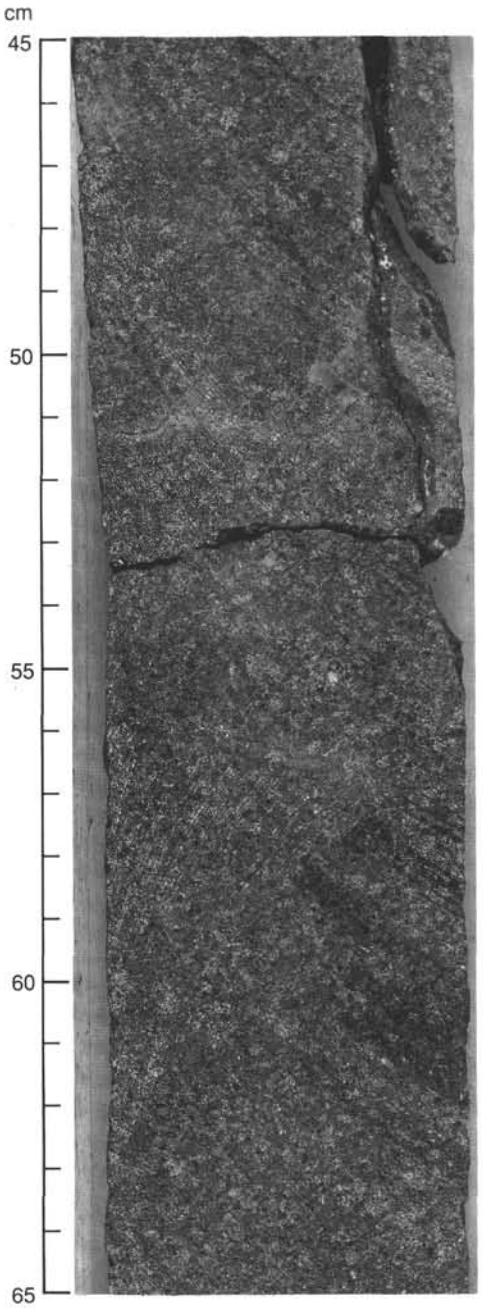

Figure 38. Core photograph of coarsely porphyritic plagioclase dolerite in Unit 2 (Section 127-794C-2R-1, 45–65 cm).

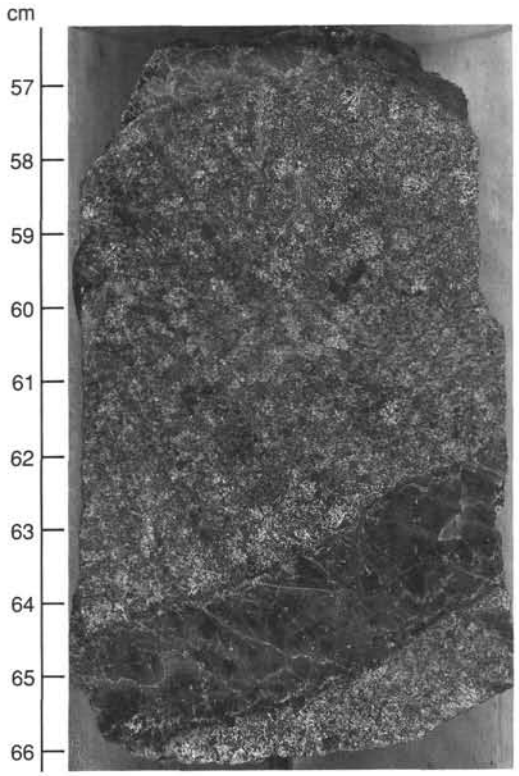

Figure 39. Core photograph of clay-filled vein in Unit 2 (Section 127-794C-4R-4, 56–66 cm).

Unit 4: Aphyric Dolerite

This unit is defined from Section 127-794C-10R-1, Piece 1, to Section 127-794C-11R-2, Piece 6C (622.8–629.2 mbsf, or 6.4 m). No upper or lower contacts were observed. The upper limit of the unit is poorly defined above Section 127-794C-10R-1 by a change in rock chemistry. The base of the unit is poorly defined by an decrease in nickel and $(Nb/Zr)_N$ from Section 127-794C-11R-2 to Section 127-794C-12R-1, and by a change to a finer groundmass in the latter section (Unit 5). Unit 4 is composed of massive, vesicular, medium- to fine-grained aphyric dolerite. The upper half of the unit is highly fractured, whereas the lower half contains few fractures.

The rock is dominated by subhedral to euhedral plagioclase in an intergranular and intersertal texture, with relict subophitic clinopyroxene. Small amounts of euhedral to skeletal magnetite (< 0.5 mm) and rare, irregular grains of sulfide (pyrite?; up to 1.5 mm) also occur. The unit is highly altered, with the mesostasis and most mafic silicate minerals replaced by greenish-brown clays. The plagioclase is partially replaced by brown clay, and trace amounts of secondary calcite and pyrite are found in the mesostasis and vesicles.

Unit 5: Aphyric Dolerite

Unit 5 is defined from Section 27-794C-12R-1, Piece 1A, to Section 127-794C-13R-1, Piece 4 (634.3–644.1 mbsf, or 9.8 m). The upper contact was not directly observed and is delineated by a change in grain size and rock chemistry. The lower extent of Unit 5 is sharply defined by a baked contact with tuffaceous sediments. Fractures within the unit are randomly orientated and irregular in occurrence, and some portions of the unit contain no fractures. Most of the unit is highly vesicular (Fig. 41).

Unit 5 is dominated by subhedral laths of plagioclase intergrown with smaller amounts of ophitic and subophitic clinopyroxene. The unit margins exhibit microlitic texture that coarsens to intergranular and seriate textures in the interior. Small amounts of euhedral to skeletal magnetite (to 1 mm) are found throughout, together with sporadic and irregular blebs of sulfide (pyrite?; to 0.5 mm). The basal part of the unit is a moderately plagioclase phyric basalt, containing reddish-brown Cr-spinel in the formerly glassy to spherulitic groundmass and in olivine pseudomorphs. The entire unit is highly altered, with all of the mesostasis and most mafic silicate minerals replaced by brown clays. Plagioclase is only slightly altered in the unit interior, but is highly to very highly altered to brown clays in the lower marginal part of the unit.

Unit 6: Aphyric to Moderately Plagioclase Phyric Basalt

Unit 6 is defined from Section 127-794C-13R-2, Pieces 4–15 (645.8–646.7 mbsf, or 0.9 m). It is delineated at the top by a chilled, intrusive margin against post-depositionally welded tuff

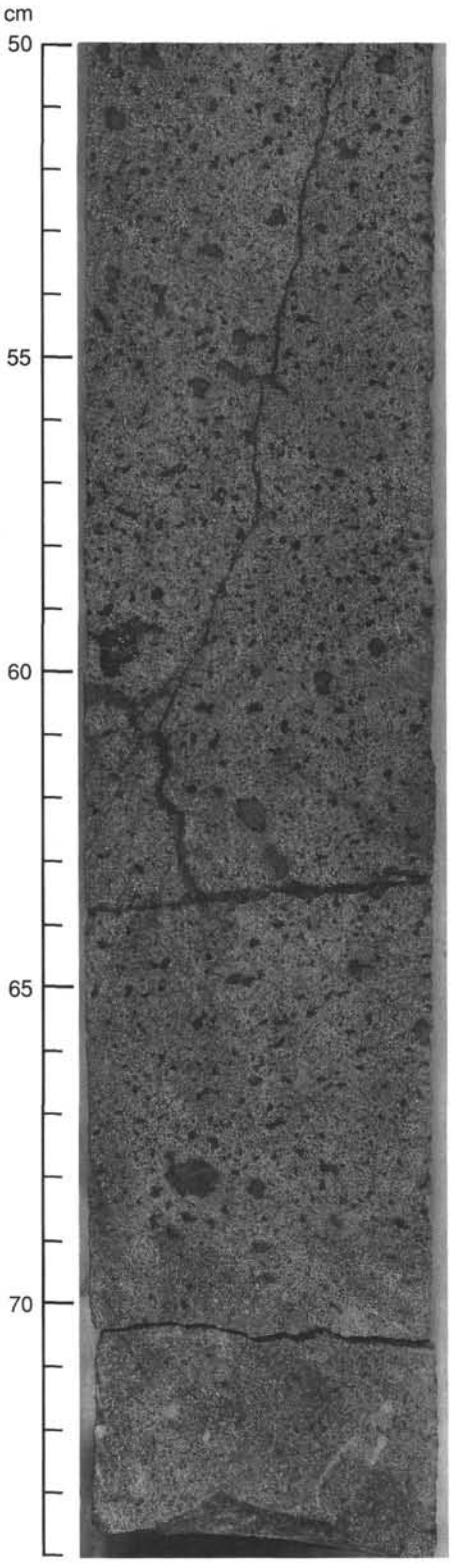

Figure 40. Core photograph of fractures and clay-filled vesicles in aphyric dolerite, Unit 3 (Section 127-794C-7R-1, 50–74 cm.

(see "Lithostratigraphy" section, this chapter), and extends to the end of the recovered core. The interior of the unit is massive and fine-grained. The basalt contains euhedral crystals of plagioclase and pseudomorphs of olivine set in what was formerly a glassy to microlitic groundmass, with Cr-spinel occurring in

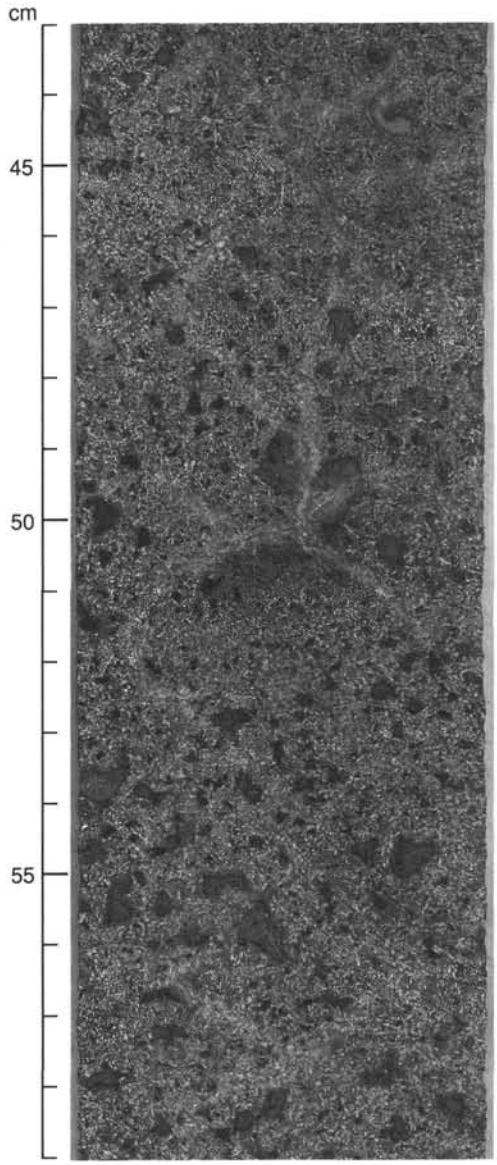

Figure 41. Core photograph of highly vesicular aphyric dolerite in Unit 5 (Section 127-794C-12R-3, 43–59 cm). Vesicles are filled with clays.

the groundmass and as inclusions in olivine. The rock is very highly altered; all of the olivine and groundmass are totally replaced by tan and brown clays. The plagioclase is highly to very highly altered to brown clays, and the vesicles are filled with clay.

Drilling Rubble within Unit 3

Loose pieces of drilling rubble were found at the top of Core 127-794C-7R (Pieces 1 to 3). These consist of fine-grained, moderately plagioclase phyric basalt. Section 127-794C-7R-1, Piece 1, shows a baked, irregular, possibly intrusive contact with tuff and claystone. This very highly altered basalt contains clay pseudomorphs of plagioclase and olivine phenocrysts, both with altered Cr-spinel inclusions, in a glassy to spherulitic groundmass now totally altered to clays. Consideration of the mineralogy and of the sediments in contact indicates that this fragment could possibly represent the margin of Unit 1. Alternately, it could represent an unrecognized unit.

Chemistry of Basement Rocks

X-ray fluorescence (XRF) whole-rock analyses of basement samples from Leg 127 Holes 794B and 794C are given in Table 10. The actual composition of the magmas from which these samples crystallized is difficult to ascertain, due to the highly to very highly altered nature of the rocks. The overall compositions of these igneous rocks indicate that they are tholeiitic in character. The calculated loss on ignition (LOI) is generally over 2% and is as much as 5.5%, and is consistent with the degree of alteration observed in thin section. In contrast, measured water contents in fresh tholeiitic basaltic glasses typically range from about 0.1% to 0.7 % (e.g., Michael and Chase, 1987). The relative mobility of individual elements with respect to alteration may be estimated by comparing their relative correlation with LOI from analyses of samples from Unit 5, which is visible in continuous core within Sections 127-794C-12R-1 to 127-794C-13R-1. K_2O, MgO, FeO, Rb, and Ba show a positive correlation with LOI, and CaO and Sr show a negative correlation with LOI. MgO correlates more strongly with LOI than FeO, so that $Mg/(Mg + Fe^{2+})$ (or Mg#) correlates positively with LOI. In contrast, Ni, Cr, TiO_2, Nb, and Zr show relatively little inter-unit variation and relation to LOI. As a result, we have used these elements and the chondrite-normalized ratio Nb/Zr (Sun et al., 1979) to infer unit boundaries. Figure 42 shows the N-MORB normalized amount of selected elements for representative samples from each unit (Pearce et al., 1981).

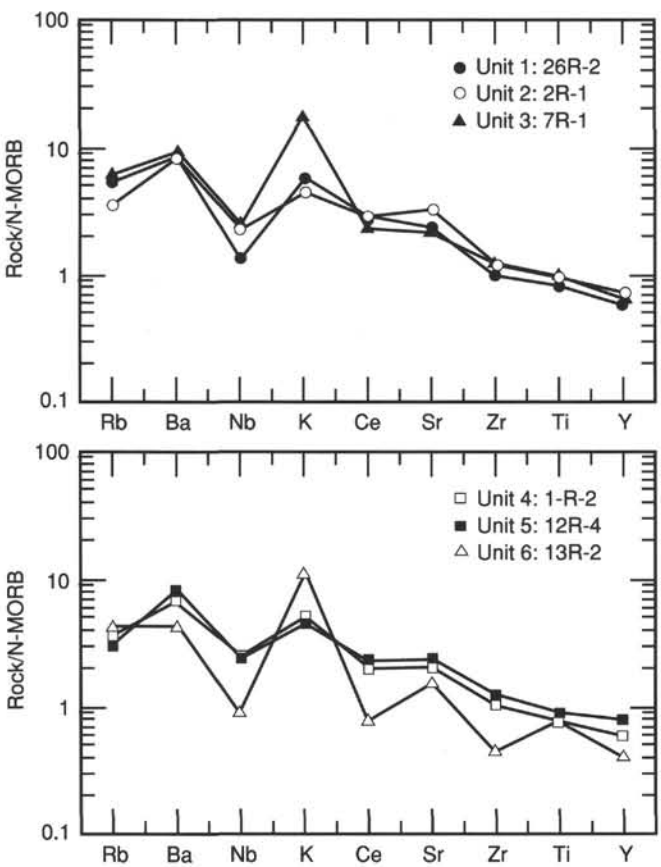

Figure 42. Compositions of selected basalts at Site 794 normalized to N-type MORB (Pearce et al., 1981). The order of the elements is after Sun et al. (1979). Rubidium, barium, and potassium have been strongly affected by hydrothermal alteration, as has strontium to a lesser extent.

The high Ni and Cr contents of some of the samples indicate that they are quite primitive. The high $Mg/(Mg + Fe^{2+})$ ratios of these samples are consistent with this interpretation, although in many samples, these ratios have clearly been substantially increased during alteration. Comparisons of the rock analyses in Table 10 with the igneous units defined in the core (Fig. 42) show that there are several groups of igneous rock: an upper group, consisting of porphyritic, relatively evolved, high-Nb/Zr rocks from Units 1 and 2; aphyric, primitive, low Nb/Zr rocks of Unit 3; a middle group of predominantly aphyric, primitive rocks with high Nb/Zr of Units 4 and 5; and the primitive Unit 6 with relatively low amounts of Nb, Ce, Zr, and Y. These assemblages may represent individual pulses of magmatic activity.

The samples are similar to mid-ocean ridge basalts (MORB's) and back-arc basin basalts (BABB's) in terms of their TiO_2, Nb, and Zr contents (e.g., Saunders and Tarney, 1984; Erlank and Kable, 1976; Sun et al., 1979; Hawkins, 1976; Sinton and Fryer, 1987). The Ce contents of all samples and the Al_2O_3, SiO_2, and Na_2O contents of the least-altered samples are consistent with this observation. The Sr contents of the most unaltered samples are higher than typically seen in MORB's, but are similar to those reported from some BABB's (Saunders and Tarney, 1984), and perhaps reflect a volcanic arc affinity.

Summary

We interpret the basement units to represent sills intruded into soft sediments. Our evidence for this assessment includes: (1) the horizontal and baked contacts with sediments; (2) the relatively coarse grain size of the sampled rock; (3) the horizontal, laterally extensive nature of the reflectors in the seismic sections; and (4) the thick, massive character of the units. The Site 794 results are a local confirmation of the proposal by Tokuyama et al. (1987a, b) that significant portions of the Yamato Basin are underlain by sill and sediment complexes. The extensive and potassic nature of the alteration indicates intense hydrothermal alteration of the dolerites and basalts, with formation of K-rich clays in the sills by the hydrothermal solution transfer of potassium from the surrounding clay- and K-rich sediments.

The Site 794 dolerites and basalts are similar in chemistry and mineralogy to other basaltic flows and doleritic sills of middle Miocene age that are found on the western coast of northern Honshu (Tsuchiya, 1988 and 1989). These middle Miocene basalts and dolerites were erupted and emplaced in a marine setting during regional subsidence that was probably associated with the opening of the Japan Sea (Tsuchiya, 1989).

Sill and sediment complexes such as that drilled at Site 794 have previously been found by drilling in other back-arc basins, including the Shikoku Basin, the South Fiji Basin, and the Caribbean (Dick et al., 1980; Stoeser, 1975; Donnelly et al., 1973). These sill and sediment complexes may be typical of back-arc basin settings. Sills of similar thickness to those found at Site 794 have been intruded into sediments in the Guaymas Basin, Gulf of California (Einsele, 1982). Like the Yamato Basin, the Gulf of California in the region of the Guaymas Basin is characterized by having a greater crustal thickness than is typical of ocean crust (Phillips, 1964). Einsele (1982) believes that the anomalously thick crust of the Guaymas Basin results from the repeated injection of sills above the basement into the overlying sediments during spreading, thereby thickening the crust. The presence of numerous horizontal sills intruding sediment at Site 794 suggests the possibility that a similar process may have occurred during the rifting of the Yamato Basin.

An unresolved question is the lower vesicularity of the upper dolerite group (Units 1 and 2) as compared to that of the stratigraphically lower Units 3 to 6. The lower vesicularity of the upper dolerite units may represent lower magmatic volatile con-

tents than those of the lower units. Alternatively, the lower vesicularity may reflect intrusion of the upper assemblage into sediments at higher confining pressures. These higher intrusion pressures could be caused by greater sediment overburden or water depth, which would imply significant age differences between the two groups of sills.

PHYSICAL PROPERTIES

Introduction

The physical property measurement program at Site 794 was used to better understand the factors that control the physical properties of marine sediments and rocks, to aid in the calculation of sediment accumulation rates, and for calibration of the seismic stratigraphy. A full program of physical property measurements was conducted on Site 794 cores, including magnetic susceptibility, GRAPE density, and *P*-wave velocity on the multisensor track (MST), index properties, thermal conductivity, *P*-wave velocity using the Hamilton Frame, and the formation factor. The physical property data are presented in Table 11 for Holes 794A, 794B, and 794C. The physical property results correlate well with the lithostratigraphy, with the basement lithology, and with the downhole logging results, and are discussed in more detail below.

Index properties and thermal conductivity were obtained once per section, on average. The formation factor was determined twice per section. In addition, two of the index property samples from each core were analyzed for grain size, carbonate content, and total organic carbon content. The methodologies are described in the "Explanatory Notes" chapter (this volume) for Sedimentology (grain-size analyses) and Chemistry (carbonate and total organic carbon content).

Data Quality

APC and XCB Cores

Cores taken using the extended core barrel (XCB) are disturbed to such a degree that some of the physical properties are altered from their *in-situ* condition. The effect of the XCB disturbance is illustrated in Figure 43A where the sonic velocity from downhole logs (see "Downhole Measurements" section, this chapter) is compared with the velocity determined using the *P*-wave logger (PWL). There is very good agreement between the two data sets for piston cores (APC), but the PWL consistently underestimates the velocity in the XCB cores. The opal-A/opal-CT boundary at about 293 mbsf is not reflected in the PWL measurements, whereas the boundary is clearly evident in the sonic log. All of the other physical property parameters also show a pronounced change at this depth. Thus we conclude that the PWL data are only valid for the APC cores.

The GRAPE density is less affected by the XCB coring disturbance than is the PWL velocity (Fig. 43B), though upon close examination there is an offset in the GRAPE density at the change from APC to XCB coring. In contrast, the wet-bulk density of relatively undisturbed, discrete samples do not show such a marked change at the APC/XCB changeover. The GRAPE and wet-bulk densities compare well with the lithodensity logging results (Fig. 43B). A number of anomalously high porosities (greater than 90%) occur in the XCB section and may represent disturbed samples.

Thermal Conductivity and Porosity

The accuracy of the thermal conductivity values in Table 11 is estimated to be ± 5%. The individual thermal conductivity measurements show great variability. The average value in the upper 100 m is about 0.9 W/m/K. Previous measurements in this area yield values of 0.74 W/m/K in the upper 2.5 m and 0.84 W/m/K between 2.5 and 5 m (Yamano et al., 1987). The sediments between 150 and 270 mbsf were mechanically disturbed during XCB coring, and no measurements were attempted. No measurements were taken between 350 and 470 mbsf because of poor core recovery and intense disturbance by rotary coring.

A comparison of thermal conductivity values with the porosity reveals possible errors with either or both of these parameters. In marine sediments, the thermal conductivity depends most strongly on the porosity. A plot of the thermal conductivity vs. porosity is presented in Figure 44. The solid curves represent the thermal conductivity vs. porosity relations based on the widely used geometric mean model for two-component aggregates, in this case solid grains in seawater. Curves for four different grain thermal conductivities are shown. The highest porosity sediments require that the solid component have a high thermal conductivity to obtain a fit to the data. Even high-conductivity constituents such as carbonates, which are scarce in these sediments (see "Organic Geochemistry" section, this chapter), would barely fit the data. Thus, we suggest that either the shipboard porosity determinations are systematically in error by + 5%, or that the thermal conductivity measurements are systematically in error by a similar amount. In contrast, the thermal conductivity measurements obtained for the igneous rocks cluster close to the model curve for a grain thermal conductivity of 1.7 W/m/K, which is a representative thermal conductivity for fresh low-porosity oceanic basalts.

Formation Factor

The formation factor measurements exhibit a great deal of scatter. The average magnitude is in general agreement with estimates from the downhole resistivity logs. However, the seawater reference we used did not give consistent results and added to the uncertainty of each measurement. The variation in the resistivity of the seawater reference was about 10%, leading to an estimated error of about 20% in the formation factor.

Correlation with Lithostratigraphy

The general patterns and trends that are apparent in the data are outlined first. Then the correlation of the physical properties with the specific lithostratigraphic units is presented. We have used the lithostratigraphic units as defined in the "Lithostratigraphy" section (this chapter).

General Trends and Features

The wet-bulk, dry-bulk, and grain densities, and the thermal conductivity decrease (Figs. 45A through 45D), and the porosity and water content increase (Figs. 45E and 45F) from the seafloor down through the sedimentary section to about 250 mbsf. These trends are opposite to that usually observed in marine sedimentary sections. We think this is due to an increasing diatom content with depth. At the opal-A/opal-CT boundary, at approximately 293 mbsf, these trends in the index properties reverse sharply, and a more normal increase in wet- and dry-bulk densities, and a decrease in porosity and water content are observed.

The grain-size analyses of physical property samples indicate that the sediment is mostly silt with minor amounts of clay, with little depth variation (see "Lithostratigraphy" section, this chapter). Similarly, the carbonate content is virtually zero except for the occasional carbonate concretion (see "Organic Geochemistry" section, this chapter). Consequently, the observed physical property variations are not related to variations in the grain size or carbonate content.

The combined downhole sonic velocity (see "Downhole Measurements" section, this chapter) and laboratory acoustic velocity profile (Fig. 45G) shows a steady increase with depth in

Table 11. Site 794 physical properties data.

Core, section, interval (cm)	Depth (mbsf)	Densities: Wet bulk (g/cm³)	Densities: Dry bulk (g/cm³)	Densities: Grain (g/cm³)	Porosity (%)	Water content (%)	Void ratio	Water ratio	Velocity (m/s): A	Velocity (m/s): B*	Velocity (m/s): C	Thermal conductivity (W/m · K)	Formation factors: H	Formation factors: V	Formation factors: Mean	Anisotropy
127-794A-																
1H-1, 45–47	0.45												1.89	1.83	1.86	0.98
1H-1, 75–77	0.75									1515			1.14	1.34	1.24	1.08
1H-1, 100–102	1.00	1.34	0.48	2.71	84.5	64.6	5.47	1.81		1509			1.49	1.63	1.56	1.05
1H-2, 50–52	2.00									1509			1.68	1.70	1.69	1.01
1H-2, 100–102	2.50	1.45	0.64	2.77	79.4	56.1	3.85	1.27		1501		1.142	1.94	2.01	1.97	1.02
1H-3, 50–52	3.50									1512			1.53	1.67	1.60	1.04
1H-3, 100–102	4.00	1.33	0.51	2.59	80.5	62.0	4.14	1.63		1510			1.63	1.60	1.61	0.99
1H-4, 50–52	5.00									1514			1.68	1.64	1.66	0.99
1H-4, 100–102	5.50	1.29	0.45	2.35	82.3	65.4	4.64	1.87		1515		0.821	1.57	1.61	1.59	1.01
1H-5, 30–32	6.30									1508			2.24	2.15	2.19	0.98
1H-5, 50–52	6.50	1.46	0.75	2.78	69.8	49.0	2.31	0.96		1505			2.36	2.22	2.29	0.97
2H-1, 50–51	7.30									1515		0.906	1.48	2.36	1.87	1.26
2H-1, 100–102	7.80	1.42	0.63	2.59	77.7	56.1	3.49	1.27		1450		1.121	1.91	2.29	2.09	1.09
2H-2, 40–42	8.70									1516			2.72	2.32	2.51	0.92
2H-2, 100–102	9.30	1.44	0.58	2.90	83.8	59.6	5.17	1.49		1505			1.95	2.06	2.00	1.03
2H-3, 50–51	10.30									1503		0.903	1.75	1.78	1.76	1.01
2H-3, 100–102	10.80	1.32	0.44	2.89	85.8	66.6	6.05	2.00		1509		0.829	1.45	1.48	1.46	1.01
2H-4, 50–51	11.80									1504		0.923	1.94	2.08	2.01	1.04
2H-4, 100–102	12.30	1.44	0.63	2.66	78.9	56.1	3.74	1.27		1509		1.206	1.83	1.81	1.82	0.99
2H-5, 50–52	13.30									1512			1.66	1.69	1.67	1.01
2H-5, 100–102	13.80	1.62	0.90	2.89	70.1	44.3	2.35	0.79		1524			2.41	2.65	2.53	1.05
2H-6, 50–51	14.80									1511		0.930	2.16	2.22	2.19	1.01
2H-6, 100–102	15.30	1.50	0.73	2.09	74.5	50.9	2.93	1.04		1512		1.004	2.14	2.19	2.16	1.01
2H-7, 40–42	16.20									1514			1.87	2.14	2.00	1.07
2H-7, 50–52	16.30	1.37	0.50	4.60	84.5	63.2	5.47	1.72		1510						
3H-1, 50–51	16.80											0.984	2.00	2.05	2.02	1.01
3H-1, 100–102	17.30	1.39	0.56	2.86	80.5	59.3	4.13	1.47				1.053	1.73	1.86	1.79	1.04
3H-2, 50–52	18.30									1467			1.63	1.69	1.66	1.02
3H-2, 100–102	18.80	1.47	0.67	2.50	77.8	54.2	3.50	1.18					2.13	2.11	2.12	1.00
3H-3, 50–51	19.80											1.000	2.25	2.15	2.20	0.98
3H-3, 100–102	20.30	1.48	0.68	2.66	77.6	53.7	3.47	1.16				0.914	2.19	2.39	2.29	1.04
3H-4, 50–52	21.30									1458			2.08	2.07	2.07	1.00
3H-4, 100–102	21.80	1.44	0.58	2.83	83.5	59.4	5.06	1.48		1455			1.98	2.03	2.00	1.01
3H-5, 50–51	22.80									1525		1.052	2.49	2.50	2.49	1.00
3H-5, 100–102	23.30	1.48	0.67	2.79	79.1	54.8	3.79	1.21		1517		1.104	2.18	2.17	2.17	1.00
3H-6, 50–52	24.30									1518			1.28	2.05	1.62	1.27
3H-6, 100–102	24.80	1.59	0.89	2.65	68.0	43.8	2.12	0.78		1523			2.49	2.52	2.50	1.01
3H-7, 25–26	25.55									1511		0.909				
3H-7, 40–42	25.70	1.50	0.74	2.54	74.1	50.6	2.86	1.03		1515			2.23	2.15	2.19	0.98
4H-1, 50–51	26.30											0.924	2.17	2.51	2.33	1.08
4H-1, 100–102	26.80	1.63	0.93	2.78	67.9	42.7	2.11	0.75		1532		1.028	2.43	2.62	2.52	1.04
4H-2, 15–17	27.45												1.34	1.40	1.37	1.02
4H-2, 40–42	27.70									1521			2.11	2.17	2.14	1.01
4H-2, 100–102	28.30	1.49	0.69	2.48	77.9	53.6	3.53	1.16		1519			2.23	2.18	2.20	0.99
4H-3, 50–51	29.30									1504		1.070	1.69	1.71	1.70	1.01
4H-3, 100–102	29.80	1.45	0.64	2.35	78.9	55.7	3.75	1.27		1512		0.925	1.91	1.95	1.93	1.01
4H-4, 50–52	30.80									1515			2.20	2.26	2.23	1.01
4H-4, 100–102	31.30	1.42	0.57	2.61	82.8	59.7	4.83	1.49		1522			1.68	1.82	1.75	1.04
4H-5, 50–51	32.30									1514		0.860	1.65	1.64	1.64	1.00
4H-5, 100–102	32.80	1.59	0.81	2.87	76.0	49.0	3.17	0.96		1513		0.930	2.07	2.11	2.09	1.01
4H-6, 50–52	33.80									1520			1.87	2.11	1.99	1.06
4H-6, 100–102	34.30	1.54	0.80	2.82	72.7	48.4	2.67	0.94		1518			2.20	2.04	2.12	0.96
4H-7, 30–32	35.10	1.62	0.90	2.69	69.8	44.1	2.31	0.79		1520						
5H-1, 50–51	35.80									1520		0.872	1.67	1.73	1.70	1.02
5H-1, 100–102	36.30	1.42	0.63	2.62	77.6	56.0	3.47	1.26		1519		1.122	1.79	1.83	1.81	1.01
5H-2, 50–52	37.30									1529			1.81	1.87	1.84	1.02
5H-2, 100–102	37.80	2.15	1.50	3.38	64.0	30.5	1.78	0.44		1519			2.03	2.25	2.14	1.05
5H-3, 50–51	38.80									1503		0.887	1.62	1.74	1.68	1.04
5H-3, 100–102	39.30	1.60	0.87	2.70	70.9	45.4	2.44	0.84		1512		1.025	2.32	2.45	2.38	1.03
5H-4, 50–52	40.30									1510			2.29	2.39	2.34	1.02
5H-4, 100–102	40.80	1.46	0.63	2.69	81.2	57.0	4.32	1.33		1503			1.96	2.00	1.98	1.01
5H-5, 45–46	41.75									1543		0.740	1.93	2.03	1.98	1.03
5H-5, 100–102	42.30	1.49	0.67	2.72	79.7	54.8	3.92	1.22		1511		1.060	1.84	1.98	1.91	1.04
5H-6, 50–51	43.30									1511		0.937	2.15	2.18	2.16	1.01
5H-6, 100–102	43.80	1.41	0.59	2.62	80.4	58.4	4.10	1.41		1511		0.822	2.09	2.13	2.11	1.01
6H-1, 50–51	45.30									1512		0.793	1.75	1.81	1.78	1.02
6H-1, 100–102	45.80	1.37	0.52	2.40	82.5	61.7	4.70	1.61		1509		0.898	1.73	1.80	1.76	1.02
6H-2, 50–52	46.80									1510			1.69	1.76	1.72	1.02
6H-2, 100–102	47.30	1.53	0.65	2.96	85.3	57.1	5.81	1.34		1509						
6H-2, 110–112	47.40									1508			3.16	12.53	6.29	1.99
6H-3, 50–51	48.30									1510		1.016	2.10	2.53	2.30	1.10
6H-3, 100–102	48.80	1.45	0.60	2.80	82.7	58.4	4.77	1.40		1503		0.872	1.74	1.90	1.82	1.04
6H-4, 50–52	49.80									1507			2.04	2.05	2.04	1.00
6H-4, 100–102	50.30	1.44	0.57	2.68	85.4	60.8	5.87	1.55		1515			2.37	3.66	2.95	1.24
6H-5, 50–51	51.30									1514		0.983	2.28	2.34	2.31	1.01
6H-5, 100–102	51.80	1.52	0.72	2.65	78.3	52.8	3.60	1.12		1506		0.974	2.07	2.15	2.11	1.02
6H-6, 50–52	52.80									1537			2.61	2.79	2.70	1.03
6H-6, 100–102	53.30	1.57	0.79	2.92	76.1	49.7	3.19	0.99		1512			2.08	2.41	2.24	1.08
6H-7, 45–47	54.25	1.69	1.04	2.68	63.2	38.3	1.72	0.62		1525						
6H-7, 50–51	54.30									1522		1.103	2.59	2.50	2.54	0.98
7H-1, 50–51	54.80									1512		0.983	2.41	2.75	2.57	1.07
7H-1, 100–102	55.30	1.74	1.12	2.62	60.3	35.5	1.52	0.55		1547		1.095	2.91	2.94	2.92	1.01
7H-2, 46–48	56.26									1516			2.36	2.52	2.44	1.03

Table 11 (continued).

Core, section, interval (cm)	Depth (mbsf)	Densities: Wet bulk (g/cm³)	Densities: Dry bulk (g/cm³)	Densities: Grain (g/cm³)	Porosity (%)	Water content (%)	Void ratio	Water ratio	Velocity (m/s): A	Velocity (m/s): B*	Velocity (m/s): C	Thermal conductivity (W/m · K)	Formation factors: H	Formation factors: V	Formation factors: Mean	Anisotropy
127-794A- (Cont.)																
7H-2, 100–102	56.80	1.62	0.88	2.69	72.0	45.5	2.57	0.83		1521			2.51	2.53	2.52	1.00
7H-3, 50–51	57.80									1513		1.011	2.54	2.52	2.53	1.00
7H-3, 100–102	58.30	1.74	1.06	2.75	66.6	39.2	1.99	0.65		1532		0.971	2.67	2.74	2.70	1.01
7H-4, 50–52	59.30									1521			2.07	2.18	2.12	1.03
7H-4, 100–102	59.80	1.48	0.71	2.50	75.0	51.9	2.99	1.08		1511			2.17	2.39	2.28	1.05
7H-5, 50–51	60.80									1513		0.895	2.04	2.14	2.09	1.02
7H-5, 100–102	61.30	1.44	0.60	2.56	81.8	58.2	4.50	1.40		1505		0.918	1.72	1.79	1.75	1.02
7H-6, 50–52	62.30									1515			2.35	2.46	2.40	1.02
7H-6, 100–102	62.80	1.54	0.77	2.76	74.6	49.6	2.94	0.99		1516			2.34	2.46	2.40	1.03
7H-7, 50–52	63.80	1.48	0.66	2.62	80.1	55.4	4.03	1.24		1528		0.920	1.89	2.02	1.95	1.03
8H-1, 50–51	64.30											0.926	1.78	1.86	1.82	1.02
8H-1, 100–102	64.80	1.43	0.62	2.47	78.8	56.5	3.71	1.29				0.873	1.83	1.81	1.82	0.99
8H-2, 50–52	65.80									1520			1.60	1.61	1.60	1.00
8H-2, 100–102	66.30	1.48	0.71	2.71	74.8	51.8	2.97	1.07		1531			1.82	1.85	1.83	1.01
8H-3, 50–51	67.30									1515		0.916	2.10	2.10	2.10	1.00
8H-3, 100–102	67.80	1.45	0.62	2.70	80.8	57.1	4.21	1.34		1537		0.878	2.01	1.92	1.96	0.98
8H-4, 50–52	68.80									1515			1.83	1.90	1.86	1.02
8H-4, 100–102	69.30	1.60	0.83	2.46	74.9	48.0	2.99	0.93		1527			2.00	2.53	2.25	1.12
8H-5, 50–51	70.30									1532		1.073	2.68	2.75	2.71	1.01
8H-5, 100–102	70.80	1.41	0.57	2.59	81.7	59.4	4.48	1.47		1525		0.865	2.10	2.13	2.11	1.01
8H-6, 50–52	71.80									1604			2.04	2.05	2.04	1.00
8H-6, 100–102	72.30	1.48	0.69	2.70	76.9	53.2	3.34	1.13		1534			1.79	1.83	1.81	1.01
8H-7, 40–41	73.20									1528		0.915				
9H-1, 50–51	73.80									1472		0.817	2.09	2.00	2.04	0.98
9H-1, 100–102	74.30	1.38	0.56	2.56	79.9	59.3	3.97	1.46				0.901	2.02	2.04	2.03	1.00
9H-2, 50–52	75.30												2.14	3.68	2.81	1.31
9H-2, 100–102	75.80	1.47	0.65	2.61	79.9	55.7	3.97	1.27					2.14	2.85	2.47	1.15
9H-3, 50–51	76.80											0.902	2.09	2.24	2.16	1.04
9H-3, 100–102	77.30	1.59	0.74	2.57	82.7	53.3	4.78	1.15				0.735				
9H-3, 110–112	77.40												2.09	2.16	2.12	1.02
9H-4, 50–52	78.30									1527			2.08	2.28	2.18	1.05
9H-4, 100–102	78.80	1.42	0.60	2.47	79.8	57.6	3.96	1.36		1529			2.01	2.03	2.02	1.00
9H-5, 50–51	79.80									1529		0.927	1.93	2.02	1.97	1.02
9H-5, 100–102	80.30	1.30	0.47	2.37	81.3	64.1	4.36	1.78		1542		0.682	1.89	1.94	1.91	1.01
9H-6, 50–52	81.30									1542			2.05	2.14	2.09	1.02
9H-6, 100–102	81.80	1.33	0.50	2.41	80.4	61.9	4.09	1.64		1552			1.95	2.01	1.98	1.02
10H-1, 50–51	83.30									1530		0.833	1.64	1.69	1.66	1.02
10H-1, 100–102	83.80	1.39	0.52	2.85	85.1	62.7	5.72	1.69		1534		0.772	1.60	1.70	1.65	1.03
10H-2, 52–54	84.82												1.77	2.53	2.12	1.20
10H-2, 100–102	85.30	1.44	0.58	2.23	84.0	59.8	5.26	1.49		1526			1.75	1.79	1.77	1.01
10H-3, 50–51	86.30									1535		0.872	1.82	1.86	1.84	1.01
10H-3, 100–102	86.80	1.38	0.55	2.62	81.2	60.3	4.33	1.52		1545		0.827	1.79	1.83	1.81	1.01
10H-4, 52–54	87.82									1542			1.78	1.83	1.80	1.01
10H-4, 100–102	88.30	1.40	0.54	2.27	83.5	61.1	5.06	1.57		1550			1.84	1.86	1.85	1.01
10H-5, 48–50	89.28									1552			2.21	2.47	2.34	1.06
10H-5, 100–102	89.80	1.44	0.59	2.57	82.9	59.0	4.84	1.44		1530			1.88	1.96	1.92	1.02
10H-6, 50–52	90.80									1544			2.05	2.18	2.11	1.03
10H-6, 100–102	91.30	1.43	0.61	2.65	80.3	57.5	4.07	1.34		1537			2.07	2.55	2.30	1.11
11H-1, 50–51	92.80											0.860	1.56	1.56	1.56	1.00
11H-1, 100–102	93.30	1.41	0.54	2.21	85.2	61.9	5.74	1.62		1468		0.869	1.65	1.77	1.71	1.04
11H-2, 50–52	94.30												1.67	1.73	1.70	1.02
11H-2, 100–102	94.80	1.40	0.54	2.46	83.6	61.2	5.11	1.58		1465			1.78	1.83	1.80	1.01
11H-3, 50–51	95.80									1539		0.829	1.66	1.70	1.68	1.01
11H-3, 100–102	96.30	1.42	0.54	2.54	85.8	61.9	6.06	1.61		1533		0.860	1.75	2.06	1.90	1.08
11H-4, 50–52	97.30												1.69	1.69	1.69	1.00
11H-4, 100–102	97.80	1.39	0.52	2.56	85.5	63.0	5.89	1.69		1530			1.71	1.77	1.74	1.02
11H-5, 50–51	98.80									1521		0.832	1.77	1.81	1.79	1.01
11H-5, 100–102	99.30	1.40	0.51	2.84	86.6	63.4	6.45	1.74		1524		0.843	1.79	2.29	2.02	1.13
11H-6, 50–52	100.30									1529			1.69	1.81	1.75	1.03
11H-6, 100–102	100.80	1.34	0.52	1.94	80.4	61.5	4.10	1.60		1543			1.77	1.83	1.80	1.02
12H-1, 50–51	102.30									1529		0.851	1.96	1.98	1.97	1.01
12H-1, 100–102	102.80	1.39	0.53	2.68	84.3	62.1	5.36	1.63		1532		0.818	2.22	2.28	2.25	1.01
12H-2, 50–52	103.80									1528			1.85	1.82	1.83	0.99
12H-2, 100–102	104.30	1.37	0.51	2.53	84.0	62.8	5.26	1.68		1522			1.72	1.73	1.72	1.00
12H-3, 50–51	105.30											0.851	1.71	1.71	1.71	1.00
12H-3, 100–102	105.80	1.39	0.50	2.49	86.8	64.0	6.59	1.79		1520		0.817	1.83	1.85	1.84	1.01
12H-4, 50–52	106.80									1439			1.88	2.38	2.12	1.13
12H-4, 100–102	107.30	1.50	0.68	2.69	80.4	54.9	4.10	1.22		1532			1.96	2.07	2.01	1.03
12H-5, 50–51	108.30									1529		0.840	1.65	1.69	1.67	1.01
12H-5, 100–102	108.80	1.34	0.49	2.43	83.1	63.5	4.93	1.73		1530		0.835	1.83	1.83	1.83	1.00
12H-6, 50–52	109.80									1535			1.85	1.84	1.84	1.00
12H-6, 100–102	110.30	1.41	0.55	2.31	83.3	60.5	5.00	1.54		1530			1.93	1.95	1.94	1.01
12H-7, 22–24	111.02	1.35	0.51	2.36	82.6	62.7	4.76	1.67		1543						
12H-7, 40–42	111.20									1542			1.96	1.93	1.94	0.99
13H-1, 50–51	111.80									1532		0.845	2.01	2.20	2.10	1.05
13H-1, 100–102	112.30	1.32	0.46	2.46	84.0	65.2	5.26	1.88		1538		0.773	2.00	2.16	2.08	1.04
13H-2, 50–52	113.30									1524			2.43	2.29	2.36	0.97
13H-2, 100–102	113.80	1.40	0.55	2.48	83.1	60.8	4.91	1.54		1529			2.29	2.12	2.20	0.96
13H-3, 50–51	114.80									1537		0.804	1.99	2.11	2.05	1.03
13H-3, 100–102	115.30	1.37	0.50	2.46	84.8	63.4	5.57	1.74		1532		0.852	2.02	2.00	2.01	1.00
13H-4, 50–52	116.30									1525			2.32	2.43	2.37	1.02
13H-4, 100–102	116.80	1.42	0.58	2.68	82.2	59.3	4.63	1.45		1520			2.77	2.57	2.67	0.96
13H-5, 50–51	117.80									1524		0.951	2.25	2.29	2.27	1.01
13H-5, 100–102	118.30	1.36	0.51	2.33	82.9	62.4	4.83	1.65		1524		0.863	1.95	2.01	1.98	1.02
13H-6, 50–51	119.30									1533		0.997	2.93	2.82	2.87	0.98

Table 11 (continued).

Core, section, interval (cm)	Depth (mbsf)	Densities: Wet bulk (g/cm³)	Densities: Dry bulk (g/cm³)	Densities: Grain (g/cm³)	Porosity (%)	Water content (%)	Void ratio	Water ratio	Velocity (m/s): A	Velocity (m/s): B*	Velocity (m/s): C	Thermal conductivity (W/m · K)	Formation factors: H	Formation factors: V	Formation factors: Mean	Anisotropy
127-794A- (Cont.)																
13H-6, 100-102	119.80	1.56	0.76	2.88	77.9	51.2	3.52	1.05		1527		1.007	2.25	2.17	2.21	0.98
13H-7, 20-22	120.50												2.62	2.66	2.64	1.01
13H-7, 38-40	120.68	1.47	0.62	2.37	83.0	57.8	4.90	1.38								
14H-1, 50-51	121.30									1535		0.870	1.69	1.79	1.74	1.03
14H-1, 100-102	121.80	1.51	0.71	2.54	78.0	52.9	3.55	1.13		1527		0.929	1.82	1.89	1.85	1.02
14H-2, 50-52	122.80									1541			1.76	1.88	1.82	1.03
14H-2, 100-102	123.30	1.49	0.69	2.67	78.5	54.0	3.65	1.17		1543			1.99	1.97	1.98	0.99
14H-3, 50-51	124.30									1536		0.905	1.65	1.73	1.69	1.02
14H-3, 100-102	124.80	1.44	0.61	2.68	81.0	57.6	4.28	1.35		1521		0.896	2.11	2.15	2.13	1.01
14H-4, 50-52	125.80									1524			1.83	1.79	1.81	0.99
14H-4, 100-102	126.30	1.56	0.82	2.74	71.9	47.2	2.56	0.90		1542			2.04	2.05	2.04	1.00
14H-5, 50-51	127.30									1536		0.996	2.19	2.33	2.26	1.03
14H-5, 100-102	127.80	1.40	0.58	2.55	80.2	58.7	4.06	1.42		1524		0.833	1.89	1.88	1.88	1.00
14H-6, 50-51	128.80									1546		0.922	2.71	2.54	2.62	0.97
14H-6, 100-102	129.30	1.51	0.69	2.76	80.1	54.3	4.03	1.19		1530		0.874	2.15	2.34	2.24	1.04
14H-7, 22-24	130.02	1.56	0.78	2.43	76.4	50.2	3.24	1.01		1540						
14H-7, 40-42	130.20									1533			2.11	2.23	2.17	1.03
15H-1, 50-51	130.80									1539		0.803	1.77	1.79	1.78	1.01
15H-1, 100-102	131.30	1.55	0.79	2.60	74.2	49.0	2.88	0.96		1547		0.912	2.62	2.69	2.65	1.01
15H-2, 50-52	132.30									1548			1.92	1.97	1.94	1.01
15H-2, 100-102	132.80	1.31	0.46	2.23	82.8	64.8	4.80	1.83		1540			1.77	1.82	1.79	1.01
15H-3, 50-51	133.80									1550		0.793	1.86	1.90	1.88	1.01
15H-3, 100-102	134.30	1.38	0.55	2.48	80.8	60.0	4.21	1.49		1548		0.793	2.19	2.20	2.19	1.00
15H-4, 50-52	135.30									1547			2.24	1.95	2.09	0.93
15H-4, 100-102	135.80	1.51	0.59	3.04	89.1	60.5	8.18	1.54		1549			2.14	2.20	2.17	1.01
15H-5, 50-51	136.80									1552		0.850	1.86	1.92	1.89	1.02
15H-5, 100-102	137.30	1.39	0.54	2.28	83.0	61.2	4.87	1.56		1556		0.808	1.98	1.98	1.98	1.00
15H-6, 40-42	138.20									1550			1.80	1.83	1.81	1.01
15H-6, 50-51	138.30									1547		0.834				
15H-6, 100-102	138.80	1.36	0.53	2.44	81.4	61.3	4.38	1.58		1556		0.803	1.80	2.67	2.19	1.22
15H-7, 60-62	139.90	1.36	0.50	2.83	84.1	63.4	5.30	1.71		1540						
16X-1, 50-51	140.30									1550		0.786	1.62	1.73	1.67	1.03
16X-1, 100-102	140.80	1.43	0.51	3.10	90.0	64.5	8.95	1.80				0.746	1.63	1.85	1.74	1.07
16X2, 50-51	141.80									1551		0.798				
16X-2, 100-102	142.30	1.44	0.55	2.99	86.8	61.8	6.56	1.61		1532		0.737				
16X-3, 50-51	143.30									1580		0.818				
16X-3, 100-102	143.80	1.36	0.46	2.08	87.6	66.0	7.08	1.94		1543		0.757				
16X-4, 50-51	144.80									1538		0.821				
16X-4, 100-102	145.30	1.34	0.47	2.51	85.3	65.2	5.79	1.86		1535		0.783				
16X-5, 50-51	146.30									1535		0.789				
16X-5, 100-102	146.80	1.40	0.47	2.49	90.3	66.1	9.30	1.95		1542		0.700				
16X-6, 50-51	147.80									1534		0.771				
16X-6, 100-102	148.30	1.40	0.44	2.88	94.0	68.8	15.60	2.21		1535		0.763				
17X-1, 100-102	150.50	1.33	0.55	2.45	76.1	58.6	3.18	1.42								
17X-2, 100-102	152.00	1.37	0.46	1.89	88.7	66.3	7.86	1.97								
17X-3, 100-102	153.50	1.39	0.48	2.71	88.8	65.5	7.93	1.90								
17X-4, 100-102	155.00	1.34	0.45	2.48	86.9	66.4	6.65	1.99								
17X-5, 100-102	156.50	1.37	0.48	2.04	86.7	64.8	6.52	1.84								
17X-6, 100-102	158.00	1.28	0.43	2.28	83.1	66.5	4.92	1.99								
17X-7, 30-32	158.80	1.37	0.48	2.98	86.8	64.9	6.56	1.85								
19X-1, 100-102	169.50	1.32	0.50	1.95	80.1	62.2	4.03	1.63								
19X-2, 100-102	171.00	1.41	0.52	2.23	87.2	63.4	6.80	1.72								
19X-3, 100-102	172.50	1.38	0.50	2.57	86.0	63.8	6.14	1.77								
19X-4, 100-102	174.00	1.37	0.48	2.34	87.0	65.1	6.68	1.86								
19X-5, 100-102	175.50	1.42	0.51	2.58	89.2	64.4	8.26	1.80								
20X-1, 100-102	179.20	1.32	0.48	1.69	82.2	63.8	4.63	1.77								
20X-2, 100-102	180.70	1.37	0.50	2.24	84.7	63.3	5.52	1.72								
20X-3, 100-102	182.20	1.43	0.56	2.79	85.2	61.0	5.76	1.55								
20X-4, 100-102	183.70	1.40	0.53	2.97	85.1	62.3	5.71	1.64								
20X-5, 100-102	185.20	1.36	0.48	2.48	85.4	64.3	5.84	1.81								
20X-6, 100-102	186.70	1.43	0.57	2.29	84.1	60.3	5.28	1.51								
20X-7, 30-32	187.50	1.43	0.52	2.67	88.6	63.5	7.73	1.75								
21X-1, 110-112	189.00	1.31	0.45	2.41	83.5	65.3	5.04	1.89								
21X-2, 110-112	190.50	1.38	0.52	2.61	83.8	62.2	5.16	1.65								
21X-3, 110-112	192.00	1.31	0.47	2.33	82.2	64.3	4.62	1.80								
21X-4, 110-112	193.50	1.30	0.50	2.29	78.0	61.5	3.55	1.60								
21X-5, 80-82	194.70	1.35	0.45	2.57	87.3	66.3	6.90	1.98								
22X-1, 110-112	198.60	1.32	0.48	2.11	82.4	64.0	4.68	1.76								
22X-2, 110-112	200.10	1.36	0.49	2.32	84.5	63.7	5.45	1.75								
22X-3, 110-112	201.60	1.33	0.46	2.35	85.5	65.9	5.88	1.91								
22X-4, 110-112	203.10	1.37	0.47	2.45	87.7	65.6	7.10	1.91								
22X-5, 110-112	204.60	1.27	0.46	2.30	79.0	63.7	3.76	1.74								
22X-6, 110-112	206.10	1.34	0.50	2.17	82.1	62.8	4.58	1.69								
23X-1, 100-102	208.20	1.37	0.49	2.30	86.0	64.3	6.16	1.80								
23X-2, 100-102	209.70	1.33	0.43	2.55	88.3	68.0	7.55	2.12								
23X-3, 100-102	211.20	1.37	0.49	2.51	85.3	63.8	5.82	1.77								
23X-4, 100-102	212.70	1.30	0.42	2.21	85.6	67.5	5.92	2.08								
23X-5, 100-102	214.20	1.27	0.41	1.99	84.3	68.0	5.37	2.12								
23X-6, 100-102	215.70	1.37	0.52	2.49	83.3	62.3	5.00	1.65								
25X-1, 100-102	227.50	1.27	0.38	2.36	87.2	70.3	6.81	2.37								
25X-2, 100-102	229.00	1.27	0.37	2.30	87.2	70.3	6.83	2.39								
25X-3, 100-102	230.50	1.27	0.39	2.38	85.7	69.1	5.98	2.25								
25X-4, 100-102	232.00	1.27	0.37	2.13	87.7	70.7	7.12	2.44								
25X-5, 34-36	232.84	1.89	1.28	2.91	59.9	32.5	1.50	0.48								
25X-5, 100-102	233.50	1.25	0.36	2.28	87.1	71.4	6.75	2.51								

Table 11 (continued).

Core, section, interval (cm)	Depth (mbsf)	Densities: Wet bulk (g/cm³)	Densities: Dry bulk (g/cm³)	Densities: Grain (g/cm³)	Porosity (%)	Water content (%)	Void ratio	Water ratio	Velocity (m/s): A	Velocity (m/s): B*	Velocity (m/s): C	Thermal conductivity (W/m · K)	Formation factors: H	Formation factors: V	Formation factors: Mean	Anisotropy
127-794A- (Cont.)																
26X-1, 100-102	237.20	1.35	0.42	2.54	90.6	68.8	9.69	2.22								
26X-2, 100-102	238.70	1.30	0.41	2.54	87.0	68.6	6.68	2.17								
26X-3, 100-102	240.20	1.26	0.39	2.48	85.2	69.3	5.77	2.24								
26X-4, 100-102	241.70	1.36	0.45	2.77	89.1	67.1	8.14	2.05								
26X-5, 100-102	243.20	1.30	0.40	2.01	87.9	69.3	7.29	2.28								
26X-6, 100-102	244.70	1.34	0.47	2.29	85.1	65.1	5.70	1.84								
27X-1, 100-102	247.00	1.26	0.37	2.27	86.2	70.1	6.25	2.37								
27X-2, 100-102	248.50	1.31	0.44	2.14	85.2	66.6	5.75	1.99								
27X-3, 100-102	250.00	1.30	0.40	2.43	88.4	69.7	7.64	2.27								
27X-4, 100-102	251.50	1.32	0.40	2.32	90.3	70.1	9.28	2.32								
27X-5, 100-102	253.00	1.35	0.43	2.79	89.9	68.2	8.86	2.15								
27X-6, 100-102	254.50	1.25	0.37	2.41	86.3	70.7	6.31	2.42								
28X-1, 100-102	256.70	1.32	0.42	2.42	87.4	67.8	6.96	2.13								
28X-2, 70-72	257.90	1.30	0.39	2.36	88.4	69.7	7.63	2.32								
29X-1, 80-82	266.20	1.34	0.45	2.23	86.9	66.4	6.66	2.00								
29X-2, 80-82	267.70	1.32	0.43	2.33	86.4	67.1	6.37	2.06								
29X-3, 50-51	268.90											0.776				
29X-3, 80-82	269.20	1.44	0.56	2.72	85.7	61.0	6.00	1.56								
29X-3, 94-95	269.34											0.853				
29X-4, 80-82	270.70	1.34	0.45	2.57	86.8	66.4	6.60	1.97								
29X-5, 50-51	271.90											0.774				
29X-5, 80-82	272.20	1.35	0.51	2.53	81.8	62.1	4.51	1.63								
29X-5, 100-101	272.40											0.766				
29X-6, 80-82	273.70	1.31	0.39	1.90	89.8	70.2	8.81	2.36								
30X-1, 100-102	276.10	1.28	0.41	2.49	85.7	68.6	5.97	2.16								
30X-2, 100-102	277.60	1.30	0.40	2.53	88.7	69.9	7.82	2.29								
30X-3, 100-102	279.10	1.38	0.51	2.20	84.6	62.8	5.50	1.69				0.790				
30X-4, 100-102	280.60	1.40	0.51	2.80	87.1	63.7	6.73	1.76								
30X-5, 65-66	281.75											0.767				
30X-5, 100-102	282.10	1.43	0.54	2.91	86.6	62.0	6.49	1.64								
31X-1, 100-102	285.60	1.32	0.44	2.29	86.0	66.7	6.16	2.00								
31X-2, 100-102	287.10	1.28	0.40	2.08	85.9	68.8	6.08	2.17								
31X-3, 50-51	288.10											0.788				
31X-3, 90-91	288.50											0.741				
31X-3, 100-102	288.60	1.33	0.42	2.76	88.8	68.4	7.93	2.15								
31X-4, 100-102	290.10	1.33	0.42	2.56	88.5	68.2	7.71	2.15								
31X-5, 40-41	291.00											0.830				
31X-5, 73-74	291.33											0.831				
31X-5, 100-102	291.60	1.36	0.44	2.86	89.4	67.3	8.47	2.07								
31X-6, 100-102	293.10	1.32	0.48	2.23	82.4	64.0	4.70	1.76								
32X-1, 100-102	294.50	1.37	0.54	2.61	80.5	60.2	4.12	1.52								
32X-2, 100-102	296.00	1.47	0.64	2.59	80.5	56.1	4.12	1.28								
32X-3, 50-51	297.00											0.973				
32X-3, 100-102	297.50	1.52	0.76	2.57	74.4	50.1	2.91	1.01				0.948				
33X-1, 100-102	304.30	1.50	0.72	2.70	75.8	51.8	3.13	1.07								
33X-2, 100-102	305.80	1.65	0.94	2.68	69.0	42.8	2.23	0.75								
33X-3, 50-51	306.80											1.058				
33X-3, 95-96	307.25											1.066				
33X-3, 100-102	307.30	1.64	0.88	2.80	74.3	46.4	2.89	0.87								
33X-4, 100-102	308.80	1.61	0.84	2.84	75.5	48.0	3.09	0.92								
33X-5, 100-102	310.30	1.72	0.97	2.78	72.9	43.4	2.69	0.77								
33X-6, 100-102	311.80	1.62	0.94	2.54	66.7	42.2	2.00	0.73								
33X-7, 30-32	312.60	1.67	0.92	2.65	73.2	44.9	2.73	0.81								
34X-1, 133-135	313.93	2.03	1.40	3.11	61.8	31.2	1.62	0.46								
34X-2, 105-107	315.15	1.72	1.00	2.77	70.4	41.9	2.38	0.72								
34X-CC, 17-19	315.77	1.71	0.98	2.64	71.6	42.9	2.53	0.75								
35X-1, 100-102	323.20	1.61	0.93	2.32	66.1	42.1	1.95	0.73								
35X-2, 100-102	324.70	1.68	0.98	2.58	68.1	41.5	2.14	0.71								
35X-3, 41-42	325.61											0.945				
35X-3, 100-102	326.20	1.66	0.95	2.51	69.0	42.6	2.23	0.74				0.886				
35X-4, 100-102	327.70	1.67	0.93	2.60	72.1	44.2	2.58	0.79								
35X-5, 100-102	329.20	1.59	0.85	2.52	72.3	46.6	2.61	0.87								
35X-6, 63-64	330.33											0.964				
35X-6, 100-102	330.70	1.56	0.84	2.51	69.9	45.9	2.32	0.85								
35X-6, 108-109	330.78											0.973				
35X-7, 20-22	331.40	1.56	0.80	2.64	74.5	48.9	2.92	0.96								
36X-1, 100-102	332.90	1.42	0.62	2.72	77.6	56.0	3.47	1.28								
36X-2, 100-102	334.40	1.51	0.77	2.51	72.5	49.2	2.64	0.97								
36X-3, 69-70	335.59											0.900				
36X-3, 100-102	335.90	1.56	0.86	2.49	68.7	45.1	2.19	0.82								
36X-4, 51-52	336.91											0.810				
36X-4, 100-102	337.40	1.63	0.92	2.46	69.0	43.4	2.22	0.76								
36X-5, 24-25	338.14											0.893				
36X-5, 54-56	338.44	1.65	0.94	2.68	69.4	43.1	2.26	0.76				0.982				
37X-1, 100-102	342.60	1.52	0.73	2.66	76.9	51.8	3.33	1.08								
37X-2, 50-51	343.60											0.932				
37X-2, 100-102	344.10	1.56	0.80	2.43	74.5	48.9	2.92	0.96				0.962				
37X-3, 50-51	345.10											0.976				
37X-3, 85-86	345.45											0.979				
37X-3, 100-102	345.60	1.53	0.72	2.87	79.4	53.2	3.86	1.14								
37X-4, 15-16	346.25											1.016				
127-794B-																
1R-1, 100-102	155.40	1.30	0.42	2.29	85.6	67.5	5.92	2.09								
1R-2, 100-102	156.90	1.30	0.42	2.32	86.0	67.8	6.15	2.09								

Table 11 (continued).

Core, section, interval (cm)	Depth (mbsf)	Densities: Wet bulk (g/cm³)	Densities: Dry bulk (g/cm³)	Densities: Grain (g/cm³)	Porosity (%)	Water content (%)	Void ratio	Water ratio	Velocity (m/s): A	Velocity (m/s): B*	Velocity (m/s): C	Thermal conductivity (W/m · K)	Formation factors: H	Formation factors: V	Formation factors: Mean	Anisotropy
127-794B- (Cont.)																
1R-3, 50–52	157.90	1.28	0.39	2.39	87.4	70.0	6.91	2.30								
2R-1, 48–50	164.48	2.89	2.59	3.10	29.5	10.5	0.42	0.12	4460	4539	4649					
2R-1, 100–102	165.00	1.32	0.47	2.36	83.3	64.7	4.99	1.81								
3R-1, 103–105	213.23	1.34	0.48	2.53	84.4	64.5	5.40	1.81								
3R-2, 100–102	214.70	1.32	0.45	2.36	84.6	65.7	5.51	1.93								
3R-3, 100–102	216.20	1.32	0.43	2.38	86.8	67.4	6.59	2.08								
3R-4, 100–102	217.70	1.29	0.39	2.22	87.2	69.3	6.82	2.28								
4R-1, 100–102	222.90	1.31	0.42	2.46	87.1	68.1	6.77	2.15								
5R-1, 100–102	339.30	1.58	0.87	2.43	69.7	45.2	2.30	0.82								
5R-2, 100–102	340.80	1.58	0.84	2.50	72.5	47.0	2.63	0.88								
5R-2, 115–117	340.95								3002	3286						
5R-3, 100–102	342.30	1.70	0.97	2.66	71.0	42.8	2.45	0.75								
9R-1, 11–13	376.11	1.98	1.54	2.29	42.6	22.0	0.74	0.28	2071	2224						
10R-1, 120–122	386.80	1.66	0.97	2.77	67.5	41.7	2.08	0.71								
10R-2, 67–69	387.77	1.95	1.22	3.39	71.5	37.6	2.51	0.60								
11R-1, 59–61	395.79	1.84	1.24	2.88	58.9	32.8	1.43	0.49								
11R-CC, 3–5	395.93								2023	2176	2172					
12R-1, 100–102	405.90	1.74	1.09	2.72	63.6	37.4	1.75	0.60								
12R-1, 110–112	406.00	1.88	1.38	2.53	48.9	26.6	0.96	0.36	1890	1999	1982					
12R-2, 110–112	407.50	1.84	1.31	2.61	51.7	28.8	1.07	0.41	1739	1797	1786					
13R-1, 117–119	415.67	1.90	1.42	2.62	46.7	25.2	0.87	0.34		1975	1941					
13R-2, 86–88	416.86	2.07	1.58	2.72	48.4	24.0	0.94	0.31	1936	2047	2075					
13R-3, 60–62	418.10	2.37	2.01	2.86	35.5	15.3	0.55	0.18	2202	2136	2084					
14R-1, 87–89	425.07	1.90	1.36	2.73	52.2	28.1	1.09	0.39	1963	2094	2130					
14R-2, 93–95	426.63	1.89	1.27	2.74	60.6	32.8	1.54	0.49	1863	1960	1929					
15R-1, 64–66	434.44	1.98	1.53	2.52	43.5	22.5	0.77	0.29	2304	2425	2410					
15R-2, 108–110	436.38	2.04	1.62	2.53	41.0	20.6	0.69	0.26	2220	2400	2380					
16R-1, 64–66	443.84	1.86	1.33	2.67	51.5	28.4	1.06	0.40	1849	1942	1934					
16R-2, 102–104	445.74	1.90	1.32	2.55	56.2	30.3	1.28	0.43	1846	1978	2014					
16R-3, 67–69	446.87	2.52	2.30	2.71	21.9	8.9	0.28	0.10	3126	3456	3584					
17R-1, 68–70	453.58	1.81	1.24	2.61	56.0	31.7	1.27	0.46								
18R-1, 50–51	463.10											1.303				
18R-1, 74–76	463.34	1.76	1.15	2.56	59.2	34.5	1.45	0.53	1606	1639	1645					
18R-1, 98–99	463.58											1.076				
18R-3, 55–56	466.15											1.223				
18R-3, 100–101	466.60											1.248				
18R-5, 43–44	469.03											1.133				
18R-5, 103–104	469.63											1.218				
19R-1, 51–52	472.81											1.309				
19R-1, 99–101	473.29	1.92	1.37	2.62	53.4	28.5	1.15	0.40	1731	1752	1760					
19R-1, 116–117	473.46											1.163				
19R-2, 95–97	474.75	2.00	1.46	2.71	52.4	26.8	1.10	0.37	1811	1898	1911					
19R-3, 28–30	475.58	2.15	1.67	2.65	46.7	22.3	0.88	0.29	2005	2132	2108					
19R-3, 33–34	475.63											1.410				
19R-3, 113–114	476.43											1.103				
20R-1, 48–50	482.48	1.82	1.24	2.64	56.2	31.6	1.28	0.46	1707	1770	1756					
20R-1, 55–56	482.55											0.896				
20R-1, 95–100	482.95											1.075				
20R-1, 108–109	483.08											0.822				
20R-3, 32–34	485.32	1.94	1.42	2.54	50.6	26.7	1.02	0.37	1765	1876	1863					
20R-3, 50–51	485.50											1.075				
20R-3, 103–104	486.03											1.157				
21R-1, 74–75	492.44											0.943				
21R-1, 100–102	492.70	1.54	0.71	2.83	80.8	53.8	4.20	1.17	1748	1777	1766					
21R-2, 102–104	494.22	1.54	0.78	2.63	74.7	49.7	2.95	0.98	1726	1781	1771					
21R-3, 38–39	495.08											1.039				
21R-3, 72–74	495.42								1763	1783	1773					
21R-3, 98–100	495.68	1.65	0.89	2.75	74.0	45.9	2.84	0.85				1.068				
21R-4, 98–100	497.18								1749	1807	1814					
21R-4, 98–100	497.18								1742	1765	1768					
21R-5, 35–36	498.05											1.405				
21R-5, 64–65	498.34											1.038				
21R-5, 107–109	498.77	1.55	0.77	2.56	75.9	50.2	3.16	1.01								
21R-5, 127–128	498.97											1.109				
21R-7, 49–50	501.19											1.091				
22R-1, 52–54	501.72	1.73	1.05	2.86	67.0	39.7	2.03	0.66	1816	1840	1837					
23R-1, 44–46	511.34	1.89	1.30	2.77	57.8	31.3	1.37	0.46	1951	1941	1963					
24R-1, 95–97	521.55	1.93	1.39	2.91	52.9	28.1	1.12	0.39								
24R-3, 70–72	524.30	1.60	0.86	2.77	72.5	46.4	2.64	0.87	1698	1763	1730					
24R-3, 84–86	524.44	1.68	0.93	2.82	72.8	44.4	2.67	0.80		1766	1759					
24R-3, 103–113	524.63											0.986				
24R-4, 110–122	526.20											1.214				
24R-4, 138–140	526.48	1.82	1.20	2.74	60.4	34.0	1.52	0.52	1689	1736	1737					
24R-5, 92–94	527.52	2.16	1.58	2.99	56.8	26.9	1.32	0.37								
25R-1, 14–16	530.44	1.85	1.22	2.92	61.4	34.0	1.59	0.51								
26R-1, 113–115	541.13	2.06	1.58	2.78	46.7	23.2	0.88	0.30	1766	1792	1819					
26R-1, 136–143	541.36											1.304				
26R-2, 91–93	542.41	2.23	1.82	2.67	39.7	18.2	0.66	0.22	2384	2602	2591	1.298				
26R-2, 98–100	542.48	2.49	2.31	2.71	17.7	7.3	0.22	0.08			4070					
26R-CC, 17–19	542.74	2.55	2.43	2.71	12.0	4.8	0.14	0.05			4529	1.480				
26R-CC, 17–19	542.74										4471					
27R-1, 10–20	544.40											1.570				
27R-1, 48–50	544.78	2.62	2.53	2.72	9.2	3.6	0.10	0.04			4588					
27R-1, 48–50	544.78										4603					

Table 11 (continued).

Core, section, interval (cm)	Depth (mbsf)	Densities: Wet bulk (g/cm³)	Densities: Dry bulk (g/cm³)	Densities: Grain (g/cm³)	Porosity (%)	Water content (%)	Void ratio	Water ratio	Velocity (m/s): A	Velocity (m/s): B*	Velocity (m/s): C	Thermal conductivity (W/m · K)	Formation factors: H	Formation factors: V	Formation factors: Mean	Anisotropy
127-794C-																
1R-1, 48–50	560.28	2.64	2.54	2.74	9.9	3.8	0.11	0.04			4695	1.352				
2R-1, 76–78	564.76	2.63	2.53	2.76	9.5	3.7	0.10	0.04			4737	1.465				
3R-1, 122–125	573.22	2.69	2.61	2.77	7.6	2.9	0.08	0.03			5145	1.518				
4R-1, 44–46	581.94	2.71	2.64	2.77	6.5	2.4	0.07	0.03			5186	1.530				
4R-2, 6–8	583.02	2.72	2.65	2.78	6.9	2.6	0.07	0.03			5215	1.555				
4R-2, 93–95	583.89										5078					
4R-2, 93–95	583.89										5121					
4R-3, 7–9	584.53	2.72	2.64	2.79	7.4	2.8	0.08	0.03			5086	1.528				
4R-3, 88–90	585.34										4710					
4R-4, 3–5	585.92	2.65	2.55	2.79	9.7	3.8	0.11	0.04			4880					
4R-4, 24–31	586.13											1.479				
5R-1, 72–74	586.72	2.53	2.37	2.73	15.4	6.3	0.18	0.07			4199					
5R-2, 88–90	588.21	2.58	2.44	2.77	13.4	5.3	0.15	0.06			4238	1.291				
5R-2, 88–90	588.21										4380					
6R-1, 37–39	592.07	2.55	2.43	2.73	12.1	4.9	0.14	0.05			4291	1.411				
7R-1, 46–48	601.36	2.47	2.28	2.74	18.7	7.7	0.23	0.08			3878					
7R-1, 46–48	601.36										3963					
7R-1, 116–127	602.06											1.379				
7R-2, 11–13	602.29	2.46	2.25	2.76	20.6	8.5	0.26	0.09			3917					
8R-1, 2–4	605.12	2.56	2.41	2.76	14.4	5.7	0.17	0.06			4196	1.423				
9R-1, 131–133	615.91	2.48	2.29	2.73	18.2	7.5	0.22	0.08			3881	1.350				
10R-1, 120–122	624.00	2.54	2.37	2.77	16.2	6.5	0.19	0.07			4040	1.311				
10R-2, 102–104	625.32	2.56	2.39	2.77	16.1	6.5	0.19	0.07			4140					
11R-1, 50–52	627.80	2.57	2.42	2.79	14.2	5.7	0.17	0.06			4160	1.423				
11R-2, 52–54	628.95	2.55	2.39	2.77	16.0	6.5	0.19	0.07			4191					
12R-1, 25–27	634.55	2.48	2.30	2.73	17.7	7.3	0.21	0.08			3878					
12R-1, 104–106	635.34	2.52	2.32	2.79	19.0	7.7	0.23	0.08			3665					
12R-2, 132–134	637.06	2.57	2.38	2.82	19.0	7.6	0.23	0.08			3317	1.447				
12R-3, 71–73	637.89	2.52	2.31	2.81	20.7	8.4	0.26	0.09			3819					
12R-4, 85–88	639.53	2.60	2.44	2.81	15.3	6.0	0.18	0.06			4008	1.399				
12R-5, 138–141	641.58	2.54	2.35	2.78	18.2	7.3	0.22	0.08			3680					
12R-6, 130–132	642.96	2.46	2.27	2.72	19.0	7.9	0.23	0.09			3895	1.379				
12R-7, 17–19	643.21	2.44	2.23	2.73	20.1	8.4	0.25	0.09			3525					
13R-1, 21–23	643.91	2.47	2.30	2.67	17.0	7.1	0.20	0.08			3759	1.469				
13R-1, 110–112	644.80	2.19	1.80	2.67	38.0	17.8	0.61	0.22	2397	2592	2614					
13R-2, 5–7	645.25	2.14	1.78	2.65	35.1	16.8	0.54	0.20			2539	1.469				
13R-2, 91–93	646.11	2.50	2.34	2.70	15.5	6.4	0.18	0.07			3509	1.457				

the sediment section. The bulk density, on the other hand, is slightly decreasing or constant above the opal-A/opal-CT boundary. The velocity is a function of the moduli (strengths) of the material and of the inverse of the density as:

$$V^2 = (k + 4\mu/3)/\rho_B \quad (1)$$

where V is the acoustic velocity, k is the bulk modulus, μ is the shear modulus, and ρ_B is the wet-bulk density. For constant moduli, the velocity will increase as the density decreases. Normally, however, the moduli decrease more rapidly than the density, so that the velocity decreases as the density decreases. In this case, we believe that the increase in diatom content with depth may explain the unusual trends observed in the upper 300 m of sediment at Site 794. Diatoms have a relatively open cellular structure, as seen in Figure 46 (Koizumi, pers. comm., from Schrader and Schuette, 1981), and thus can possess significant intraparticle porosity while maintaining grain-to-grain contact. This in part may explain the higher velocity paradoxically coupled with lower density in the sediment section above the opal-A/opal-CT boundary.

The velocity profile has a small discontinuity at the opal-A/opal-CT boundary, where diatoms cease to be present in significant numbers. Below this boundary, the variability in the velocity increases markedly, possibly indicative of alternating harder (more consolidated) and softer (less consolidated) layers (see also "Downhole Measurements" section, this chapter).

The formation factor measurements taken in the upper 140 m of the sediment section show great variability (Fig. 47A), and the data might have greater scatter than might normally be the case because of problems with the seawater reference as described earlier. The degree of anisotropy, as defined in the "Explanatory Notes" chapter (this volume), is an expression of the degree to which grains and minerals are aligned parallel to the bedding. The highest anisotropy occurs where readings were taken across ash layers or distinct sequences of thin beds (Fig. 47B).

Detailed Unit Correlation

The mean, standard deviation, maximum, and minimum values for each of the physical properties of each unit are listed in Tables 12 through 17. The standard deviation, in particular, is representative of the degree of variability in the physical properties of a given unit.

Unit IA (0–63.8 mbsf, Holocene to Pleistocene; Table 12) is characterized by highly variable physical properties. The porosity and water content decrease slightly, on average, and the wet- and dry-bulk densities increase with depth. A number of ash layers occur and can be discerned as peaks in the index properties and PWL velocity (Figs. 43 and 45).

In Unit IB (63.8–92.3 mbsf, Pleistocene to Pliocene), the wet- and dry-bulk densities, the grain density, and the thermal conductivity continue to decrease, and the porosity and water content rise, but the variability is markedly lower, and the standard deviations are correspondingly less (Table 12). A general trend of increasing diatom content with depth begins in this unit, along with the associated changes in the physical properties.

Unit IIA (92.3–216.9 mbsf, Pliocene to late Miocene) is a diatomaceous ooze. The bulk densities, thermal conductivity, po-

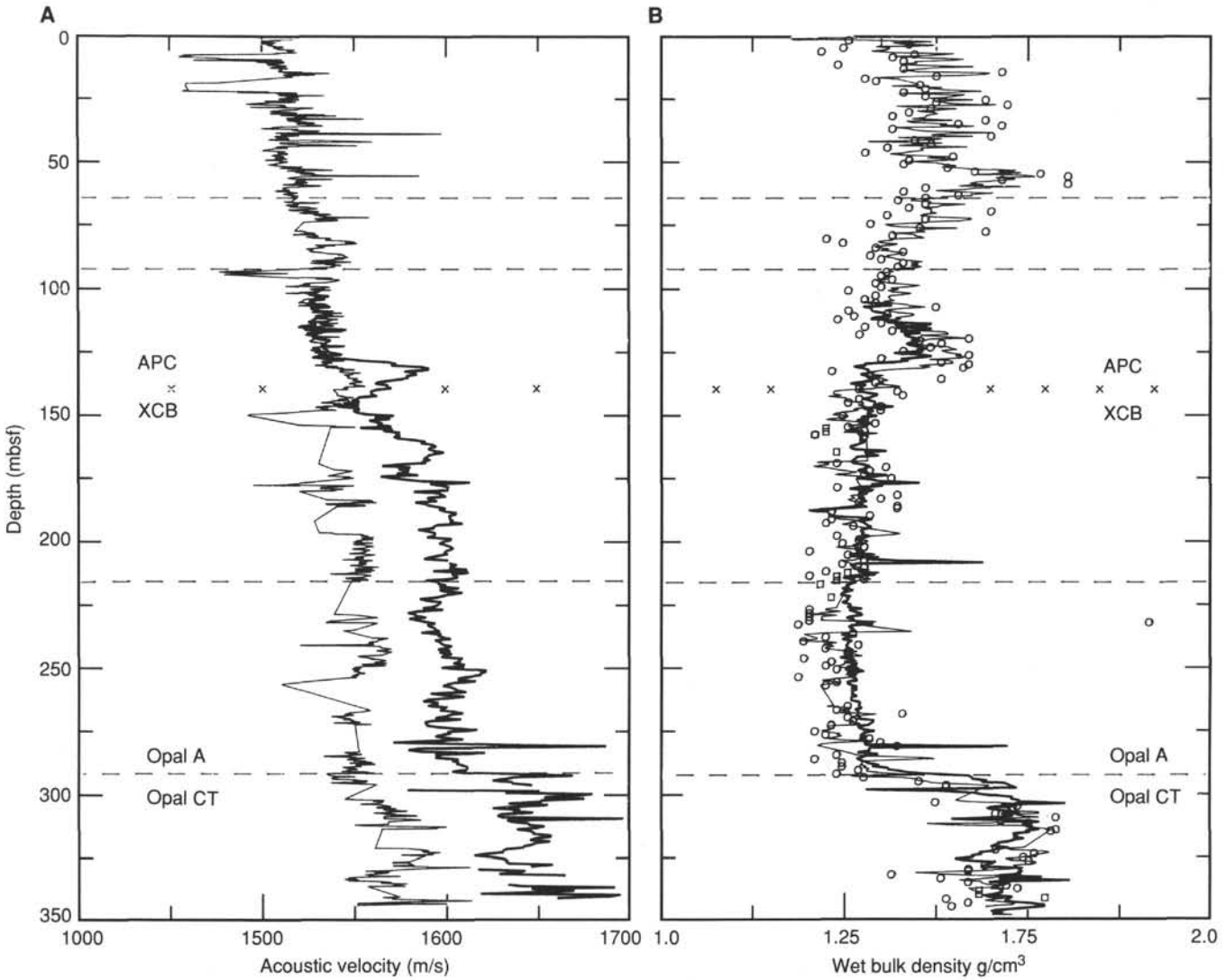

Figure 43. **A.** Comparison of the *P*-wave logger (PWL) velocity (thin curve on left) with sonic log acoustic velocity (thick curve on right) vs. depth in Hole 794A. The two data sets are in good agreement in the APC-cored interval, but depart significantly in the lower APC and in the XCB-cored sections, i.e., below about 140 mbsf. The PWL velocity does not change at the opal-A/opal CT boundary, while the sonic velocity does. The horizontal dashed lines delineate the unit and subunit boundaries, and the "X" line demarcates the change from APC to XCB coring. **B.** Comparison of the wet-bulk density (open circles), GRAPE density (light curve), and lithodensity log density (thick curve), in the APC-and XCB-cored intervals as in **A** for Holes 794A and 794B. Note the good agreement, even in the XCB-cored intervals, indicating that the GRAPE and index properties are less affected by XCB disturbance. The unit and subunit boundaries and the APC/XCB changeover are marked as in **A**.

rosity, and water content are surprisingly uniform throughout this unit. Porosities and water contents are anomalously high, and the bulk and grain densities are low for these depths of burial (Table 13). The grain density has some significant variability, but the lowest grain densities, representative of almost pure diatomaceous ooze, occur in this unit. As an example, Sample 127-794A-20X-1, 100–102 cm, is almost entirely composed of diatoms. The trend in the physical properties throughout this unit suggests increasing diatom content.

The minimum average densities and maximum average porosity and water content are reached in Unit IIB (216.9–293.5 mbsf, late Miocene), a diatomaceous clay (Table 13). These minimum values may, however, be an artifact of the XCB coring. The trends in the physical properties observed in the higher stratigraphic units culminate in this unit, but the variability is somewhat higher than in Units IB and IIA. The base of Unit IIB is marked by the opal-A/opal-CT boundary, a significant lithologic, chemical, and physical transition.

Below the opal-A/opal-CT boundary, in Unit IIIA (293.5–351.3 mbsf in Hole 794A, late Miocene), the porosity and water content are much lower than in the overlying units, and the densities and thermal conductivity are higher (Table 14). The increase in grain density, in particular, reflects the loss of the diatoms. The thermal conductivity and acoustic velocity increase steadily through the unit. This trend continues into Unit IIIB (347.8–491.7 mbsf in Hole 794B, late to middle Miocene), as shown in Figure 45.

Unit IV (491.7–520.6 mbsf, middle Miocene) is a tuff, with markedly higher porosity and water content, and lower bulk densities and acoustic velocity (Table 15). There is, however, a trend across Unit IV and into Unit V of decreasing porosity and water content, and an associated increase in bulk densities and acoustic velocity.

Unit V (520.6–542.5 mbsf, middle Miocene) is a basal claystone unit. The minimum water content and porosity, and the associated maximum acoustic velocity and bulk densities (Table

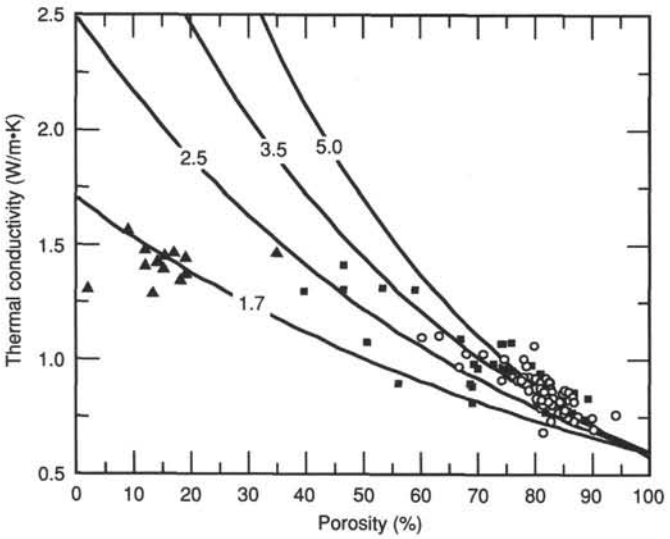

Figure 44. Thermal conductivity vs. porosity for Site 794. The open circles are for Hole 794A, the squares for Hole 794B, and the solid triangles are the data from the igneous units. The thermal conductivity of water at 23°C is taken to be 0.597 W/m · K. Note the high grain density required to obtain a fit between the model curves and the higher porosity data. Calcite has a grain thermal conductivity of about 5 W/m · K.

16) occur at the very base of the unit and are consistent with the presence of a contact with the underlying igneous sill.

The deepest sedimentary unit encountered at Site 794, Unit VI (644.15–645.8 mbsf), lies between two igneous units, a dolerite above and a basalt below. The unit is thin, and the amount of data is small, but the index properties and velocity are consistent with a moderately consolidated sedimentary sequence (Table 17).

Basement Rocks

General Features and Trends

The physical properties of the igneous rocks from Holes 794B and 794C are quite variable with depth, and apparently correlate with the degree of alteration (see "Basement Rocks" section, this chapter). The grain density is the exception, varying little about a mean value of about 2.75 g/cm^3, though there are subtle but distinct changes in the grain density in a few units. The porosity and acoustic velocity (Fig. 48A), and the wet-bulk density and thermal conductivity (Fig. 48B) illustrate the general features that are typical of the physical properties in the igneous units. The porosity decreases and the other properties correspondingly increase toward the center of Unit II, where the degree of alteration is lowest. Units III, IV, and V show some variability as the rock varies from coarse- to fine-grained, and the degree of alteration varies. The highly altered igneous rocks have an average thermal conductivity of 1.44 W/m/K. This compares with a mean thermal conductivity of 1.66 W/m/K for a suite of less-altered oceanic basalts from the flanks of the Mid-Atlantic Ridge (Hyndman et al., 1977).

The acoustic velocity depends in a regular fashion on the porosity (Fig. 49). The grain velocities vary from about 6400 m/s for the relatively unaltered rock to about 5500 m/s (or less) for the more altered samples, when the data are compared with model curves computed using the Wyllie et al. (1956) time average equation. The time-average model is approximately valid for materials of low porosity (less than about 30%).

Detailed Unit Correlation

The number of data points in the igneous units is small, and the standard deviation is not presented. Instead, only the minimum and maximum physical property values are listed in Table 18 to show the scatter in the data. The units are identical with those of basement rocks.

Unit I (524.5 to approx. 555 mbsf) is the basal unit found in Hole 794B, and is characterized by relatively high porosity and water content and low bulk densities and acoustic velocity (Table 18). The bulk densities, thermal conductivity, and acoustic velocity increase, and the porosity and water content decrease with depth. The grain density is slightly less in Unit I than in the underlying units.

The porosity and water content continue to decrease, and the velocity and bulk densities continue to increase in Unit II (approx. 555–592.7 mbsf) (Table 18). The lowest water content and porosity, and the highest bulk densities, velocity, and thermal conductivity occur near the central, less altered portion of Unit II. The values change significantly in the lower portion of the unit just above the boundary with Unit III. The water content and porosity sharply increase, with associated decreases in the bulk densities, the velocity, and the thermal conductivity.

Units III, IV, and V, on the other hand, are more variable, fractured, porous, and altered than Unit II (see "Basement Rocks" section, this chapter), which is reflected in the physical properties (Fig. 48 and Table 18). Unit VI occurs at the bottom of Hole 794C and cannot be adequately characterized on the basis of one sample. The properties of that one sample, however, are similar to those for the relatively porous units above.

Summary

The physical properties correlate very well with the lithologic units. We observed increases in water content, decreases in bulk densities, and a decrease in grain density in the upper two lithostratigraphic units. These correspond to an increase in diatom content. There is an abrupt change in all physical properties at the opal-A/opal-CT boundary. The physical properties are variable in the lower lithostratigraphic units of the sedimentary section, but a general decrease in water content and an increase in bulk density, acoustic velocity, and thermal conductivity with depth is present. The physical properties in the igneous units correlate well with the degree of alteration and the presence of significant porosity.

DOWNHOLE MEASUREMENTS

Operations

Downhole measurements were made in two of the three holes drilled at Site 794. In Hole 794A, 13 measurements of temperature ahead of the bit were attempted using the Barnes/Uyeda instrument. In Hole 794B, a complete suite of logs were run. Hole 794C was abandoned prematurely due to a stuck drill pipe; none of the planned logs or packer/hydrofracture experiments were run in this hole.

Temperature Measurements

Eight of the downhole temperature runs yielded accurate and valid temperatures, and data from two runs indicate a slight disturbance to the probe while in the sediment. The two deepest runs (12 and 13) showed evidence of strong disturbance. The temperatures in the sediment for the two deepest runs are judged not to be representative of formation temperatures. The virgin formation temperatures for all of the runs for which valid data were obtained are shown in Table 19 and plotted vs. depth in Figure 50. The data describe a nearly uniform increase of temperature with depth, with a best-fit gradient of 125°C/km.

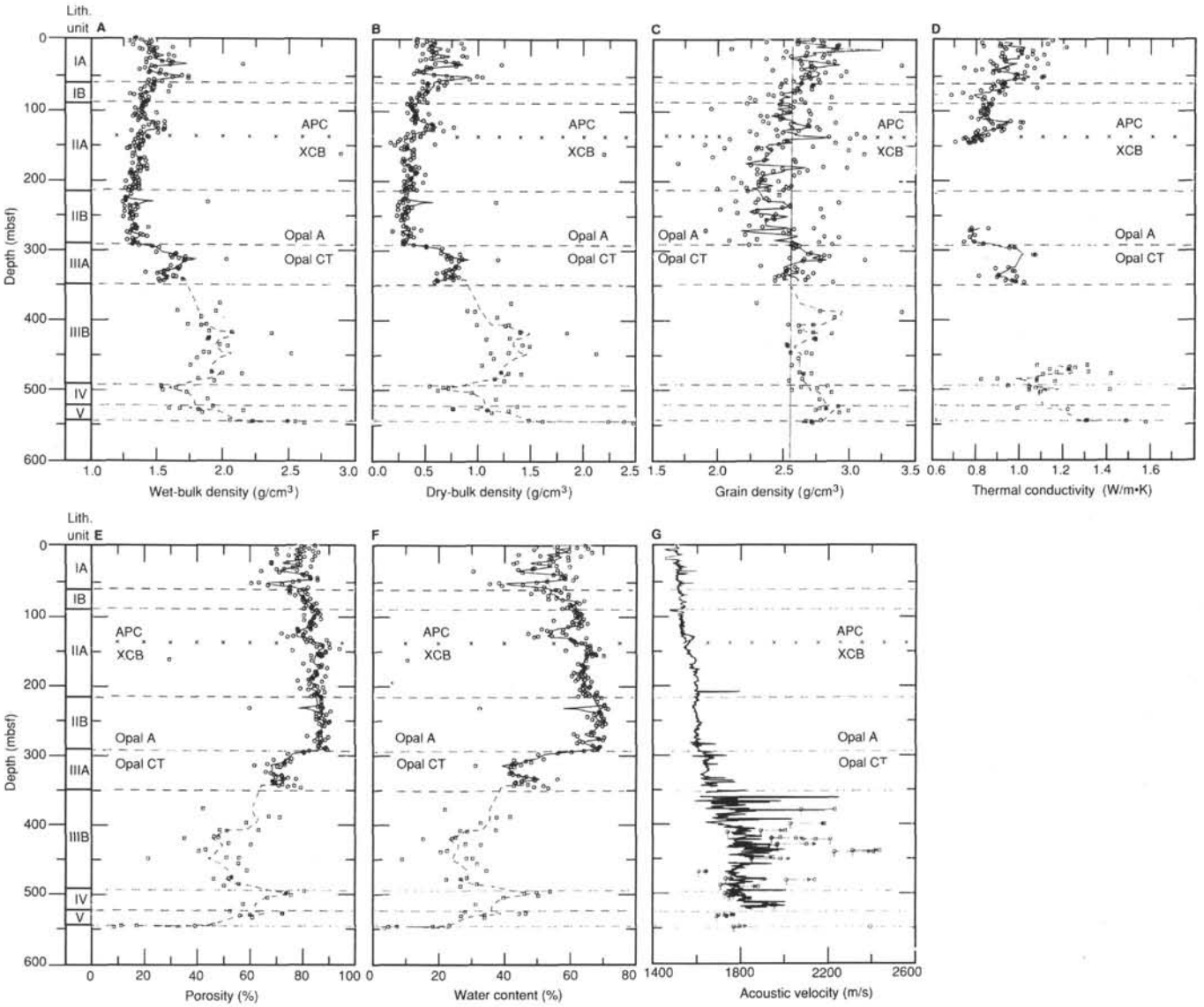

Figure 45. Density and thermal conductivity vs. depth for Holes 794A (open circles and solid curve) and 794B (open squares and dashed curve). The curves represent the five-point tapered running mean. Note the close correspondence between the lithostratigraphic units and the physical property variations. **A.** Wet-bulk density. **B.** Dry-bulk density. The dry-bulk density is the salt-corrected dry weight divided by the wet volume. It is a measure of the solid content of the wet sample. **C.** Grain density. The vertical solid line represents the average grain density for the sedimentary section, 2.55 g/cm^3. **D.** Thermal conductivity. The opal-A/opal-CT boundary and the top of the basement sill are marked. Individual measurements are shown as open circles, and the solid curve is the five-point running mean. **E.** Porosity. **F.** Water content. **G.** Acoustic velocity. The PWL velocity is used for APC cores (thin line), and the sonic log velocity is used in the XCB-cored intervals (thick line). The Hamilton Frame velocities are shown as open circle and vertical tick mark, open square, and open triangle directions. The lines denote the range of velocity values for a given sample. Note the variability in Unit IIIB.

The virgin formation temperatures were estimated by extrapolating the temperature history after penetration to equilibrium using plots of temperature vs. 1/time. Most of the valid histories show that the probes are close to equilibrium at the end of the 20-min observation period (see Figs. 51 and 52). The temperatures measured during the two deepest runs yielded values that are much lower than expected if the temperature-depth profile shown in Figure 52 is extrapolated downward. We think that these measurements are contaminated by cold water that penetrates down to the tip of the probe along fractures that were opened when the probe was forced into the semi-consolidated sediments found at this depth.

A feature that appears on all runs (illustrated by the run shown in Fig. 51) is that the temperatures recorded while holding the probe at the seafloor after pullout are higher than during the wait at the mud line before penetration. The temperatures at the seafloor before penetration are 0.02°C. This value agrees well with hydrographic measurements of deep-water temperatures measured in the Japan sea. We were able to demonstrate by pumping water down the pipe while holding the probe at mud line that the higher temperatures after penetration are caused by warmer water in the sub-bottom part of the hole being drawn up the drill pipe as the core barrel containing the probe is retrieved. The significance of this result for future measurements is that the current practice of holding the probe at the mud line after penetration does not provide an accurate *in-situ* calibration of the probe; however, it does provide a useful check of proper instrument operation.

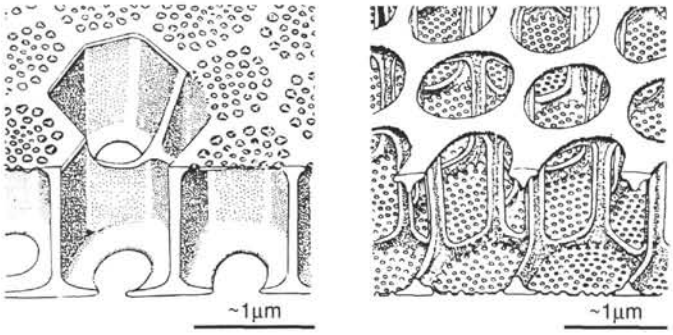

Figure 46. Schematic picture of the frustule structure of two diatom species: *Coscinodiscaceae* (left) and *Thalassiosiraceae* (right). Note the high volume of pore space. The 1-µm scale is approximate (Koizumi, pers. comm., from Schrader and Schuette, 1981, Fig. 2).

Thermal conductivity measurements were made on cores from all of the holes at Site 794 using the needle probe technique (Von Herzen and Maxwell, 1959) in unconsolidated and semi-consolidated sediments, and the "half-space" technique for indurated sediments and igneous rock samples. These measurements are presented in more detail in the "Physical Properties" section (this chapter). For estimating the heat flow associated with the thermal gradient measured in Hole 794A, the conductivity measurements were corrected to *in-situ* conditions using the Ratcliffe (1960) relations. Figure 53 shows *in-situ* conductivity vs. depth.

In-situ conductivity measurements provide a determination of the thermal resistance of the section between the seafloor and the depth of each temperature measurement (Table 19). A plot of virgin formation temperatures vs. thermal resistance is shown in Figure 54. The slope $\Delta T/\Delta R$ of the linear regression to the data points equals the heat flow through the upper 300 m of sediment if the thermal regime is conductive. The slope of the line shown in Figure 54 indicates a heat flow of 103 mW/m^2. Nearly all of the error associated with this heat-flow determination is due to uncertainties in the thermal conductivity values (± 5%). This value is in accord with earlier seafloor heat-flow measurements reported by Yasui and Watanabe (1965), Yasui et al. (1968), Yamano et al. (1987), and Yamano and Uyeda (1988), as well as the mean heat flow from the Yamato Basin of 98 mW/m^2 (Tamaki, 1986).

The thermal conductivity measurements in the sedimentary and igneous section below 300 m and the heat-flow values allow temperatures at deeper, unsampled levels of the section to be estimated by extrapolation. On this basis, estimated temperatures downsection are as follows: at the opal-CT boundary, 36°C; at the transition to quartz, 46°–47°C; at the top of dolerite sill, 60°C; and at the deepest level reached, 67°C. The temperature gradient in basement is about 71°C/km.

The uniformity of heat flow with depth (Fig. 54) indicates that heat transport through the sediment is purely conductive. There is no discernible contribution to the seafloor heat flow by

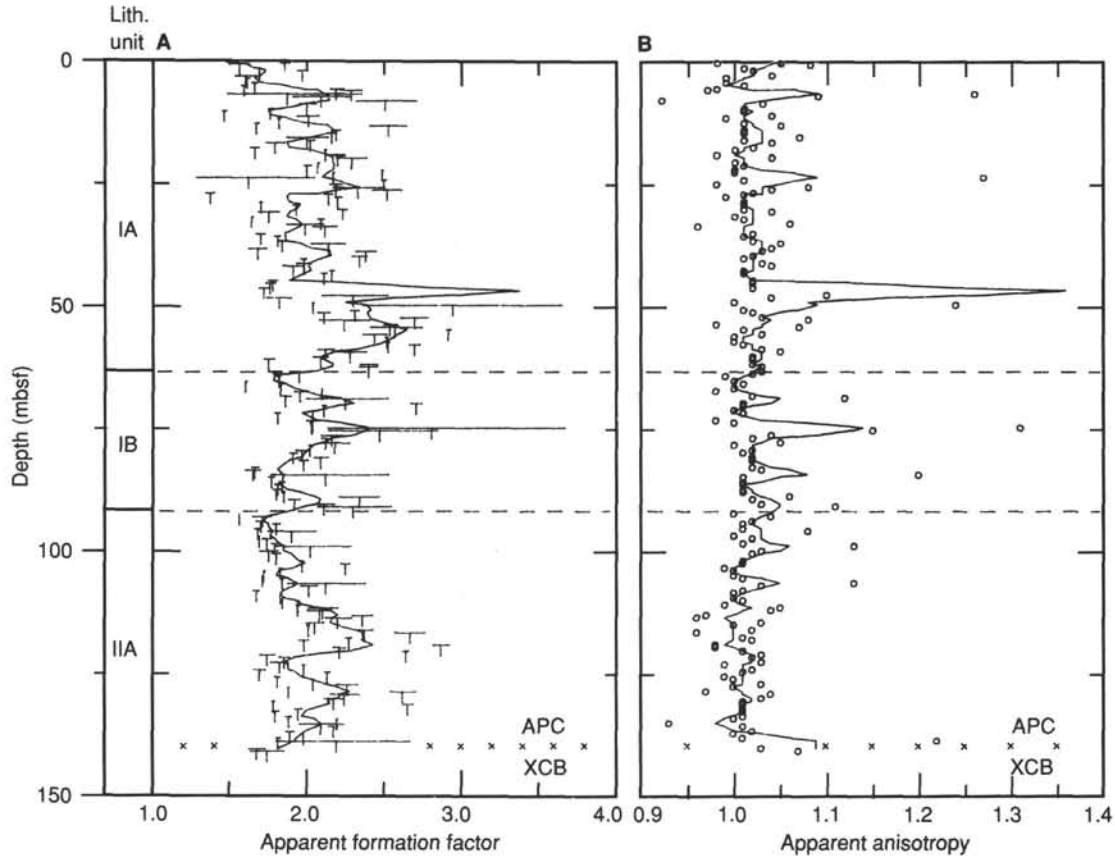

Figure 47. **A.** Apparent formation factor vs. depth for Hole 794A. Formation factor could only be determined for the APC cores. The horizontal line shows the range of the horizontal and vertical formation factor measurements, and the vertical tick indicates the mean formation factor. The solid curve represents the five-point tapered running mean. **B.** Apparent anisotropy vs. depth for Hole 794A. Symbols and curves are as defined in Figure 42.

Table 12. Statistical characteristics of Unit I physical properties.

	Units	Mean	Standard deviation	Minimum	Maximum
Unit IA (0–63.8 mbsf; Holocene to Pleistocene)					
Wet-bulk density	g/cm^3	1.50	0.14	1.29	2.15
Dry-bulk density	g/cm^3	0.72	0.20	0.44	1.50
Grain density	g/cm^3	2.73	0.34	2.09	4.60
Porosity	%	76.9	6.3	60.3	85.8
Water content	%	53.0	7.9	30.5	66.6
Acoustic velocity	m/s	1513	23	1440	1867
Thermal conductivity	W/m · K	0.965	0.101	0.740	1.206
Mean formation factor		2.06	0.34	1.24	2.95
Formation anisotropy		1.03	0.05	0.92	1.27
Unit IB (63.8–92.3 mbsf, Pleistocene to Pliocene)					
Wet-bulk density	g/cm^3	1.44	0.07	1.30	1.60
Dry-bulk density	g/cm^3	0.61	0.09	0.47	0.83
Grain density	g/cm^3	2.55	0.15	2.23	2.85
Porosity	%	80.5	2.7	74.8	85.1
Water content	%	57.6	3.9	48.0	64.1
Acoustic velocity	m/s	1532	14	1453	1612
Thermal conductivity	W/m · K	0.868	0.084	0.682	1.073
Mean formation factor		2.02	0.26	1.61	2.81
Formation anisotropy		1.04	0.06	0.98	1.31

Table 13. Statistical characteristics of Unit II physical properties.

	Units	Mean	Standard deviation	Minimum	Maximum
Unit IIA (92.3–216.9 mbsf; Pliocene to late Miocene)					
Wet-bulk density	g/cm^3	1.39	0.07	1.27	1.56
Dry-bulk density	g/cm^3	0.53	0.09	0.41	0.82
Grain density	g/cm^3	2.47	0.27	1.69	3.20
Porosity	%	83.9	3.8	71.9	94.0
Water content	%	62.1	4.3	47.2	68.8
Acoustic velocity	m/s	1534	14	1439	1608
Thermal conductivity	W/m · K	0.839	0.065	0.700	1.007
Mean formation factor		1.81	0.16	1.56	2.25
Formation anisotropy		1.03	0.04	0.99	1.13
Unit IIB (216.9–293.5 mbsf, late Miocene)					
Wet-bulk density	g/cm^3	1.33	0.10	1.25	1.89
Dry-bulk density	g/cm^3	0.45	0.14	0.35	1.28
Grain density	g/cm^3	2.42	0.26	1.90	2.91
Porosity	%	86.4	4.8	59.9	90.6
Water content	%	66.8	6.2	32.5	71.4
Thermal conductivity	W/m · K	0.792	0.033	0.741	0.853

Table 14. Statistical characteristics of Unit III physical properties.

	Units	Mean	Standard deviation	Minimum	Maximum
Unit IIIA (293.5–351.3 mbsf in Hole 794A, late Miocene)					
Wet-bulk density	g/cm^3	1.61	0.12	1.37	2.03
Dry-bulk density	g/cm^3	0.86	0.16	0.54	1.40
Grain density	g/cm^3	2.64	0.16	2.32	3.11
Porosity	%	72.4	4.7	61.8	80.5
Water content	%	46.6	5.7	31.2	60.2
Thermal conductivity	W/m · K	0.957	0.061	0.810	1.066
Unit IIIB (347.8–491.7 mbsf in Hole 794B, late to middle Miocene)					
Wet-bulk density	g/cm^3	1.95	0.18	1.66	2.52
Dry-bulk density	g/cm^3	1.42	0.28	0.97	2.30
Grain density	g/cm^3	2.67	0.19	2.29	3.39
Porosity	%	51.5	10.2	21.9	71.5
Water content	%	27.7	7.1	8.9	41.7
Thermal conductivity	W/m · K	1.147	0.148	0.822	1.410
Acoustic velocity, A	m/s	1918	186	1606	2304
Acoustic velocity, B	m/s	2012	302	1639	2425
Acoustic velocity, C	m/s	1993	199	1645	2410

Table 15. Statistical characteristics of Unit IV physical properties.

	Units	Mean	Standard deviation	Minimum	Maximum
Unit IV (491.7–520.6 mbsf, Middle Miocene)					
Wet-bulk density	g/cm^3	1.65	0.13	1.54	1.89
Dry-bulk density	g/cm^3	0.92	0.20	0.71	1.30
Grain density	g/cm^3	2.73	0.11	2.56	2.86
Porosity	%	71.7	7.4	57.8	80.8
Water content	%	45.1	7.5	31.3	53.8
Thermal conductivity	W/m · K	1.099	0.134	0.943	1.045
Acoustic velocity, A	m/s	1785	73	1726	1951
Acoustic velocity, B	m/s	1813	57	1765	1941
Acoustic velocity, C	m/s	1813	66	1766	1963

Table 16. Statistical characteristics of Unit V physical properties.

	Units	Mean	Standard deviation	Minimum	Maximum
Unit V (520.6–542.5 mbsf, middle Miocene)					
Wet-bulk density	g/cm^3	1.92	0.21	1.60	2.23
Dry-bulk density	g/cm^3	1.32	0.31	0.86	1.82
Grain density	g/cm^3	2.83	0.10	2.67	2.99
Porosity	%	57.9	10.8	39.7	72.8
Water content	%	31.9	9.2	16.2	46.4
Thermal conductivity	W/m · K	1.201	0.129	0.986	1.304
Acoustic velocity, A	m/s	1884	290	1689	2384
Acoustic velocity, B	m/s	1932	336	1736	2602
Acoustic velocity, C	m/s	1927	333	1730	2591

Table 17. Statistical characteristics of Unit VI physical properties.

	Units	Mean	Standard deviation	Minimum	Maximum
Unit VI (644.15–645.8 mbsf)					
Wet-bulk density	g/cm^3	2.17	—	2.14	2.19
Dry-bulk density	g/cm^3	1.38	—	1.36	1.39
Grain density	g/cm^3	2.6	—	2.65	2.67
Porosity	%	36.5	—	35.1	38.0
Water content	%	17.3	—	16.8	17.8
Acoustic velocity, A	m/s	2397	—	—	—
Acoustic velocity, B	m/s	2592	—	—	—
Acoustic velocity, C	m/s	2577	—	2539	2614

heat production within the sedimentary section to at least 300 m, as had been suggested by Kobayashi and Nomura (1972).

In view of the relatively young age estimate for the formation of the Yamato Basin (15 Ma), the heat flow of 103 mW/m^2 is lower than expected if the lithosphere that underlies the basin was formed by seafloor spreading processes. The empirical relations of Parsons and Sclater 1977 predict a heat flow of about 130 mW/m^2. This suggests that either the age estimate of the Yamato Basin is low, or that Yamato Basin did not form by the same tectonic and magmatic processes that form lithosphere at mid-oceanic spreading centers.

Logging

Three Schlumberger tool strings were run at Hole 794B: the geophysical/lithodensity tool string, the geochemical tool string and the formation microscanner (FMS). Additionally, the Lamont-Doherty temperature logging tool (TLT) was attached to the bottom of each Schlumberger tool string. Logging commenced in lithologic Unit II at 100 mbsf.

The logging operations in Hole 794B were conducted between 0 and 537 mbsf. The geophysical/lithodensity and geo-

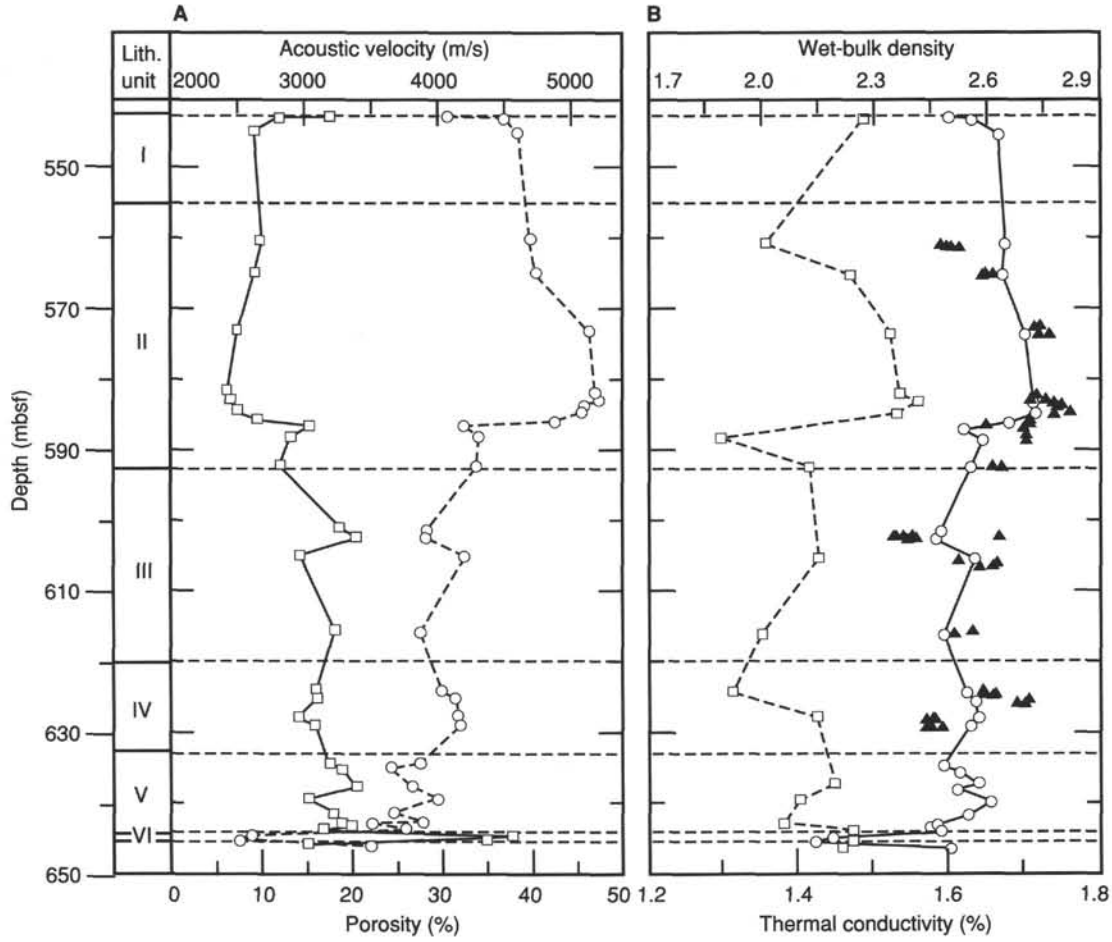

Figure 48. **A.** Acoustic velocity (open circles and dashed curve) and porosity (open squares and solid curve) vs. depth in the igneous units, Hole 794C. The unit boundaries are shown as horizontal dashed lines. The lower sedimentary Unit VI is quite distinct. Note the maximum velocity and minimum porosity in Unit 2. **B.** Wet-bulk density (open circles and solid curve) and thermal conductivity (open squares and dashed curve) vs. depth for the igneous units. The 2-min GRAPE density is also shown (solid triangles) for comparison.

chemistry logging tool strings were run through the drill pipe from 0 to 100 mbsf. The FMS tool string was run in the open hole from 68 to 537 mbsf, the driller having raised the drill pipe 32 m per our request. A summary of logging depths reached for each tool string is presented as Table 20.

Regarding the geophysical/lithodensity and geochemistry tool strings run behind the drill pipe, every tool of the geochemical tool string and only the natural gamma-ray tool (NGT) of the geophysical/lithodensity tool string yield measurements that can be corrected for drill pipe effects. An additional factor bearing on the geochemistry logs was the use of KCl mud at a 1% concentration to combat anticipated clay swelling problems. It was not possible to obtain logs in the basement of Hole 794B because of debris infilling. Also, it was not possible for each tool to reach the total logging depth because the tools were stacked in the logging tool string.

Log Quality and Processing

The quality of the logging data acquired is excellent. Tool calibration was done both before and after each logging run to insure quality control. Tension on the tool string was normal and uniform throughout and there were no bridges to impede progress of the logging tool. Each log showed consistent depth information, and no depth shifts were required to correlate log responses between the geochemical and geophysical/lithodensity tool string runs. The sonic log showed significant cycle-skipping over the intervals 330–360 mbsf and 440–460 mbsf (Fig. 55). The cycle-skipping coincides with the occurrence of alternating, thin high- and low-velocity layers. The thin, high-velocity layers might represent chert layers below the opal-A-opal-CT transition zone.

Agreement between the physical properties data and the logging data was excellent for the density and velocity logs over the interval cored by the APC. Below this, the XCB was used and core recovery was sporadic. Even so, log and physical property densities agreed well over this lower interval, but the log velocities were 100–150 m/s faster than the velocities measured on samples (see "Physical Properties" section, this chapter). The log measurements clearly delineated both the opal-A/-opal-CT and opal-CT/quartz diagenetic boundaries that the physical properties measurements had difficulty resolving due to incomplete core recovery.

The sonic log was edited for spurious data points but no further processing was completed in time for publication of this volume. Similarly, the final processing of the FMS and geochemistry logs were not completed in time for this volume.

Resistivity, Sonic Velocity, Density

Figure 55 shows the variation of the resistivity, sonic velocity, and density logs with depth for Site 794. Lithologic Unit II con-

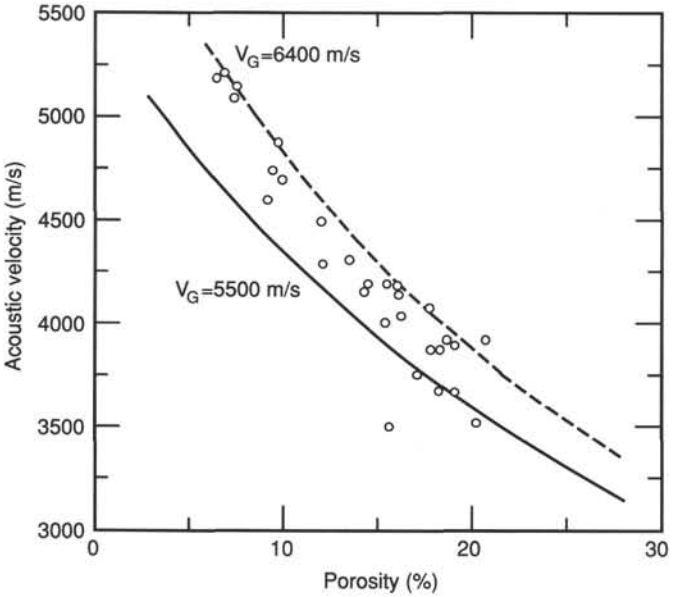

Figure 49. Acoustic velocity vs. porosity for the igneous units. The data are shown (open circles) in comparison with two model curves for different grain velocities: 5500 m/s (the lower curve) and 6400 m/s (the upper curve). Note that the general trend of the data appears to be from the higher grain velocity at low porosities (less alteration) to the lower grain velocity at higher porosities (more fracturing and alteration).

sists of clay with a minor lithology of diatomaceous ooze and extends from 92 to 290 mbsf. The resistivity log shows a discernible negative gradient with values decreasing from 0.5 to 0.3 ohm-meters over this unit. The gradient becomes less steep in Unit IIB. The density log shows densities varying from 1.4–1.5 g/cm^3 between 100 and 130 mbsf. The density log shows a uniform character from 140 to 290 mbsf. Thin intervals of high density occur at 218 and 283 mbsf. The sonic log also shows a remarkably uniform character over Unit II. Two intervals of high sonic velocity are present at 218 and 283 mbsf corresponding to the intervals of high density measurements. Because these two intervals are above the opal-A/Opal-CT transition zone, it is unlikely that they represent chert. Instead they most likely represent dolomite- or calcite-cemented zones with the dolomite or calcite causing higher density and sonic velocity values.

Lithologic Unit III is composed primarily of siliceous claystone and extends from 290 to 490 mbsf. The opal-A/opal-CT transition occurs at the Unit II–Unit III boundary. Coincident with this boundary are large increases in density and resistivity and a minor increase in velocity. Densities range from 1.5 to 1.7 g/cm^3 in Unit III and, like the resistivity and velocity logs, the density log shows high variability due to the reduction of water content. Resistivity values increase to about 0.5 ohm-meters in the upper part of Unit IIIA. The average resistivity decreases slightly in Unit IIIB and the resistivity values become more variable. The sonic log becomes more variable in the lower third of Unit IIIA and into Unit IIIB where velocities vary from 1700 to 2000 m/s. The zones of high variability in Units IIIA and IIIB caused significant noise problems on the original log. We used the algorithm of Srivastava, Arthur, Clement, et. al., (1987) to edit these spurious values on the Site 794 sonic log.

Lithologic Unit IV consists mostly of blue tuff and lapilli tuff (see "Lithostratigraphy" section, this chapter) from 490 to 510 mbsf. The log responses over this interval include a decrease in density and resistivity. The sonic velocity varies little from the Unit III values.

Table 18. Physical properties of igneous units.

	Units	Mean	Minimum	Maximum
		Unit 1 (542.5–approx. 555 mbsf)		
Wet-bulk density	g/cm^3	2.55	2.49	2.62
Dry-bulk density	g/cm^3	2.48	2.43	2.53
Grain density	g/cm^3	2.71	2.71	2.72
Porosity	%	13.0	9.2	17.7
Water content	%	5.2	3.6	7.3
Thermal conductivity	W/m · K	1.525	1.480	1.570
Acoustic velocity, C	m/s	4452	4070	4603
		Unit 2 (approx. 555–592.7 mbsf)		
Wet-bulk density	g/cm^3	2.64	2.53	2.72
Dry-bulk density	g/cm^3	2.49	2.31	2.59
Grain density	g/cm^3	2.76	2.73	2.79
Porosity	%	9.8	6.5	15.4
Water content	%	3.9	2.4	6.3
Thermal conductivity	W/m · K	1.459	1.291	1.555
Acoustic velocity, C	m/s	4783	4199	5215
		Unit 3 (592.7–approx. 620 mbsf)		
Wet-bulk density	g/cm^3	2.49	2.46	2.56
Dry-bulk density	g/cm^3	2.04	1.95	2.19
Grain density	g/cm^3	2.75	2.73	2.76
Porosity	%	18.0	14.4	20.6
Water content	%	7.4	5.8	8.5
Thermal conductivity	W/m · K	1.367	1.311	1.423
Acoustic velocity, C	m/s	3967	3878	4196
		Unit 4 (approx. 620–approx. 633 mbsf)		
Wet-bulk density	g/cm^3	2.56	2.54	2.57
Dry-bulk density	g/cm^3	2.15	2.13	2.20
Grain density	g/cm^3	2.78	2.77	2.79
Porosity	%	15.6	14.2	16.2
Water content	%	6.3	5.7	6.5
Thermal conductivity	W/m · K	1.367	1.311	1.423
Acoustic velocity, C	m/s	4133	4040	4191
		Unit 5 (approx. 633–644.15 mbsf)		
Wet-bulk density	g/cm^3	2.51	2.44	2.60
Dry-bulk density	g/cm^3	2.05	1.95	2.20
Grain density	g/cm^3	2.76	2.67	2.82
Porosity	%	18.4	15.3	20.7
Water content	%	7.5	6.0	8.4
Thermal conductivity	W/m · K	1.424	1.379	1.469
Acoustic velocity, C	m/s	3727	3317	4008

Table 19. Temperature measurements in Hole 794A.

Measurement number	Depth (mbsf)	Temperature (°C)	Thermal resistance (m^2 · C/W)
0	0.0	0.2	0.0
4	26.8	3.83	28.2
7	55.3	6.91	59.5
9	74.3	9.72	80.3
13	112.3	13.42	126.56
16	140.8	17.0*	—
19	169.5	19.90	203.5
23	208.2	26.42	245.3
26	237.6	29.30	282.7
29	266.4	33.78	319.2
32	294.5	37.5*	352.7
36	332.9	21.3**	—
38	351.3	35.5**	—

* These temperature measurements are disturbed but appear to give reasonable values.
** These measurements are disturbed and temperature values are judged to be invalid.

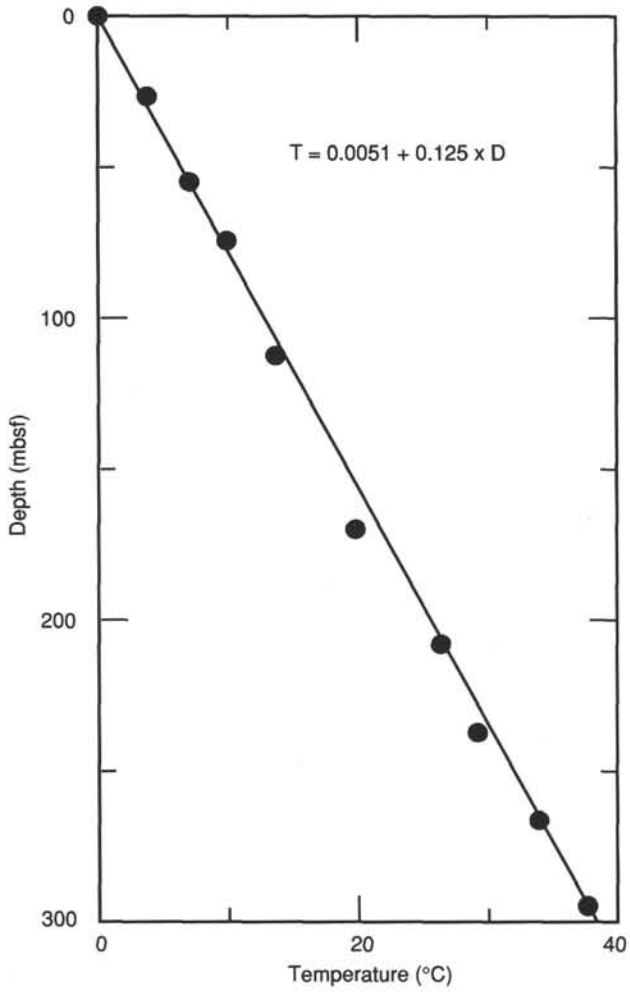

Figure 50. Downhole temperatures vs. depth for Hole 794A. The line is a linear regression showing a nearly uniform gradient of 125°/km.

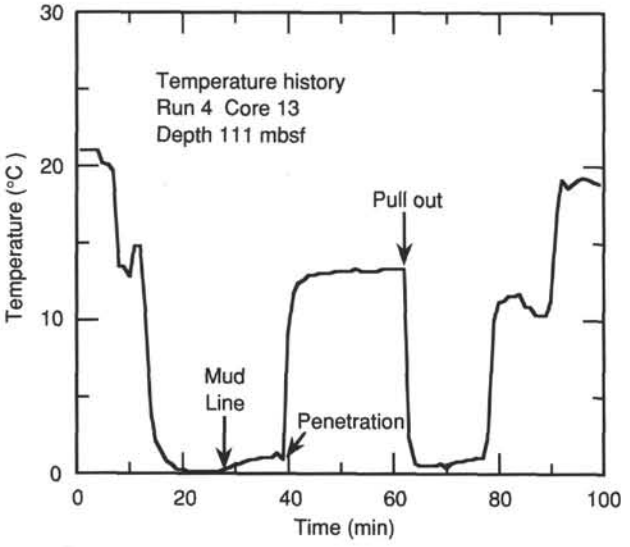

Figure 51. Typical history of a downhole temperature run in Hole 794A. The one shown was made after 12 cores had been taken.

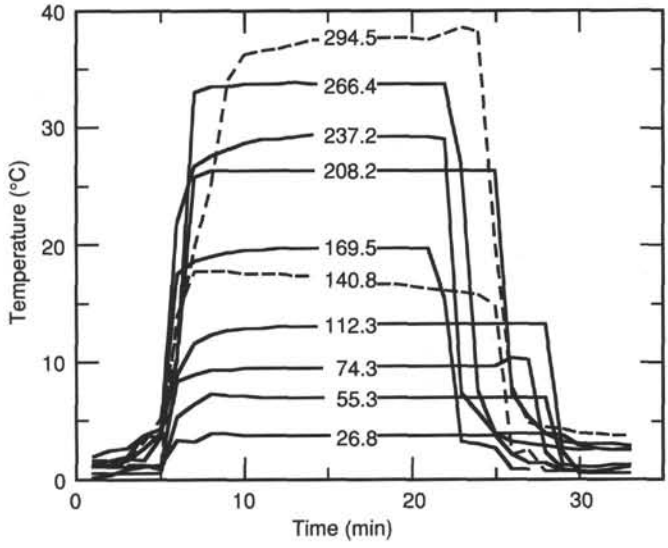

Figure 52. Multiple plot of 10 temperature records labeled by depth (mbsf) in Hole 794A showing the history just before, during, and after penetration.

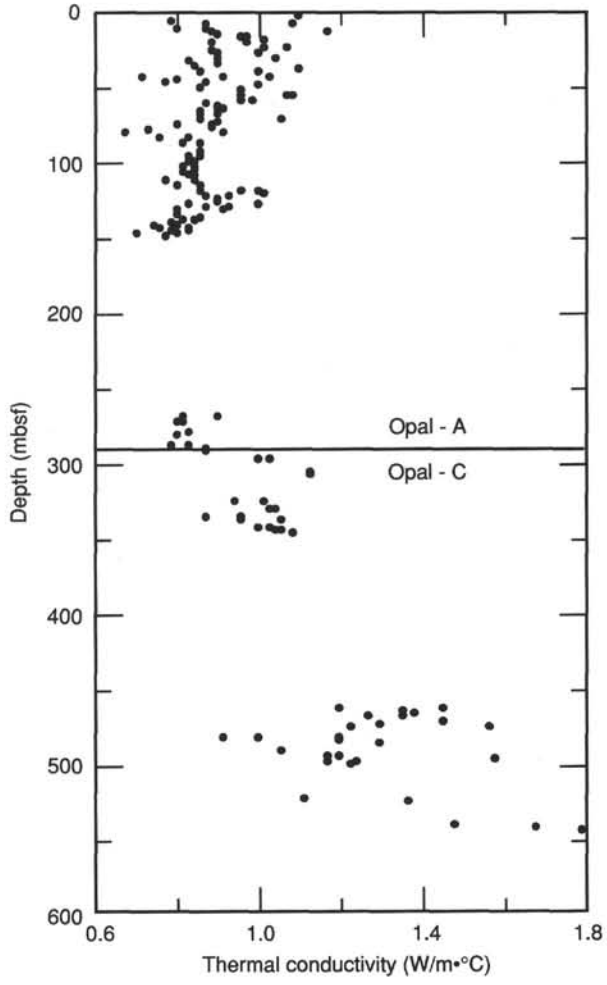

Figure 53. Thermal conductivity measurements in Hole 794A, corrected to *in-situ* conditions.

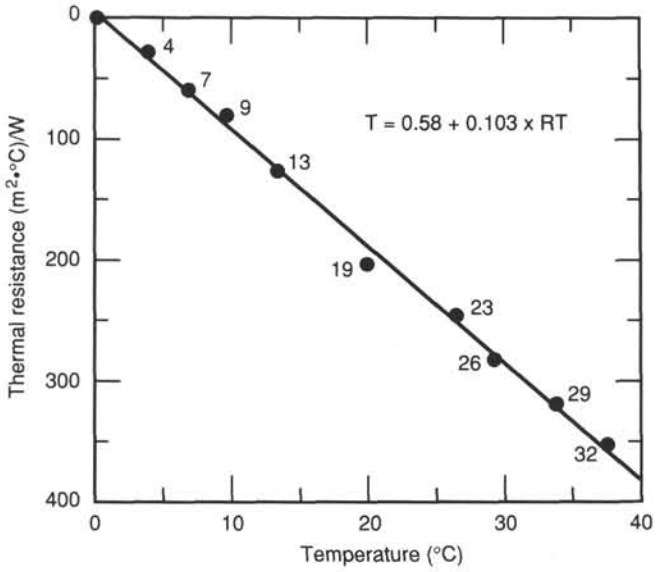

Figure 54. Downhole temperatures vs. the thermal resistance of the interval between the seafloor and the measurement depth. The slope of the linear regression line gives the heat flow; in this case 0.103 W/m^2 for Site 794.

Table 20. Summary of logging depths reached in Hole 794B for each tool string.

Seafloor (m)*	2810.9		
Seafloor to rig floor (m, ft)	2821.8, 9257.9		
Rig floor height (m)	10.8		
Total depth drilled (m) ~	549.0		
Deepest log (m)	537.7		
Basement depth (m)	542.4		
Tool	Geophysics	Geochemistry	Formation microscanner
Shallowest depth			
(mbsf)	−6.4	−7.3	68.6
below rig floor (ft)	9237.0	9234.0	9482.9
Deepest depth			
(mbsf)	537.1	537.6	537.7
below rig floor (ft)	11020.0	11021.5	11021.9
Upgoing (yes/no)	yes	yes	yes
Hole condition (open, drill pipe)	0–100 m	0–100 m	#
KCl mud (%)	2	2	2
Side entry sub (yes/no)	no	no	no

* From Leg 127 Introduction/Objectives, Principal Results Section, Table 1.
\# drill pipe raised 30 m for FMS run.
~ 653.7m penetration at 794C including basement but not logged

Lithologic Unit V consists of calcareous silty claystone. The log characteristics, values and degree of variability of this unit are very similar to those of Unit III.

Porosity, Caliper, Compensated Gamma Ray

The gamma-ray, caliper, and neutron porosity logs vs. depth are displayed in Figure 56. The gamma-ray and caliper logs are commonly displayed together because the clay content determined from the gamma-ray reflects consolidation changes readily apparent in the caliper log. Changes in porosity indicated by the porosity log often correlate well with caliper log changes.

The dominant feature of the gamma-ray log is a large increase in clay content across the opal-A/opal-CT boundary (Unit II to Unit III). The gamma-ray counts are variable in Unit III, indicating a variable clay content. In contrast, Unit IV shows a marked decrease in clay content. This decrease is most likely related to the presence of blue tuff that contains potassium-poor clays (see "Lithostratigraphy" section, this chapter).

The caliper log measures the radius of the borehole. In Unit II the borehole was enlarged to an average diameter of 33 cm. At the opal-A/opal-CT boundary the sediments became more competent, and at 350 mbsf the hole diameter constricted to 26.7 cm., indicating good sediment consolidation. The hole is not significantly enlarged again until about 460 mbsf. This enlargement coincides with difficult and slow drilling conditions encountered when first penetrating basement. The greater circulation rates used during this drilling resulted in the washing out of the bottom part of the hole.

The porosity log is highly variable throughout the hole, but this apparent porosity variation is not supported by the physical properties data (see "Physical Properties" section, this chapter). In Units II and III, the porosity logs underestimate the porosity by almost 20% relative to the shipboard physical properties measurements on core samples. Below the opal-A/opal-CT diagenetic boundary, there is better agreement between log measurements and physical property results.

Formation Microscanner

The formation microscanner is a microresistivity tool. Changes in sedimentary features such as fractures, bioturbation, concretions, and nodules produce resistivity changes that can be imaged throughout the length of the hole. Unfortunately, final processed FMS images were not available for this publication. However, the raw images used aboard ship delineated possible chert layers in Unit III and parts of Unit IV that coincide with high variability in the sonic and density logs.

Geochemistry

The geochemical tool is an important instrument string because of its ability to see behind the casing. Important corrections must be made for the effects of background chlorine before these data can be interpreted. Unfortunately, final processed logs were not available for this volume, so only the raw data are given in Figure 57.

Temperature Tool

As with the FMS and geochemistry logs, the temperature log data were not analyzed in time for publication of this volume. These data should be useful in constructing a thermal conductivity profile.

SEISMIC STRATIGRAPHY

Available Data

The original proposal for Site 794 was made on the basis of single-channel seismic reflection data of the Geological Survey of Japan (Tamaki et al., 1985). The data were obtained by systematic single-channel seismic reflection surveys that were carried out in 1978 at an interval of 15 nmi over a wide area of the Japan Sea (Honza, 1979). Two site-survey cruises for Site 794 were carried out since the proposal was submitted. A single track line of seismic reflection survey was carried out by the DELP85 research cruise in 1985 (Tokuyama et al., 1987a, b), and four seismic reflection survey lines were obtained by the KT88-9 research cruise in 1988. A multichannel (six-channel) seismic reflection system was used in both cruises. Two track lines of single-channel digital seismic reflection profiling were obtained during the approach of the *JOIDES Resolution* to Site 794 (see "Operations" section, this chapter).

Seismic Stratigraphy

The seismic stratigraphy of the northern Yamato Basin differs from that of the Japan Basin and the central part of the Yamato Basin in that a densely stratified layer prevails in the uppermost section of the sedimentary column. This densely stratified layer corresponds to turbidites deposited on the abyssal plains of the Japan and Yamato Basins. As the northern Yamato Basin comprises a bathymetric sill between the Japan Basin and the deeper Yamato Basin to the south, the area is free from turbidite deposits and lacks the uppermost densely stratified layer.

Six distinct seismic intervals are recognized in the northern Yamato Basin (Figs. 10 and 58). From top to bottom they are: Interval 1, an upper well-stratified interval; Interval 2, a transparent or faintly-stratified interval; Interval 3, a middle well-stratified interval; Interval 4, a lower moderately well-stratified interval; Interval 5, a lowermost highly reflective interval; and an acoustic basement, representing an unstratified, acoustically-opaque zone.

The thickness of Interval 1 in the area around the site varies between 0.15 and 0.25 s (two-way traveltime; hereafter this unit is used for the thickness of seismic intervals). The boundary between Interval 1 and Interval 2 is gradual and conformable. The thickness of Interval 2 is variable between 0.15 and 0.2 s in the area. The reflectors in Interval 2 are faint and hummocky. Interval 3 is the most stratified interval of the seismic sections in the area. The reflectors of Interval 3 are strongly parallel and onlap basement highs. The thickness of Interval 3 is in the range of 0.1 to 0.15 s in the area. The reflectors of Interval 4 have lower frequencies and lower amplitudes than those of Interval 3. Interval 4 has a thickness of 0.1 to 0.13 s. Interval 4 is generally parallel with Interval 3, but in some places shows a slight disconformable relationship. Interval 4 also onlaps the basement high. Interval 5 is widely observed above the acoustic basement in the northern part of the Yamato Basin. Reflections of Interval 5 have high-amplitudes associated with reverberation that normally mask the contact between Interval 5 and the acoustic basement.

Correlation between Seismic Stratigraphy and Lithology of Site 794

Correlation between seismic stratigraphy and lithostratigraphy was done by using physical property velocity data, logging velocity data, and a synthetic seismogram. A synthetic *P*-wave seismogram was calculated based on logging and physical property measurements (Fig. 59). Sonic velocity and bulk density profile data from logging were used for the calculations in the sedimentary section. Physical property measurements were used for igneous rocks and for the intervening tuff layers, because the logging run was completed only in the sedimentary column. The wavelet used was the 50-Hz Ricker type. Attenuation is not accounted for in the synthetic seismogram, but internal multiples are included.

The synthetic seismogram calculated is displayed in Figure 59 with the digital seismic trace at Site 794 that was obtained by the *JOIDES Resolution*. Although this synthetic seismogram is only roughly calculated using the shipboard computer, the correlation between the underway reflection data and the synthetic seismogram is generally good.

Two distinct horizons beneath the seafloor provide key markers for the correlation of seismic intervals with lithostratigraphy. These are the opal-A/opal-CT transition and the top of the dolerite sills. The top of dolerite sills at 543 mbsf unequivocally correlates with the top of Interval 5, because of its extraordinarily reflective nature and horizontal occurrence. The opal-A/opal-CT transition at 293 mbsf is well constrained by major changes in almost all of the physical properties and in the logging data (see "Physical Properties" and "Downhole Measurements" sections, this chapter) and correlate with the top of Interval 3. Other boundaries between Intervals 1 and 2, Intervals 3 and 4, and Interval 5 and acoustic basement are rather ambiguous, having more transitional acoustic natures.

Results of the correlation between the seismic stratigraphy and the lithostratigraphy are summarized in Figure 60. The thickness of each interval observed from the *JOIDES Resolution* Site 794 approach seismic survey is: 0.18 s for Interval 1; 0.20 s for Interval 2; 0.12 s for Interval 3; 0.16 s for Interval 4; and 0.075 s for Interval 5.

Interval 1 correlates to Unit I and the uppermost part of Unit II. Interval 2 correlates to the rest of Unit II. The boundary between Intervals 1 and 2 at 136 mbsf coincides with the boundary between the overlying diatomaceous clay and the underlying diatomaceous ooze. The change of lithology from diatomaceous clay to diatomaceous ooze appears to be consistent with the change from the stratified character of Interval 1 to the transparent character of Interval 2, the diatomaceous ooze having a more transparent acoustic nature. Formation microscanner data also shows the common occurrence of stratification in Interval 1 and rare stratification in Interval 2. Unit IA (0–92.3 mbsf) with well-bedded structure may account for the stronger stratification of the upper Interval 1. The boundary between Intervals 1 and 2 is also coincident with the change from APC to XCB coring in Hole 794A (140 mbsf), suggesting that the lithofacies boundary may also coincide with the lithification front.

Interval 3 corresponds to the upper part of Unit III; its top is coincident with the opal-A/opal-CT transition. The strongly stratified character of Interval 3 reflects the abundant occurrence of dolomite and porcellanite layers within this unit. This is suggested by the sonic velocity log that shows correspondingly high variability, suggesting intercalation of layers with different physical properties. Interval 4 corresponds to the lower part of Unit III and to all of Units IV and V. This part of the sonic velocity log shows less variability than the above interval, consistent with moderate stratification.

Interval 5 includes igneous Units 1–6 and the interbedded sedimentary Unit VI. The seismic Interval 6 corresponds to acoustic basement that was not penetrated in Holes 794A, 794B, or 794C. The boundary between Interval 5 and acoustic basement is commonly masked by reverberation of the strong reflectors from Interval 5. Nevertheless, we have estimated the thickness of Interval 5 to be 0.075 s (165 m). If this estimate is correct, then drilling was stopped about 55 m short of the top of acoustic basement.

CONCLUSIONS

We accomplished two of our three main objectives at Site 794: (1) to gain information on the style and dynamics of rifting through a determination of the age and nature of basement; and (2) to characterize the sedimentation, subsidence, and oceanographic history of the area. Because of hole problems we were unable to reach our third goal, a measurement of the magnitude and direction of the present stress field. A detailed summary of the results and conclusions for Site 794 can be found at the beginning of this chapter. For emphasis, in the sections below we highlight the key findings as they relate to our principal objectives.

Style and Dynamics of Rifting

A dolerite sill complex constitutes acoustic basement at Site 794. These rocks comprise highly altered dolerite and basalt that have intruded 15- to 16-Ma sediments. The overall chemical compositions of these igneous rocks indicate that they are tholeiitic in nature, but the high degree of alteration does not permit definitive characterization. They are similar to other back-

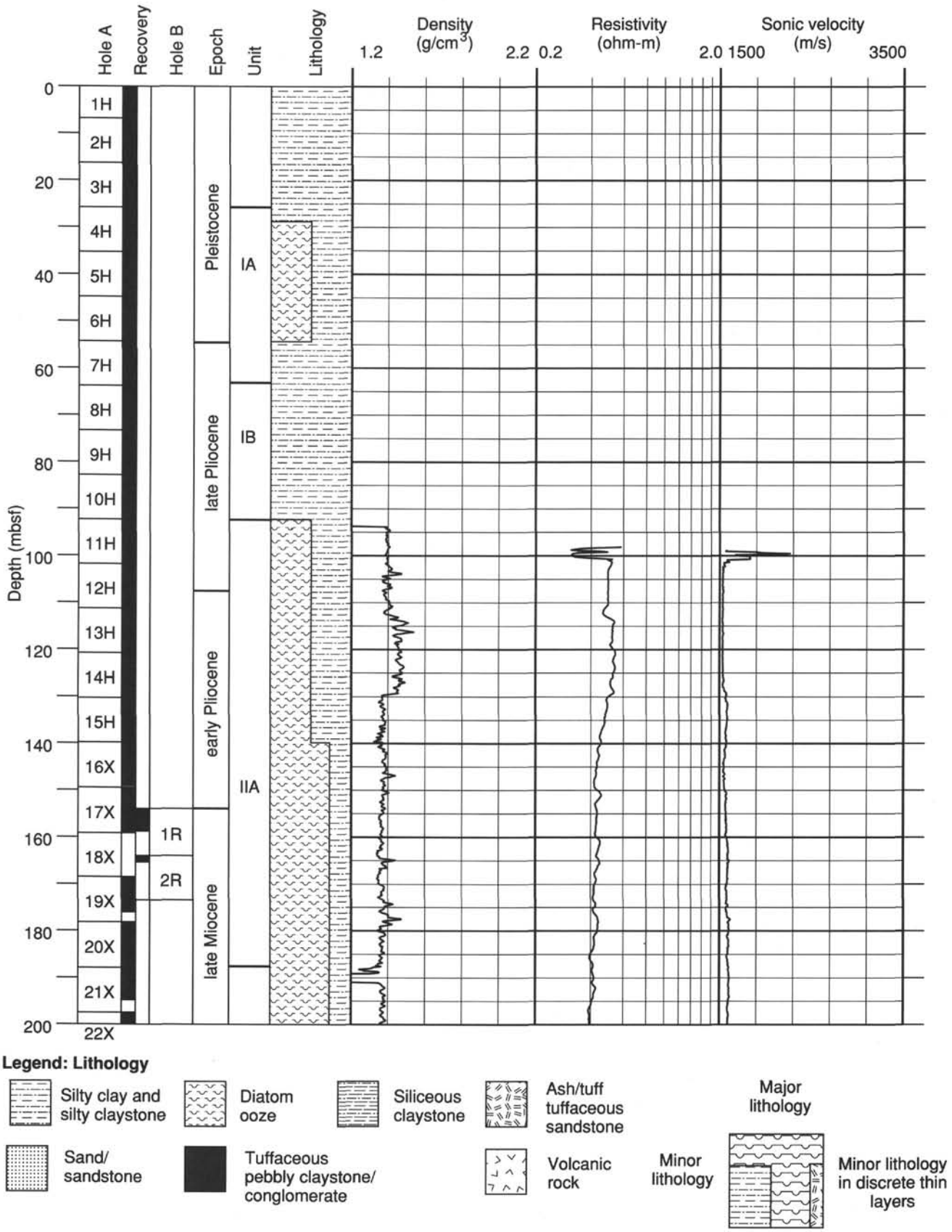

Figure 55. Resistivity, sonic velocity, and density logs vs. depth, Site 794.

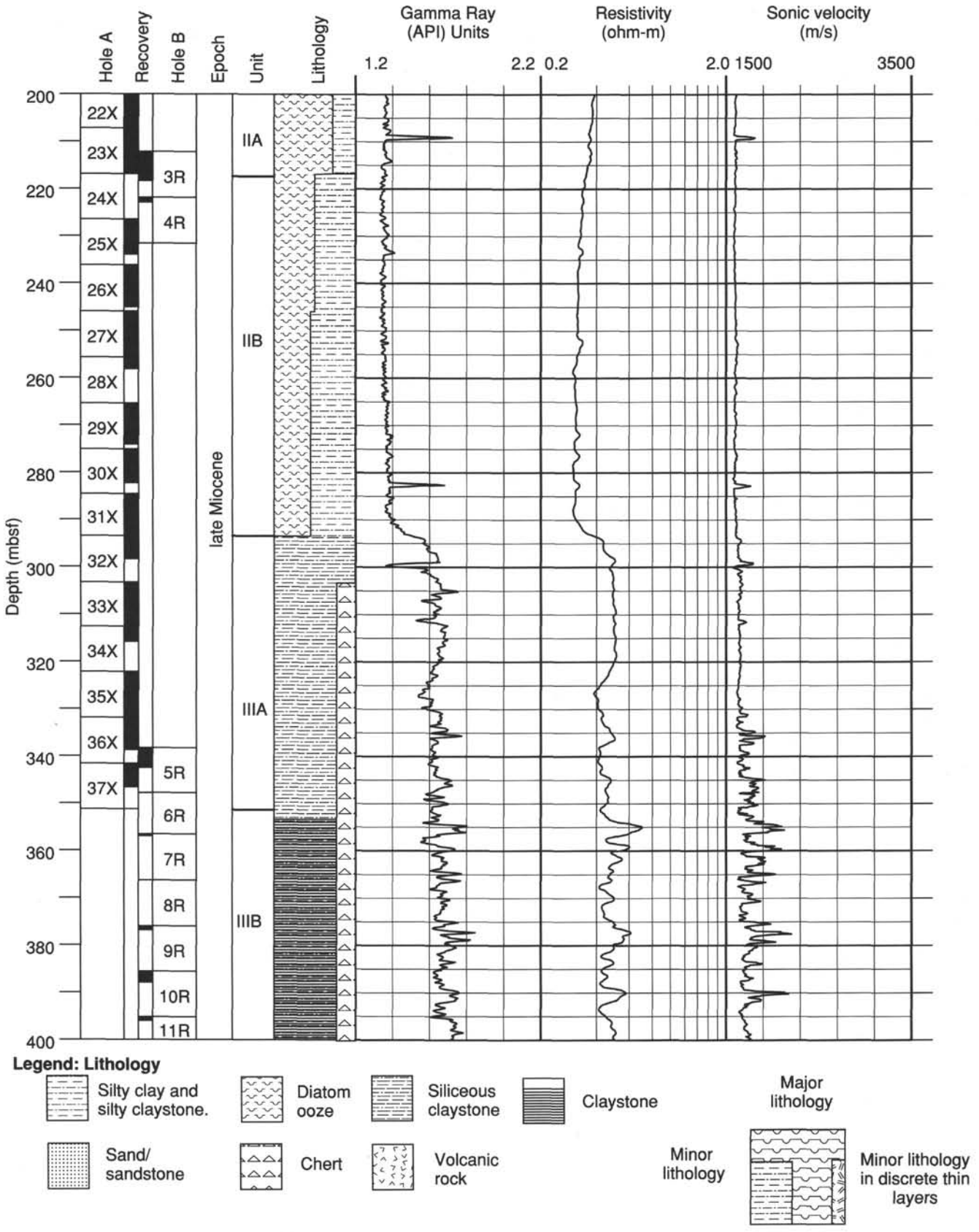

Figure 55 (continued).

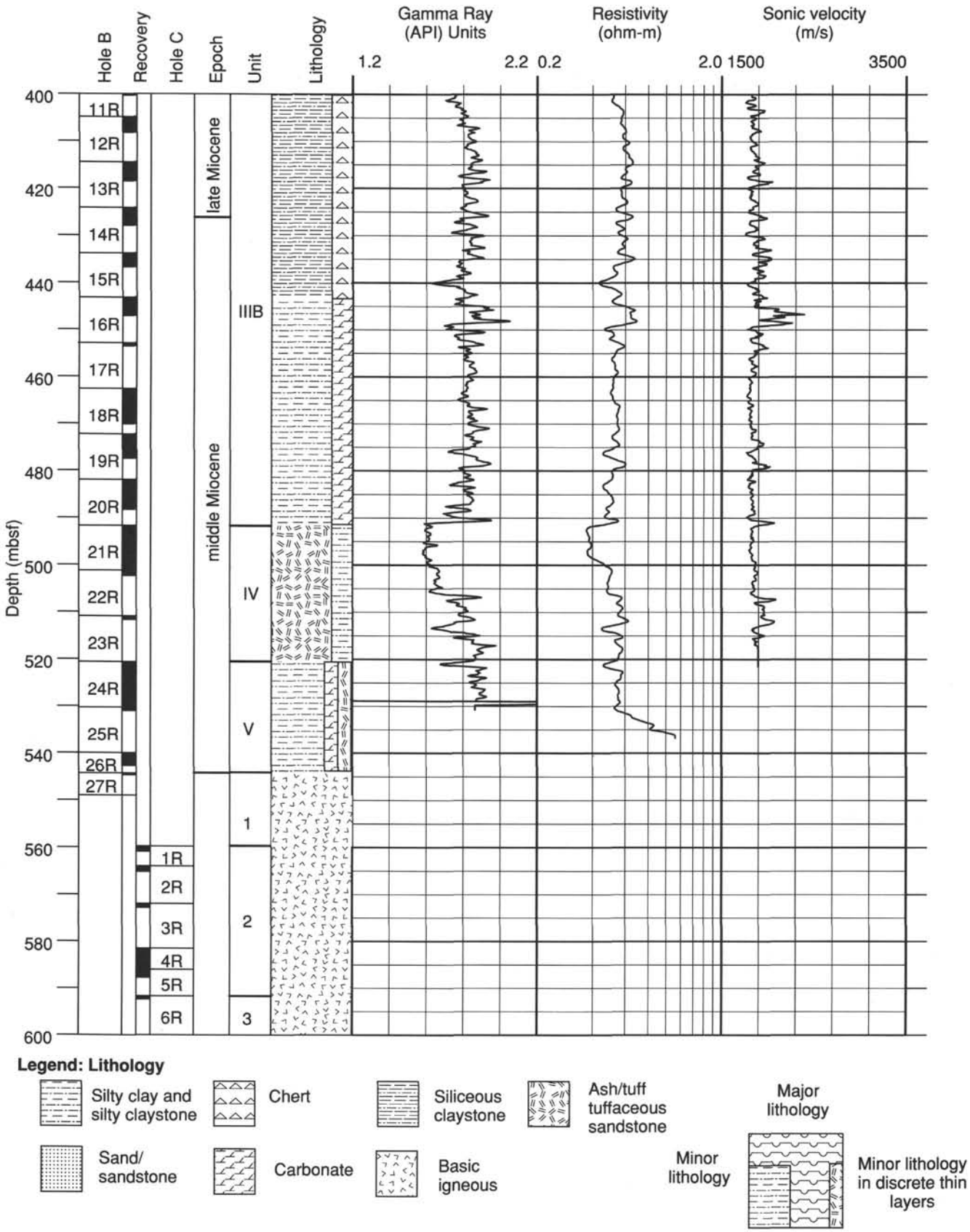

Figure 55 (continued).

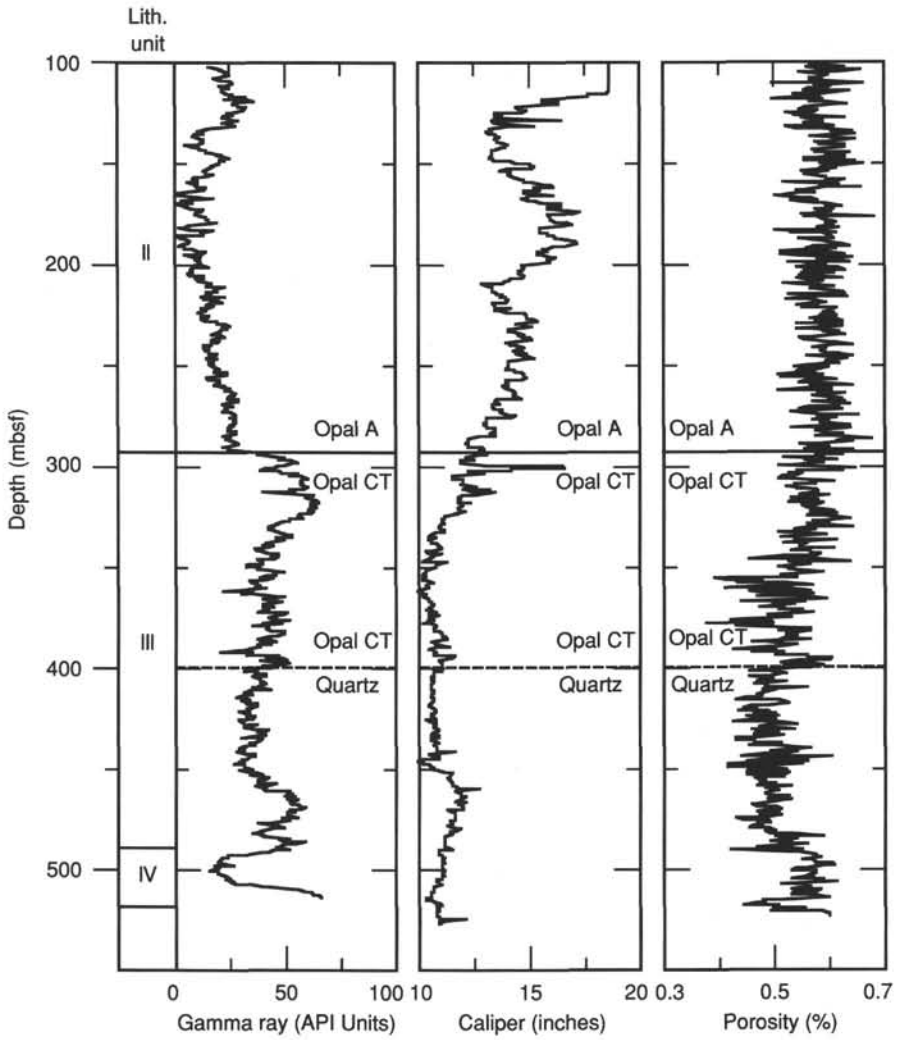

Figure 56. Gamma-ray, caliper, and porosity logs vs. depth, Site 794.

arc basin basalts in terms of their TiO_2, Zr, and Ce contents. This similarity is also suggested by the Al_2O_3, SiO_2, Na_2O, and Sr contents of the least-altered samples. These results suggest that this sill-complex represents basaltic lavas that were injected into soft sediments during the formation of the Yamato Basin at 15–16 Ma.

Oceanographic and Sedimentation History

The sedimentary succession encountered at Site 794 indicates four probable stages in the oceanographic and sedimentation history of this area. The earliest recognized stage began with early middle(?) Miocene deposition of bioturbated claystones and fine-grained graded tuffs in an oxygenated basinal setting. This was followed by middle Miocene submarine volcanism and deposition of upper middle bathyal bioturbated, hemipelagic clays and gravity flow tuffs on a slope or borderland ridge in cool, suboxic marine waters. The area subsided to lower middle bathyal depths during the late middle Miocene, and diatomaceous sedimentation prevailed in a well-oxygenated environment through the early Pliocene. Conditions changed again in the late Pliocene and Quaternary when diatomaceous sedimentation decreased, terrigeneous input increased, and climate oscillated between arctic and subarctic conditions to produce complex interbedding of light-colored, clayey silts alternating with dark-layered diatomaceous, pyritic, and organic-rich layers. Except for parts of the Quaternary, this sequence was largely deposited below the CCD.

This sequence has been overprinted by significant diagenetic changes, the most striking of which is the wholesale alteration of opaline diatomaceous sediments to hard siliceous claystones containing opal-CT and quartz. The diagenetic transitions of opal-A to opal-CT and opal-CT to quartz are well documented by a variety of data including geochemical and physical property profiles and downhole logs. Both alterations occur along upward-migrating diagenetic fronts that are parallel to the seafloor. The opal-A/opal-CT transition is manifested in seismic reflection records of this area as a prominent bottom-simulating reflector.

REFERENCES

Baker, P. A., and Burns, S. J., 1985. Occurrence and formation of dolomite in organic-rich continental margin sediments. *AAPG Bull.*, 69: 1917–1930.

Berggren, W. A., Kent, D. V., Flynn, J. J., and Van Couvering, J. A., 1985a. Cenozoic Geochronology. *Geol. Soc. Am. Bull.*, 96:1407–1418.

Berggren, W. A., Kent, D. V., and Van Couvering, J. A., 1985b. The Neogene: Part 2. Neogene geochronology and chronostratigraphy. *In* Snelling, N. J. (Ed.), *The Chronology of the Geological Record.* Geol. Soc. Am. Mem., 10:211–260.

Boggs, S., Jr., 1984. Quaternary sedimentation in the Japan arc-trench system. *Geol. Soc. Am. Bull.*, 95:669–685.

Bouma, A. H., 1975. Deep-sea fan deposits from Toyama Trough, Sea of Japan. *In* Karig, D. E., Ingle, J. C., Jr., et al., *Init. Repts. DSDP,* 31: Washington (U.S. Govt. Printing Office), 489–495.

Cadet, J. P., and K. Fujioka, 1980. Neogene volcanic ashes and explosive volcanism: Japan Trench transect, Leg 57, Deep Sea Drilling Project. *In* Scientific Party, *Init. Repts. DSDP,* 57 (Pt. 2): Washington (U.S. Govt. Printing Office), 1027–1041.

Davis, E. E., and Lister, C.R.B., 1977. Heat flow measured over the Juan de Fuca Ridge: evidence for widespread hydrothermal circulation in a highly heat transportive crust. *J. Geophys. Res.*, 82: 4845–4860.

Dick, H.J.B., Marsh, N. G., and Bullen, T. D., 1980. Abyssal basalts from the Shikoku Basin: Their petrology and major-element geochemistry. *In* Klein, G. deV., Kobayashi, K., et al., *Init. Repts. DSDP,* 58: Washington (U.S. Govt. Printing Office), 843–872.

Donnelly, T. W., Melson, W., Kay, R., and Rogers, J.J.W., 1973. Basalts and dolerites of Late Cretaceous age from the central Caribbean. *In* Edgar, N. T., Saunders, J. B., et al., *Init. Repts. DSDP,* 15: Washington (U.S. Govt. Printing Office), 989–1012.

Einsele, G., 1982. Mechanism of sill intrusion into soft sediment and expulsion of pore water. *In* Curray, J. R., Moore, D. G., et al., *Init. Repts. DSDP,* 64 (Pt. 2): Washington (U.S. Govt. Printing Office), 1169–1176.

Emeis, K.-C., and Kvenvolden, K. A., 1986. Shipboard Organic Geochemistry on JOIDES Resolution. *ODP Tech. Note,* 7: College Station, TX (Ocean Drilling Program.

Erlank, A. J., and Kable, E.J.D., 1976. The significance of incompatible elements in Mid-Atlantic Ridge basalts from 45°N, with particular reference to Zr/Nb. *Earth Planet. Sci. Lett.*, 54:281–291.

Espitalié, J., Madec, M., and Tissot, B., 1980. Role of mineral matrix in kerogen pyrolysis: Influence on petroleum generation and migration. *AAPG Bull.*, 64:59–66.

Espitalié, J., Madec, M., Tissot, B., Mennig, J. J., and Leplat, P., 1977. Source rock characterization method for petroleum exploration. *Proc. 9th Ann. Offshore Tech. Conf.*, 3:439–448.

Fukao, Y., and Furamoto, M., 1975. Mechanism of large earthquakes along the eastern margin of the Japan Sea. *Tectonophysics*, 25: 247–266.

Geological Survey of Japan, 1982. *Geologic Atlas of Japan*. Tokyo.

Gieskes, J. M., 1981. Deep-sea drilling interstitial water studies: implications for chemical alteration of the oceanic crust, Layers I and II. *In* Warmer, T. E., Douglas, R. C., and Winterer, E. L. (Eds.), *The Deep Sea Drilling Project: A Decade of Progress*. SEPM Spec. Publ., 32:49–167.

Gieskes, J. M., and Peretsman, G., 1986. Water chemistry procedures aboard JOIDES Resolution—some comments. *ODP Tech. Note,* 5: College Station, TX (Ocean Drilling Program).

Gieskes, J. M., Elderfield, H., Lawrence, J. R., Johnson, J., Meyers, B., and Campbell, A., 1982. Geochemistry of interstitial waters and sediments, Leg 64, Gulf of California. *In* Curray, J. R., Moore, D. G., et al., *Init. Repts. DSDP,* 64: Washington (U.S. Govt. Printing Office), 675–694.

Hawkins, J. W., 1976. Petrology and geochemistry of basaltic rocks of the Lau Basin. *Earth Planet Sci. Lett.*, 28:283–297.

Hays, J. D., 1970. Stratigraphy and evolutionary trends of Radiolaria in North Pacific deep-sea sediments. *Geol. Soc. Am. Mem.*, 126: 185–218.

Hays, J. D., and Shackleton, N. J., 1976. Globally synchronous extinction of radiolarian *Stylatractus universus*. *Geology,* 4:649–652.

Heier, K. S., and Billings, G. K., 1970. Rubidium. *In* Wedepohl, K. H. (Ed), *Handbook of Geochemistry* (Vol. 2): Berlin (Springer-Verlag).

Hey, R., 1977. A new class of "pseudofaults" and their bearing on plate tectonics. *Earth Planet Sci. Lett.*, 37:321–325.

Hirata, N., Kinoshita, H., Suyehiro, K., Suyemasu, M., Matsuda, N., Ouchi, T., Katao, H., Koresawa, S., and Nagumo, S., 1987. Report on the DELP 1985 cruises in the Japan Sea, part II: seismic refraction experiment conducted in the Yamato Basin, southeast Japan Sea. *Bull. Earthquake Res. Inst., Univ. Tokyo,* 62:347–365.

Hirata, N., Tokuyama, H., and Chung, T. W., in press. An anomalously thick layering of the crust of the Yamato Basin, southeastern Japan Sea: the final stage of back-arc spreading. *Tectonophysics.*

Honza, E. (Ed.), 1979. Geological investigation of the Japan Sea. April–June 1978 (GH78-2 Cruise). *Cruise Rep., Geol. Surv. Japan,* 13:1–99.

Hyndman, R. D., von Herzen, R. P., Erickson, A. J., and Jolivet, J., 1977. Heat-flow measurements DSDP Leg 37. *In* Aumento, F., Melson, W. G., et al., *Init. Repts. DSDP,* 37: Washington (U.S. Govt. Printing Office), 347–362.

Ichikawa, M., 1971. Reanalysis of mechanism of earthquakes which occurred in and near Japan, and statistical studies on the nodal plane solutions obtained, 1929–1968. *Geophys. Mag.,* 35:207–273.

Ishii, T., Yamashita, S., Kobayashi, H., Kitamura, A., Shimizu, T., Konishi, K., Tsuchi, R., and Kobayashi, K., 1988. Description of dredged samples from Erimo Seamount and Meiyo-Daini Seamount (Japan Sea), during KH 86-2 cruise. *In* Kobayashi, K. (Ed.), *Geophysical and Geological Investigation of the Northeastern part of the Japan Sea and Japan Trench. Prelim. Rep. Hakuho Maru Cruise KH 86-2 (April 21–May 15, 1986),* 60–64.

Ishikawa, Y., Takeo, M., Hamada, N., Katsumata, M., Satake, K., Abe, K., Kikuchi, M., Sudo, K., Takahashi, M., Kashiwabara, S., and Mikami, N., 1984. Mechanism of the central Japan Sea earthquake, 1983. *Chikyu (The Earth Monthly),* 6:11–17 (in Japanese).

Iwabuchi, Y., 1968. Submarine geology of the southeastern part of the Japan Sea. *Tohoku Univ., Inst. Geol. Paleontol. Contr.,* 66:1-76 (in Japanese).

Johnson, D. A., and Nigrini, C. A., 1985. Synchronous and time-transgressive Neogene radiolarian events in the tropical Indian and Pacific Oceans. *Mar. Micropaleontol.,* 9:489–523.

Kaneoka, I., 1986. Constraints on the time of the evolution of the Japan Sea based on radiometric ages. *J. Geomag. Geoelectr.,* 38: 475–485.

Kaneoka, I., and Yuasa, M., 1988. ^{40}Ar-^{39}Ar age studies on igneous rocks dredged from the central part of the Japan Sea during the GH78-2 cruise. *Geochem. J. Japan,* 22:195–204.

Kaneoka, I., Notsu, K., Takigami, Y., Fujioka, K., and Sakai, H., in press. Constraints on the evolution of the Japan Sea based on ^{40}Ar-^{39}Ar ages and Sr isotopic ratios for volcanic rocks of Yamato Seamount chain in the Japan Sea. *Earth Planet. Sci. Lett.*

Karig, D. E., Ingle, J. C., Jr., et al., 1975. *Init. Repts. DSDP,* 31: Washington, (U.S. Govt. Printing Office).

Katz, B. J., 1983. Limitations of rock eval pyrolysis for typing organic matter. *Org. Geochem.,* 4:195–199.

Kobayashi, K., and Nomura, M., 1972. Iron sulfide in the sediment cores from the Sea of Japan and their geophysical implications. *Earth Planet. Sci. Lett.,* 16:200–206.

Koizumi, I., 1979. The geological history of the Sea of Japan–based on sediments and microfossils. *Nihonkai (Japan Sea),* 10:69–90 (in Japanese).

Koizumi, I., and Tanamura, Y., 1985. Neogene diatom biostratigraphy of the middle latitude western North Pacific, Deep Sea Drilling Project Leg 86. *In* Heath, G. R., Burckle, L. H., et al., *Init. Repts. DSDP,* 86: Washington (U.S. Govt. Printing Office), 269–300.

Ludwig, W. J., Murauchi, S., and Houtz, R. E., 1975. Sediments and structure of the Japan Sea. *Geol. Soc. Am. Bull.*, 86:651–664.

Manheim, F. T., and Sayles, F. L., 1974. Composition and origin of interstitial waters of marine sediments based on deep sea drill cores. *In* Goldberg, E. D. (Ed.), *The Sea* (Vol. 5): New York (Wiley), 527–568.

Matoba, Y., 1984. Paleoenvironment of the Sea of Japan. *In* Oertli, H. J. (Ed.) Benthos '83, 2nd Int. Symp. on Benthic Foraminifera (Pau, April 1983), 409–414.

McDuff, R. E., and Gieskes, J. M., 1976. Calcium and magnesium profiles in DSDP interstitial waters: diffusion or reaction? *Earth Planet. Sci. Lett.,* 33:1–10.

Michael, P. J., and Chase, R. L., 1987. The influence of primary magma composition, H_20 and pressure on mid-ocean ridge basalt differentiation. *Contrib. Mineral. Petrol.,* 96:245–263.

Nakamura, K., 1983. Possible nascent trench along the eastern Japan Sea as the convergent boundary between Eurasian and North American plates. *Bull. Earthquake Res. Inst. Univ. Tokyo,* 58:711–722 (in Japanese with English abstract).

Okada, H., and Niitsuma, N., 1989. Detailed paleomagnetic records during the Brunhes-Matuyama geomagnetic reversal, and a direct determination of depth lag for magnetization in marine sediments. *Phys. Earth Planet Int.,* 56:133–150.

Oremland, R. S., and Taylor, B. F., 1978. Sulfate reduction and methanogenesis in marine sediments. *Geochim. Cosmochim. Acta.*, 42: 209–214.

Parsons, B., and Sclater, J. G., 1977. An analysis of the variation of oceanic bathymetry and heat flow with age. *J. Geophys. Res.*, 82: 803–827.

Pearce, J. A., Alabaster, T., Shelton, A. W., and Searle, M. P., 1981. The Oman ophiolite as a Cretaceous arc-basin complex: Evidence and implications. *Phil. Trans. R. Soc. Lond.*, A300, 299–317.

Peters, K. E., 1986. Guidelines for evaluating petroleum source rock using programmed pyrolysis. *AAPG Bull.*, 32:318–329.

Phillips, R. P., 1964. Seismic refraction studies in the Gulf of California. *In* van Andel, Tj. H., and Shor, G. G. (Eds.), *Marine Geology of the Gulf of California.* AAPG Mem., 3:90–121.

Ratcliffe, E. H., 1960. The thermal conductivities of ocean sediments. *J. Geophys. Res.*, 65:1535–1541.

Reynolds, R. A., 1980. Radiolarians from the western North Pacific, Leg 57, Deep Sea Drilling Project. *In* Scientific Party, *Init. Repts. DSDP,* 56, 57 (Pt. 2): Washington (U.S. Govt. Printing Office), 735–769.

Saunders, A. D., and Tarney, J., 1984. Geochemical characteristics of basaltic volcanism within back-arc basins. *In* Kokelaar, B. P., and Howells, M. F. (Eds.), *Marginal Basin Geology*: Oxford, U.K. (Blackwell Scientific Publications), 59–76.

Schrader, H.-J., and Schuette, G., 1981. Marine diatoms. *In* Emiliani, C. (Ed.), *The Sea* (Vol. 7): New York (Wiley), 1179–1232.

Seno, T., and Eguchi, T., 1983. Seismotectonics of the western Pacific region. *In* Hilde, T.W.C., and Uyeda, S. (Eds.), *Geodynamics of the western Pacific.* Am. Geophys. Union-Geol. Soc. Am. Geodynamics Ser., 11:5–40.

Sinton, J. M., and Fryer, P., 1987. Mariana Trough lavas from 18°N: implications for the origin of backarc basin basalts. *J. Geophys. Res.*, 92:12,782–12,802.

Srivastava, S. P., Arthur, M., Clement, B., et al., 1987. *Proc. ODP, Init. Repts.,* 105: College Station, TX (Ocean Drilling Program).

Steiness, E., Heier, K. S., and Billings, G. K., 1972. Lithium. *In* Wedepohl, K. H. (Ed.), Handbook of Geochemistry (Vol. 2): Berlin (Springer-Verlag).

Stoeser, D. B., 1975. Igneous rocks from Leg 30 of the Deep Sea Drilling Project. *In* Andrews, J. E., Packham, G., et al., *Init. Repts. DSDP,* 30: Washington (U.S. Govt. Printing Office), 401–414.

Suess, E., von Huene, R., et al., 1988. *Proc. ODP, Init. Repts.,* 112: College Station, TX (Ocean Drilling Program).

Sun, S.-S., Nesbitt, R. W., and Sharaskin, A. Y., 1979. Geochemical characteristics of mid-ocean ridge basalts. *Earth Planet. Sci. Lett.*, 44:119–138.

Tamaki, K., 1986. Age estimation of the Japan Sea on the basis of stratigraphy, basement depth, and heat flow data. *J. Geomag. Geoelectr.*, 38:427–446.

_____, 1988. Geological structure of the Japan Sea and its implications. *Bull. Geol. Surv. Japan,* 39:269–365.

Tamaki, K., and Honza, E., 1985. Incipient subduction and obduction along the eastern margin of the Japan Sea. *Tectonophysics,* 119: 381–406.

Tamaki, K., Honza, E., Yusa, M., Nishimura, K., and Murakami, F., 1981. Geological map of the central Japan Sea. Marine Geol. Map Ser. 15, Japan Geol. Surv. Scale is 1:1,000,000.

Tamaki, K., Kobayashi, K., Isezaki, N., Sayanagi, K., Nakanishi, N., and Park, C. H., 1988. Measurement of geomagnetic total force by a proton precession magnetometer. *In* Kobayashi, K. (Ed.), *Geophysical and geological investigation of the northeastern part of the Japan Sea and Japan Trench. Prelim. Rep. Hakuho Maru Cruise KH 86-2 (April 21–May 15, 1986),* 7–9.

Tokuyama, H., Suyemasu, M., Tamaki, K., Nishiyama, E., Kuramoto, S., Suyehiro, K., Kinoshita, H., and Taira, A., 1987a. Report on DELP 1985 cruises in the Japan Sea Part III: seismic reflection studies in the Yamato Basin and the Yamato Rise area. *Bull. Earthquake Res. Inst., Univ. Tokyo,* 62:367–390.

_____, 1987b. Report on DELP 1985 cruises in the Japan Sea Part II: Seismic experiment conducted in the Yamato Basin, Southeast Japan Sea. *Bull. Earthquake Res. Inst., Univ. Tokyo,* 62:347–365.

Tsuchiya, N., 1988. Distribution and chemical composition of the middle Miocene basaltic rocks in Akita-Yamagata oil fields of northeastern Japan. *J. Geol. Soc. Japan,* 94:591–608 (Japanese with English abstract).

_____, 1989. Submarine basalt volcanism of Miocene Aosawa Formation in the Akit-Yamagata oil field basin, back-arc region of northeast Japan. *Mem. Geol. Soc. Japan,* 32:399–408.

Von Herzen, R. P., and Maxwell, A. E., 1959. The measurement of thermal conductivity of deep-sea sediments by a needle probe method. *J. Geophys. Res.*, 65:1535–1541.

Wlotzka, F., 1972. Nitrogen. *In* Wedepohl, K. H (Ed.), *Handbook of Geochemistry* (Vol. 2): Berlin (Springer-Verlag).

Wyllie, M.R.J., Gregory, A. R., and Gardner, L. W., 1956. Elastic wave velocities in heterogeneous and porous media. *Geophysics,* 21:41–70.

Yamano, M., Uyeda, S., Uyeshima, M., Kinoshita, M., Fujisawa, H., Nagihara, S., Boh, R., and Fujisawa, 1987. Report on DELP 1985 cruises in the Japan Sea, Part V: Heat flow measurements. *Bull. Earthquake Res. Inst., Univ. Tokyo,* 62:417–432.

Yamano, M., and Uyeda, S., 1988. Heat flow. *In* Nairn, E. M., Stehli, F. G., and Uyeda, S. (Eds.), *The Ocean Basins and Margins,* 7B: 523–557.

Yamashita, S., 1988. Andesitic lava recovered from Meiyo-Daini Seamount in Yamato Basin during KH 86-2 cruise. *In* Kobayashi, K. (Ed.), *Geophysical and geological investigation of the northeastern part of the Japan Sea and Japan Trench. Prelim. Rep. Hakuho Maru Cruise KH 86-2 (April 21–May 15, 1986),* 67–74.

Yasui, M., and Watanabe, T., 1965. Studies of the thermal state of the Earth: the 16th paper: terrestrial heat flow in the Japan Sea (1). *Bull. Earthquake Res. Inst., Univ. Tokyo,* 43:549–563.

Yasui, M., Kishii, T., Watanabe, T., and Uyeda, S., 1968. Heat flow in the Sea of Japan. *In* Knopoff, L., et al. (Eds.), *Crust and Upper Mantle of the Pacific Area.* Am. Geophys. Union Geophysical Monograph 12, 3–16.

Ms 127A-104

NOTE: All core description forms ("barrel sheets") and core photographs have been printed on coated paper and bound as Section 3, near the back of the book, beginning on page 425.

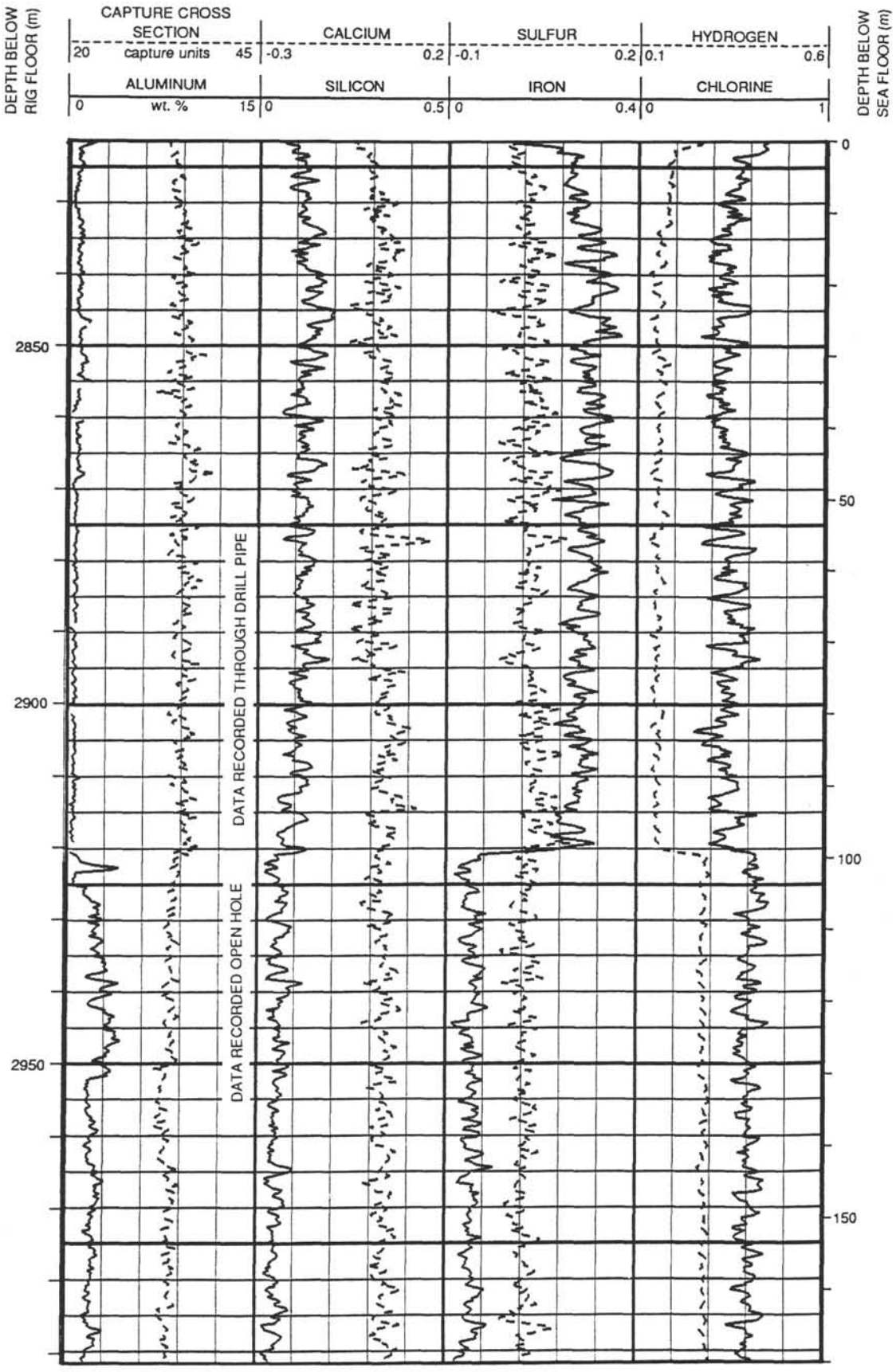

Figure 57. Geochemical logs from Hole 794B. Uncorrected element readings, capture cross section, and aluminum weight percent are displayed.

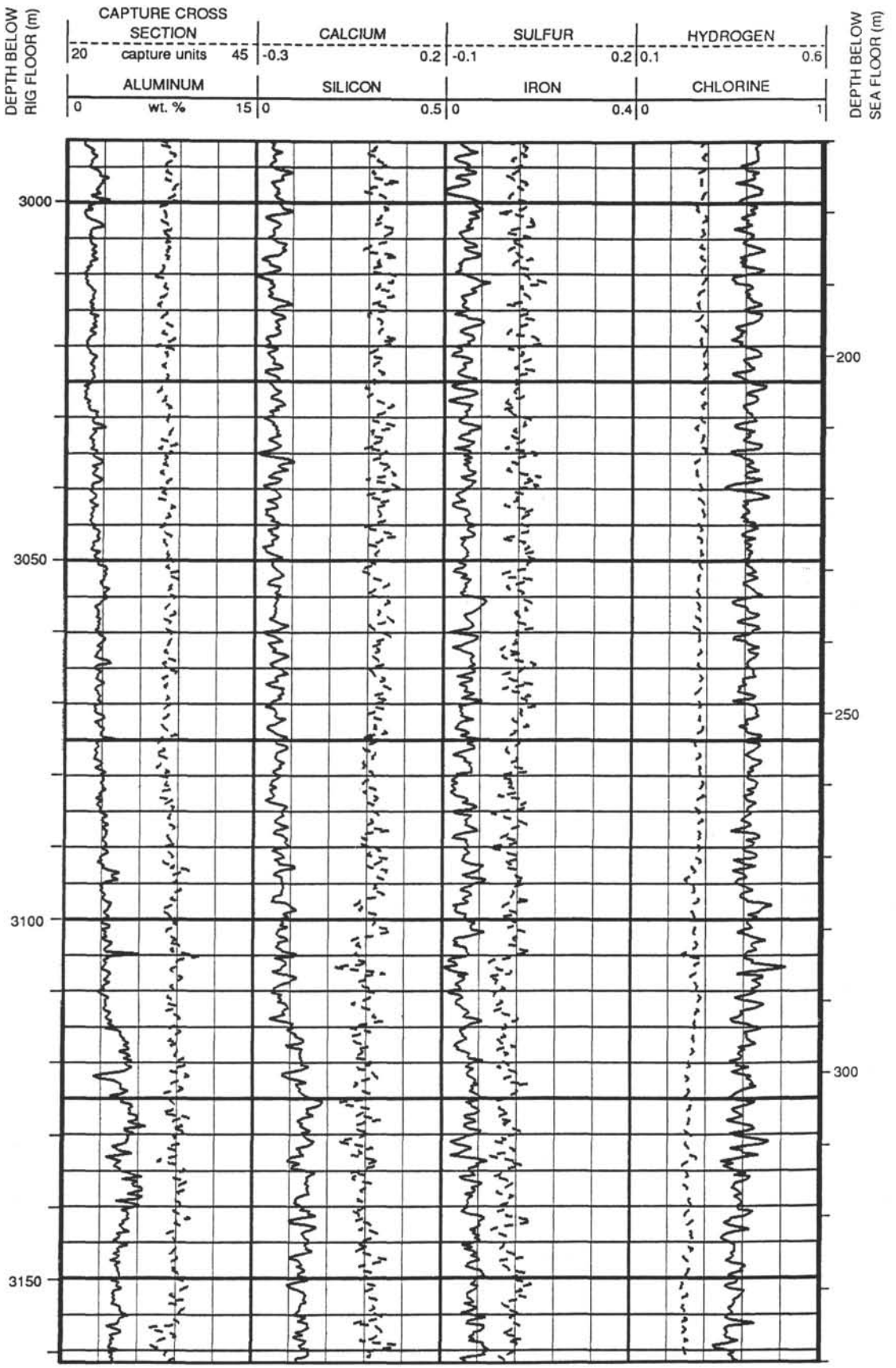

Figure 57 (continued).

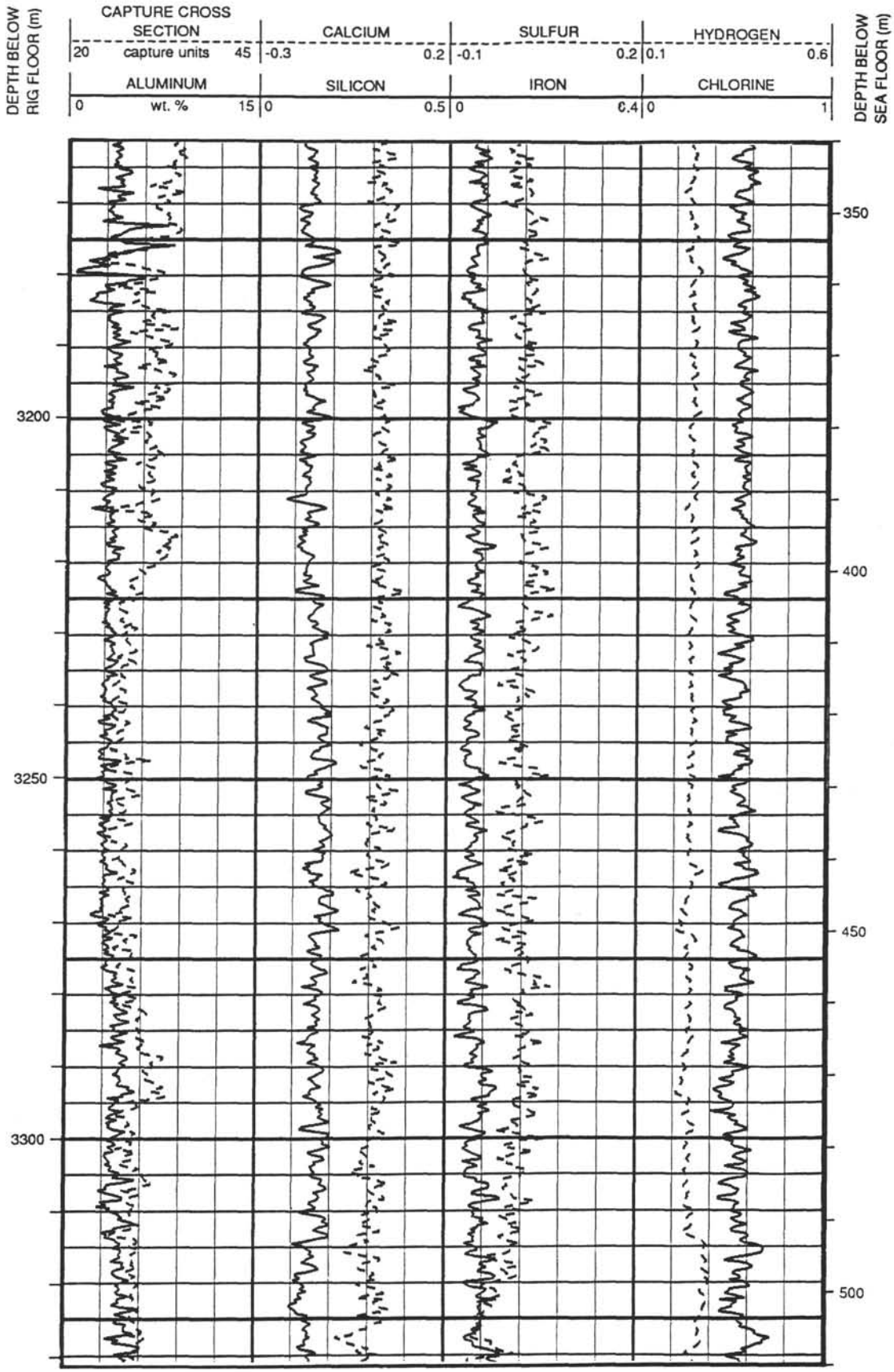

Figure 57 (continued).

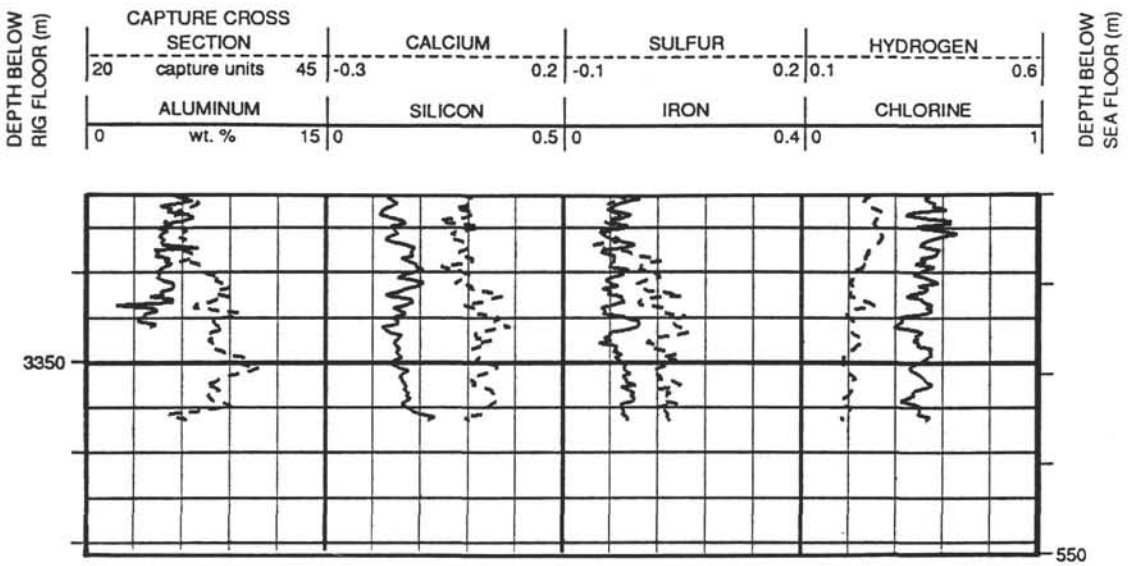

Figure 57 (continued).

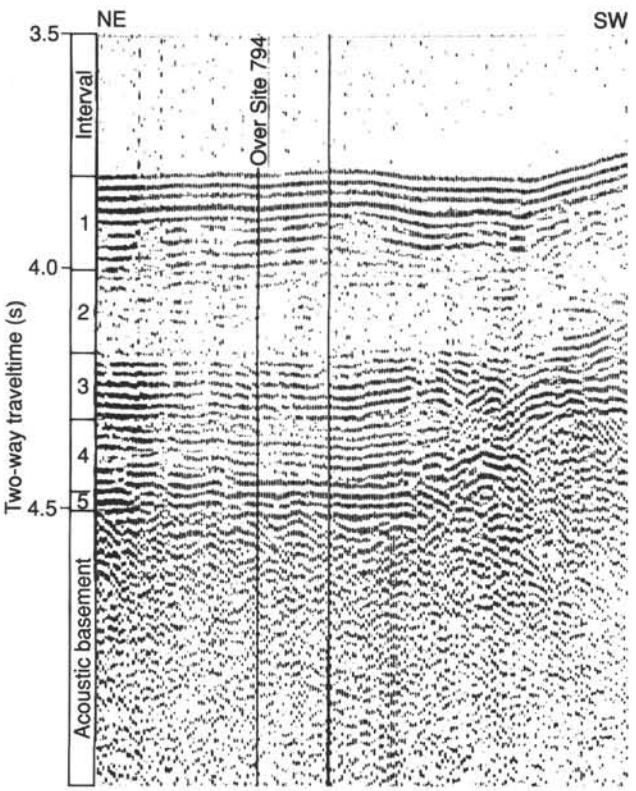

Figure 58. Detail of *JOIDES Resolution* single-channel seismic reflection record obtained during the approach to Site 794, with assignment of acoustic intervals. For track lines, see "Operations" section, this chapter.

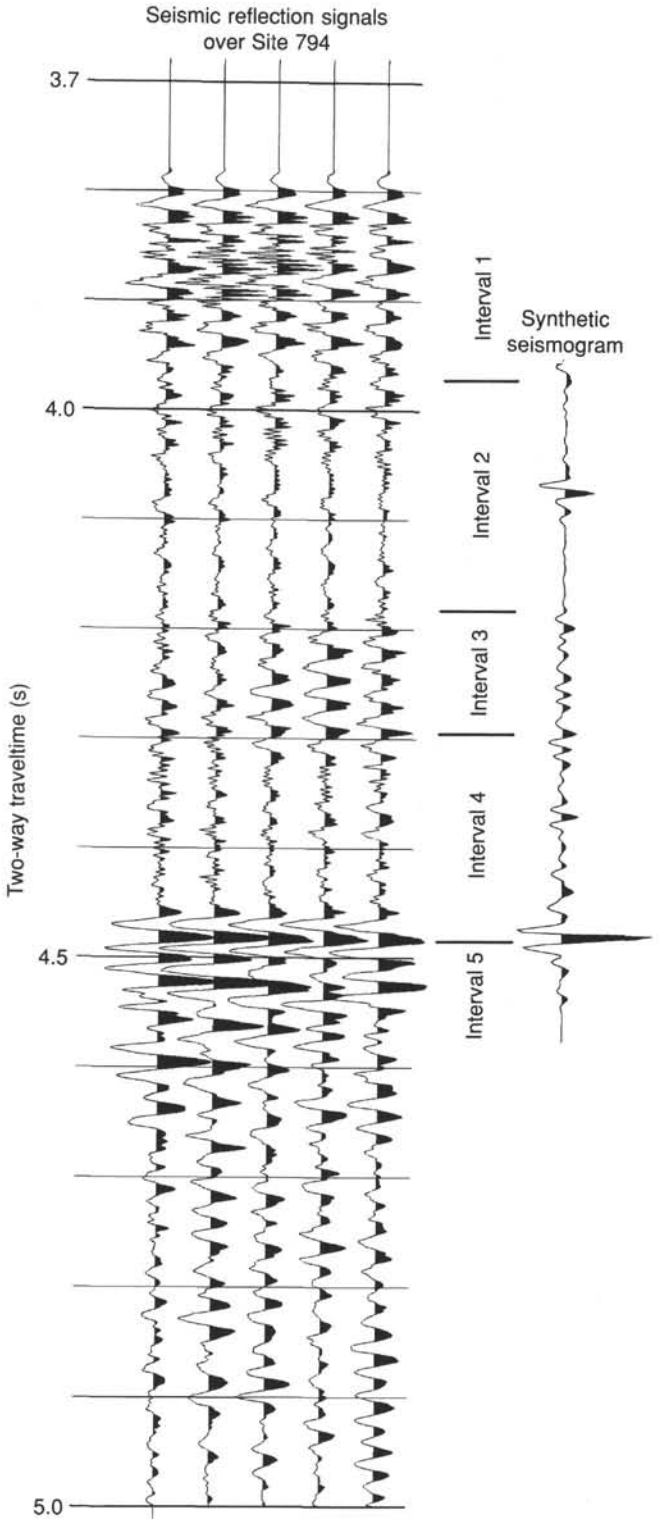

Figure 59. Correlation of the synthetic seismogram based on logging data in Hole 794B, with seismic reflection traces over Site 794 obtained during the site approach by the *JOIDES Resolution*. For track lines, see "Operations" section, this chapter.

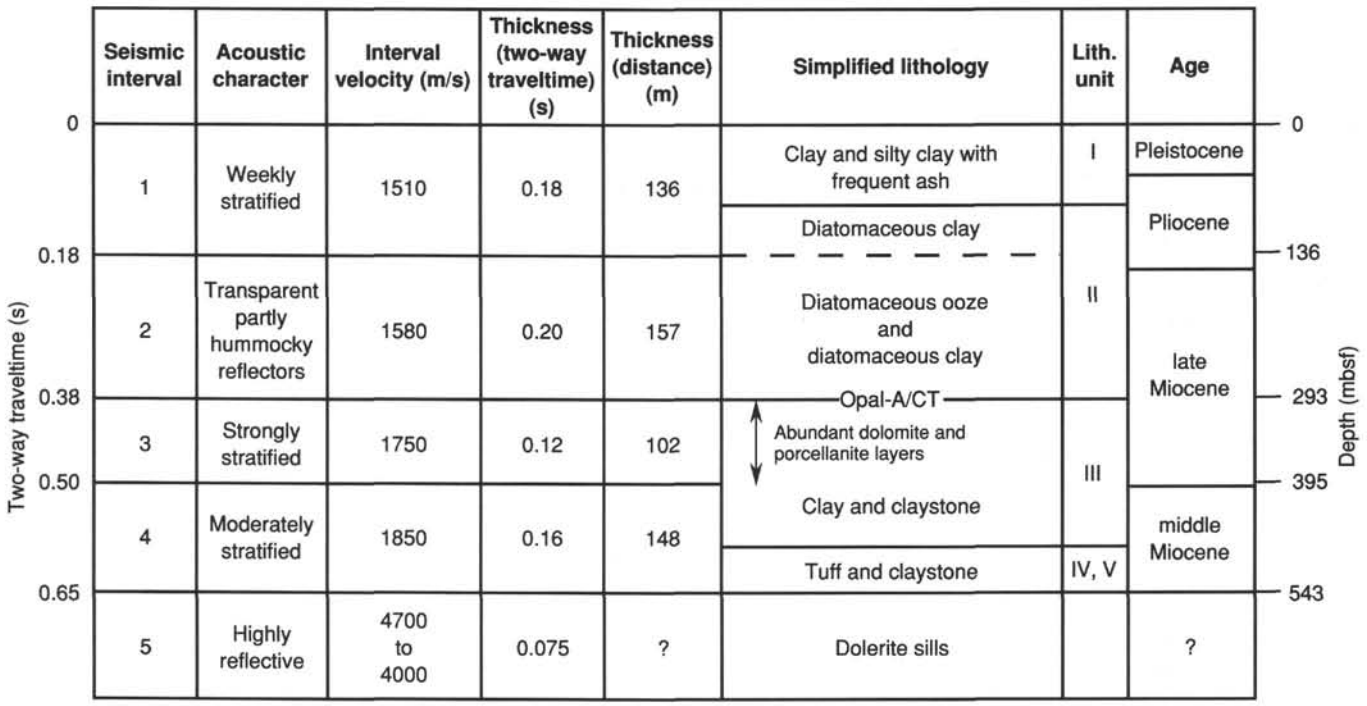

Figure 60. Summary of the seismic stratigraphy of Site 794 and its correlation with lithostratigraphy.

Summary Log for Site 794

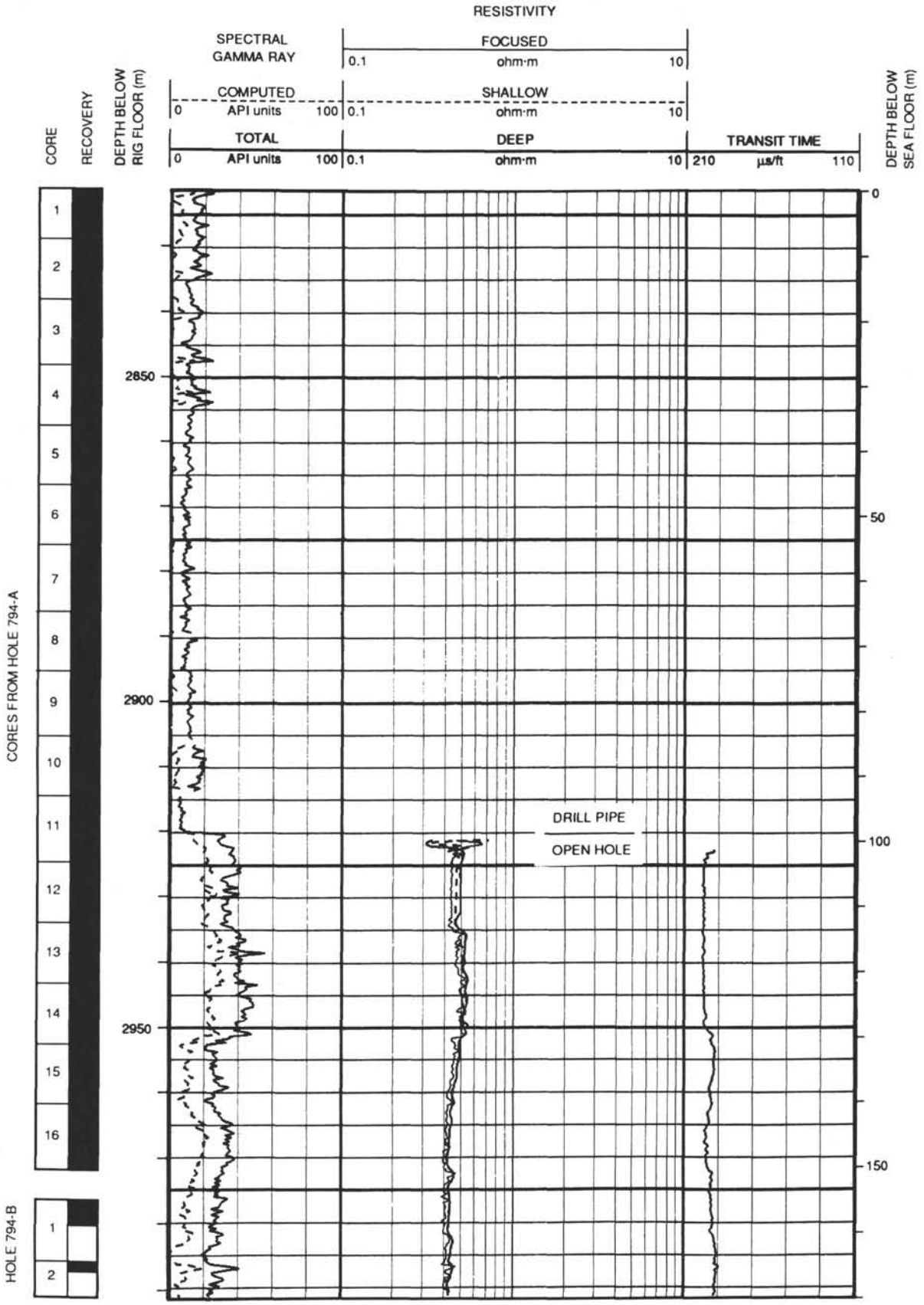

Summary Log for Site 794 (continued)

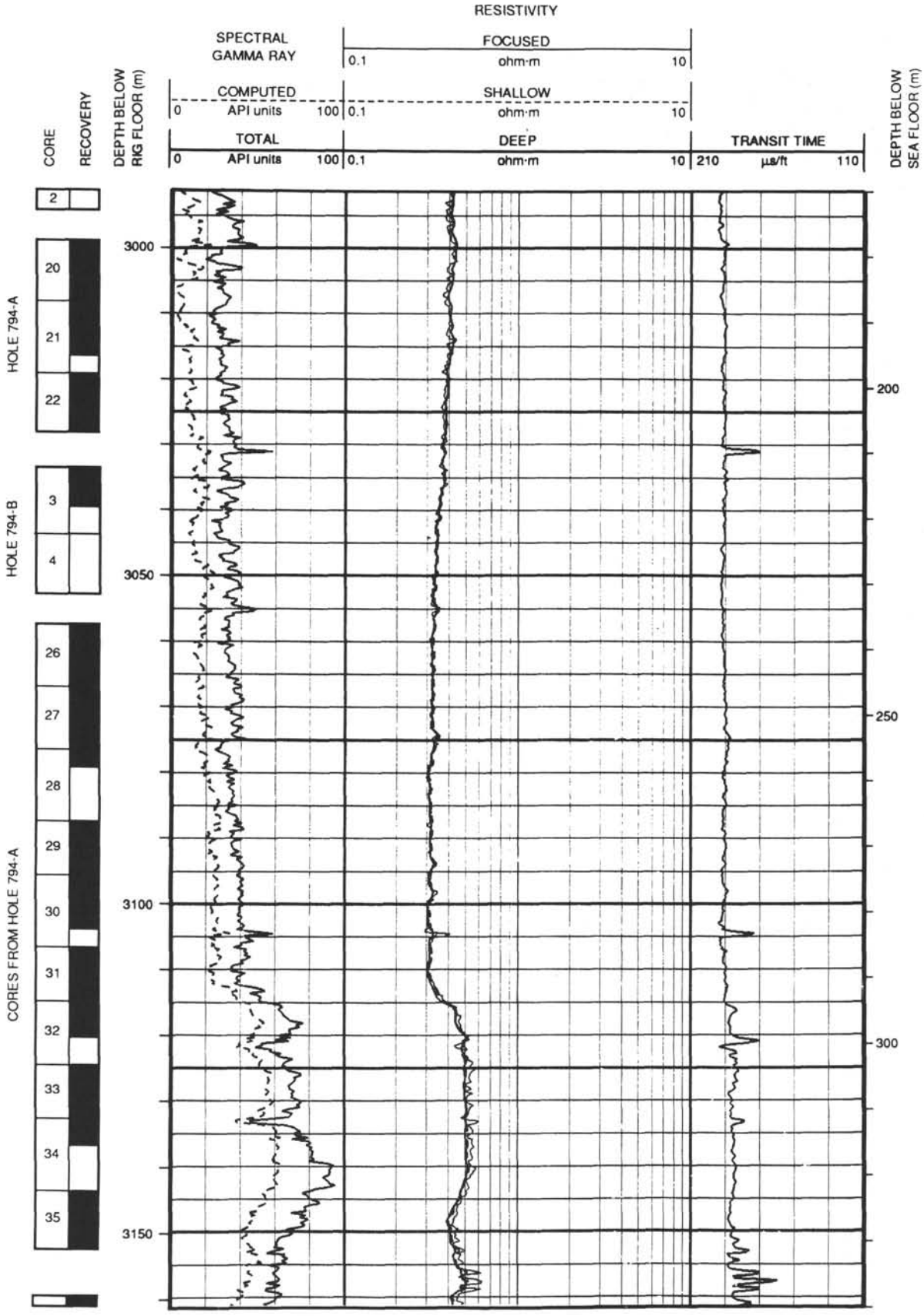

Summary Log for Site 794 (continued)

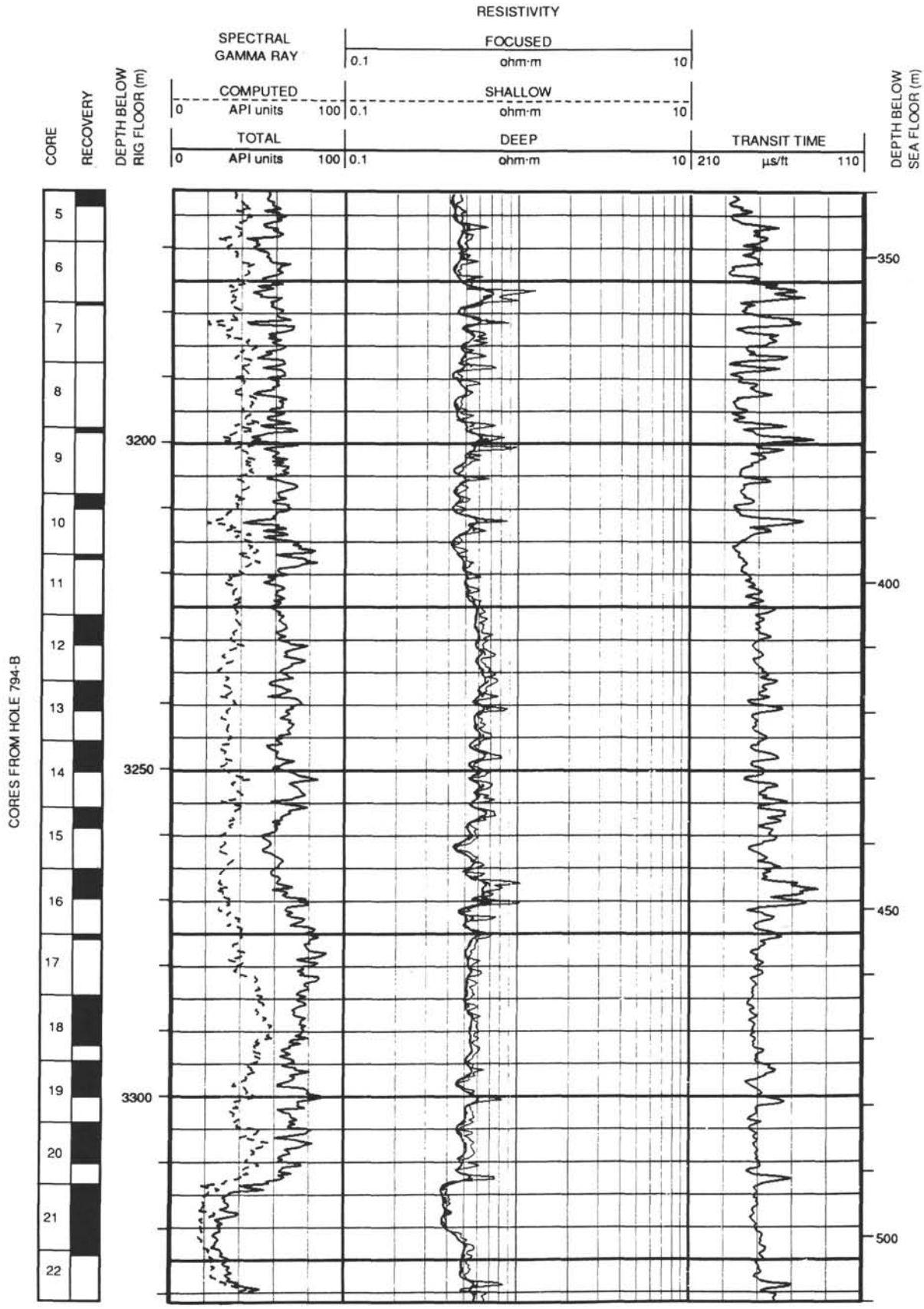

Summary Log for Site 794 (continued)

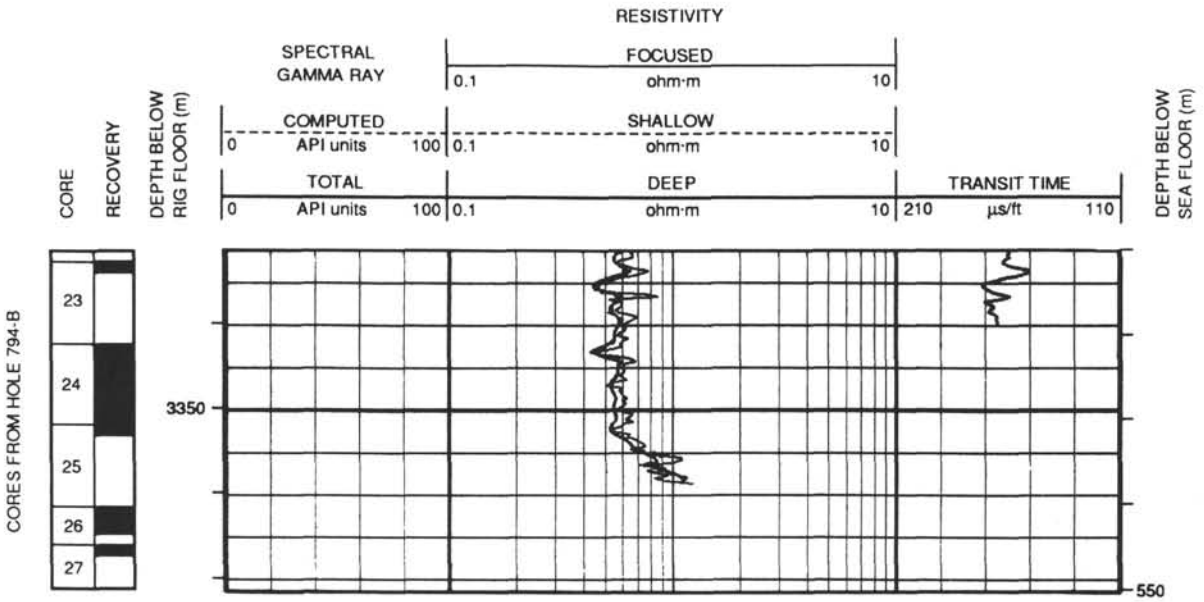

Summary Log for Site 794 (continued)

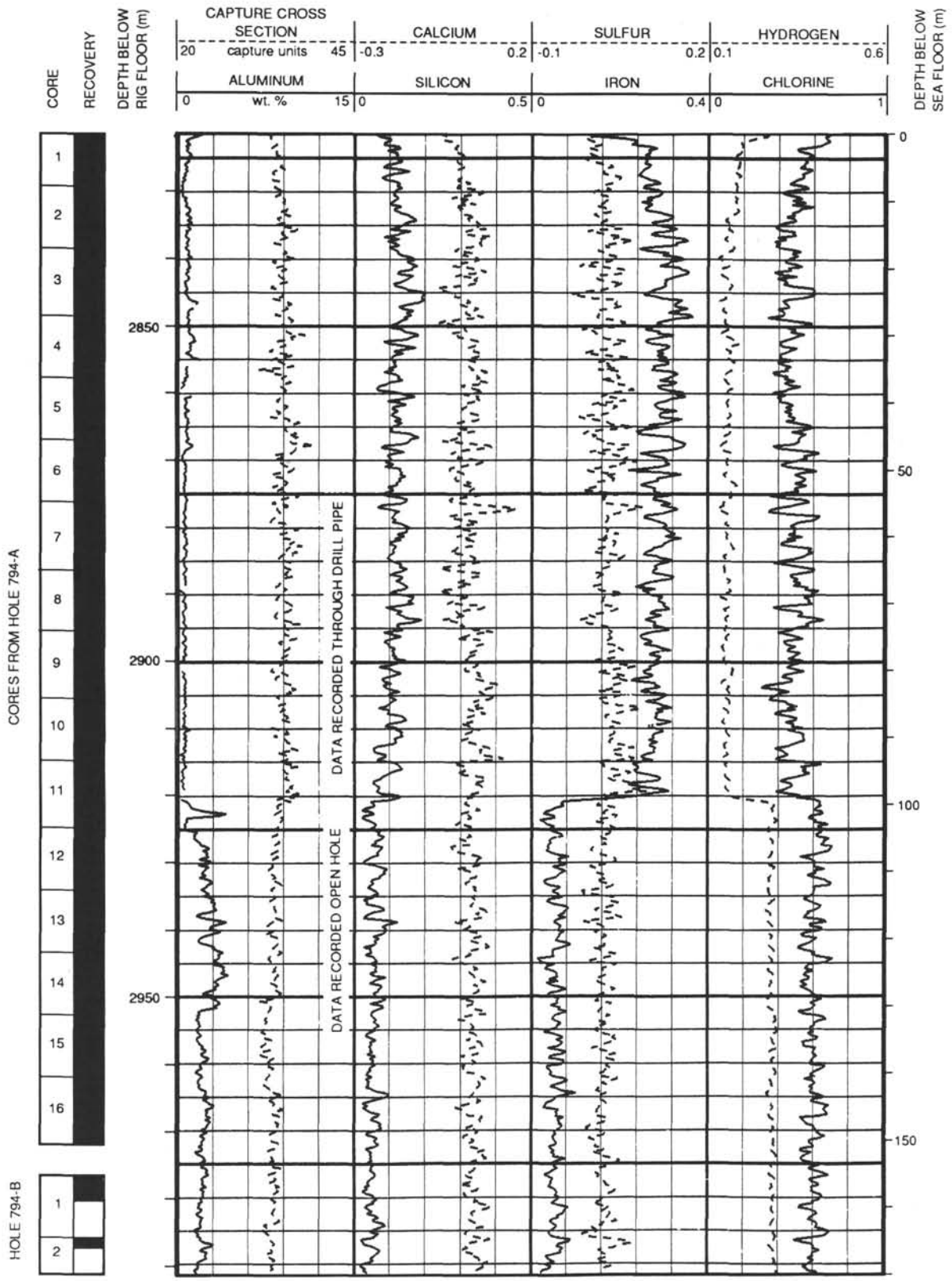

Summary Log for Site 794 (continued)

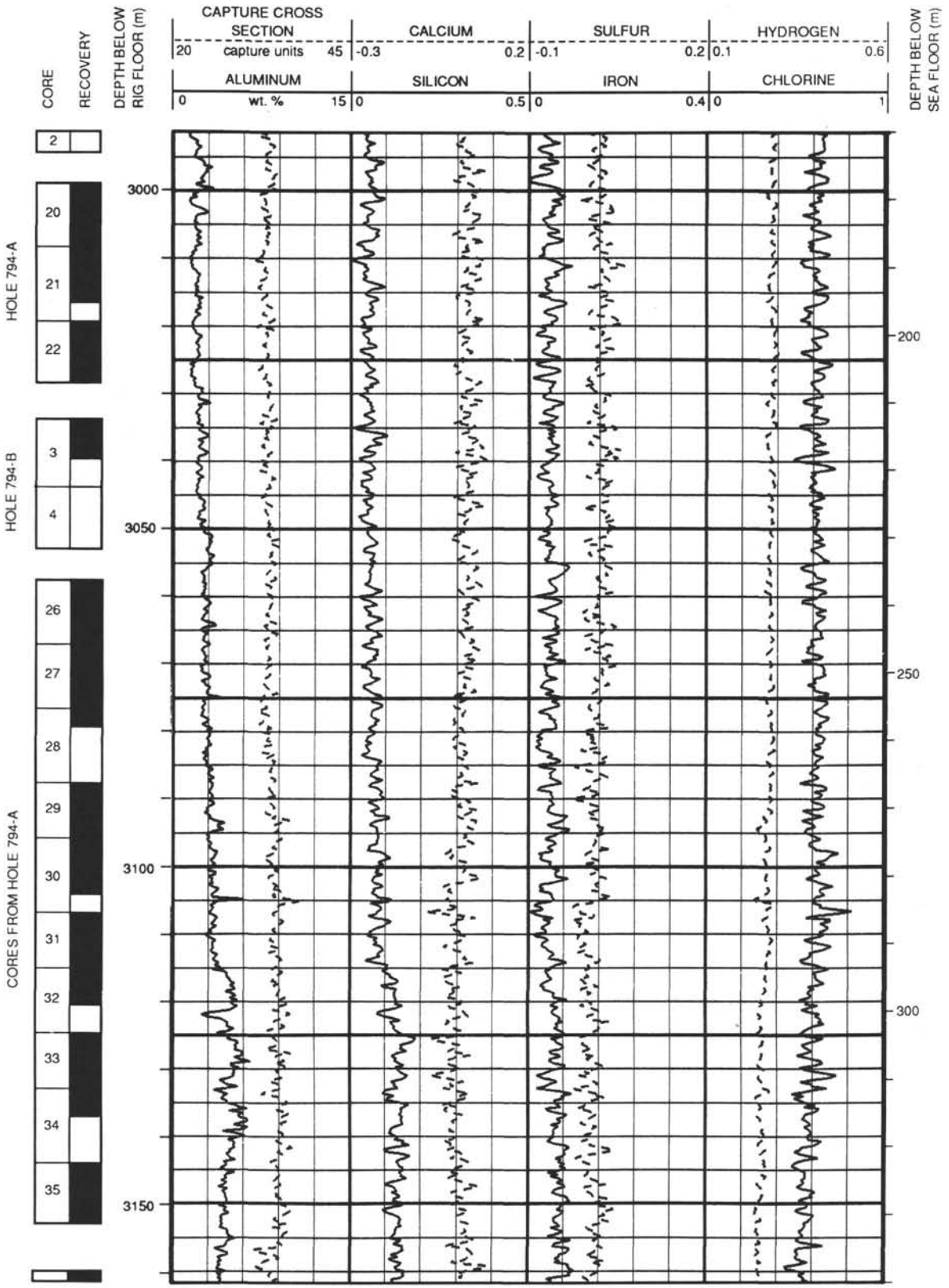

Summary Log for Site 794 (continued)

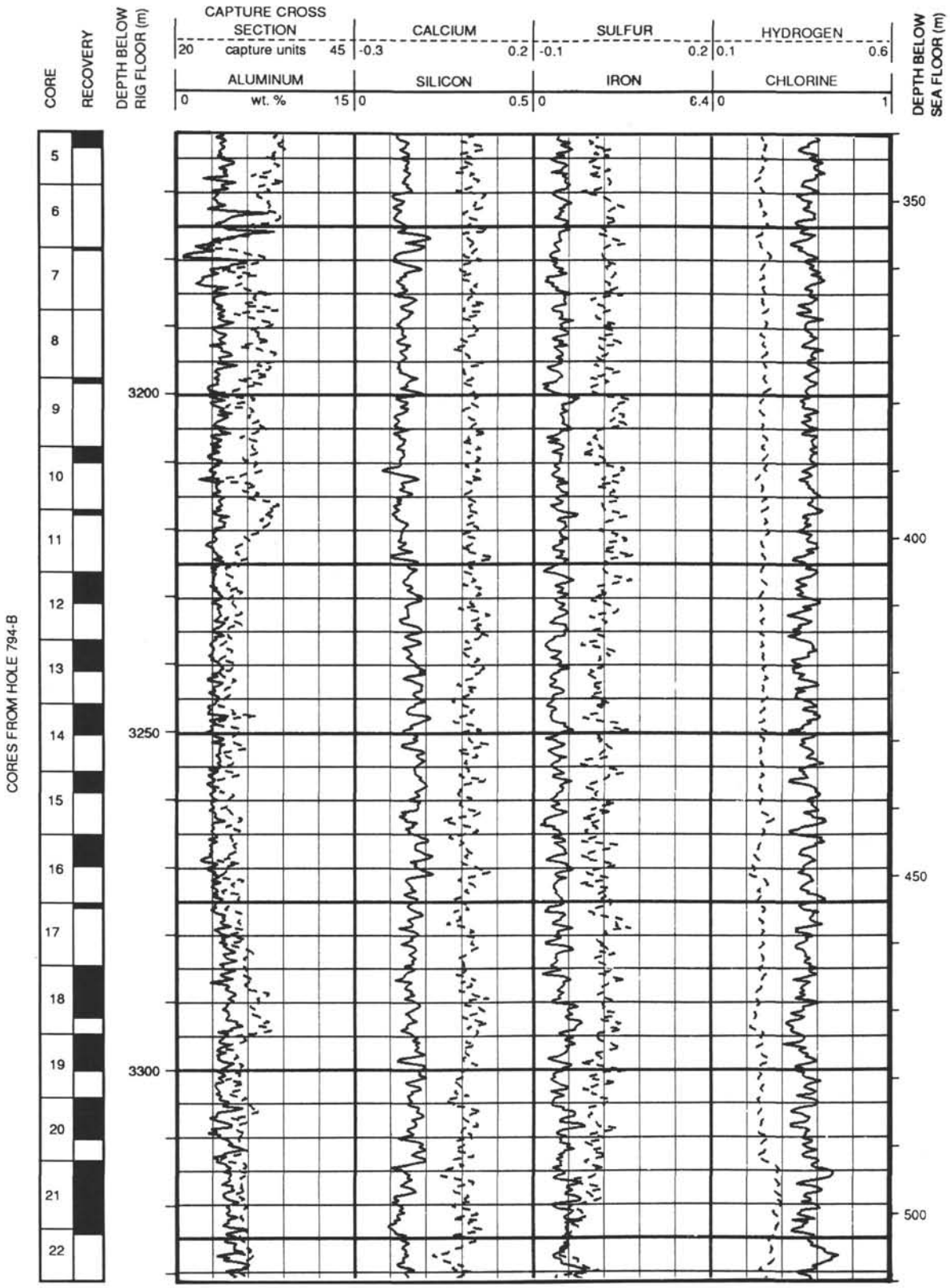

Summary Log for Site 794 (continued)

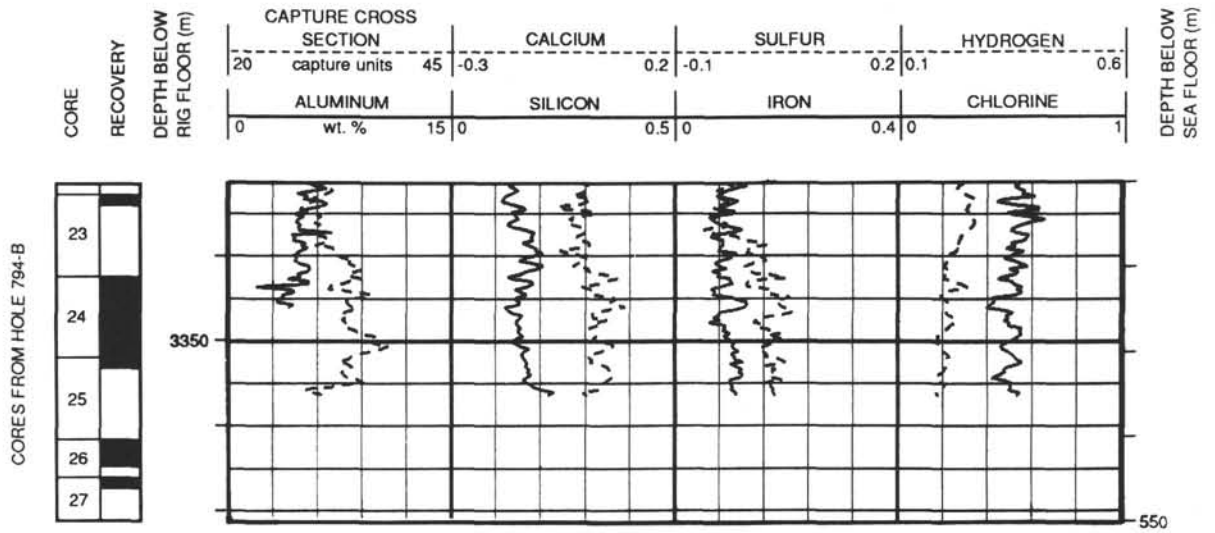

Summary Log for Site 794 (continued)

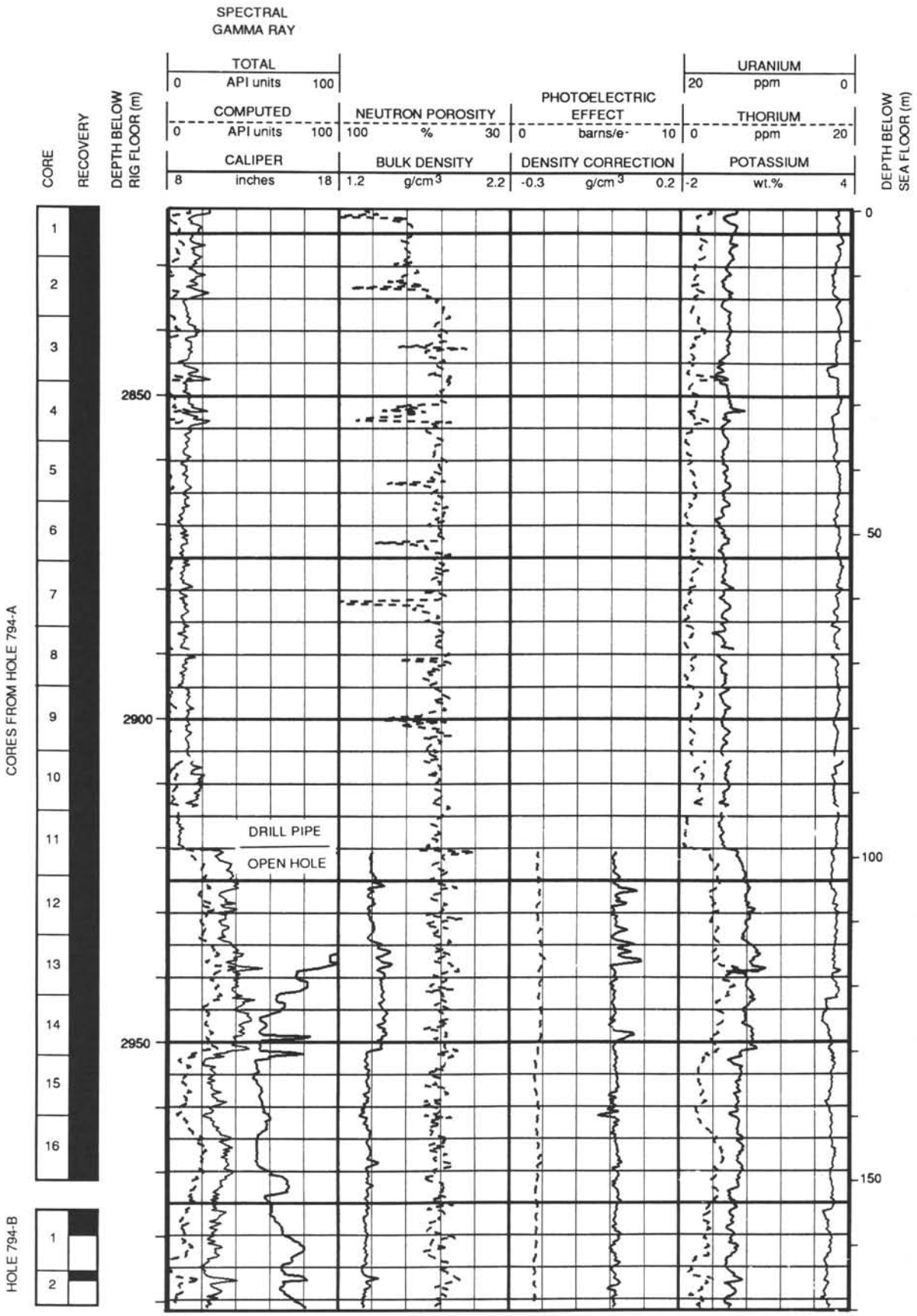

Summary Log for Site 794 (continued)

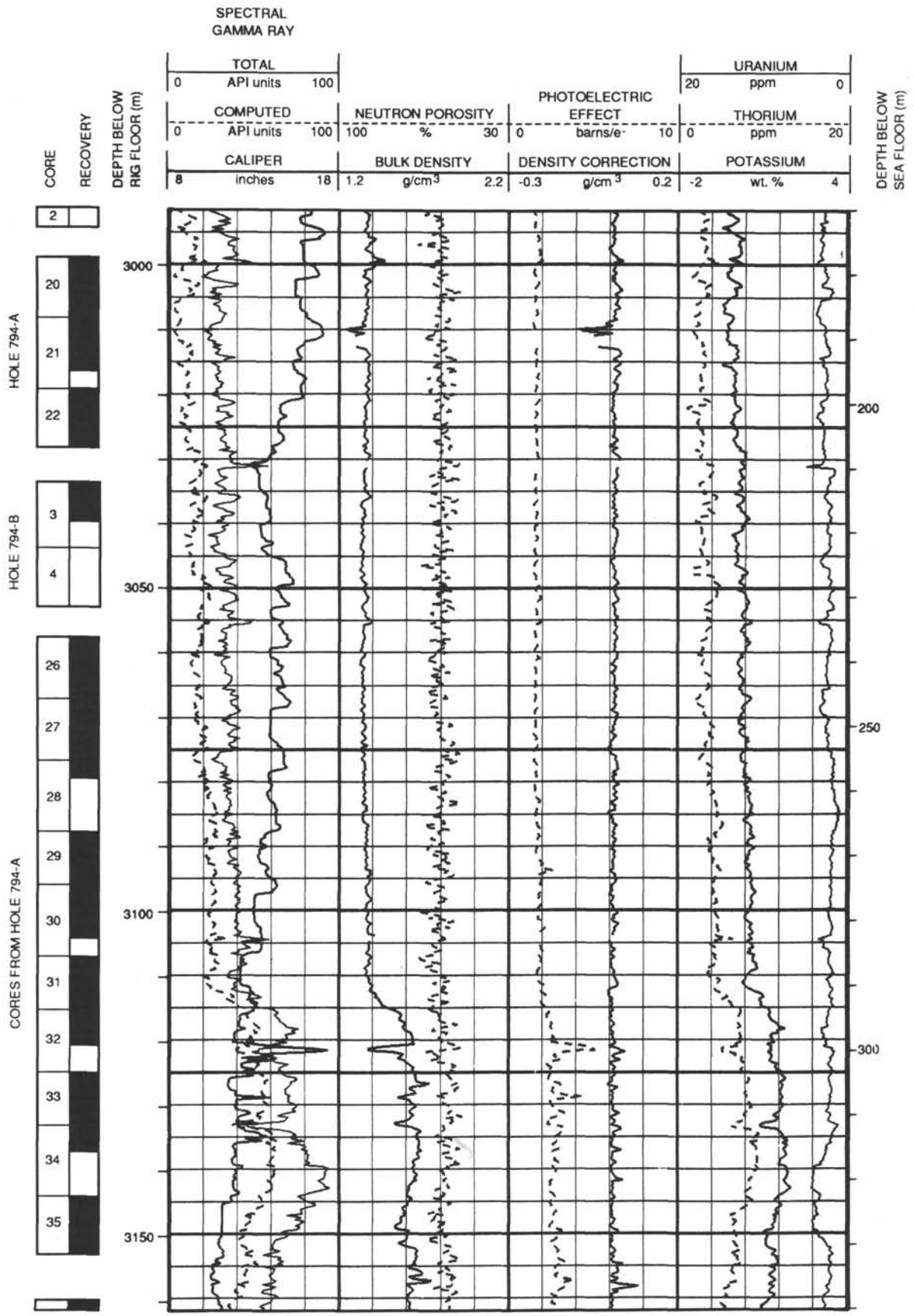

Summary Log for Site 794 (continued)

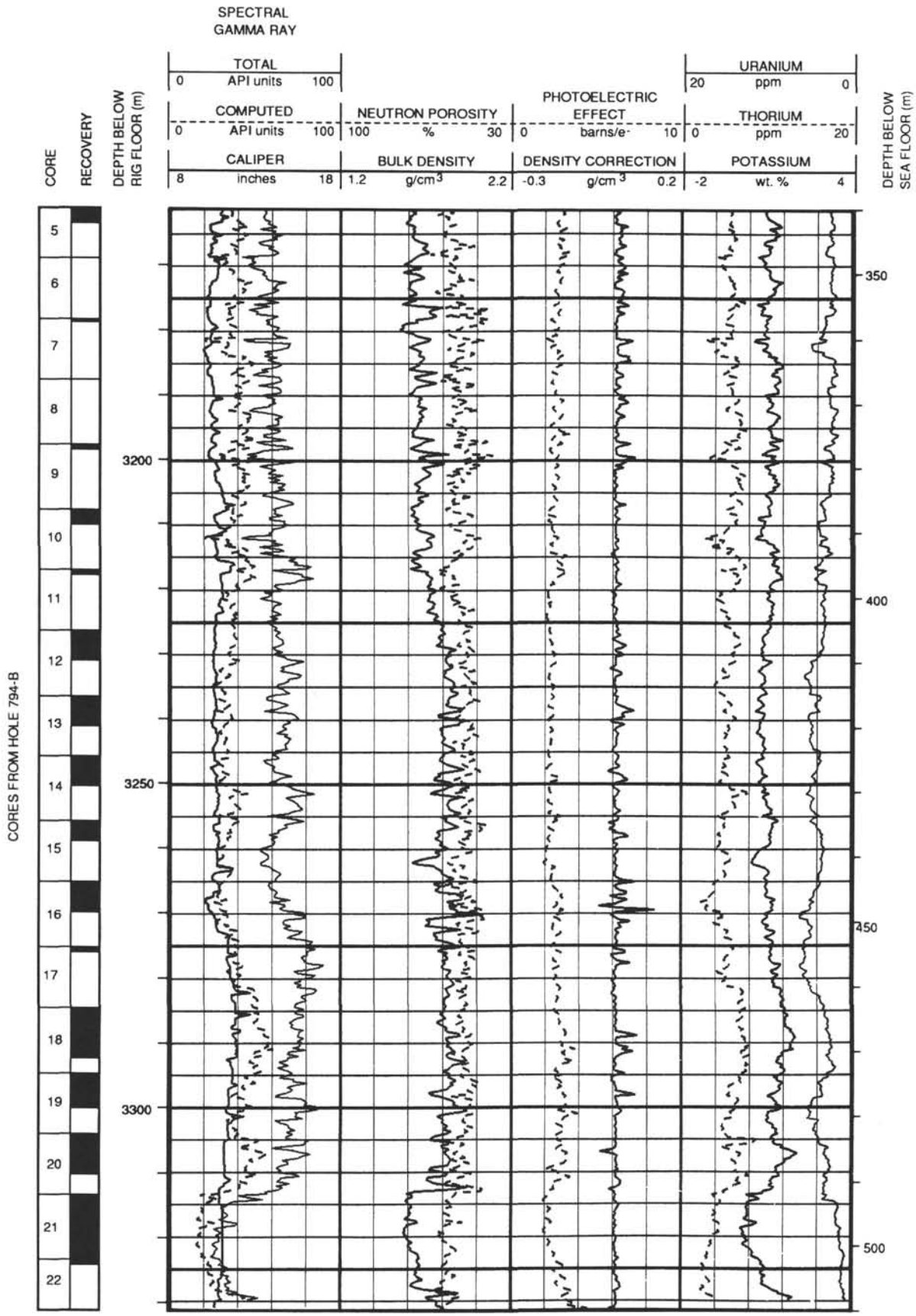

Summary Log for Site 794 (continued)